DEPARTMENT OF THE AIR FORCE

AIR UNIVERSITY

AIR FORCE INSTITUTE OF TECHNOLOGY

Wright-Patterson Air Force Base, Ohio

AFIT/DS/ENG/98-03

Optical Physics of Microcavity Surface Emitting Lasers

DISSERTATION

Michael J. Noble
Captain, USAF

AFIT/DS/ENG/98-03

The views expressed in this dissertation are those of the author and do not reflect the official policy or position of the Department of Defense or the United States Government.

AFIT/DS/ENG/98-03

Optical Physics of Microcavity Surface Emitting Lasers

DISSERTATION

Presented to the Faculty of the School of Engineering
of the Air Force Institute of Technology
Air University
In Partial Fulfillment of the
Requirements for the Degree of
Doctor of Philosophy

Michael J. Noble, B.S.E.E., M.S.E.E.
Captain, USAF

March, 1998

AFIT/DS/ENG/98-03

Optical Physics of Microcavity Surface Emitting Lasers

Michael J. Noble, B.S.E.E., M.S.E.E.

Captain, USAF

Approved:

James A. Lott Research Advisor	Date
Peter J. Collins Committee Member	Date
John P. Loehr Committee Member	Date
Won B. Roh Committee Member	Date
David E. Weeks Committee Member	Date
Robert L. Hengehold Dean's Representative	Date

Robert A. Calico, Jr
Dean

Acknowledgements

"Remember, no man is a failure who has friends."

... Clarence *It's a wonderful life*

Dissertation research is *not* a one man job. I owe an enormous debt of gratitude to many people, without whose help this dissertation and my graduation would not have been possible. I received most of my guidance from my advisor, Maj. Jim Lott, and my sponsor, Dr. John Loehr. I thank Jim for his unwavering support, and belief in me and this research. I thank John for teaching me how to be a good theoretician. I would also like to thank the rest of my committee: Prof. Dave Weeks for exposing me to the exciting physics of thresholdless lasers, Prof. Won Roh for providing senior oversight of this work, and Maj. Pete Collins for helping me with the electromagnetic theory used extensively in this research.

Since my research was entirely theoretical, I relied heavily on the computer resources at AFIT and the major shared resource center (MSRC). Therefore, I owe a tremendous amount of thanks to the people who "control the spice," the system administrators and MSRC scientists: Dan Zambon, Dave Doak, Tony Schooler, Gary Mauersberger, and the rest of the AFIT administrators; Dr. Paul Sotirelis, Dr. C.J. Suchyta, Dan Schornak, and the rest of the MSRC staff.

The people who run the show *aren't* the professors and scientists, but rather the administrative folks. Thanks goes to the fine administrators whom I've come to rely on over the past five years: Diana Jordan, Mary Jane McCormick, Angela Wilson, and Carolyn Mallory.

I have had the opportunity to become involved with several excellent extracurricular organizations during my stay at AFIT. A special thanks goes to: the Wright Patterson Tae Kwon Do club, for giving me—a much needed—opportunity to blow off steam; North Coast and team Savage Guacamole, for providing a lot of summertime fun playing sand volleyball (Yes, *sand* volleyball in Dayton); and the Wright Patterson Jewish community, for embracing Michelle and I, and giving us respite from our school work.

I owe the most thanks to my friends and family, there is no way I could have done it without their support. In fact, I will undoubtedly cherish the friendships I have made here

more than anything else I take away from my AFIT experience. Finally, I thank my wife Michelle for her patience, support, and love. To her I bestow the highest honor. To her I dedicate this dissertation.

Michael J. Noble

Table of Contents

List of Figures

List of Tables

Abstract

I present an in-depth theoretical analysis of the optical impact of transverse index confinement on the lasing modes of microcavity surface emitting lasers. Using two different variational techniques—the weighted index method and the finite element method—I solve Maxwell's equations for several azimuthally symmetric laser designs to compute the relevant laser parameters: modal resonance, field profile, confinement factor, and threshold gain. Through my weighted index analysis, I discovered two new effects of transverse field confinement: a polarization dependent change in mirror reflectance with aperture radius, previously only noted in edge-emitting lasers, and a mode dependent blueshift. Comparing my blueshift predictions against measured results for devices operating at nominally 850 nm and 780 nm, I found excellent agreement between theory and experiment. For a sufficiently sharp gain spectrum, this blueshift may be used to achieve low threshold, single mode lasing by exploiting the dispersion in blueshift rates amongst the various transverse eigenmodes to spectrally select the single desired lasing mode. Through my finite element analysis, I ascertained the physical mechanisms responsible for diffraction in microcavity lasers. These are: the transverse confinement of the optical mode, the degree of tilt of the mode propagation vector away from normal to the mirror surfaces, and the density of parasitic modes in the spectral vicinity of the lasing mode. This knowledge is of vital importance for low threshold design analyses, since diffraction is the dominant loss source in this regime. Based on the success of the parasitic mode loss picture for describing diffraction in the stratified surface emitting laser geometry, I augmented my weighted index model, via a rigorous electromagnetic calculation of lasing-to-parasitic modes coupling, to compute diffractive loss and total threshold gain. Incorporating this new weighted index/parasitic mode calculation with a semiconductor bandstructure and gain model, I computed spontaneous emission rates for a low threshold laser using a new optical mode density model specifically designed to address the partial field confinement afforded by, for example, oxide apertures. Finally, the optical, gain, and emission results were combined to compute light verses current, threshold current, and spontaneous emission factors for the same low threshold device.

Optical Physics of Microcavity Surface Emitting Lasers

I. Introduction

1.1 Foreword

The advances in semiconductor and optoelectronic technology over the last quarter century have opened the door for the theoretical researcher to probe concepts not only of purely scientific interest but of great practical application as well. This is perhaps best exemplified by the archetypical semiconductor laser, whose understanding requires the mastery of several branches of physics and yet boasts wide sweeping application ranging from compact disc players, to environmental sensors, to aircraft avionics, etc. These lasers have established a growing strong-hold within the optical source genre due in a large part to their cost, size, and exceptional operating characteristics, many of which are unobtainable by their gas and solid state counterparts—at any cost. Indeed, as anyone who has worked with them can attest, the idea of a ND^{3+}–YAG, ruby, or CO_2 laser operating with an efficiency of 50% off batteries and costing pennies on the dollar belongs in an Arthur C. Clarke novel. Yet semiconductor lasers have achieved all these feats and more. A prime example is amplitude modulation by direct modulation of the drive current, a feature ideally suiting these lasers for fiber-optic sources, the backbone of the communications industry. The prominence of these lasers is largely attributable to the advances in semiconductor growth and microfabrication technology, permitting the researcher to control device construction literally down to the atomic level and to realize truly quantum mechanical structures—as Steven Wright quipped—"the dreams stuff are made of." Most notably, this technology facilitated the creation of heterojunctions and quantum wells, the optical sources within most lasers, and until then a purely theoretical entity of quantum mechanics. Despite the relative maturity of the semiconductor laser, the research activity has not slowed, maintaining a frenzied pace driven by the continual emergence of new applications and the demand for increased performance. A large percentage of the work is focused on conquering new material systems

to achieve reliable lasers at wavelengths outside of the well developed red-to-near-infrared range. The elusive blue laser, the last leg of the triad required for high-brightness, flat-panel displays, and the mid-infrared intraband quantum cascade laser, which uses the well established GaAs/AlGaAs material system, are excellent examples of this type of work. Although this research is exceptionally significant in the material science and quantum mechanics disciplines, optically these lasers differ very little from their predecessors. This is not the case though with vertical cavity surface emitting lasers, or VCSELs, another highly active area of laser research, and the foundation of this thesis.

The VCSEL is a relatively recent spin-off of the more traditional edge-emitting laser, whose primary differences—cavity orientation, size, and design—are optical in nature; a typical VCSEL and edge emitter are illustrated in Figure 1.1. As the name implies, the VCSEL cavity is normal to the growth direction. VCSEL mirrors are either monolithically grown semiconductor or post-growth deposited dielectric distributed Bragg reflectors (DBRs): alternating quarter-wave layers of high and low index of refraction materials. A drawback of the vertical cavity is a very short gain region, often necessitating extremely thick DBRs of 80 layers or more to achieve the greater than 99% reflection required for lasing. On the other hand, however, the typical VCSEL cavity is only a few wavelengths long, roughly two orders of magnitude shorter than most in-plane lasers. An immediate result being the lasing threshold, which scales roughly with active volume, is also orders of magnitude smaller, unfortunately at the expense of the ability to generate high output powers. Additionally due to the short cavity length, VCSELs only support a single longitudinal mode. The large spacing between spectrally sharp longitudinal modes—due to the high reflectance DBRs—makes the VCSEL cavity the optical analog of the quantum well, a quasi-two dimensional structure. This feature has been thoroughly investigated, focusing on the potential for cavity design to effect the quantum nature of light, enhancing or suppressing spontaneous emission to lower the lasing threshold beyond the active volume limit. From the results of analyses on the simple planar VCSEL came predictions that with further optical confinement, lower order quantum systems could be imitated and lower thresholds obtained.

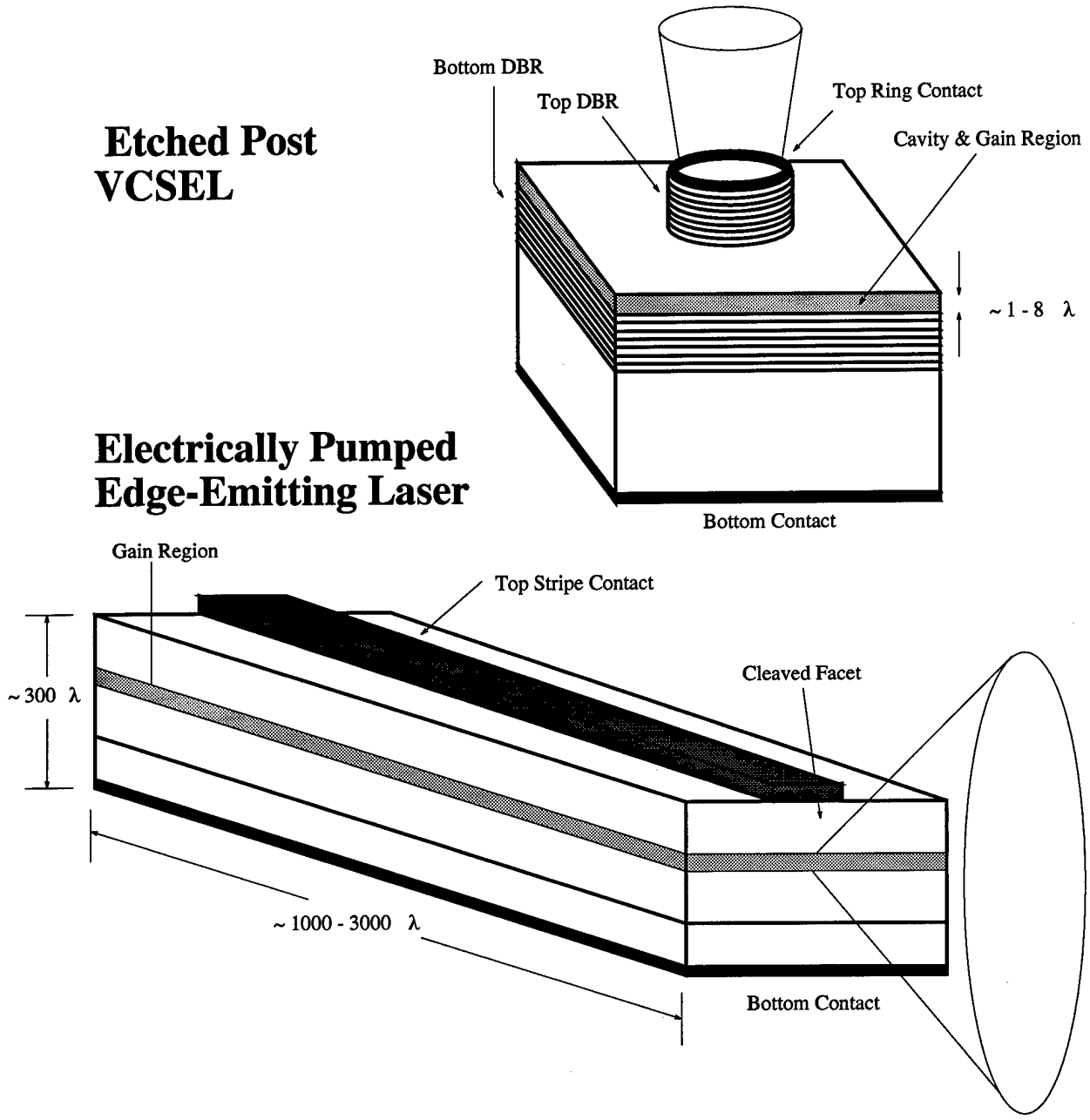

Figure 1.1 Illustration of a simple etched post vertical cavity surface emitting laser and an edge-emitting laser.

The first embodiment of a three-dimensionally index confined vertical cavity laser came in the form of an etched post, with DBRs providing one dimension of confinement and the air-to-semiconductor interface providing the other two. Although it would seem this device would provide the closest replica of the classical "particle in a box", it was not practical. It suffered terribly from surface recombination electrical losses, as well as optical scattering losses, and was therefore quickly abandoned. Nonetheless, in its short life-span a great deal of analysis was performed on it, with the most noteworthy result being a prediction that in a true zero dimensional system the threshold could be made to completely disappear. The potential of this device is enormous; a zero threshold device would require zero bias power. This untapped potential served to motivate researchers both interested in the practical application of such a device as well as those intrigued by the exciting new physics embodied in them. The breakthrough came when the microelectronics group at the University of Texas (U.T.) found that by replacing proton implantation with native oxidation for current confinement, they achieved the additional benefit of index confinement of the optical field without the immense electrical losses associated with etching [31]. The idea caught on like wildfire and over the few short years since its inception, oxidation has essentially replaced implantation as the method of choice for carrier and field confinement.

However, the oxide is not perfect. It clearly provides a transverse index step, but the total effect of the step is not well understood, as evidenced by the large variety of oxide designs throughout the research community. For example, two leading universities in VCSEL research, the University of California at Santa Barbara (U.C.S.B.) and the University of Texas, report optimized designs based on wholly different concepts of the oxide optical effect. Santa Barbara reports that thinner oxides placed further from the gain region at nodes of the field standing wave are superior, minimizing the diffraction loss of the lasing mode [30]. Texas reports just the opposite; thicker oxides placed near the gain region at antinodes are better, providing more transverse confinement/waveguiding to the mode [19]. Both groups have enjoyed success with their respective approaches, achieving extremely low thresholds [33]. Their results suggest that the primary effects of the oxide differ depending on the cavity and oxide aperture design. These results may also be interpreted to mean

the use of oxides has not yet been optimized and the ultimate threshold limit has not yet been achieved. A further reduction in threshold must be preceded by a better understanding of the oxide effects. A complete model must explain these two seemingly opposing results. Once in hand, this "Grand Unified VCSEL Optical Theory" may be used to predict the *ideal* oxide aperture and VCSEL cavity design for achieving the ultimate limit in low threshold lasing. It is precisely this model which is the goal of this dissertation.

1.2 Optical Problem

The fact that the optical problem has persisted so long reflects the extreme difficulty in solving the differential equations governing the fields in VCSELs. The equations are themselves simple enough. They are, of course, Maxwell's equations, given in differential form (in MKS units) as

$$\begin{aligned} \nabla \times \vec{E} &= -\frac{\partial \vec{B}}{\partial t}, \\ \nabla \times \vec{H} &= \frac{\partial \vec{D}}{\partial t} + \vec{J}, \\ \nabla \cdot \vec{D} &= \rho_v, \\ \nabla \cdot \vec{B} &= 0. \end{aligned} \tag{1.1}$$

Here the two source terms are the current density $\left(\vec{J}\right)$ and the volume charge density (ρ_v). Assuming isotropic media, the electric $\left(\vec{D}\right)$ and magnetic $\left(\vec{B}\right)$ fluxes are related to the electric $\left(\vec{E}\right)$ and magnetic $\left(\vec{H}\right)$ fields by the material parameters (μ, ε) and the constitutive relations

$$\begin{aligned} \vec{D} &= \varepsilon_0 \varepsilon_r \vec{E}, \\ \vec{B} &= \mu_0 \mu_r \vec{H}; \end{aligned} \tag{1.2}$$

μ_0, μ_r, ε_0, and ε_r are the free-space and relative permeability, and the free-space and relative permittivity, respectively. The relative permittivity is related to the more commonly used

index of refraction by

$$\varepsilon_r \equiv \eta^2. \tag{1.3}$$

Absorptive loss and material gain result from a negative or positive imaginary part of ε_r or η. Since lasing fields are spectrally sharp—nearly delta functions in frequency—the fields may be approximated as harmonic, depending on time as $\exp(i\omega t)$, where $i = \sqrt{-1}$ and ω is the radial frequency. Furthermore, assuming non-magnetic material ($\mu_r = 1$), which is the case for all semiconductor laser materials, the Maxwell curl equations may be combined to derive the vector Helmholtz equation,

$$\nabla \times \nabla \times \vec{E} - \omega^2 \mu_0 \varepsilon_0 \varepsilon_r \vec{E} = -i\omega\mu_0 \vec{J}. \tag{1.4}$$

The vector Helmholtz equation and the MKS Maxwell's equations serve as the foundation for all my optical laser analysis. The primary challenge in solving (1.4) results from the apertured VCSEL geometry. The geometry introduces two fundamental difficulties: (1) the relative permittivity, and therefore the vector Helmholtz equation, is not separable due to the aperture or etched post; (2) the planar Fabry-Perot cavity has very high Q. The non-separability is intrinsic to the apertured VCSEL design; without it there could be no index confinement[1]. Similarly, the high Q is vital for lasing to occur in the short VCSEL cavities. These two intrinsic VCSEL attributes conspire to greatly complicate optical modeling efforts.

1.3 Semianalytic Calculations

Since analytic calculations generally yield not only a specific solution to a given problem, but insight into the physical underpinnings of the problem, they are often preferred over numerical techniques. Moreover, analytic calculations are as a rule much faster than numerical approaches, favoring them for iterative design work. Hence, the majority of the optical modeling efforts have involved an analytic or semianalytic representation of the fields. The most obvious approach is to actually solve the full vector Helmholtz equation in each region of constant index of refraction, coupling the solutions via the tangential field continu-

[1]This is not strictly true, but does hold for *all* current VCSEL designs. This issue will be revisited later in Chapter V.

ity conditions [12]. In this approach the field is represented by an infinite weighted sum of eigenfunctions (for example, trigonometric or Bessel functions) for each region, the weighting determined by mode matching to adjacent regions. But this technique works well only when the refractive index profile separates in some preferred coordinate system, reducing the infinite expansions to a single term. If, as in realistic VCSEL structures, the refractive index profile does not separate in *any* coordinate system, then simple single-term special-function solutions to the governing partial differential equations do not represent exact solutions for the modes and analytic methods become quite cumbersome. Despite this difficulty, most previous analytic calculations have introduced, at some point in the treatment, a single product term to describe a particular electromagnetic field component [21,26]. It is vital to realize that this is equivalent to assuming the underlying differential equation separates.

Since separable descriptions facilitate closed-form expressions, rapid calculation, and comparison with well-understood "textbook" problems, there is considerable motivation to improve and justify them. Therefore, in Chapter II, I generalize the weighted index method (WIM)—a separable approximation—to compute cavity modes in cylindrically-symmetric dielectric VCSEL structures. I also show (in Appendix A), using the calculus of variations, that this technique provides the *best* separable solution to the scalar Helmholtz equation. In Chapter III, I apply the WIM to both oxide-apertured and etched-post VCSEL designs to calculate the spatial profile, optical confinement factor, resonant frequency, and mirror and absorption losses of the fundamental and higher-order lasing modes. Furthermore, I compare the WIM lasing mode resonance predictions to measurement for two different apertured device designs, validating the WIM results. Ignoring diffraction effects, I show in Appendix B that the threshold conditions based on the WIM optical losses are a generalization of the classical Fabry-Perot round-trip amplitude and phase conditions [65].

1.4 Numerical Solutions

For aperture sizes approaching the field wavelength, diffraction becomes the dominant loss mechanism, rendering the original WIM incomplete. In this realm, any threshold prediction based solely on the WIM losses will be inaccurate—the smaller the aperture, the

less accurate the results. I would prefer to augment the WIM to incorporate diffraction and make it a complete optical model. But, before this can be accomplished it is crucial to understand the *true* physical mechanisms which determine the diffraction in VCSELs. Ideally, this could be done experimentally. Several devices of different oxide aperture radii could be fabricated and the threshold current measured. The threshold current, however, strongly depends on the electrical parasitics—surface recombination and leakage current—both of which vary significantly for small aperture VCSELs. Hence, it is extremely difficult to ferret out optical loss information from threshold current measurements, necessitating the use of modeling to understand the purely optical effects of oxide confinement.

Volumetric numerical methods, although computationally intensive, are ideally suited for rigorous analysis of non-separable partial differential equations (PDEs) over a closed domain. These techniques approximate the true answer by a numerical one, formed by discretizing either the PDE—by replacing the derivatives with finite differences—or the solution—by expanding the function over a weighted basis set. These methods are *quasi-exact*, in that their accuracy increases with the number of unknowns and becomes exact in the infinite limit. To date, only one numerical method has been applied to the VCSEL optical problem. G.R. Hadley [27] estimated the diffractive losses due to oxide apertures using a finite difference eigensolver. But his solution was limited in two primary respects: (1) the finite difference approach only works on a Cartesian grid, and (2) it may only be used to solve for *scalar* fields. His model can not handle tapered oxides, touted by Santa Barbara and Sandia National Laboratories as the optimal oxide design. Furthermore, for VCSEL designs with oxides in or near the cavity—such as the University of Texas's design—the vector nature of the fields may be important. To extend his results, in Chapter IV, I derive a new *vector* finite element method (FEM). The FEM explicitly solves for all three electric field vector components in azimuthally symmetric VCSELs[2]. The method is based on a variational solution of the full vector Helmholtz equation. Unlike finite difference approaches, the FEM is not limited to a Cartesian grid and can easily incorporate any azimuthally symmetric dielectric geometry, including complex loss. In this method, the Helmholtz equation boundary value

[2]I present the *vector* finite element functions in Appendix C

problem is transformed to a large, sparse, non-Hermitian, generalized eigenvalue problem. For each cavity mode the eigenvalues correspond to the complex radial frequency (ω) and the eigenvectors are the basis expansion coefficients determining the fields. Since the method may only be applied on a closed domain, in Appendix D, I derive a new artificial absorbing layer designed to mimic the unbounded nature of the fields. I conclude Chapter IV by applying the FEM to a novel oxide apertured, oxide DBR VCSEL, reported to be the smallest working (photopumped) device ever built [67]. From the eigenvalue and eigenvector, I derive *all* the pertinent mode data: resonant wavelength, confinement factor, field distribution, and *total* threshold gain including diffractive loss. This analysis should be the *most accurate* field calculation performed to date. From these results, I infer the fundamental mechanisms governing VCSEL diffraction.

1.5 Parasitic Modes

Perhaps the most referenced calculation addressing diffraction in VCSELs is a model based on an "unfolded cavity" [29]. In this model, a Gaussian mode, whose shape is determined by the effective "fiber optic" waveguide [26], is propagated through a series of oxide apertures. The energy lost to diffraction in one cavity round-trip is calculated and then extrapolated, based on mirror losses (e.g., emitted light), to estimate the threshold gain. This model is popular for several reasons: (1) it yields an intuitive semianalytic field solution, the VCSEL analog of the standard laser solution, (2) it runs quickly and does not demand the computational horsepower of numerical techniques, and most importantly (3) it qualitatively predicts many of the experimental observations. Based on this model, Santa Barbara derived their VCSEL design: thin oxides placed at nodes of the field standing wave one or two wavelengths from the cavity. However, the current (repeatable) threshold record belongs to the Texas group, whose design, as discussed above, is diametrically opposed to Santa Barbara's. The problem with the unfolded cavity model is it fails to incorporate the fact that the VCSEL field diffracts into a dielectric layered structure, similar to a slab waveguide, and *not* into free space [19].

D.G. Deppe (U.T.) has proposed a different picture of VCSEL diffraction, considering it as energy loss to "parasitic modes." These are slab waveguide modes, nearly resonant with the lasing mode, propagating in the transverse direction[3]. Based on this picture, his group performed qualitative estimates of diffractive loss in various cavity structures [20]. Their interpretation of the loss mechanisms support my conclusions from the FEM analysis, suggesting the validity of the parasitic mode concept. Most remarkably, both calculations (Texas's and my FEM) consistently explain the seemingly opposite U.C.S.B. and U.T. optimized designs. Following the Texas success, in Chapter V, I incorporate parasitic mode loss into the WIM to complete the optical model. Since the WIM is primarily intended as a fast approximate technique, I improve the efficiency of the method—without sacrificing significant accuracy—by adopting the linear polarization (or paraxial) approximation. This allows me to treat the lasing mode (but not the parasitic modes) as a scalar field, greatly simplifying the field representation and cutting run times by roughly a factor of two. I validate this approximation through comparisons with previously obtained vector WIM results.

1.6 Complete Laser Modeling

The principal threshold metric is the spontaneous emission factor (β), describing the percentage of photons (spontaneously) emitted into the lasing (or any other) mode. For traditional lasers with cavity dimensions much larger than the optical wavelength, this can be accurately estimated using the three-dimensional density of optical modes—proportional to ω^2. In VCSELs, the short, high Q cavity quantizes the propagation constant in the longitudinal direction and the appropriate density of modes is two-dimensional—proportional to ω. Furthermore, the quantum well emission becomes anisotropic in the cavity, increasing spontaneous emission in some directions at the expense of others [8, 10, 18]. The combination of these two phenomena result in lasing mode β's much larger than traditional lasers. Extrapolating this effect to lower dimensional systems (i.e., more degrees of confinement), the density of modes may be further reduced and larger β's obtained. In the theoretical, zero-dimensional limit—where all cavity dimensions are on the order of the wavelength—the

[3]More precisely, the parasitic modes propagate *at least* in the transverse direction; they may also propagate in the longitudinal direction as well.

density of modes becomes a series of delta functions. If these modes are spaced sufficiently apart, only one mode may interact with the gain media. In this case, all the spontaneous emission will be channeled into this mode, β will go to 1/2 (due to polarization degeneracy), and the threshold will disappear [4, 5]. In realistic VCSELs this limit (currently) can't be reached. Parasitic optical and electrical losses destroy any quantum optical benefits well before the theoretical minimum cavity size. However, as evidenced by record low thresholds, oxide apertured devices must receive some quantum optical benefits over planar devices. Since the oxide confinement is incomplete, one could envision the optical density of modes as a set of discrete cavity modes, similar to the zero-dimensional case, superimposed on the background two-dimensional density of modes. In Chapter VI, I employ this new approach using my WIM optical modes to estimate the spontaneous emission factor for the University of Texas's low threshold VCSEL. Integrating these results with J.P. Loehr's gain model [42], the photon and carrier related rate equations are solved to estimate the threshold *current* and the light-vs-current characteristics—the ultimate goal of laser modeling.

II. Vector Weighted Index Method

In this chapter, I generalize the weighted index method (WIM)—a separable approximation to the Helmholtz equation—to compute cavity modes in cylindrically-symmetric dielectric VCSEL structures [50, 51]. I calculate the electric and magnetic vector potentials and use these to compute the resulting fields. Using the calculus of variations in Appendix A, I show that this technique provides the *best* separable solution to the scalar Helmholtz equation. The method allows me to approximate the spatial profile, optical confinement factor, resonant frequency, and mirror and absorption losses of cavity modes in both oxide-apertured and etched-post VCSELs. The method explicitly considers complex media, allowing me to include free carrier losses. A central flaw of the technique, however, is an exclusion of diffraction, the dominant loss mechanism in recent low threshold designs. I remedy this later in Chapter V, by *perturbatively* including these losses in the general WIM formalism as presented below.

2.1 Vector Field Equations

I want to find the electric $\left(\vec{E}\right)$ and magnetic $\left(\vec{H}\right)$ field profiles, the resonant wavelength (λ), and the mirror and absorption losses $\left(\alpha^{(\text{mirror})} + \alpha^{(\text{absorption})}\right)$ for each cavity mode in azimuthally-symmetric VCSEL structures. For this I must solve a vector-wave equation subject to appropriate boundary conditions at each interface. Because there are several equivalent electromagnetic descriptions of any system, I can write wave equations for the electric and magnetic fields, scalar potentials, or vector potentials. The most powerful and convenient method for this problem is to solve for the magnetic $\left(\vec{A}\right)$ and electric $\left(\vec{F}\right)$ vector potentials and use them to compute the fields. The steady-state, time-harmonic vector potentials $\vec{A}$ and $\vec{F}$ satisfy the three-dimensional vector Helmholtz equation (in MKS units)

$$\left\{\nabla^2 + \frac{\omega^2}{c^2}\varepsilon_r(\rho, z)\right\} \left\{ \begin{array}{c} \vec{A}(\rho, \phi, z) \\ \vec{F}(\rho, \phi, z) \end{array} \right\} = 0. \tag{2.1}$$

Here $\vec{A}$ and $\vec{F}$ depend on time as $e^{i\omega t}$, $\omega = 2\pi c/\lambda$, and I have assumed a cylindrically-symmetric, complex dielectric function ε_r. Note that

$$\sqrt{\varepsilon_r} = \eta \equiv n + i\kappa, \tag{2.2}$$

where η is the (complex) refractive index; material gain is incorporated by taking κ positive in the active region. I assume $\mu_r = 1$ in all regions.

For azimuthally symmetric structures, the vector potentials are separable in ϕ, depending on it as $e^{im\phi}$. Furthermore, expressing the potentials in cylindrical coordinates, the $\hat{z}$ components obey a *scalar* Helmholtz equation,

$$\left\{ \frac{\partial^2}{\partial\rho^2} + \frac{1}{\rho}\frac{\partial}{\partial\rho} + \frac{\partial^2}{\partial z^2} + \left(\frac{\omega^2}{c^2}\varepsilon_r(\rho,z) - \frac{m^2}{\rho^2} \right) \right\} \left\{ \begin{array}{c} A_z(\rho,z) \\ F_z(\rho,z) \end{array} \right\} = 0. \tag{2.3}$$

To generate transverse magnetic (to $\hat{z}$) (TM) modes I must solve for A_z, while to generate transverse electric (TM) modes I must solve for F_z [28]. Since an arbitrary mode can be represented as a superposition of TE and TM modes, I need only solve for the two unknown scalar functions A_z and F_z, a dramatic simplification over solving (2.1) for all six vector components. Note that despite the fact that I may solve a scalar equation (2.3) to find modes, the vector nature of the solution remains—manifested in the *boundary conditions.* The power of the vector potential approach comes from the fact that I may generate all the vector field components by taking derivatives of the $\hat{z}$ components of the vector potentials, therefore requiring no *a-priori* knowledge of the ρ or z dependence. The fields themselves are related to the vector potentials by [36]

$$\vec{E} = -\frac{i}{\omega\varepsilon_0\varepsilon_r}\nabla\times\nabla\times(\hat{z}A_z) - \nabla\times(\hat{z}F_z), \tag{2.4}$$

$$\vec{H} = \nabla\times(\hat{z}A_z) - \frac{i}{\omega\mu_0}\nabla\times\nabla\times(\hat{z}F_z), \tag{2.5}$$

or, more explicitly,

$$E_\rho(\rho,z) = -\frac{i}{\omega\varepsilon_0\varepsilon_r}\frac{\partial^2}{\partial\rho\partial z}A_z(\rho,z) - \frac{1}{\rho}\frac{\partial}{\partial\phi}F_z(\rho,z), \tag{2.6}$$

$$E_\phi(\rho,z) = -\frac{i}{\omega\varepsilon_0\varepsilon_r\rho}\frac{\partial^2}{\partial\phi\partial z}A_z(\rho,z) + \frac{\partial}{\partial\rho}F_z(\rho,z), \tag{2.7}$$

$$E_z(\rho,z) = \frac{i}{\omega\varepsilon_0\varepsilon_r}\left\{\frac{\partial^2}{\partial\rho^2} + \frac{1}{\rho}\frac{\partial}{\partial\rho} - \frac{m^2}{\rho^2}\right\}A_z(\rho,z), \tag{2.8}$$

$$H_\rho(\rho,z) = \frac{1}{\rho}\frac{\partial}{\partial\phi}A_z(\rho,z) - \frac{i}{\omega\mu_0}\frac{\partial^2}{\partial\rho\partial z}F_z(\rho,z), \tag{2.9}$$

$$H_\phi(\rho,z) = -\frac{\partial}{\partial\rho}A_z(\rho,z) - \frac{i}{\omega\mu_0\rho}\frac{\partial^2}{\partial\phi\partial z}F_z(\rho,z), \tag{2.10}$$

$$H_z(\rho,z) = \frac{i}{\omega\mu_0}\left\{\frac{\partial^2}{\partial\rho^2} + \frac{1}{\rho}\frac{\partial}{\partial\rho} - \frac{m^2}{\rho^2}\right\}F_z(\rho,z). \tag{2.11}$$

In separable geometries, the two-dimensional, azimuthally-symmetric scalar Helmholtz equation (2.3) may be solved exactly by separation of variables, yielding the potential profiles, resonant wavelength, and mirror and absorption losses for each cavity mode. Realistic VCSEL structures, however, are not separable, greatly complicating the solution of (2.3). An exact semianalytic solution could be obtained by expanding A_z and F_z in terms of the general solutions in each region, then matching boundary conditions to determine the (infinite) set of expansion coefficients. In practice, this technique requires considerable care to implement, though it does have the advantage of incorporating non-separable behavior in the solutions [12]. Below, I present an alternative technique to generate the best *separable* approximations to (2.3).

2.2 The Weighted Index Method

Equation (2.3) represents two uncoupled partial differential equations—one each for A_z and F_z—which are quite difficult to solve. For separable geometries, I can exactly replace each equation in (2.3) with two independent ordinary differential equations, and these can be solved exactly. For non-separable geometries, I approximate the solutions to (2.3). In general, there are two possible approximation techniques. The most common approach is to maintain the exact equations (2.3) and construct an approximate *function* that "almost"

solves them. An alternative approach is to replace the exact equations (2.3) with approximate *equations*, and solve these approximate equation exactly. I take the latter approach, and approximate each equation in (2.3) with two *coupled* ordinary differential equations. I accomplish this by extending the weighted index method (WIM)—which was first developed to calculate waveguide modes in horizontal-cavity ridge-waveguide lasers [39,61]—to address the eigenmodes of cylindrical cavities. This technique has the advantage of giving the *best* separable solution to (2.3) in the variational sense, and allows me to estimate the field profile, optical confinement factor, resonant wavelength, and mirror and absorption losses for each cavity mode. Below I derive the WIM equations; in Appendix A, I prove that their solution yields the best separable approximation to (2.3).

Proceeding as if separable solutions to (2.3) exist, I take

$$\begin{aligned} A_z(\rho,z) &= P(\rho)Q(z), \\ F_z(\rho,z) &= R(\rho)S(z). \end{aligned} \tag{2.12}$$

Substituting either of these into (2.3) gives

$$\zeta''(\rho)\xi(z) + \frac{1}{\rho}\zeta'(\rho)\xi(z) + \zeta(\rho)\xi''(z) + \left(\frac{\omega^2}{c^2}\varepsilon_r(\rho,z) - \frac{m^2}{\rho^2}\right)\zeta(\rho)\xi(z) = 0, \tag{2.13}$$

where $\zeta = P$ or R and $\xi = Q$ or S. For each potential in (2.12), I can separate the resulting equation (2.13) by integrating it against $\zeta^*(\rho)$ or $\xi^*(z)$. This procedure yields the axial equation

$$\xi''(z) + \left(\beta^{\alpha}_{eff}(z)\right)^2 \xi(z) = 0, \tag{2.14}$$

and the radial equation

$$\zeta''(\rho) + \frac{1}{\rho}\zeta'(\rho) + \left[\left(k^{\alpha}_{eff}(\rho)\right)^2 - \frac{m^2}{\rho^2}\right]\zeta(\rho) = 0, \tag{2.15}$$

for each potential. These axial and radial equations are *coupled* by the weighted axial and radial propagation constants, given respectively by

$$\left(\beta^{\alpha}_{eff}(z)\right)^2 \equiv \frac{(\omega^2/c^2)\langle\,\zeta\,|\,\varepsilon_r(\rho,z)\,|\,\zeta\,\rangle + \langle\,\zeta\,|\,\zeta''\,\rangle + \langle\,\zeta\,|\,\rho^{-1}\,|\,\zeta'\,\rangle - m^2\langle\,\zeta\,|\,\rho^{-2}\,|\,\zeta\,\rangle}{\langle\,\zeta\,|\,\zeta\,\rangle}, \tag{2.16}$$

and

$$\left(k^{\alpha}_{eff}(\rho)\right)^2 \equiv \frac{(\omega^2/c^2)\langle\,\xi\,|\,\varepsilon_r(\rho,z)\,|\,\xi\,\rangle + \langle\,\xi\,|\,\xi''\,\rangle}{\langle\,\xi\,|\,\xi\,\rangle}. \tag{2.17}$$

Here $\langle\ |\ \rangle$ denotes an inner-product over z or ρ, respectively defined by

$$\langle\,A(z)\,|\,B(z)\,\rangle = \int_{-\infty}^{\infty} A^*(z)B(z)\,dz, \tag{2.18}$$

and

$$\langle\,A(\rho)\,|\,B(\rho)\,\rangle = \int_{0}^{\infty} A^*(\rho)B(\rho)\rho\,d\rho. \tag{2.19}$$

Since the weighted propagation constants depend on whether I solve for A_z or F_z, I have introduced an additional superscript α = TE or TM to distinguish between TE modes resulting from F_z (involving averages over $\zeta = R$ and $\xi = S$) and TM modes resulting from A_z (involving averages over $\zeta = P$ and $\xi = Q$). Coupling occurs only between the radial and axial equations for a given vector potential A_z or F_z: the two potentials remain uncoupled in (2.14) and (2.15). But A_z and F_z will be coupled later by *boundary conditions* when I solve for hybrid modes.

2.3 Weighted Boundary Conditions and Solutions

In this section I discuss the solutions of (2.14) and (2.15) in piecewise-constant refractive index profiles, paying particular attention to the interfacial boundary conditions. A sample structure is shown in Figure 2.1. Since I will work exclusively with piecewise-constant geometries, I simplify my notation by taking $\varepsilon_r(\rho,z) \to \varepsilon_{r:i,j}$, where i and j index the radial and axial regions, respectively. Thus I also have $k^{\alpha}_{eff}(\rho) \to k^{\alpha}_{i}$ and $\beta^{\alpha}_{eff}(z) \to \beta^{\alpha}_{j}$, and (2.14) and (2.15) reduce, respectively, to the one-dimensional Helmholtz equation and Bessel's equation.

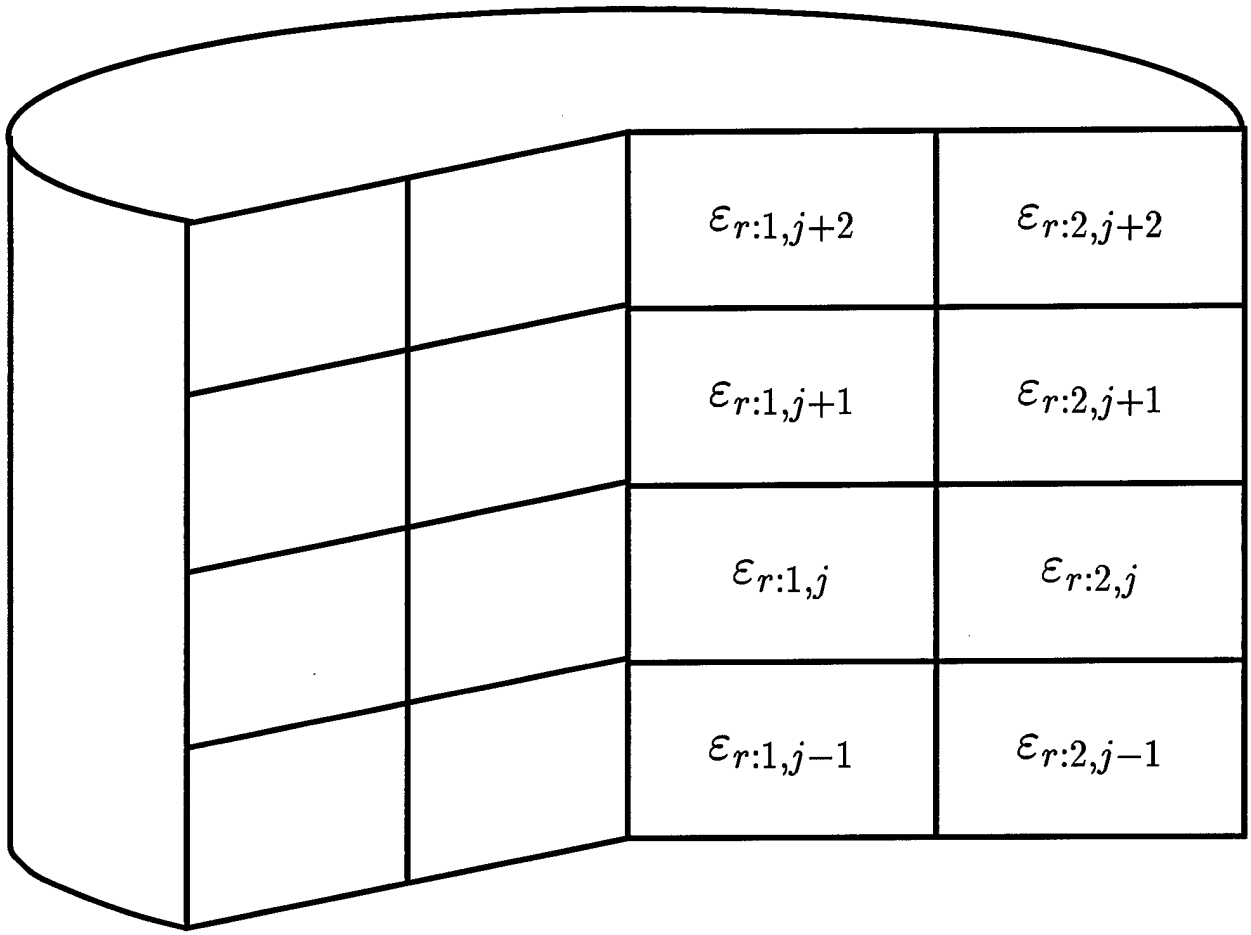

Figure 2.1 Illustration of the piecewise constant permittivity notation for an axially symmetric VCSEL.

To solve these equations subject to the refractive index profile $\varepsilon_{r:i,j}$ of etched-post or oxide-apertured VCSEL structures, I must supplement (2.14) and (2.15) with an appropriate set of interface and endpoint boundary conditions. The interfacial boundary conditions are the usual continuity requirements on the normal and tangential components of various electromagnetic fields. Therefore I cannot directly enforce boundary conditions on P, Q, R, and S, but must perform the intermediate step of computing the electric and magnetic fields via (2.6)–(2.11). Furthermore, since the underlying partial differential equations (2.3) do not separate, these boundary conditions cannot be satisfied at all points on the boundary surfaces—if they could, (2.3) would be separable.

In preparation for generating approximate boundary conditions, I rewrite the weighted index formulas (2.16) and (2.17). By integrating (2.15) against $\zeta^*(\rho)$ I have

$$\langle \zeta \,|\, \zeta'' \rangle + \langle \zeta \,|\, \rho^{-1} \,|\, \zeta' \rangle - m^2 \langle \zeta \,|\, \rho^{-2} \,|\, \zeta \rangle = -\langle \zeta \,|\, (k_i^\alpha)^2 \,|\, \zeta \rangle, \tag{2.20}$$

allowing me to express (2.16) as

$$(\beta_j^\alpha)^2 = \frac{(\omega^2/c^2)\langle \zeta \,|\, \varepsilon_{r:i,j} \,|\, \zeta \rangle - \langle \zeta \,|\, (k_i^\alpha)^2 \,|\, \zeta \rangle}{\langle \zeta \,|\, \zeta \rangle} \equiv \frac{\omega^2}{c^2} \langle \varepsilon_{r:\zeta,j}^\alpha \rangle - \langle k^\alpha \rangle^2, \tag{2.21}$$

where

$$\langle \varepsilon_{r:\zeta,j}^\alpha \rangle \equiv \frac{\langle \zeta \,|\, \varepsilon_{r:i,j} \,|\, \zeta \rangle}{\langle \zeta \,|\, \zeta \rangle} \quad \text{and} \quad \langle k^\alpha \rangle \equiv \sqrt{\frac{\langle \zeta \,|\, (k_i^\alpha)^2 \,|\, \zeta \rangle}{\langle \zeta \,|\, \zeta \rangle}}. \tag{2.22}$$

Similarly, by integrating (2.14) against $\xi^*(z)$ I find

$$\langle \xi \,|\, \xi'' \rangle = -\langle \xi \,|\, (\beta_j^\alpha)^2 \,|\, \xi \rangle, \tag{2.23}$$

allowing me to express (2.17) as

$$(k_i^\alpha)^2 = \frac{(\omega^2/c^2)\langle \xi \,|\, \varepsilon_{r:i,j} \,|\, \xi \rangle - \langle \xi \,|\, (\beta_j^\alpha)^2 \,|\, \xi \rangle}{\langle \xi \,|\, \xi \rangle} \equiv \frac{\omega^2}{c^2} \langle \varepsilon_{r:i,\xi}^\alpha \rangle - \langle \beta^\alpha \rangle^2, \tag{2.24}$$

where

$$\langle \varepsilon_{r:i,\xi}^\alpha \rangle \equiv \frac{\langle \xi \,|\, \varepsilon_{r:i,j} \,|\, \xi \rangle}{\langle \xi \,|\, \xi \rangle} \quad \text{and} \quad \langle \beta^\alpha \rangle \equiv \sqrt{\frac{\langle \xi \,|\, (\beta_j^\alpha)^2 \,|\, \xi \rangle}{\langle \xi \,|\, \xi \rangle}}. \tag{2.25}$$

The compact expressions (2.21) and (2.24) allow me to compute weighted variables without using the derivatives of ζ and ξ.

I specialize these expressions to VCSEL lasing modes by truncating the inner product over z, replacing (2.18) with

$$\langle A(z) \,|\, B(z) \rangle = \int_{z_{\text{bottom}}}^{z_{\text{top}}} A^*(z) B(z)\, dz, \tag{2.26}$$

where z_{bottom} and z_{top} denote the lower and upper VCSEL boundary planes. This truncation is necessary to force (2.24) to converge and reflects the assumption that most of the energy is contained inside the VCSEL cavity. In contrast, I force the radial wavefunctions to decay evanescently to zero—to find guided modes—and the inner product defined by (2.19) presents no difficulty. It is essential to realize that by forcing evanescent behavior in the radial direction, I explicitly *prohibit* diffraction from contributing to the solution. This unavoidable drawback is repaired perturbatively in Chapter V.

I now present boundary conditions and solutions for the axial and radial equations (2.14) and (2.15). The unknowns in this formalism are, for each mode, the functions $P(\rho)$, $Q(z)$, $R(\rho)$,and $S(z)$, the resonant frequency ω, and the mirror and absorption losses,

$$\alpha^{(\text{mirror})} + \alpha^{(\text{absorption})} \equiv \Gamma^{\text{tot}} 4\pi \kappa_{\text{active}} / \lambda. \tag{2.27}$$

Here Γ^{tot} is the total confinement factor and κ_{active} is the material gain in the active quantum well region required to *offset* the mirror and absorption losses. Note that the sum of the two losses equals the threshold modal gain which would be observed if diffraction were not present. In practice, I explicitly solve for κ_{active}, not $\alpha^{(\text{mirror})} + \alpha^{(\text{absorption})}$.

2.3.1 Axial Boundary Conditions and Solutions. I solve the axial equation (2.14) in piecewise constant geometries, such as in Figure 2.2. The general solutions of (2.14) are

given in each axial region $[z_j, z_{j+1}]$ by

$$Q_j(z) = a_j^{\mathrm{TM}} e^{i\beta_j^{\mathrm{TM}} z} + b_j^{\mathrm{TM}} e^{-i\beta_j^{\mathrm{TM}} z},$$
$$S_j(z) = a_j^{\mathrm{TE}} e^{i\beta_j^{\mathrm{TE}} z} + b_j^{\mathrm{TE}} e^{-i\beta_j^{\mathrm{TE}} z}, \tag{2.28}$$

where I explicitly denote both the TE and TM solutions for clarity. Using the iterative solution procedure described in Section 2.4, I compute β_j^{TE} and β_j^{TM} from (2.21); assume for now that they are known constants. These solutions must be joined at each interface z_j by matching the tangential electric and magnetic fields. Inserting (2.12) into (2.6)–(2.11), I compute these tangential field components as

$$E_\rho(\rho, z) = -\frac{i}{\omega\varepsilon_0\varepsilon_r} P'(\rho)Q'(z) - \frac{im}{\rho} R(\rho)S(z), \tag{2.29}$$
$$E_\phi(\rho, z) = \frac{m}{\omega\varepsilon_0\varepsilon_r\rho} P(\rho)Q'(z) + R'(\rho)S(z), \tag{2.30}$$
$$H_\rho(\rho, z) = \frac{im}{\rho} P(\rho)Q(z) - \frac{i}{\omega\mu_0} R'(\rho)S'(z), \tag{2.31}$$
$$H_\phi(\rho, z) = -P'(\rho)Q(z) + \frac{m}{\omega\mu_0\rho} R(\rho)S'(z). \tag{2.32}$$

I consider, in turn, two distinct cases: $m = 0$ and $m \neq 0$.

When $m = 0$ I can match boundary conditions with $Q = 0$ (pure TE modes) or $S = 0$ (pure TM modes). For these modes, it is sufficient to force just two tangential field components to be continuous: demanding continuity of the other component gives a redundant condition. For TE modes I require E_ϕ and H_ρ to be continuous; for TM modes I require E_ρ and H_ϕ to be continuous. As I will show below, for pure TE and TM modes the fields themselves, and not just the vector potentials, are separable. This makes it easy to generate weighted boundary conditions for these modes.

For pure TE modes, I have

$$E_\phi(\rho, z) = R'(\rho)S(z), \tag{2.33}$$
$$H_\rho(\rho, z) = -\frac{i}{\omega\mu_0} R'(\rho)S'(z). \tag{2.34}$$

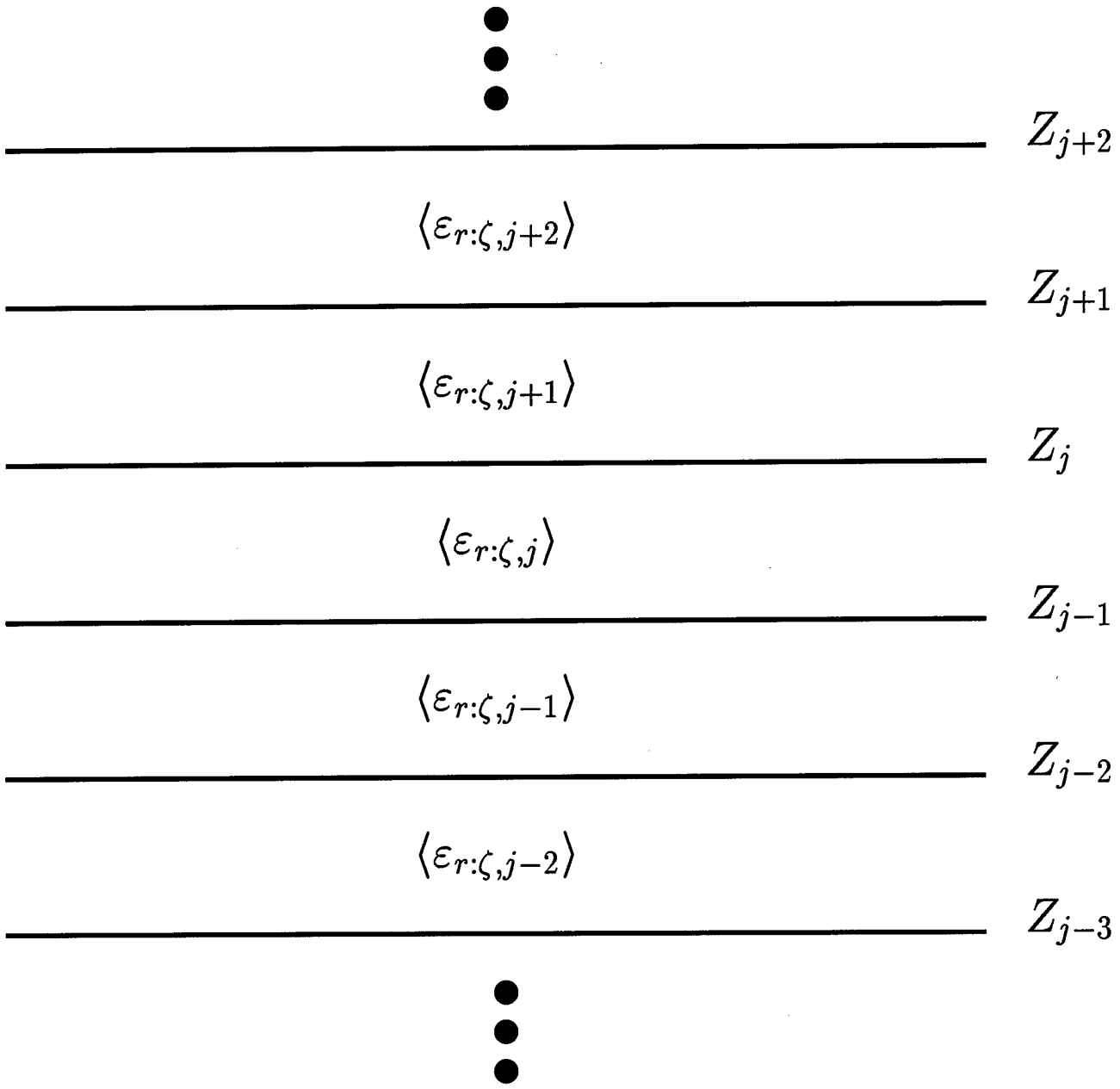

Figure 2.2 Illustration of the weighted permittivity profile, and notation, for the WIM axial solution.

Since I assume $\mu_r = 1$ in all regions, both E_ϕ and H_ρ depend on z only via $S(z)$ and $S'(z)$, respectively. Therefore I can force both tangential fields to be continuous by setting $S(z)$ and $S'(z)$ continuous across each interface.

For pure TM modes, on the other hand, I have

$$E_\rho(\rho, z) = -\frac{i}{\omega\varepsilon_0\varepsilon_r} P'(\rho)Q'(z), \tag{2.35}$$

$$H_\phi(\rho, z) = P'(\rho)Q(z). \tag{2.36}$$

Again, I can make H_ϕ continuous by forcing $Q(z)$ to be continuous across each interface. However, E_ρ depends on z through both $Q'(z)$ *and* ε_r. Since $\varepsilon_r(\rho, z)$ is not a separable function, I must weight the relative permittivity to obtain average boundary conditions holding for all ρ. Therefore I require $Q'(z)/\langle\varepsilon_{r:P}^{\mathrm{TM}}\rangle$ to be continuous at each interface, where $\langle\varepsilon_{r:P,j}^{\mathrm{TM}}\rangle$ has already been defined in each region by (2.25). (I could also have generated average boundary conditions using $\langle\frac{1}{\varepsilon_r}\rangle$, but this approach gave inferior results.)

Inserting the functional forms (2.28) and applying the continuity conditions for either $\alpha = \mathrm{TE}$ or $\alpha = \mathrm{TM}$ modes, I relate a_j^α, b_j^α to a_{j+1}^α, b_{j+1}^α at each axial boundary $z = z_j$ through the transfer matrices

$$L_j^\alpha \begin{bmatrix} a_j^\alpha \\ b_j^\alpha \end{bmatrix} = R_j^\alpha \begin{bmatrix} a_{j+1}^\alpha \\ b_{j+1}^\alpha \end{bmatrix}, \tag{2.37}$$

where

$$L_j^{\mathrm{TE}} \equiv \begin{bmatrix} e^{i\beta_j^{\mathrm{TE}} z_j} & e^{-i\beta_j^{\mathrm{TE}} z_j} \\ i\beta_j^{\mathrm{TE}} e^{i\beta_j^{\mathrm{TE}} z_j} & -i\beta_j^{\mathrm{TE}} e^{-i\beta_j^{\mathrm{TE}} z_j} \end{bmatrix}, \; R_j^{\mathrm{TE}} \equiv \begin{bmatrix} e^{i\beta_{j+1}^{\mathrm{TE}} z_j} & e^{-i\beta_{j+1}^{\mathrm{TE}} z_j} \\ i\beta_{j+1}^{\mathrm{TE}} e^{i\beta_{j+1}^{\mathrm{TE}} z_j} & -i\beta_{j+1}^{\mathrm{TE}} e^{-i\beta_{j+1}^{\mathrm{TE}} z_j} \end{bmatrix}, \tag{2.38}$$

$$L_j^{\mathrm{TM}} \equiv \begin{bmatrix} e^{i\beta_j^{\mathrm{TM}} z_j} & e^{-i\beta_j^{\mathrm{TM}} z_j} \\ \frac{i\beta_j^{\mathrm{TM}}}{\langle\varepsilon_{r:P,j}^{\mathrm{TM}}\rangle} e^{i\beta_j^{\mathrm{TM}} z_j} & \frac{-i\beta_j^{\mathrm{TM}}}{\langle\varepsilon_{r:P,j}^{\mathrm{TM}}\rangle} e^{-i\beta_j^{\mathrm{TM}} z_j} \end{bmatrix}, \; R_j^{\mathrm{TM}} \equiv \begin{bmatrix} e^{i\beta_{j+1}^{\mathrm{TM}} z_j} & e^{-i\beta_{j+1}^{\mathrm{TM}} z_j} \\ \frac{i\beta_{j+1}^{\mathrm{TM}}}{\langle\varepsilon_{r:P,j+1}^{\mathrm{TM}}\rangle} e^{i\beta_{j+1}^{\mathrm{TM}} z_j} & \frac{-i\beta_{j+1}^{\mathrm{TM}}}{\langle\varepsilon_{r:P,j+1}^{\mathrm{TM}}\rangle} e^{-i\beta_{j+1}^{\mathrm{TM}} z_j} \end{bmatrix}. \tag{2.39}$$

The composite transfer matrix $[T^\alpha]$ for the whole system is formed by cascading the individual transfer matrices, giving

$$[T^\alpha] = [L_1^\alpha]^{-1}[R_1^\alpha][L_2^\alpha]^{-1}[R_2^\alpha][L_3^\alpha]^{-1}[R_3^\alpha]\cdots[L_{N-1}^\alpha]^{-1}[R_{N-1}^\alpha]. \tag{2.40}$$

Here N is the number of axial regions (including substrate and air) in the problem geometry. Thus I relate the unknown coefficients in the $j = 1$ region (substrate) to the coefficients in the $j = N$ region (air) via

$$\begin{bmatrix} a_1^\alpha \\ b_1^\alpha \end{bmatrix} = \begin{bmatrix} t_{11}^\alpha & t_{12}^\alpha \\ t_{21}^\alpha & t_{22}^\alpha \end{bmatrix} \begin{bmatrix} a_N^\alpha \\ b_N^\alpha \end{bmatrix}. \tag{2.41}$$

Since I am searching for axially-emitting (lasing) modes, I permit only outgoing radiation by setting

$$b_1^\alpha = a_N^\alpha = 0. \tag{2.42}$$

Finally, substituting (2.42) into (2.41) I obtain the axial threshold condition[1]

$$t_{22}^\alpha(\omega, \kappa_{\text{active}}) = 0. \tag{2.43}$$

Setting the real and imaginary parts of t_{22}^α equal to zero gives two independent equations that I solve to obtain the modal frequency $(\omega = 2\pi c/\lambda)$, and the mirror and absorption losses $\left(\alpha^{(\text{mirror})} + \alpha^{(\text{absorption})} = \Gamma^{\text{tot}} 4\pi\kappa_{\text{active}}/\lambda\right)$ for pure TE and TM modes. The expansion coefficients a_j^α and b_j^α for each region are found by back substitution through (2.41) and (2.37).

In order to generate sensible boundary conditions when $m \neq 0$, I must construct *hybrid* modes in which both S and Q are nonzero. In this case *none* of the tangential fields are separable, since each has both TE and TM parts. Each TE and TM part is, in turn, a sum of *cylindrical wave* terms like $e^{im\phi}J_m(k\rho)e^{i\beta z}$ (P and R will turn out to be Bessel functions). An exact solution would require me to include a superposition of cylindrical

[1] As shown in Appendix B, this requirement in conjunction with the transfer matrix solution is a generalization of the classic Fabry-Perot laser round-trip amplitude and phase conditions.

waves involving all values of k, and the boundary conditions would couple all terms at each interface. Fortunately, the coupling between cylindrical waves with different k is small enough to ignore [12,34,48]. Therefore I simultaneously and independently enforce the continuity of the *dominant* TE and TM mode components of each tangential field, and my hybrid mode boundary conditions become the same as those for pure TE and TM modes. Although these boundary conditions are approximate, I feel they are reasonable within the spirit of the method. Using more rigorous boundary conditions would require a *very* complex procedure of questionable value given the fundamental approximate nature of the solution.

2.3.2 Radial Boundary Conditions and Solutions. I solve the radial equation (2.15) in piecewise constant geometries, such as in Figure 2.3. The general solutions of (2.15) are given in each radial region $[\rho_i, \rho_{i+1}]$ by

$$P_i(\rho) = \begin{cases} c_i^{\mathrm{TM}} J_m(k_i^{\mathrm{TM}}\rho) + d_i^{\mathrm{TM}} Y_m(k_i^{\mathrm{TM}}\rho) & i \neq M \\ c_M^{\mathrm{TM}} K_m(ik_M^{\mathrm{TM}}\rho) + d_M^{\mathrm{TM}} I_m(ik_M^{\mathrm{TM}}\rho) & i = M \end{cases},$$

$$R_i(\rho) = \begin{cases} c_i^{\mathrm{TE}} J_m(k_i^{\mathrm{TE}}\rho) + d_i^{\mathrm{TE}} Y_m(k_i^{\mathrm{TE}}\rho) & i \neq M \\ c_M^{\mathrm{TE}} K_m(ik_M^{\mathrm{TE}}\rho) + d_M^{\mathrm{TE}} I_m(ik_M^{\mathrm{TE}}\rho) & i = M \end{cases}. \tag{2.44}$$

Here J_m and Y_m are m-th order Bessel functions of the first and second kind, I_m and K_m are modified m-th order Bessel functions of the first and second kind, and $i = 1, 2, \ldots, M$ indexes the inner to outer radial regions. Using the iterative solution procedure described in section 2.4, I compute k_i^{TE} and k_i^{TM} from (2.24); assume for now that they are known constants. These solutions must be joined at each interface ρ_j by matching tangential electric and magnetic fields. Inserting (2.12) into (2.6)–(2.11) I compute these tangential field components as

$$E_z(\rho, z) = -\frac{i}{\omega\varepsilon_0\varepsilon_r}\left(k_i^{\mathrm{TM}}\right)^2 P(\rho)Q(z), \tag{2.45}$$

$$E_\phi(\rho, z) = \frac{m}{\omega\varepsilon_0\varepsilon_r\rho}P(\rho)Q'(z) + R'(\rho)S(z), \tag{2.46}$$

$$H_z(\rho, z) = -\frac{i}{\omega\mu_0}\left(k_i^{\mathrm{TE}}\right)^2 R(\rho)S(z), \tag{2.47}$$

$$H_\phi(\rho,z) \;=\; -P'(\rho)Q(z)+\frac{m}{\omega\mu_0\rho}R(\rho)S'(z). \tag{2.48}$$

I consider, in turn, the distinct cases $m=0$ and $m\neq 0$.

As in the axial problem, when $m=0$ I can match boundary conditions with $P=0$ (pure TE modes) or $R=0$ (pure TM modes), and it is sufficient to force just two tangential field components to be continuous. For TE modes I require E_ϕ and H_z to be continuous; for TM modes I require E_z and H_ϕ to be continuous. Following the same arguments as in the axial problem, I construct weighted boundary conditions to require the continuity of

$$\left(k^{\mathrm{TE}}\right)^2 R(\rho) \text{ and } R'(\rho) \text{ (for TE modes)}, \tag{2.49}$$

$$\frac{\left(k^{\mathrm{TM}}\right)^2}{\langle\varepsilon^{\mathrm{TM}}_{r:Q}\rangle}P(\rho) \text{ and } P'(\rho) \text{ (for TM modes)}, \tag{2.50}$$

at each radial interface $\rho=\rho_i$. To generate radial boundary conditions independent of z, I have replaced $\varepsilon_{r:i,j}$ by the weighted permittivity $\langle\varepsilon^{\mathrm{TM}}_{r:i,Q}\rangle$ defined in (2.25).

Inserting the functional forms (2.44) and applying the continuity conditions for either $\alpha=$ TE or TM modes, I relate c_i^α, d_i^α to c_{i+1}^α, d_{i+1}^α at each radial boundary $\rho=\rho_i$ through the transfer matrices

$$A_i^\alpha\begin{bmatrix} c_i^\alpha \\ d_i^\alpha\end{bmatrix} = B_i^\alpha\begin{bmatrix} c_{i+1}^\alpha \\ d_{i+1}^\alpha\end{bmatrix}, \tag{2.51}$$

where

$$A_i^{\mathrm{TE}} \;\equiv\; \begin{bmatrix} \left(k_i^{\mathrm{TE}}\right)^2 J_m(k_i^{\mathrm{TE}}\rho_i) & \left(k_i^{\mathrm{TE}}\right)^2 Y_m(k_i^{\mathrm{TE}}\rho_i) \\ k_i^{\mathrm{TE}} J'_m(k_i^{\mathrm{TE}}\rho_i) & k_i^{\mathrm{TE}} Y'_m(k_i^{\mathrm{TE}}\rho_i)\end{bmatrix}, \tag{2.52}$$

$$B_i^{\mathrm{TE}} \;\equiv\; \begin{bmatrix} \left(k_{i+1}^{\mathrm{TE}}\right)^2 \Xi_m(\gamma k_{i+1}^{\mathrm{TE}}\rho_i) & \left(k_{i+1}^{\mathrm{TE}}\right)^2 \Pi_m(\gamma k_{i+1}^{\mathrm{TE}}\rho_i) \\ \gamma k_{i+1}^{\mathrm{TE}} \Xi'_m(\gamma k_{i+1}^{\mathrm{TE}}\rho_i) & \gamma k_{i+1}^{\mathrm{TE}} \Pi'_m(\gamma k_{i+1}^{\mathrm{TE}}\rho_i)\end{bmatrix}, \tag{2.53}$$

$$A_i^{\mathrm{TM}} \;\equiv\; \begin{bmatrix} \frac{\left(k_i^{\mathrm{TM}}\right)^2}{\langle\varepsilon^{\mathrm{TM}}_{r:i,Q}\rangle} J_m(k_i^{\mathrm{TM}}\rho_i) & \frac{\left(k_i^{\mathrm{TM}}\right)^2}{\langle\varepsilon^{\mathrm{TM}}_{r:i,Q}\rangle} Y_m(k_i^{\mathrm{TM}}\rho_i) \\ k_i^{\mathrm{TM}} J'_m(k_i^{\mathrm{TM}}\rho_i) & k_i^{\mathrm{TM}} Y'_m(k_i^{\mathrm{TM}}\rho_i)\end{bmatrix}, \tag{2.54}$$

$$B_i^{\mathrm{TE}} \;\equiv\; \begin{bmatrix} \frac{\left(k_{i+1}^{\mathrm{TM}}\right)^2}{\langle\varepsilon^{\mathrm{TM}}_{r:i+1,Q}\rangle} \Xi_m(\gamma k_{i+1}^{\mathrm{TM}}\rho_i) & \frac{\left(k_{i+1}^{\mathrm{TM}}\right)^2}{\langle\varepsilon^{\mathrm{TM}}_{r:i+1,Q}\rangle} \Pi_m(\gamma k_{i+1}^{\mathrm{TM}}\rho_i) \\ \gamma k_{i+1}^{\mathrm{TM}} \Xi'_m(\gamma k_{i+1}^{\mathrm{TM}}\rho_i) & \gamma k_{i+1}^{\mathrm{TM}} \Pi'_m(\gamma k_{i+1}^{\mathrm{TM}}\rho_i)\end{bmatrix}. \tag{2.55}$$

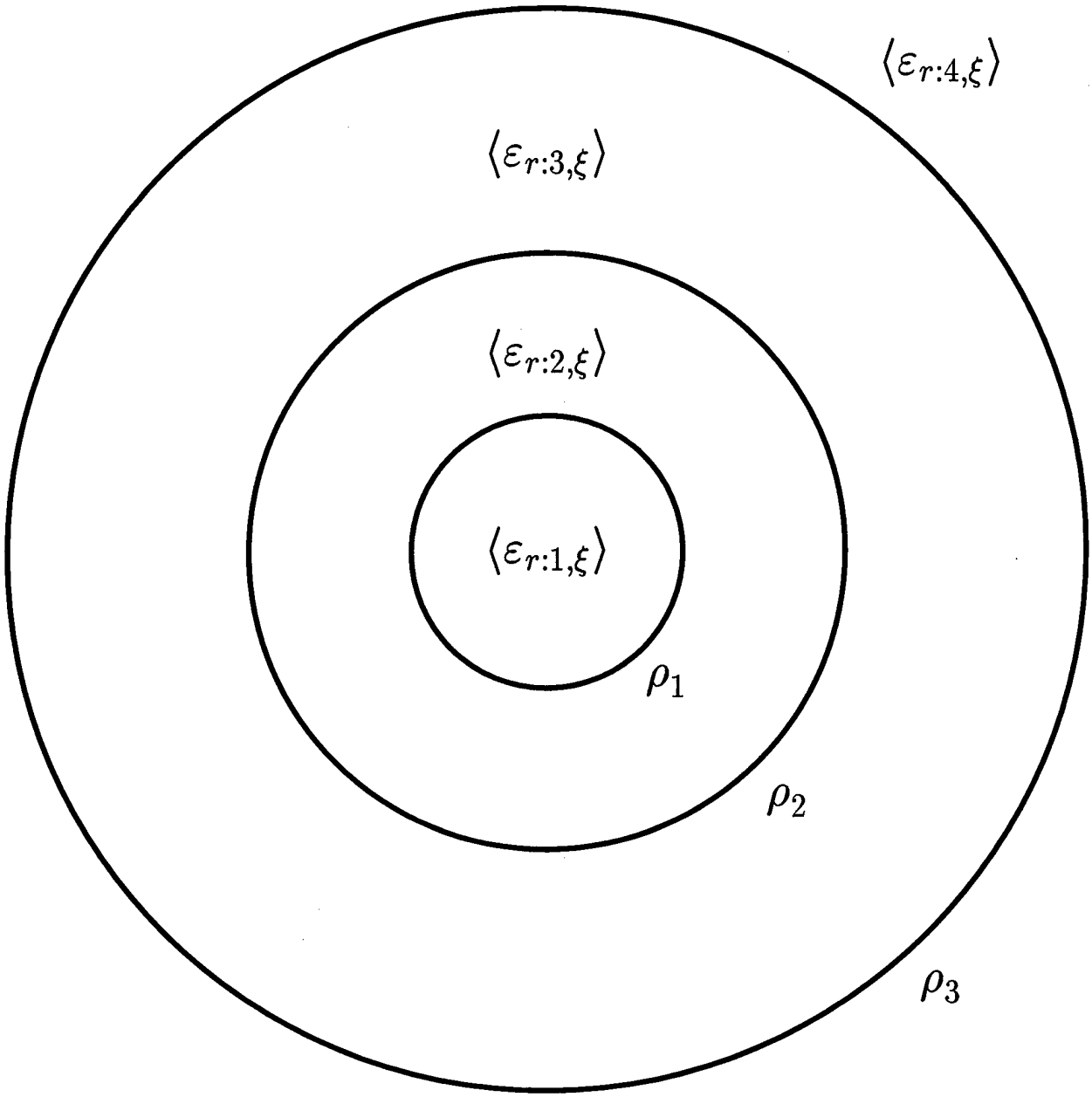

Figure 2.3 Illustration of the weighted permittivity profile, and notation, for the WIM radial solution.

Here I have defined

$$\gamma = \left\{ \begin{array}{ll} 1 & \text{inner regions} \\ \sqrt{-1} & \text{outer region} \end{array} \right\}, \; \Xi_m = \left\{ \begin{array}{ll} J_m & \text{inner regions} \\ K_m & \text{outer region} \end{array} \right\}, \; \Pi_m = \left\{ \begin{array}{ll} Y_m & \text{inner regions} \\ I_m & \text{outer region} \end{array} \right\}. \tag{2.56}$$

As in (2.40), I form a composite system matrix

$$[U^\alpha] \equiv [A_1^\alpha]^{-1}[B_1^\alpha][A_2^\alpha]^{-1}[B_2^\alpha][A_3^\alpha]^{-1}[B_3^\alpha]\cdots[A_{M-1}^\alpha]^{-1}[B_{M-1}^\alpha] \tag{2.57}$$

relating the unknown coefficients in the $i = 1$ region (core) to the coefficients in the $i = M$ region (cladding) via

$$\left[\begin{array}{c} c_1^\alpha \\ d_1^\alpha \end{array} \right] = \left[\begin{array}{cc} u_{11}^\alpha & u_{12}^\alpha \\ u_{21}^\alpha & u_{22}^\alpha \end{array} \right] \left[\begin{array}{c} c_M^\alpha \\ d_M^\alpha \end{array} \right]. \tag{2.58}$$

Since I am searching for longitudinally-propagating, laterally-confined VCSEL modes I force regularity at the origin and exponential decay as $\rho \to \infty$ by setting

$$d_1^\alpha = d_M^\alpha = 0. \tag{2.59}$$

Finally, substituting (2.59) into (2.58) I obtain the radial threshold condition

$$u_{21}^\alpha(\omega, \kappa_{\text{active}}) = 0. \tag{2.60}$$

In order to generate sensible boundary conditions when $m \neq 0$, I must construct *hybrid* modes in which both R and P are nonzero. Again, none of the tangential field components are separable and it is impossible to match them for all z at a radial interface. Furthermore, if I mirror my axial treatment and independently force the TE and TM components to be continuous I generate inconsistent boundary conditions. For example, independently forcing E_z and the TM part of E_ϕ to be continuous requires $\left(k^{\text{TM}}\right)^2 P(\rho)/\langle\varepsilon_{r:Q}^{\text{TM}}\rangle$ and $P(\rho)/\langle\varepsilon_{r:Q}^{\text{TM}}\rangle$ be continuous at each interface. But this forces k^{TM} itself to be continuous, which is absurd. I cannot hope to work with TE and TM modes independently. Therefore, I approximate my problem with an equivalent cylindrical dielectric waveguide problem, which admits analytic

solutions for hybrid modes. These approximations are used *only* to generate boundary conditions, *not* as a substitution for the actual radial and axial solutions in each region.

Cylindrical waveguide modes depend on z as $e^{i\beta z}$ or $e^{-i\beta z}$. My fields, in contrast, depend on z via (2.28). There are two differences I must overcome. First, cylindrical waveguide modes are characterized by a *single* axial propagation constant β, whereas my fields have a different axial propagation constant β_j^a for each axial region and polarization. I can easily remedy this by replacing β_j^a with $\langle\beta^\alpha\rangle$, as defined in (2.25). Second, cylindrical waveguide modes depend on z as *either* $e^{i\beta z}$ *or* $e^{-i\beta z}$. But even after replacing β_j^a with $\langle\beta^\alpha\rangle$ my fields have a different linear combination of $e^{i\langle\beta^\alpha\rangle z}$ and $e^{-i\langle\beta^\alpha\rangle z}$ in each region, depending on the relative values of a_j^α and b_j^α. Therefore, for the purpose of constructing boundary conditions, I assume that the fields approximate a "pure" standing wave in the axial direction, with

$$a_j^{\mathrm{TE}} = b_j^{\mathrm{TE}} \text{ and } a_j^{\mathrm{TM}} = -b_j^{\mathrm{TM}}. \tag{2.61}$$

I assume further that $a_j^{\mathrm{TE}} \approx a_j^{\mathrm{TM}}$, and approximate the z-dependence of my fields as

$$\begin{aligned} \tilde{Q}(z) &\equiv \sin(\langle\beta^{\mathrm{TM}}\rangle z), \\ \tilde{S}(z) &\equiv \cos(\langle\beta^{\mathrm{TE}}\rangle z). \end{aligned} \tag{2.62}$$

Substituting (2.62) into (2.46) and (2.48), I approximate the $\hat{\phi}$ field components as

$$\begin{aligned} \tilde{E}_\phi(\rho,z) &= \frac{m}{\omega\varepsilon_0\langle\varepsilon_{r:Q}^{\mathrm{TM}}\rangle\rho}P(\rho)\tilde{Q}'(z) + R'(\rho)\tilde{S}(z), \\ &\approx \left\{\frac{m\langle\beta^{\mathrm{TM}}\rangle}{\omega\varepsilon_0\langle\varepsilon_{r:Q}^{\mathrm{TM}}\rangle\rho}P(\rho) + R'(\rho)\right\}\cos\left(\langle\beta\rangle z\right) \end{aligned} \tag{2.63}$$

and

$$\begin{aligned} \tilde{H}_\phi(\rho,z) &= -P'(\rho)\tilde{Q}(z) + \frac{m}{\omega\mu_0\rho}R(\rho)\tilde{S}'(z), \\ &\approx \left\{-P'(\rho) - \frac{m\langle\beta^{\mathrm{TE}}\rangle}{\omega\mu_0\rho}R(\rho)\right\}\sin\left(\langle\beta\rangle z\right). \end{aligned} \tag{2.64}$$

Here I have replaced $\varepsilon_{r:i,j}$ by the appropriate weighted value, and have selectively assumed $\langle\beta^{\mathrm{TE}}\rangle \approx \langle\beta^{\mathrm{TM}}\rangle \approx \langle\beta\rangle$ to factor out the z dependence. Through *a-posteriori* comparison with my calculated results, I find all these assumptions well justified.

These approximate expressions for $\tilde{E}_\phi$ and $\tilde{H}_\phi$ are separable, as are expressions (2.45) and (2.47) for E_z and H_z. Therefore I can immediately construct suitable boundary conditions for radial hybrid modes by requiring the continuity of

$$\frac{\left(k^{\mathrm{TM}}\right)^2}{\langle\varepsilon_{r:Q}^{\mathrm{TM}}\rangle}P(\rho), \tag{2.65}$$

$$\left(k^{\mathrm{TE}}\right)^2 R(\rho), \tag{2.66}$$

$$\frac{m\langle\beta^{\mathrm{TM}}\rangle}{\omega\varepsilon_0\langle\varepsilon_{r:Q}^{\mathrm{TM}}\rangle\rho}P(\rho) + R'(\rho), \tag{2.67}$$

$$\text{and } P'(\rho) + \frac{m\langle\beta^{\mathrm{TE}}\rangle}{\omega\mu_0\rho}R(\rho). \tag{2.68}$$

By inserting the functional forms (2.44) and forcing all four of the above combinations to be continuous, I link the unknown coefficients at each radial interface $\rho = \rho_i$ through the 4×4 transfer matrix

$$A_i \begin{bmatrix} c_i^{\mathrm{TM}} \\ d_i^{\mathrm{TM}} \\ c_i^{\mathrm{TE}} \\ d_i^{\mathrm{TE}} \end{bmatrix} = B_i \begin{bmatrix} c_{i+1}^{\mathrm{TM}} \\ d_{i+1}^{\mathrm{TM}} \\ c_{i+1}^{\mathrm{TE}} \\ d_{i+1}^{\mathrm{TE}} \end{bmatrix}, \tag{2.69}$$

where

$$A_i \equiv \begin{bmatrix} \frac{\left(k_i^{\mathrm{TM}}\right)^2}{\langle\varepsilon_{r:i,Q}^{\mathrm{TM}}\rangle}J_m(k_i^{\mathrm{TM}}\rho_i) & \frac{\left(k_i^{\mathrm{TM}}\right)^2}{\langle\varepsilon_{r:i,Q}^{\mathrm{TM}}\rangle}Y_m(k_i^{\mathrm{TM}}\rho_i) & 0 & 0 \\ 0 & 0 & \left(k_i^{\mathrm{TE}}\right)^2 J_m(k_i^{\mathrm{TE}}\rho_i) & \left(k_i^{\mathrm{TE}}\right)^2 Y_m(k_i^{\mathrm{TE}}\rho_i) \\ \frac{m\langle\beta^{\mathrm{TM}}\rangle}{\omega\varepsilon_0\langle\varepsilon_{r:i,Q}^{\mathrm{TM}}\rangle\rho}J_m(k_i^{\mathrm{TM}}\rho_i) & \frac{m\langle\beta^{\mathrm{TM}}\rangle}{\omega\varepsilon_0\langle\varepsilon_{r:i,Q}^{\mathrm{TM}}\rangle\rho}Y_m(k_i^{\mathrm{TM}}\rho_i) & k_i^{\mathrm{TE}}J_m'(k_i^{\mathrm{TE}}\rho_i) & k_i^{\mathrm{TE}}Y_m'(k_i^{\mathrm{TE}}\rho_i) \\ k_i^{\mathrm{TM}}J_m'(k_i^{\mathrm{TM}}\rho_i) & k_i^{\mathrm{TM}}Y_m'(k_i^{\mathrm{TM}}\rho_i) & \frac{m\langle\beta^{\mathrm{TE}}\rangle}{\omega\mu_0\rho}J_m(k_i^{\mathrm{TE}}\rho_i) & \frac{m\langle\beta^{\mathrm{TE}}\rangle}{\omega\mu_0\rho}Y_m(k_i^{\mathrm{TE}}\rho_i) \end{bmatrix}, \tag{2.70}$$

$$B_i \equiv \begin{bmatrix} \frac{\left(k_{i+1}^{\mathrm{TM}}\right)^2 \Xi_m(\gamma k_{i+1}^{\mathrm{TM}}\rho_i)}{\langle \varepsilon_{r:i+1,Q}^{\mathrm{TM}} \rangle} & \frac{\left(k_{i+1}^{\mathrm{TM}}\right)^2 \Pi_m(\gamma k_{i+1}^{\mathrm{TM}}\rho_i)}{\langle \varepsilon_{r:i+1,Q}^{\mathrm{TM}} \rangle} & 0 & 0 \\ 0 & 0 & \left(k_{i+1}^{\mathrm{TE}}\right)^2 \Xi_m(\gamma k_{i+1}^{\mathrm{TE}}\rho_i) & \left(k_{i+1}^{\mathrm{TE}}\right)^2 \Pi_m(\gamma k_{i+1}^{\mathrm{TE}}\rho_i) \\ \frac{m\langle \beta^{\mathrm{TM}} \rangle \Xi_m(\gamma k_{i+1}^{\mathrm{TM}}\rho_i)}{\omega \varepsilon_0 \langle \varepsilon_{r:i+1,Q}^{\mathrm{TM}} \rangle \rho_i} & \frac{m\langle \beta^{\mathrm{TM}} \rangle \Pi_m(\gamma k_{i+1}^{\mathrm{TM}}\rho_i)}{\omega \varepsilon_0 \langle \varepsilon_{r:i+1,Q}^{\mathrm{TM}} \rangle \rho_i} & \gamma k_{i+1}^{\mathrm{TE}} \Xi_m'(\gamma k_{i+1}^{\mathrm{TE}}\rho_i) & \gamma k_{i+1}^{\mathrm{TE}} \Pi_m'(\gamma k_{i+1}^{\mathrm{TE}}\rho_i) \\ \gamma k_{i+1}^{\mathrm{TM}} \Xi_m'(\gamma k_{i+1}^{\mathrm{TM}}\rho_i) & \gamma k_{i+1}^{\mathrm{TM}} \Pi_m'(\gamma k_{i+1}^{\mathrm{TM}}\rho_i) & \frac{m\langle \beta^{\mathrm{TE}} \rangle \Xi_m(\gamma k_{i+1}^{\mathrm{TE}}\rho_i)}{\omega \mu_0 \rho_i} & \frac{m\langle \beta^{\mathrm{TE}} \rangle \Pi_m(\gamma k_{i+1}^{\mathrm{TE}}\rho_i)}{\omega \mu_0 \rho_i} \end{bmatrix}. \tag{2.71}$$

These matrices are mathematically equivalent to those for a cylindrical dielectric waveguide. Cascading the interface transfer matrices, I again derive a composite system transfer matrix

$$\begin{bmatrix} c_1^{\mathrm{TM}} \\ d_1^{\mathrm{TM}} \\ c_1^{\mathrm{TE}} \\ d_1^{\mathrm{TE}} \end{bmatrix} = \begin{bmatrix} u_{11} & u_{12} & u_{13} & u_{14} \\ u_{21} & u_{22} & u_{23} & u_{24} \\ u_{31} & u_{32} & u_{33} & u_{34} \\ u_{41} & u_{42} & u_{43} & u_{44} \end{bmatrix} \begin{bmatrix} c_M^{\mathrm{TM}} \\ d_M^{\mathrm{TM}} \\ c_M^{\mathrm{TE}} \\ d_M^{\mathrm{TE}} \end{bmatrix}, \tag{2.72}$$

relating the innermost and outermost radial coefficients. The endpoint boundary conditions (2.59) remain valid. Applying them to (2.72) and demanding nontrivial solutions gives the hybrid threshold condition

$$\begin{vmatrix} u_{21}(\omega, \kappa_{\mathrm{active}}) & u_{23}(\omega, \kappa_{\mathrm{active}}) \\ u_{41}(\omega, \kappa_{\mathrm{active}}) & u_{43}(\omega, \kappa_{\mathrm{active}}) \end{vmatrix} = 0, \tag{2.73}$$

which I solve in the complex plane for ω and κ_{active}.

2.4 Iterative Solution Procedure

I compute the longitudinal and transverse mode spectrum by self-consistently solving the radial and axial problems. The modes are specified by the longitudinal mode number, the transverse mode number, and the azimuthal mode number m. Different longitudinal modes correspond to successive roots of the axial threshold condition (2.43), while different transverse modes correspond to successive roots of the radial threshold conditions (2.60) (for TE/TM modes) or (2.73) (for hybrid modes). The energy spacing between longitudinal modes is much greater than that between transverse modes. If I let ν denote a generalized mode index corresponding to a particular TE, TM, or hybrid mode, then the explicit un-

knowns for each mode are the vector potential functions $P_\nu(\rho)$, $Q_\nu(z)$ and/or $R_\nu(\rho)$, $S_\nu(z)$, the optical mode frequency ω_ν, and the material gain values $(\kappa_{\text{active}})_\nu$. I iteratively solve the axial and radial problems as follows.

First I focus attention on a particular family of modes by fixing m: for $m = 0$ I can compute TE or TM modes, while for $m > 0$ only hybrid modes are possible. Then I solve the axial problem, taking the effective indices equal to the corresponding values for $\varepsilon_{r;1,j}$ in the innermost radial region: this solution corresponds to the standard plane-wave calculation appropriate for large-area devices. The ordered roots of the axial threshold condition (2.43) yield initial approximations $Q_{\nu_0}(z)$ and/or $S_{\nu_0}(z)$, $\omega_{\nu_0}^{(\text{axial})}$, and $\left(\kappa_{\text{active}}^{(\text{axial})}\right)_{\nu_0}$ for the mode ν_0 of interest. For VCSEL lasing mode calculations I am only interested in the first root of (2.43), corresponding to the fundamental longitudinal mode. I next compute the k_i^α by inserting $Q_{\nu_0}(z)$ and/or $S_{\nu_0}(z)$ into (2.24), giving me enough information to address the radial problem. Depending on whether I am solving for TE, TM, or hybrid modes, I then compute the roots of the radial threshold condition (2.60) or (2.73), yielding approximations for $P_{\nu_0}(\rho)$ and/or $R_{\nu_0}(\rho)$, $\omega_{\nu_0}^{(\text{radial})}$, and $\left(\kappa_{\text{active}}^{(\text{radial})}\right)_{\nu_0}$; successive roots correspond to progressively higher-order transverse modes. Then I alternate between solving the axial and radial problems, always updating β_j^α and k_i^α by inserting the most recent wavefunctions into (2.21) or (2.24) as appropriate. In this way I generate a self-consistent solution to the coupled WIM equations (2.14) and (2.15), terminating when $\omega_{\nu_0}^{(\text{axial})} = \omega_{\nu_0}^{(\text{radial})}$ and $\left(\kappa_{\text{active}}^{(\text{axial})}\right)_{\nu_0} = \left(\kappa_{\text{active}}^{(\text{radial})}\right)_{\nu_0}$ to within a prescribed tolerance. The procedure converges quite rapidly, allowing me to solve for a large number of cavity modes.

Finally, I note that the character of the modes found depends on both the differential equations and on the endpoint boundary conditions enforced. The original application of the WIM to rectangular waveguide geometries assumed propagating behavior in the $\hat{z}$ direction and evanescent decay in the $\hat{x}$ and $\hat{y}$ directions. These endpoint conditions resulted in a standard eigenvalue problem, with the longitudinal propagation constant β being the eigenvalue. In this case, the Rayleigh-Ritz variational principle asserts that the resulting approximation of β will be more accurate than the wavefunctions themselves. In my application, I have enforced evanescent decay in the radial direction and have permitted only

outward propagating waves in the $\hat{z}$ direction. This constrains the mode frequency ω *and* the material gain κ, as opposed to the propagation constant β, and these unknown parameters no longer appear as eigenvalues. Therefore the Rayleigh-Ritz principle has nothing to say about the relative accuracy of ω and κ. Nevertheless, general variational principles dictate that I have found the best separable solution, and therefore I expect the resulting values for ω and κ to be reasonably accurate. Note that I can also apply the general WIM formalism to solve for *radially* propagating modes by relaxing the evanescent decay condition on the radial functions. As it turns out, these "parasitic" modes are *precisely* what is required to capture diffraction within the general framework of the weighted index method. I append the current WIM treatment to include these modes in Chapter V. However, before this I proceed and apply the current version of the method to several popular VCSELs in the following chapter.

III. Weighted Index Method Applications and Results

In Chapter II, I presented a *new*, extremely general and rapid technique for estimating the spatial profile, optical confinement factor, resonant frequency, and mirror and absorption losses of lasing modes in cylindrically-symmetric VCSEL geometries. In this chapter, I apply the weighted index method to several VCSEL geometries of current interest. The chapter is broken into two major parts. First, I compute all the optical laser parameters, save diffraction loss, for several lowest order modes of an oxide apertured and an etched post device. I compute all these parameters as a function of oxide aperture or post radius. These general results showcase the capabilities of the method. Furthermore, from these results I ascertain the basic changes in the optical mode for small aperture geometries. These include a *blueshift* in mode resonance, a loss of transverse confinement, and a heretofore unreported polarization dependent change in DBR reflectance.

Second, I pit the weighted index method against a simpler, more popular *effective* index method for blueshift calculation. Both models are applied to two different VCSEL designs emitting near 780 nm and 850 nm. I find that the weighted index method matches the data remarkably well, while the effective index calculation underestimates the blueshift. These results show that the weighted index model may be used to match the cavity resonance of small-aperture structures to the gain peak, and thereby minimize the threshold current.

3.1 Etched Post and Oxide Apertured VCSELs

Using the methods described in the last chapter, I calculate lasing modes in etched-post [6,76] and oxide-apertured [15,32] devices fabricated from a λ =980 nm, 1.5λ-cavity VCSEL. The VCSEL reflectors consist of a 17.5 period p-type GaAs/$Al_{0.92}Ga_{0.08}As$ top Distributed Bragg Reflector (DBR) for the oxide-apertured structure, and a 4 period GaAs/Al_xO top DBR with a $\lambda/4$ p^+ GaAs contact layer for the post geometry. The bottom reflector in both structures is a 22 period n-type GaAs/$Al_{0.92}Ga_{0.08}As$ DBR. The 1.5λ-cavity is step-tapered with (intrinsic) layers of $Al_{0.98}Ga_{0.02}As$, $Al_{0.65}Ga_{0.35}As$, $Al_{0.30}Ga_{0.70}As$, and GaAs, culminating in a single $In_{0.2}Ga_{0.8}As$ quantum well. Both structures are grown on a GaAs

substrate. The etched-post structure, illustrated in Figure 3.1, is formed by etching the top GaAs/AlAs DBR down to the $\lambda/4$ GaAs contact layer, then oxidizing the AlAs layers. The oxide-apertured structure, illustrated in Figure 3.2, is formed by oxidizing the $\lambda/4$ $Al_{.98}Ga_{.02}As$ layers in the cavity. I model each region as a cylindrically-symmetric layer of constant refractive index, assuming the material parameters in Table 3.1. Free carrier losses are incorporated by taking $\kappa_{i,j}$ negative. Material gain is incorporated by taking κ_{active} positive in the active quantum well region.

Material	Index	Doping (10^{18} cm^{-3})	Loss (cm^{-1})
$In_{0.2}Ga_{0.8}As$	3.5691	none	N/A
GaAs	3.5256	none	N/A
$Al_{0.3}Ga_{0.7}As$	3.3622	none	N/A
$Al_{0.65}Ga_{0.35}As$	3.1637	none	N/A
$Al_{0.98}Ga_{0.02}As$	2.9713	none	N/A
Al_xO	1.55	none	N/A
n-GaAs	3.5256	2	10
n-$Al_{0.92}Ga_{0.08}As$	3.0067	2	10
p-GaAs	3.5256	1	11.5
p-$Al_{0.92}Ga_{0.08}As$	3.0067	1	11.5
p^+-GaAs	3.5256	5	57.5

Table 3.1 Material Parameters used for WIM Simulations

The lowest frequency, or fundamental, VCSEL lasing mode is analogous to the HEM_{11} (or HE_{11}) hybrid waveguide mode. Here the first and second subscripts refer, respectively, to the azimuthal (m) and radial mode numbers. The HEM_{11} mode is the most plane-wave like of all the propagating bound modes, despite containing both E_z and H_z [58, 69]. It is also the only waveguide mode having a radial *intensity* distribution with a maximum at the center. Following this terminology, I refer to the next higher-order VCSEL modes as HEM_{21}, TE_{01}, and TM_{01} modes; these modes make up the degenerate LP_{11} mode under the "linear polarization" approximation [70]. All three of these modes feature a radial intensity profile with a null at the center.

3.1.1 Field Profile. In Figures 3.3 and 3.4, I plot the longitudinal standing wave intensity profile for the etched-post and oxide-apertured VCSELs. For the oxide-apertured structure, the contrast between DBR layers is small and the fields penetrate deeply into

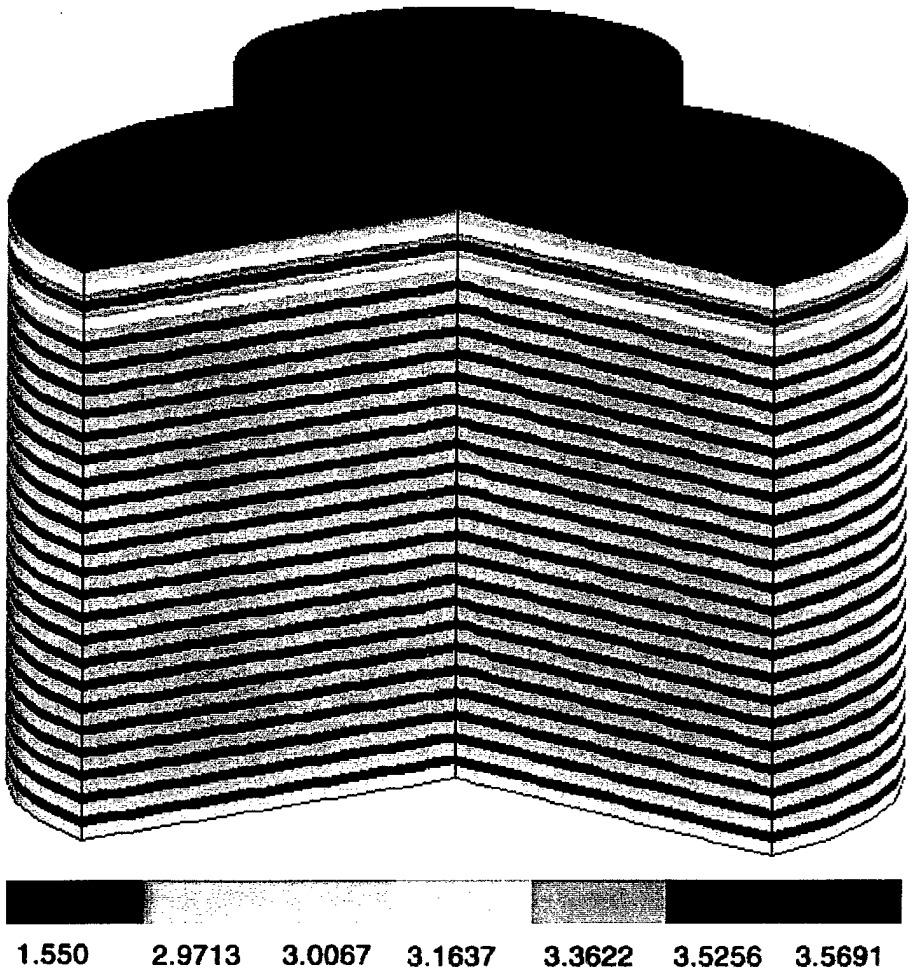

Figure 3.1 Quasi-3D plot of the etched-post VCSEL index profile.

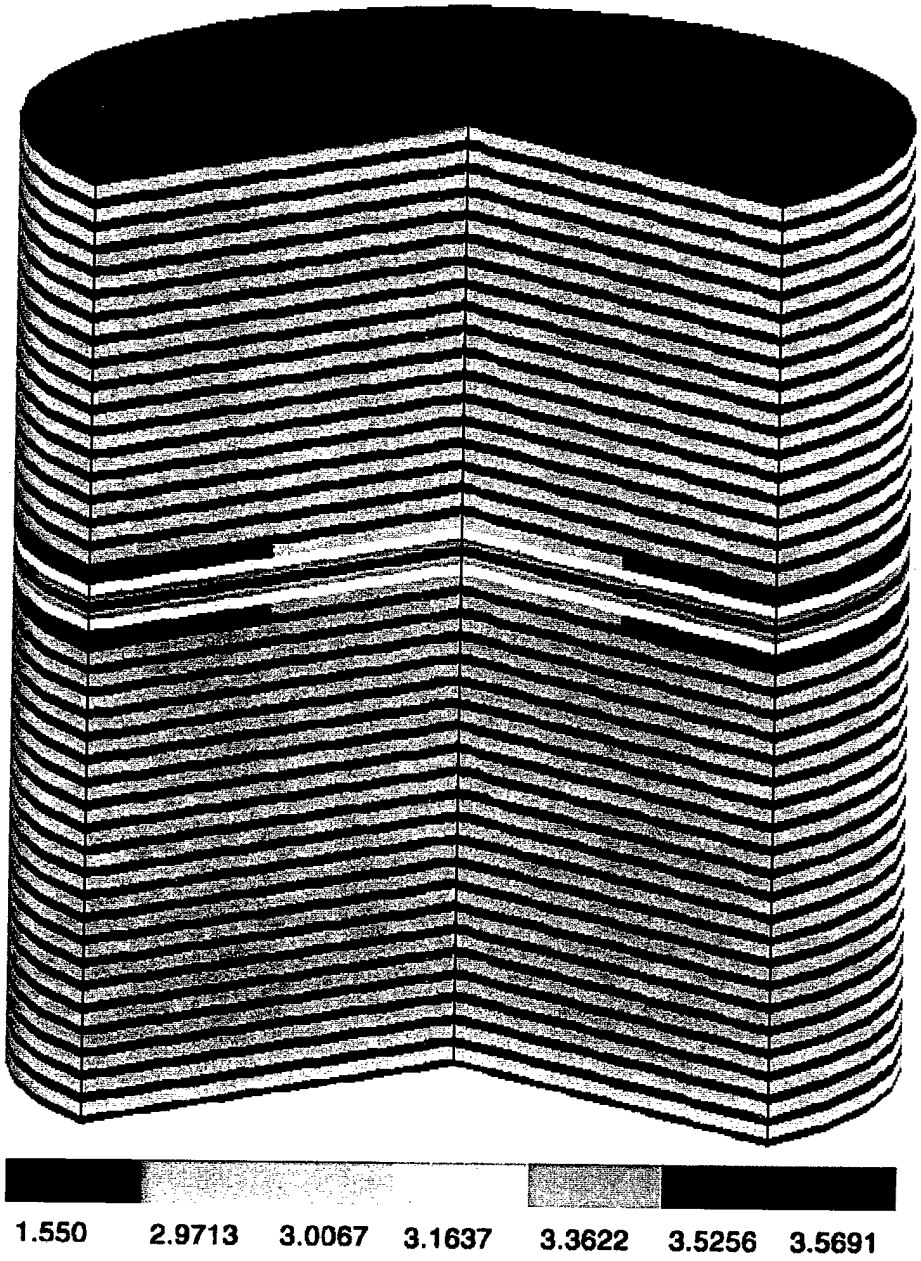

Figure 3.2 Quasi-3D plot of the oxide-apertured VCSEL index profile.

the top DBR. Therefore the large index difference between the semiconductor cavity and surrounding oxide is heavily weighted in (2.25), giving a large discontinuity in $\langle \varepsilon^{\alpha}_{r;\xi} \rangle$ between the inner and outer radial regions. As a result, the fields within the oxide-aperture VCSEL are tightly confined to the core. In contrast, for the etched-post structure the large index contrast between top DBR layers allows very little field penetration, resulting in a smaller effective index difference and a correspondingly less confined field. In both structures, the fundamental mode is more confined than higher-order modes, and smaller VCSELs exhibit less confinement than larger ones. These effects can also be seen in the three-dimensional field *energy* distribution, given by [7]

$$w = w_e + w_m = \frac{1}{4}\left[\varepsilon_0 \varepsilon_r \left|\vec{E}\right|^2 + \mu_0 \left|\vec{H}\right|^2\right]. \tag{3.1}$$

I plot w for the HEM_{11} and TE_{01} modes, for both structures, in Figures 3.5 – 3.8. Note that the familiar standing wave pattern does *not* appear in Figures 3.5 – 3.8. This is a result of the fact that these *energy* plots include both an electric and a *magnetic* field contribution. Nodes of $\vec{E}(z)$ correspond to antinodes of $\vec{H}(z)$ and vice-versa, effectively "washing out" the standing wave and leaving only the envelope function.

3.1.2 Transverse Confinement Factor. The transverse confinement factor Γ^{tr} is usually defined as

$$\Gamma^{\text{tr}} = \frac{\int_{\text{active}} |E|^2 \, ds}{\int |E|^2 \, ds}, \tag{3.2}$$

where the integral in the numerator is over the transverse extent of the active region and the integral in the denominator is over the entire transverse extent of the field. Figure 3.9 shows estimates of the transverse confinement factor for the first two modes of the etched-post and oxide-apertured VCSELs as a function of cavity radius. The estimates are generated from (3.2), using $E = E(\rho) \rightarrow \tilde{E}_\phi(\rho)$ for TE modes (2.63) and $E \rightarrow \tilde{H}_\phi(\rho)$ for TM modes (2.64); for hybrid modes I use both $\tilde{E}_\phi(\rho)$ and $\tilde{H}_\phi(\rho)$ and average the results. I use the effective ϕ components since they are already averaged over z and are representative of the total field intensity profile. As the cavity radius decreases, more of the field intensity leaks out of the active region and the confinement factors drop monotonically. This behavior becomes more

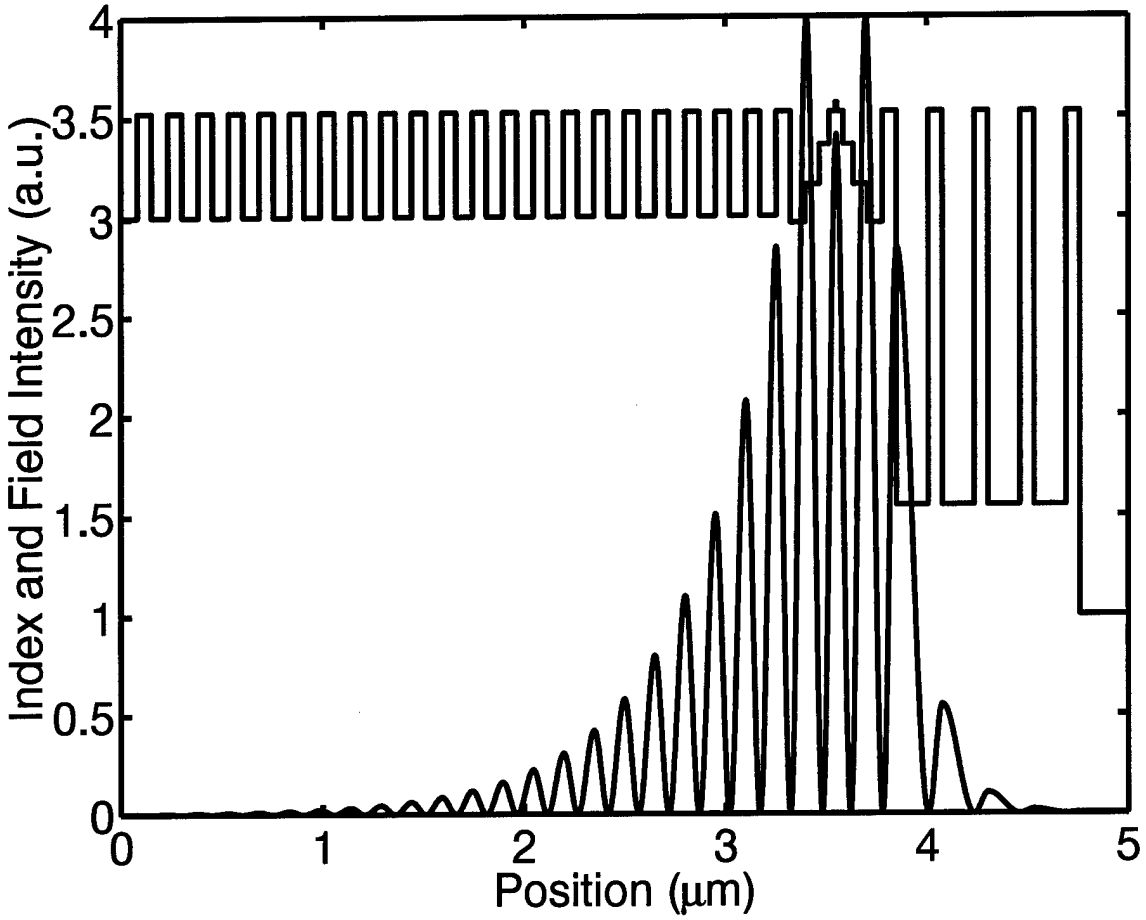

Figure 3.3 Index and standing intensity profile along the axial direction for a 1.4 μm radius etched-post VCSEL.

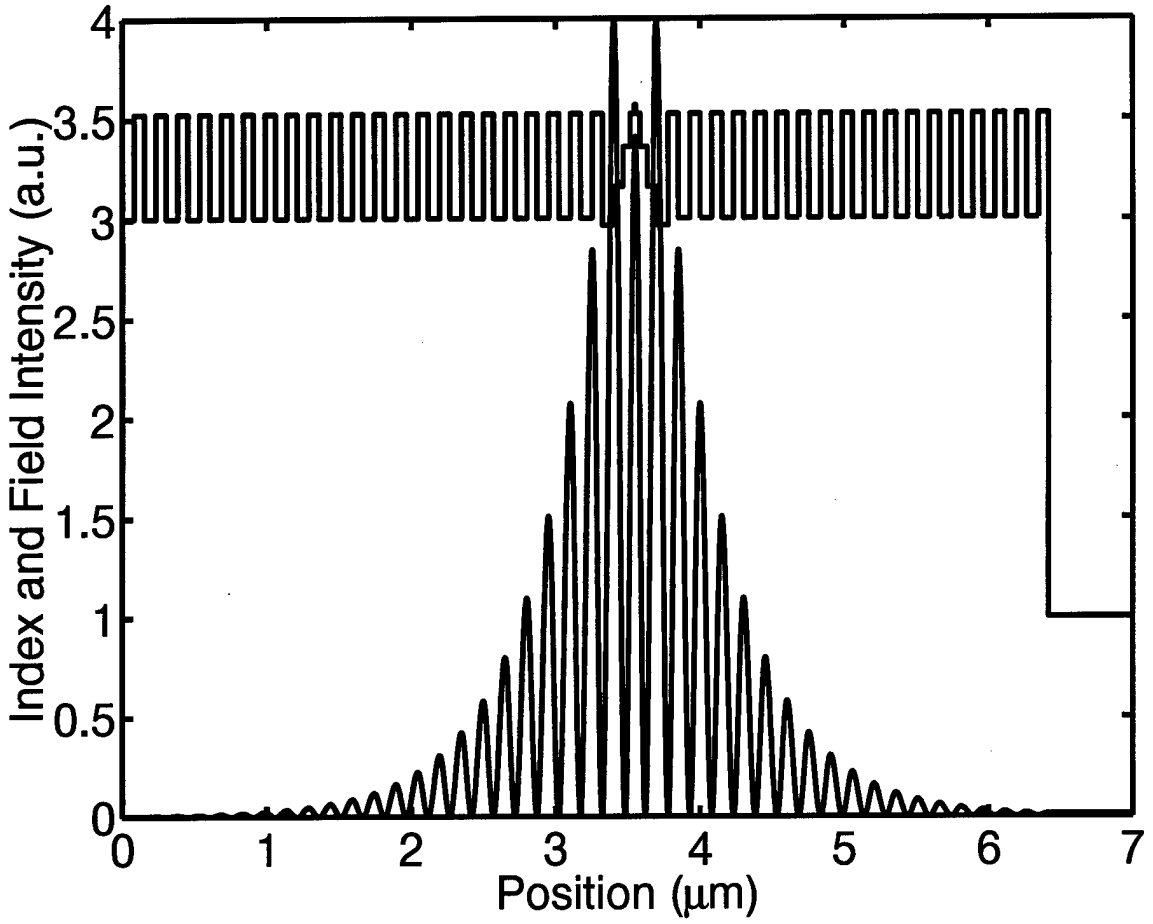

Figure 3.4 Index and standing intensity profile along the axial direction for a 1.4 μm radius oxide-apertured VCSEL.

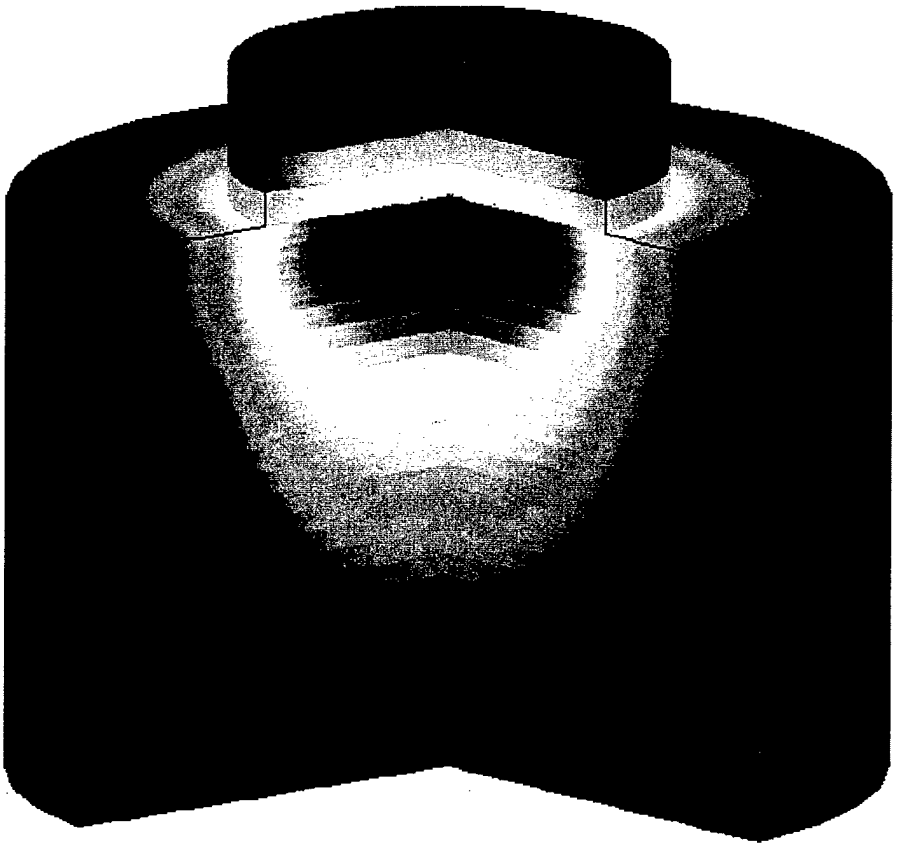

Figure 3.5 HEM_{11} mode energy profile for a 1.4 μm radius etched-post VCSEL. The energy distribution on the top surface is amplified in order to illustrated the emitted mode.

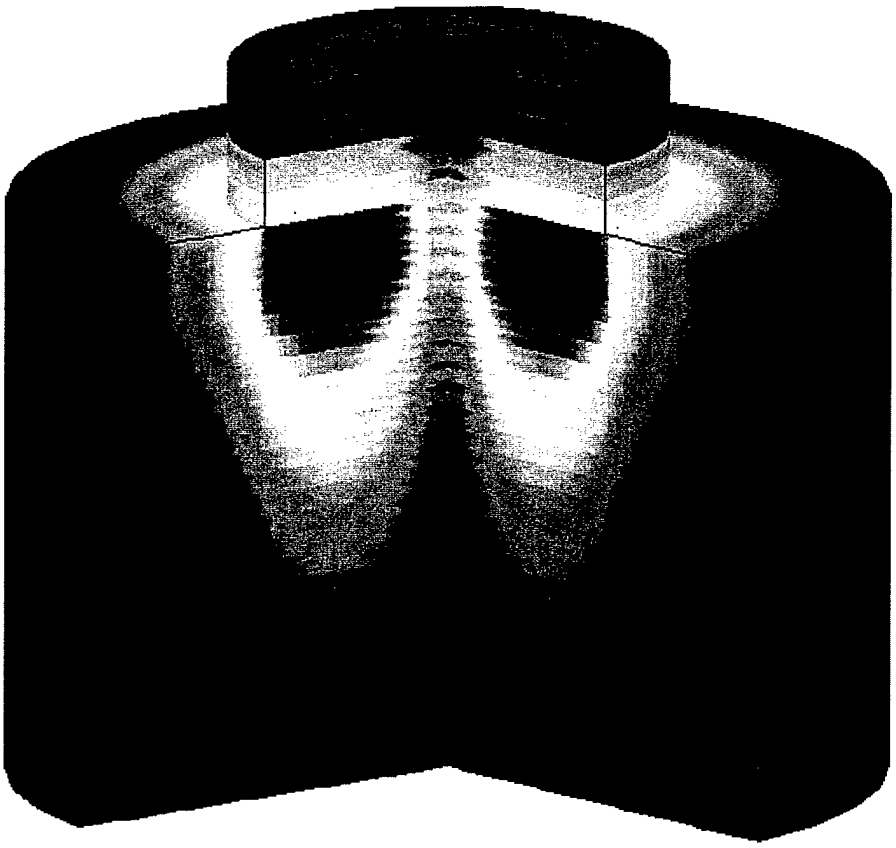

Figure 3.6 TE_{01} mode energy profile for a 1.4 μm radius etched-post VCSEL. The energy distribution on the top surface is amplified in order to illustrated the emitted mode.

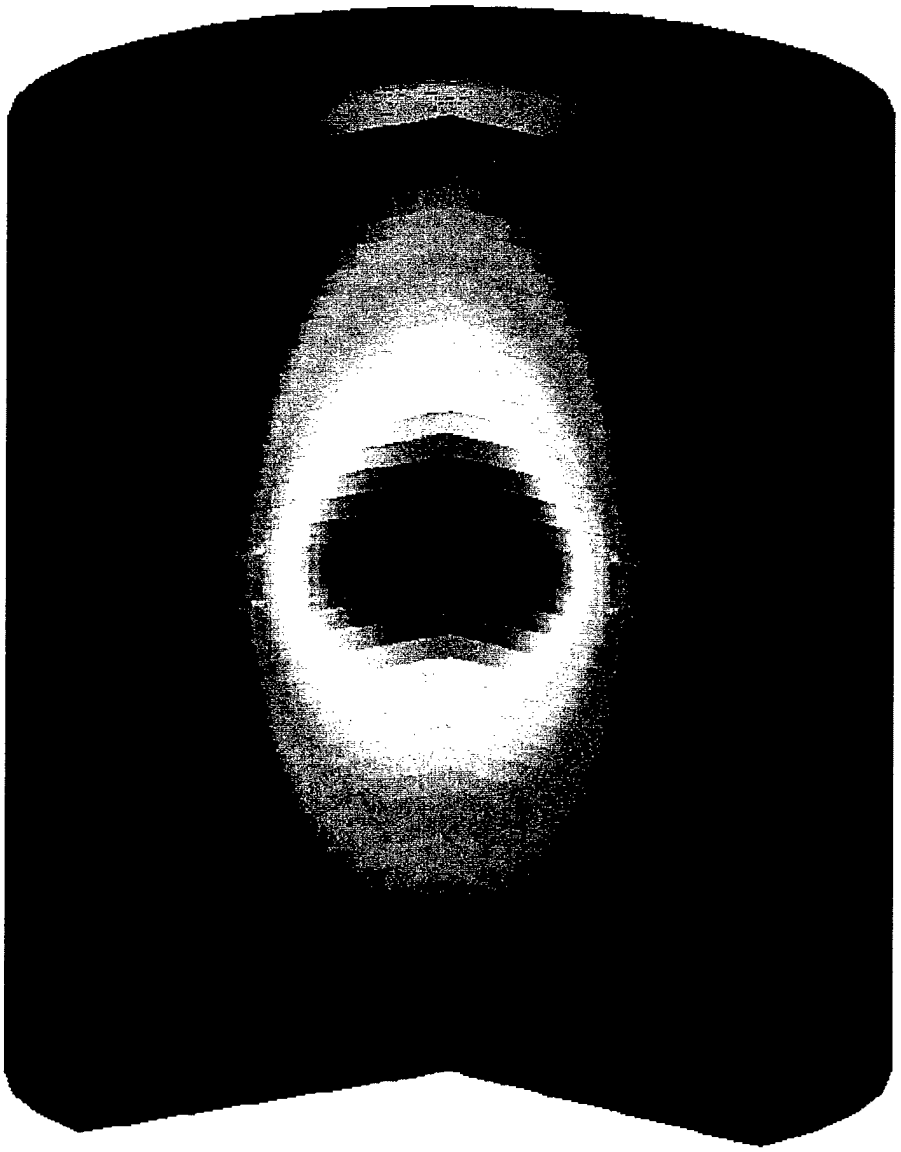

Figure 3.7 HEM_{11} mode energy profile for a 1.4 μm radius oxide-apertured VCSEL. The energy distribution on the top surface is amplified in order to illustrated the emitted mode.

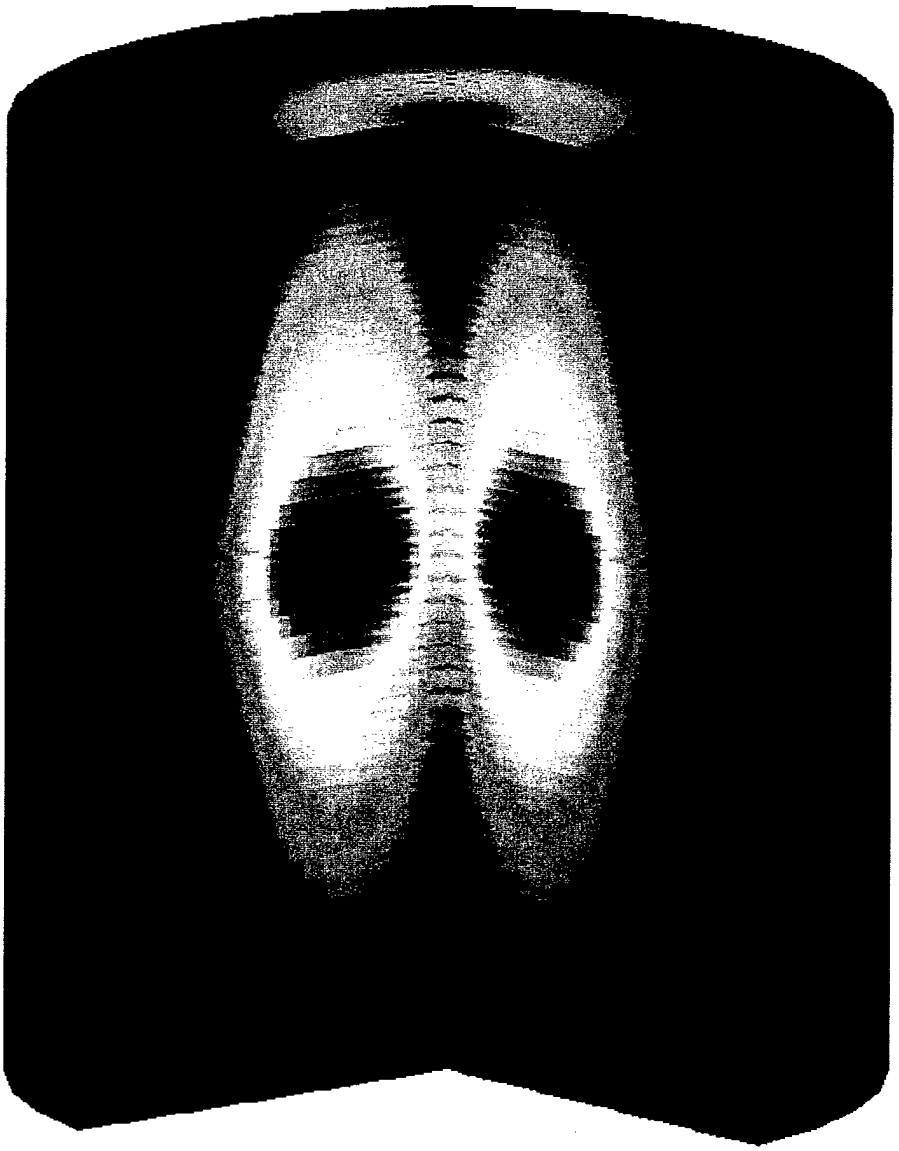

Figure 3.8 TE_{01} mode energy profile for a 1.4 μm radius oxide-apertured VCSEL. The energy distribution on the top surface is amplified in order to illustrated the emitted mode.

pronounced for higher-order modes, as illustrated in Figure 3.10. My oxide-apertured devices confine the optical mode more strongly to the active region and have higher transverse confinement factors than my etched-post structures. But the larger rate of change in confinement factor for the etched-post VCSEL, as shown in 3.9, yields better modal discrimination via Γ^{tr}. For example, a 1 μm radius device has $\Delta\Gamma^{tr} \equiv \Gamma^{tr}(\text{HEM11}) - \Gamma^{tr}(\text{TE01}) = 0.0759$ for the etched-post VCSEL, compared to only 0.0379 for the oxide-apertured VCSEL. This illustrates the effectiveness of employing a small radial index difference to introduce mode selective losses and enhance single mode lasing [27]. However, single mode lasing may also be enhanced by exploiting the *spectral* separation between transverse modes. I will show this in the following section.

3.1.3 Resonant Wavelength. In Figures 3.11 and 3.12 I plot the resonant wavelengths as a function of cavity radius for various modes in etched-post and oxide-apertured structures. The resonant wavelength blueshifts as the oxide or post diameter shrinks, a dramatic departure from plane-wave results. This wavelength shift can be easily explained by examining the weighted dispersion relations (2.21) and (2.24), both of which take the functional form

$$\langle k_\rho^2 \rangle + \langle \beta_z^2 \rangle = \frac{\omega^2}{c^2} \langle \varepsilon_r \rangle. \tag{3.3}$$

Although both $\langle k_\rho^2 \rangle$ and $\langle \beta_z^2 \rangle$ change as the radius shrinks, $\langle \beta_z^2 \rangle$ remains very close to its plane-wave value. Therefore, as $\langle k_\rho^2 \rangle$ increases from its plane-wave value of zero, ω increases, leading to the blueshift illustrated in Figures 3.11 and 3.12. This effect has been previously estimated using simpler approximations [21], but the self-consistent WIM results are more accurate, as shown in Figures 3.21 and 3.22. To construct low-threshold microcavity VCSELs, the quantum well emission peak must be matched to the blueshifted cavity resonance of the desired lasing mode.

The resonant wavelength changes more quickly with radius in my oxide-apertured VCSELs as compared with my etched-post structures. This occurs because the oxide-apertured device exhibits a larger difference in effective index between the inner and outer radial regions, resulting in a larger field confinement and a correspondingly larger value for $\langle k_\rho^2 \rangle$

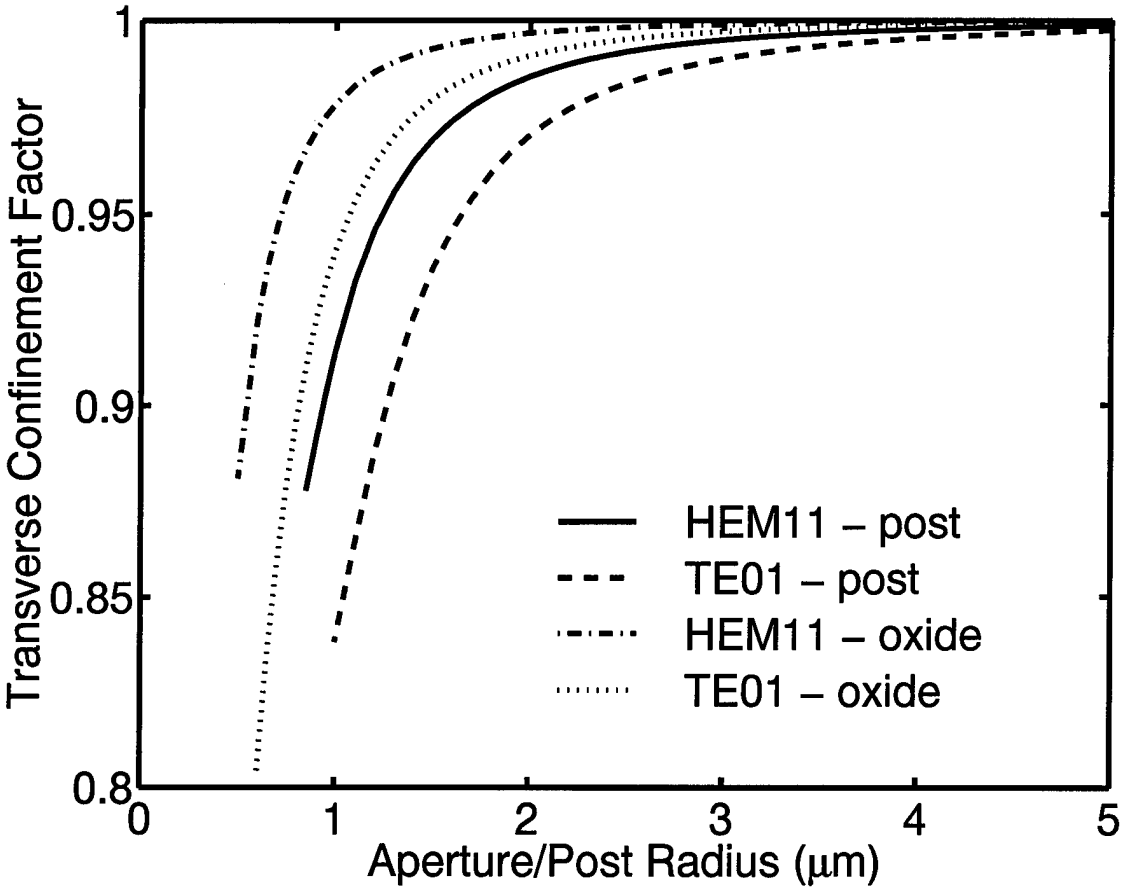

Figure 3.9 Transverse confinement factor for the first two modes of the etched-post and oxide-apertured VCSEL.

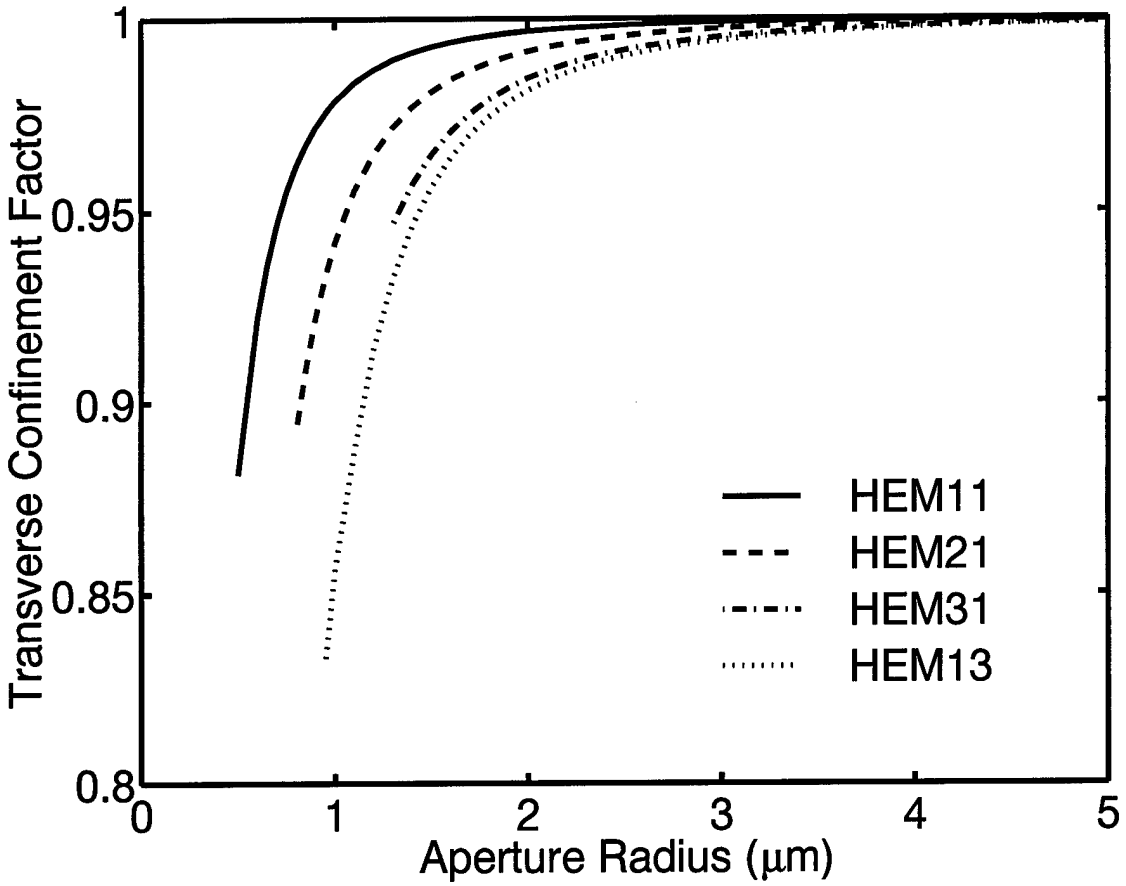

Figure 3.10 Transverse confinement factor for the fundamental, and a few sample higher order modes for the oxide-apertured VCSEL.

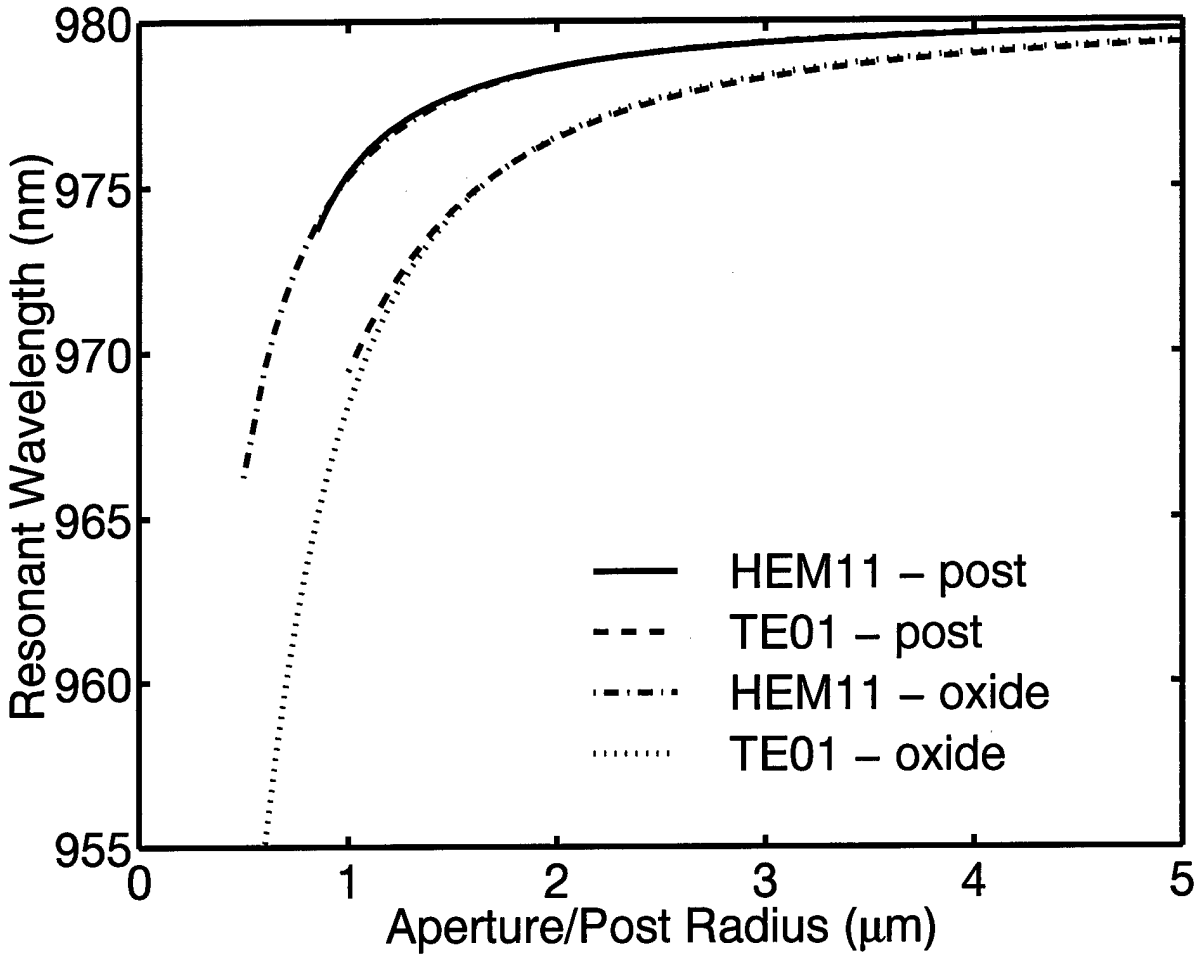

Figure 3.11 Resonant wavelength for the first two modes of the etched-post and oxide-apertured VCSEL.

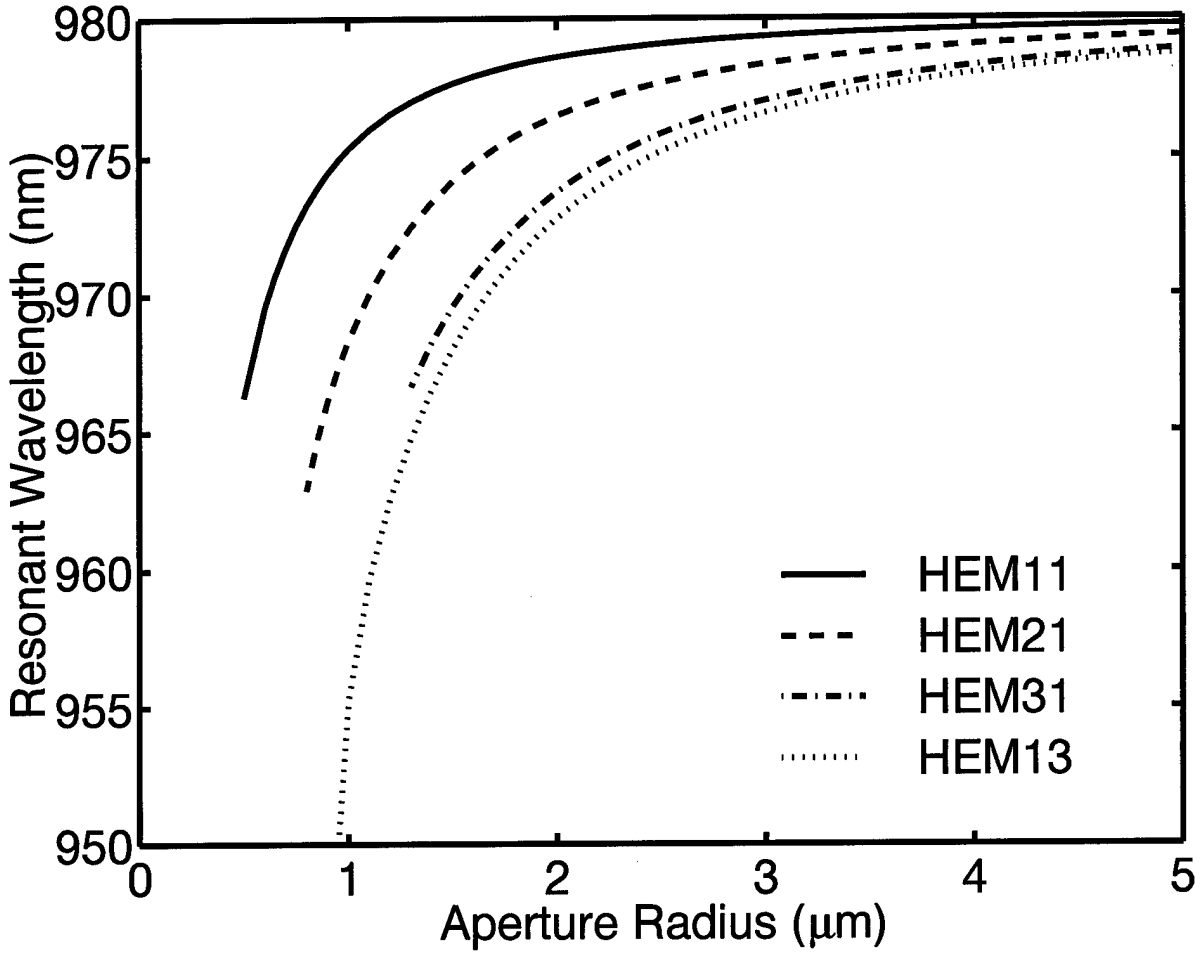

Figure 3.12 Resonant wavelength for the fundamental, and a few sample higher order modes for the oxide-apertured VCSEL.

in the waveguide core. As a result, the oxide-apertured structure provides more spectral discrimination between the VCSEL resonant modes. For example, in a 1 μm VCSEL $\Delta\lambda \equiv \lambda(\text{HEM11}) - \lambda(\text{TE01}) = 68.9$ Å for the oxide-apertured structure as compared to 59.8 Å for the etched-post. This effect might be exploited to obtain low threshold, *single mode* lasing. As discussed in my patent (pending) [22,55], if the gain spectrum is sufficiently narrow, spectral mode discrimination may be used to select the fundamental lasing mode. It is possible that a quantum dot gain region will provide the necessary narrow-band gain. In contrast, as discussed in the last section, traditional single mode designs rely on threshold gain discrimination. Here the difference in threshold gain between the fundamental and higher order modes is large and for low powers, the VCSEL will lase in a single mode. This type of design is often referred to as *anti-guiding.* The principal drawback of this method is an increased threshold for *all* the modes. By using the spectral separation, this problem may be avoided.

Finally, I plot the components of the quasi-degenerate LP_{11} mode in Figure 3.13. The results show a small, but non-zero, splitting of the mode for aperture radii $<\approx 0.85$ μm, indicating where the LP mode approximation begins to break down. Overall, however, the LP mode approximation is very good throughout the convergent range of the calculation. I exploit this fact to simplify the weighted index method to a scalar technique in Chapter V.

3.1.4 Mirror and Absorption Loss. Within the WIM framework, I approximate the VCSEL cavity *modes* as superpositions of cylindrical *waves.* Each of these, in turn, can be viewed as a superposition of TE and TM *plane* waves propagating at an angle

$$\langle\theta\rangle = \arctan\left(\frac{\langle k_\rho\rangle}{\langle\beta_z\rangle}\right) \tag{3.4}$$

to the z axis. As the cavity radius decreases, the effective transverse propagation constant $\langle k_\rho\rangle$ increases for all modes and, consequently, the average angle of incidence for the component plane waves impinging on each DBR interface increases. The power reflectivity for TE waves increases monotonically with angle until the total internal reflection angle is reached, while the power reflectivity for TM waves decreases monotonically until the Brewster angle

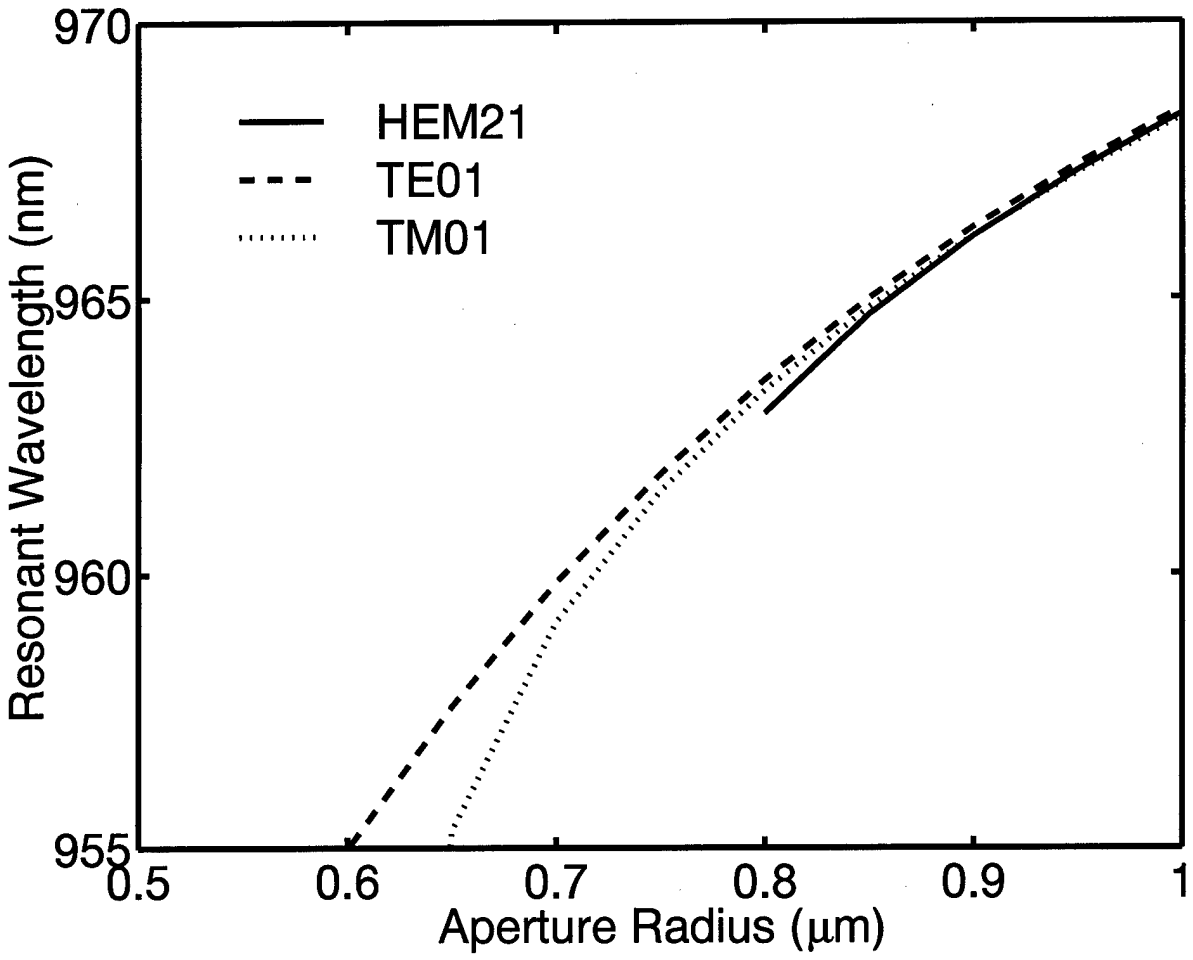

Figure 3.13 Resonant wavelength for the components of the quasi-degenerate LP_{11} mode, illustrating the point at which the degeneracy is broken.

is reached [65]. As a result, the TE wave components encounter *more* reflective DBR mirrors as the cavity radius shrinks, while the TM wave components encounter *less* reflective DBRs; Figure 3.14 illustrates this behavior for the oxide-apertured structure. Therefore the TE wave components suffer less mirror loss, the TM wave components more, and the mirror losses for pure TE VCSEL *modes* decreases with cavity radius, while the mirror losses for TM modes increases. For HEM modes—comprised of both TE and TM components—the change in reflectivity approximately cancels out. All of these trends are evident in Figures 3.15 – 3.18, which show the mirror and absorption losses *divided* by the total confinement factor Γ^{tot},

$$\frac{1}{\Gamma^{\text{tot}}}\left\{\alpha^{(\text{mirror})}+\alpha^{(\text{absorption})}\right\}\equiv 4\pi\kappa_{\text{active}}/\lambda, \tag{3.5}$$

for the fundamental and several higher order VCSEL transverse modes. The quantity I plot is precisely the threshold gain in the *absence* of diffraction loss.

The results shown in Figures 3.14 – 3.16 agree with prior in-plane laser studies that show a higher facet reflectance for TE than TM modes and a similar propagation constant (β) for both TE and TM modes [2,34,38,41]. For both VCSELs and in-plane lasers, these trends in mirror reflectivity become more pronounced for higher-order modes. The minima in the TE curves in Figures 3.15 and 3.16 occurs at the point where the change in confinement factor balances the change in mirror reflectance. For TM and HEM modes, no minima exists since the mirror reflectance is approximately constant (HEM) or decreases (TM) with decreasing radius. The radius at which each curve terminates indicates the "minimum" aperture size for each optical mode. This size effect has been previously estimated by simpler calculations [21], but the WIM values should be more accurate. Since my oxide-apertured structure confines the fields better than the etched-post structure, it supports bound modes at smaller cavity radii. This completes the overview of the WIM features. I now turn to a more challenging task for the method, prediction of experimental VCSEL data.

3.2 Experimental Verification of Blueshift Predictions

I compare measured blueshifts for two different device designs against predictions from my weighted index model and a simpler effective index model. Both models require only one

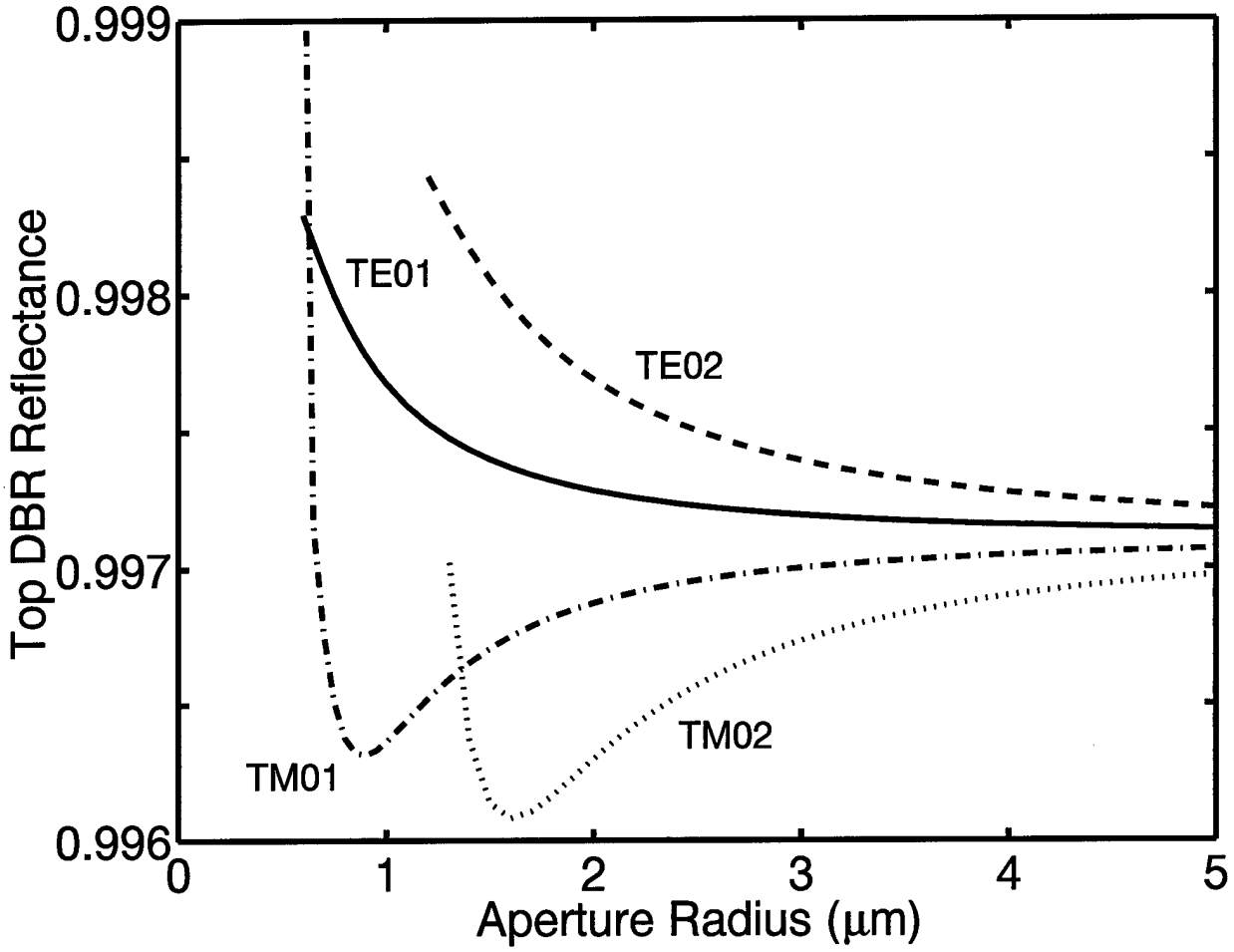

Figure 3.14 Top DBR reflectance for the TE and TM modes of the oxide-apertured VCSEL.

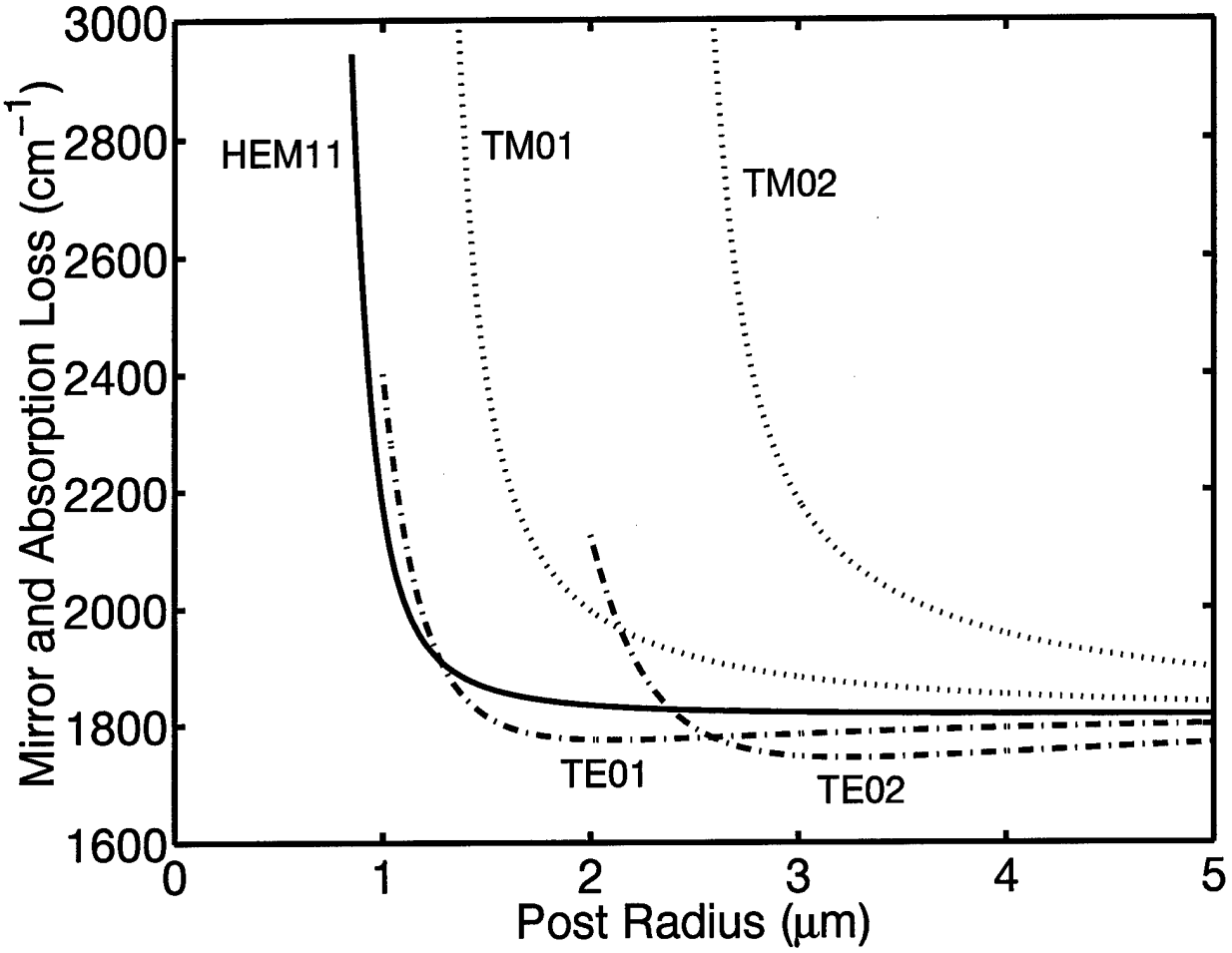

Figure 3.15 Mirror and absorption loss for the fundamental, and transverse electric and magnetic modes for the etched-post VCSEL.

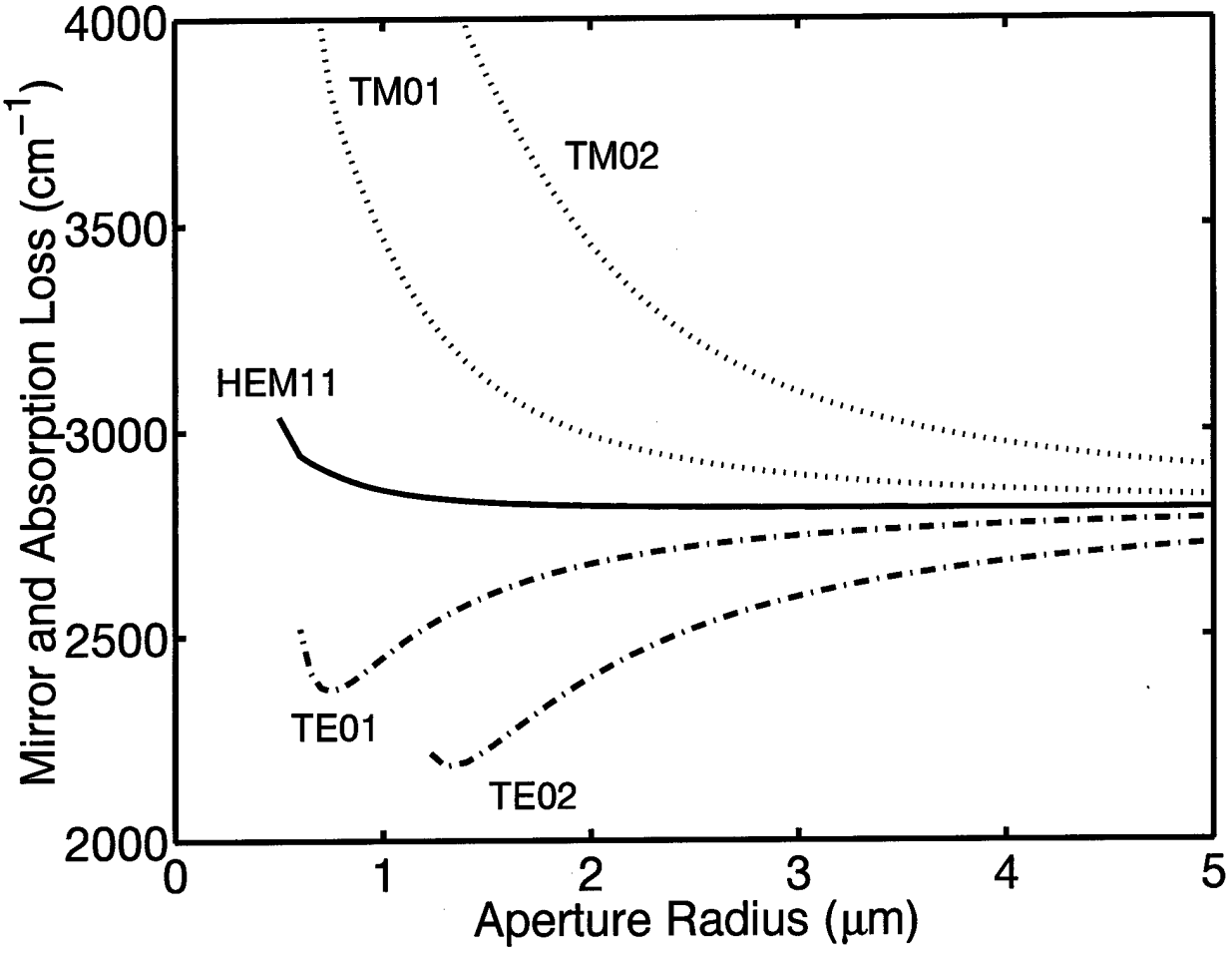

Figure 3.16 Mirror and absorption loss for the fundamental, and transverse electric and magnetic modes for the oxide-apertured VCSEL.

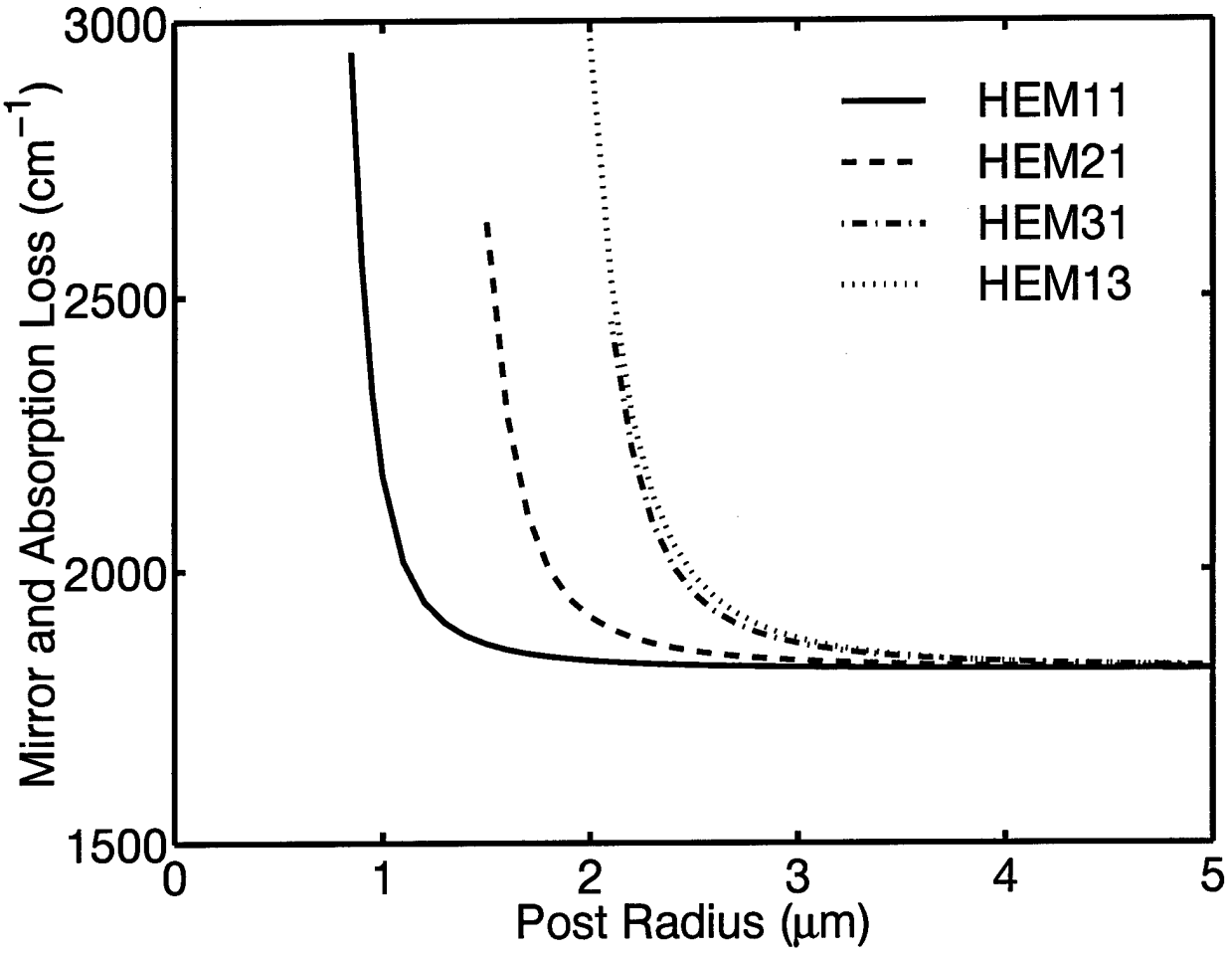

Figure 3.17 Mirror and absorption loss for the fundamental, and a few sample higher order hybrid modes for the etched-post VCSEL.

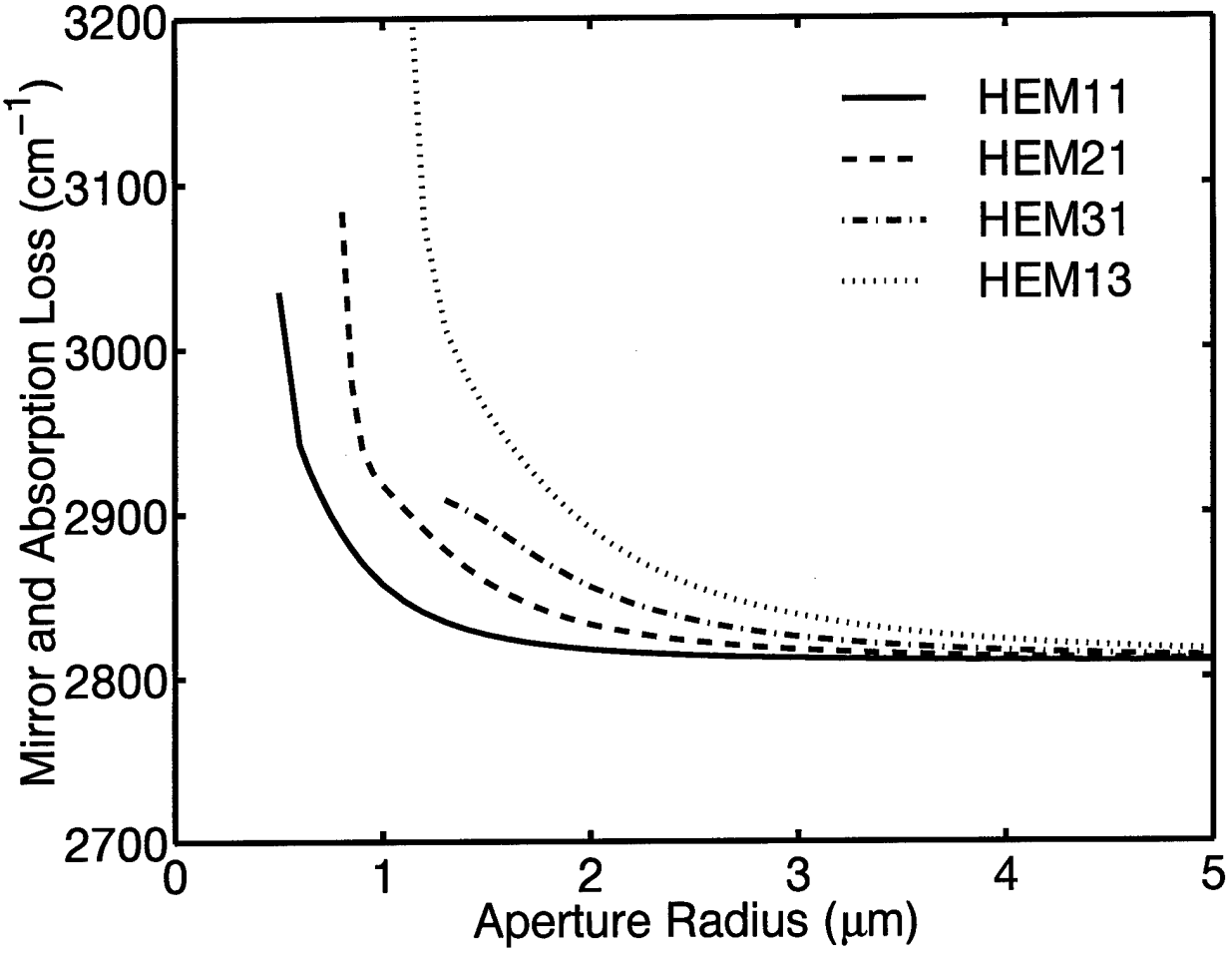

Figure 3.18 Mirror and absorption loss for the fundamental, and a few sample higher order hybrid modes for the oxide-apertured VCSEL.

adjustable parameter—the cavity thickness is adjusted to match the Fabry-Perot resonance of broad-area devices. I find that the weighted index calculation reproduces the dependence of lasing wavelength on aperture radius remarkably well, while the effective index model underestimates the blueshift.

3.2.1 Effective Index Method. A simple and popular approximation to calculate the blueshift is the *effective index method.* In this approach, an axial wavevector β is calculated for each layer by propagating plane-waves through the dielectric layer stack, using the refractive indices at $\rho = 0$ for each layer. The resulting (scalar) electric field profile $\xi(z)$ is then used to compute *effective* indices

$$n_{\text{core}} \equiv \sqrt{\frac{\int dz\ |\xi(z)|^2\ n^2(\rho=0,z)}{\int dz\ |\xi(z)|^2}},\ n_{\text{clad}} \equiv \sqrt{\frac{\int dz\ |\xi(z)|^2\ n^2(\rho=\infty,z)}{\int dz\ |\xi(z)|^2}} \tag{3.6}$$

corresponding to the core and cladding indices for an "effective" cylindrical dielectric waveguide. An effective axial wavevector $\langle\beta\rangle$ is computed similarly. The radial wave equation for this waveguide is then solved, taking regular Bessel functions inside the aperture and evanescent solutions outside. This procedure fixes the radial wavevector k, and the resonant frequency may then be calculated from a weighted dispersion relation. Augmentations of this model and applications to oxide-apertured VCSELs are given in References [26] and [21].

3.2.2 Experiment. I compare both effective- and weighted-index calculations of the blueshift against measurements performed on two different VCSEL structures. To conform with the most often *measured* modes[1], I label the VCSEL modes in accordance with the linear polarization (LP) convention [58]. Therefore, the fundamental lasing mode—characterized by a peak in intensity at the mode center—is labeled as LP_{01}. Similarly, the first higher-order VCSEL mode—characterized by a null at the mode center—is denoted by LP_{11}. These LP modes approach the exact fiber optic modes as the index difference between the core and

[1]The fact that the LP modes, *not* the vector modes, are most often observed is a result of two factors: (1) the relatively small weighted index difference between the inner and outer radial regions, which supports the "weakly guiding" assumption upon which the LP modes are based; and (2) the fact that, for small aperture radii, diffraction dominates any difference in threshold between the quasi-degenerate constituents of an LP mode. As a result of these arguments, I change the WIM to solve for LP modes in Chapter V.

cladding becomes small: the LP_{01} mode includes the doubly degenerate HEM_{11} modes, and the LP_{11} mode includes the TE_{01}, TM_{01}, and doubly degenerate HEM_{21} modes.

The first VCSEL design is a 1-λ cavity, single oxide aperture device, designed for 780 nm emission [66]. The active region has four 80 Å $Al_{0.11}Ga_{0.89}As$ quantum wells separated by 80 Å $Al_{0.3}Ga_{0.7}As$ barriers. On either side of the active region lies an $Al_{0.5}Ga_{0.5}As$ spacer layer, completing the 1-λ cavity. The upper and lower distributed Bragg reflectors (DBRs) consist of 26 and 40.5 periods of $Al_{0.3}Ga_{0.7}As/Al_{0.9}Ga_{0.1}As$, respectively. All DBR interfaces, as well as the spacer-to-DBR interfaces, are linearly graded. To facilitate oxidation, the upper-DBR low-index layer adjacent to the cavity is AlAs. When oxidized, this layer contains a square aperture. The entire structure is grown on a GaAs substrate. The structure is illustrated in Figure 3.19.

To investigate the blueshift, five devices were fabricated from this layer structure: four with small apertures (≤ 5 μm side length) and one broad area device with a 13 μm $\times$ 13 μm aperture. All five devices were located within a 0.5 mm $\times$ 0.5 mm area of the wafer, ensuring excellent device uniformity. While electrically pumping the devices at half threshold, luminescence data was collected with an optical multichannel analyzer. The electroluminescence data from the broad-area device showed a fundamental mode at 782 nm, which I interpret as the Fabry-Perot resonance of the VCSEL layer structure. The remaining measurement results for the four small-aperture devices are plotted in Figure 3.20; a semilog scale is employed to bring out the details in the electroluminescence response. For each aperture size at least two distinct resonances are visible. As the aperture size increases, more resonant modes appear, and the spacing between them decreases. To precisely locate the mode resonances, the peaks in Figure 3.20 were fitted with Lorentzian lineshape functions. Moving from right to left, the first two resonances represent the LP_{01} and LP_{11} modes.

The second VCSEL design is a 1-λ cavity, double-oxide-aperture device, designed for 850 nm emission [14]. The active region has five 80 Å GaAs quantum wells separated by $Al_{0.3}Ga_{0.7}As$ barriers. The upper and lower DBRs consist of 26 and 36.5 periods of $Al_{0.16}Ga_{0.84}As/Al_{0.92}Ga_{0.08}As$, respectively, with graded interfaces between the layers and between the DBRs and the cavity. Square apertures are formed by oxidizing 182 Å thick

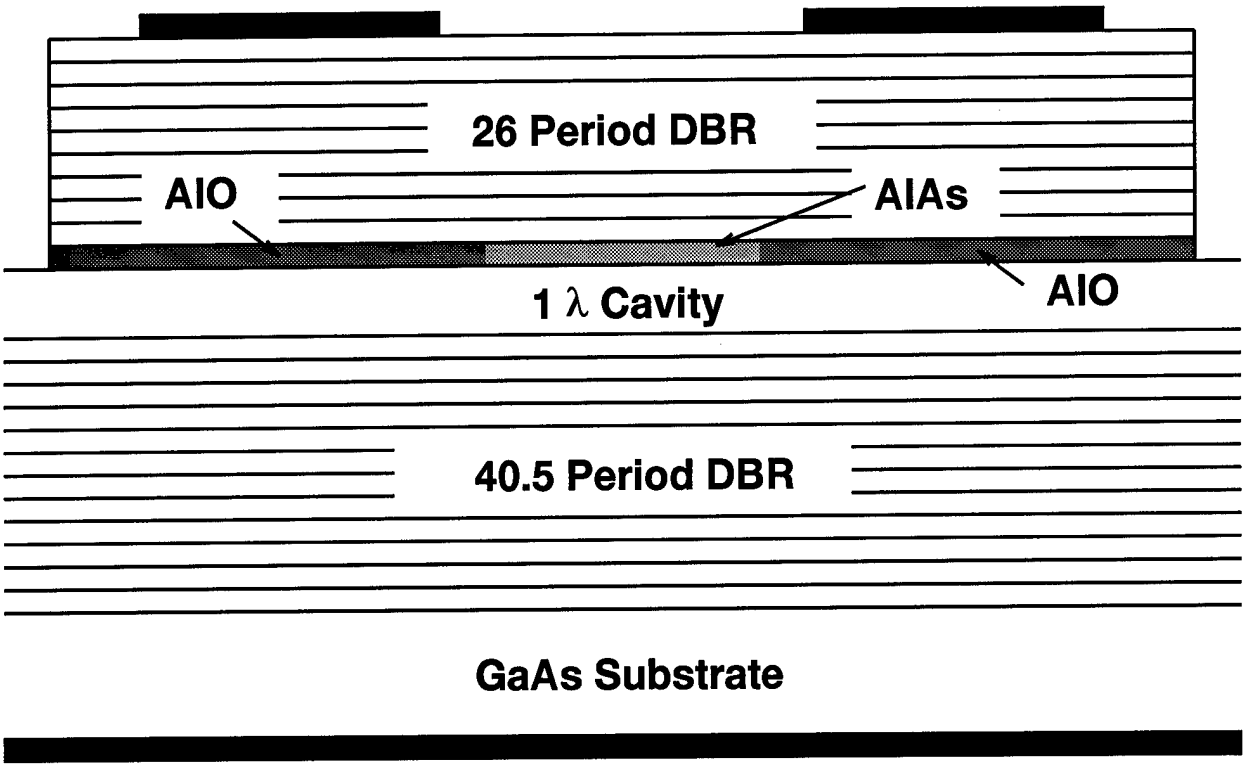

Figure 3.19 Illustration of the 780 nm test VCSEL.

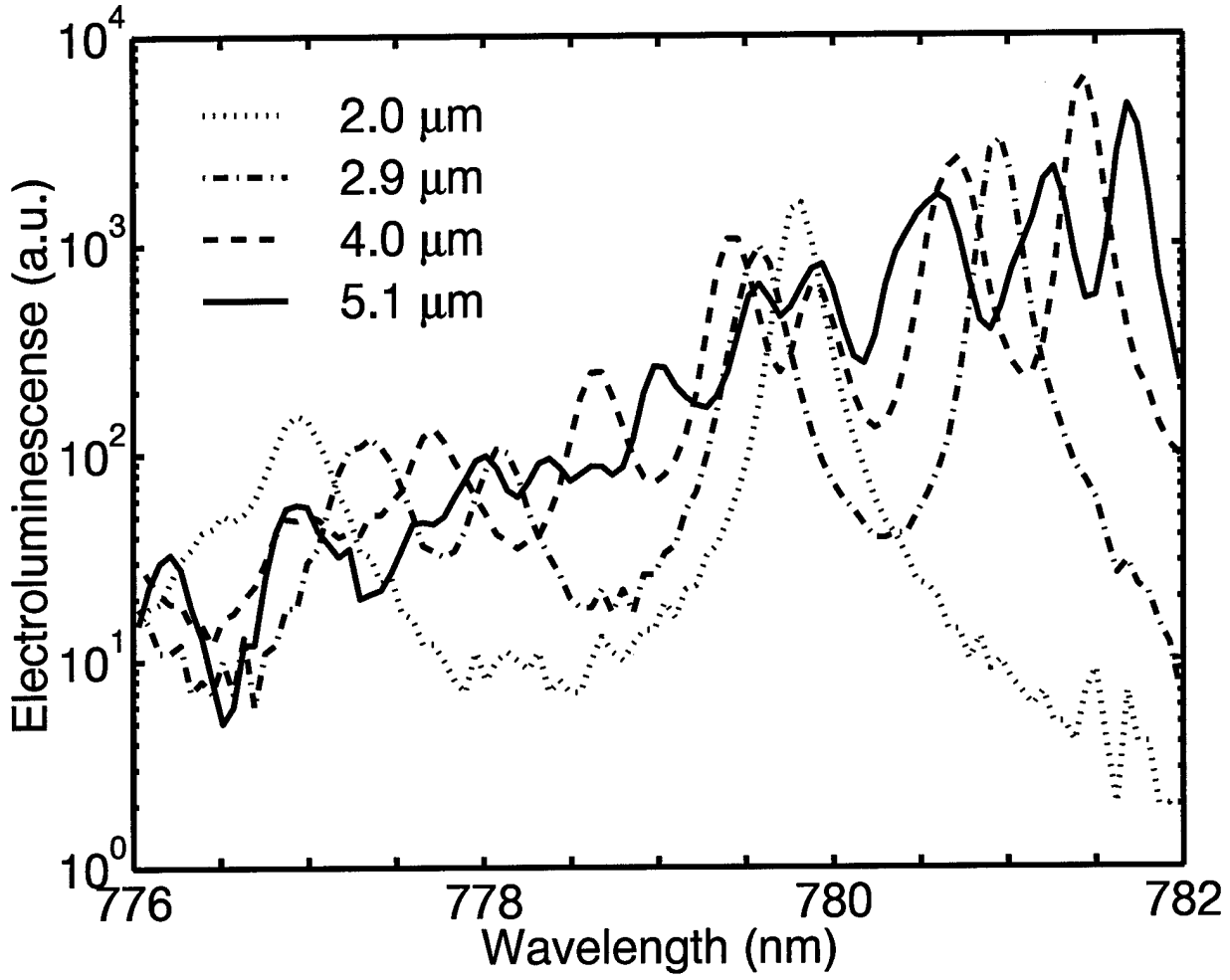

Figure 3.20 Electroluminescence data taken at 0.5 I_{th} for four different VCSELs, each labeled by square-aperture side length.

$Al_{0.98}Ga_{0.02}As$ layers, inserted in the third low-index layer away from the cavity in both the upper and lower DBRs. Due to oxidation into the graded regions, the final oxide layer is approximately 300 Å thick. The entire structure is grown on a GaAs substrate. Oxide-apertured devices of various sizes were fabricated as described in Reference [14], and the resonant frequency of the fundamental cavity mode was measured as a function of aperture size. The fundamental resonance of broad-area devices occurred at 851 nm.

3.2.3 Blueshift Comparison. Figures 3.21 and 3.22 compare both effective-index and weighted-index blueshift calculations against the measurements for the LP_{01} and LP_{11} modes [57]. Since the measurements are for a square-aperture device, while the calculation is based on a circular aperture, I compare the results by matching cross-sectional area. Therefore, the abscissa in Figures 3.21 and 3.22 is effective aperture radius:

$$r_{eff} \equiv \begin{cases} \frac{a}{\sqrt{\pi}} & \text{measurement} \\ r & \text{calculation} \end{cases}, \tag{3.7}$$

where a is the side length of the square aperture and r is the device radius in the calculation. Although this substitution cannot be rigorously justified, it does provide excellent agreement with the data. The theoretical results shown in Figures 3.21 and 3.22 were generated by analyzing device structures almost the same as those measured. (I approximated the graded interfaces with abrupt heterojunctions.) To calibrate the models to the actual structures grown, I adjusted the cavity thicknesses in both VCSEL designs so that the calculated Fabry-Perot resonance matched measurements performed on broad area devices ($\approx$ 782 nm for the first VCSEL design, $\approx$ 851 nm for the second). Apart from these layer thicknesses, my calculations included *no adjustable parameters.* Note that adjusting these layers serves primarily to *shift* the calculated curves up or down in wavelength: it does not affect the *shape* as a function of radius. All calculated curves terminate when a radially-bound mode can no longer be found. This provides an estimate of the minimum aperture radius required to laterally confine the mode. The effective index step $n_{\text{core}} - n_{\text{clad}}$, as calculated from (3.6), was equal to 0.033 for the first VCSEL design and 0.061 for the second.

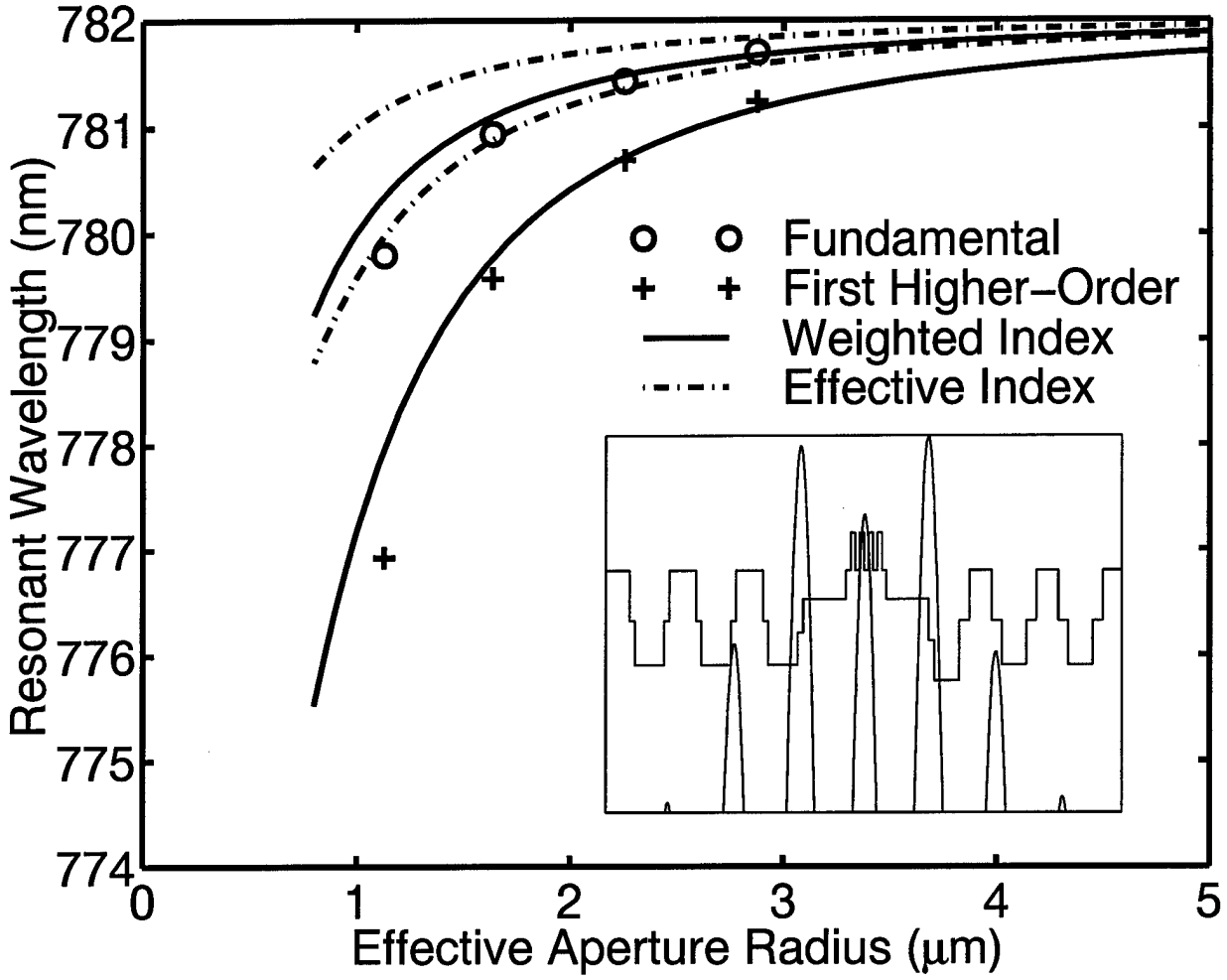

Figure 3.21 Calculated and measured resonant wavelengths of the fundamental (LP_{01}, upper curves) and first higher-order (LP_{11}, lower curves) modes as a function of aperture size for the first VCSEL design; discrete points represent measured values. The inset shows the longitudinal refractive index and field intensity profiles near the cavity.

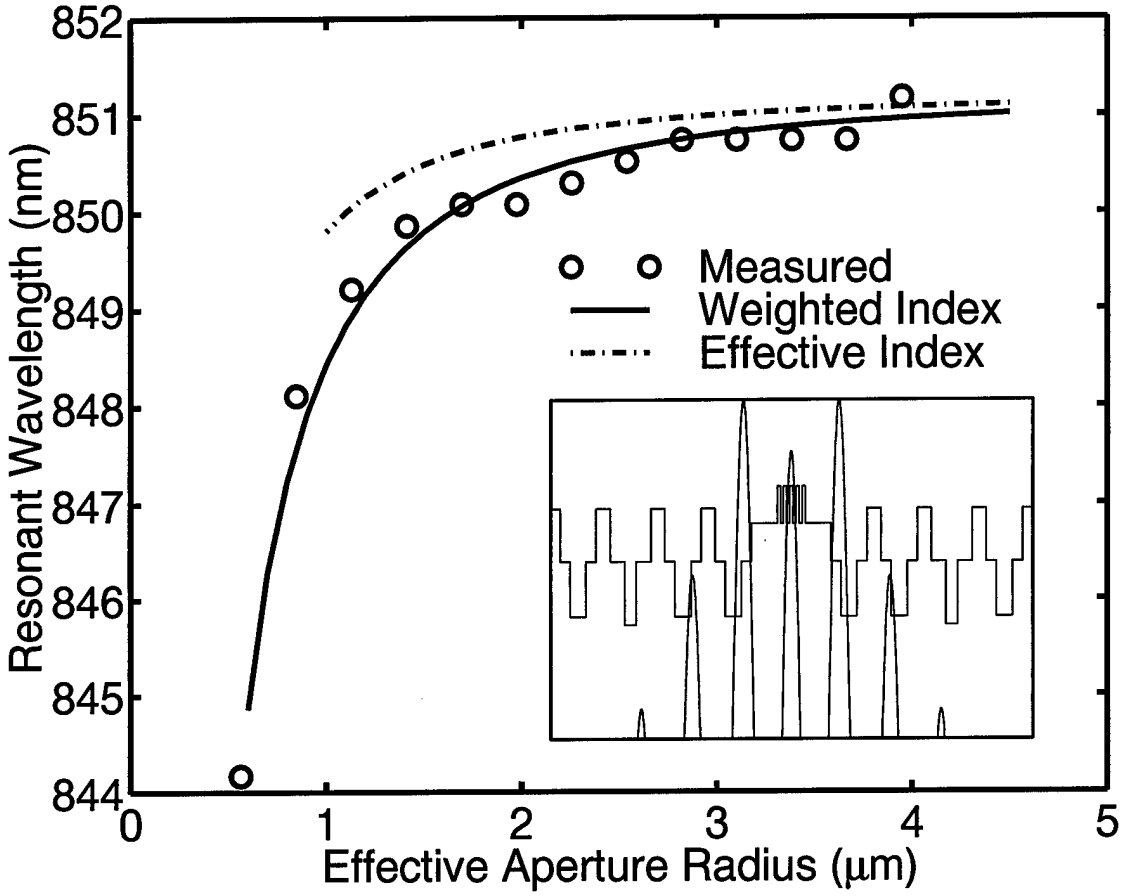

Figure 3.22 Calculated and measured resonant wavelengths of the fundamental (LP_{01}) mode as a function of aperture size for the second VCSEL design. The inset shows the longitudinal refractive index and field intensity profiles near the cavity.

From Figures 3.21 and 3.22, I see that the WIM calculation accurately predicts the dependence of wavelength on aperture size, matching the measurements remarkably well. The simple effective index calculation, on the other hand, significantly underestimates the blueshift for both the fundamental (LP_{01}) and first higher-order (LP_{11}) mode. The small differences between the WIM calculations and the measurements in Figures 3.21 and 3.22 could result from several factors. First, the model is restricted to piecewise-constant refractive indices, while the actual structures have graded interfaces. Second, the modeling of a square aperture with a circular one could introduce error. Third, the weighted index method is itself not exact, since it assumes separable solutions. Non-separable effects—such as diffractive loss—are not included, and these effects could influence the resonant wavelengths. Last, the measured aperture sizes are only accurate to within $\pm$ 0.2 μm.

I have now completed an "initial validation" of the weighted index method, verifying the resonance predictions against experiment. The ability to predict mode blueshifts is certainly valuable in device design, allowing for accurate alignment of the cavity resonance to the gain peak. However, the principal optical parameter of interest is the threshold gain. Since the WIM is inherently limited by the separability assumption, it may not be used directly to compute diffraction effects. Therefore, I forfeit the speed and efficiency of the method and turn to a computational technique. I present my *new* finite element model—capable of computing *all* optical VCSEL parameters—in the next chapter.

IV. Vector Finite Element Method

In this chapter, I present a *quasi-exact* finite element method (FEM) model for analyzing the optical modes of microcavity VCSELs [53, 54, 56]. Although computationally intensive, this model has the distinct advantage that it calculates the *total* optical loss, including diffraction. This model is based on a variational solution of the vector Helmholtz equation in microcavity geometries. The results of this model not only allow for direct calculation of lasing mode parameters, but also a better understanding of the underlying physics associated with VCSEL oxides. To derive basic oxide design rules, I apply the model to several versions of a novel oxide-aperture, oxide mirror VCSEL [67]. I find that the diffraction loss may be qualitatively understood as a coupling between the lasing eigenmode and the parasitic mode continuum [20]. Within this interpretation, the diffraction is a result of three basic physical effects: (1) the amount of transverse confinement afforded to the optical mode, (2) the relative alignment between the propagation vectors of the eigenmode and the radially radiating parasitic modes, and (3) the density of parasitic modes in the spectral vicinity of the eigenmode.

4.1 Vector Field Equations and the Variational Form

I want to find the electric $\left(\vec{E}\right)$ and magnetic $\left(\vec{H}\right)$ field profiles, the resonant wavelength (λ_0), and the threshold gain (g_{th}) for each cavity mode in azimuthally-symmetric VCSEL structures. For this I must solve Maxwell's equations subject to appropriate boundary conditions at each material interface. The steady-state, time-harmonic electric field satisfies the vector Helmholtz equation (in MKS units)

$$\nabla \times \frac{1}{\mu_r} \nabla \times \vec{E} - k_0^2 \varepsilon_r \vec{E} = -i\omega\mu_0 \vec{J}, \tag{4.1}$$

where $\vec{E}$, $\vec{H}$, and the electric current $\vec{J}$ depend on time as $e^{i\omega t}$ ($\omega = 2\pi c/\lambda$); ε_0, μ_0, and k_0 are the free space permittivity, permeability, and propagation constant, respectively. It can be shown [37] that a weak solution to (4.1) may be obtained by *extremizing* the functional

$$\mathbb{J}(\vec{E}) = \iiint_{\Omega} \frac{1}{\mu_r}\left(\nabla \times \vec{E}\right) \cdot \left(\nabla \times \vec{E}\right) dv - k_0^2 \iiint_{\Omega} \varepsilon_r \vec{E} \cdot \vec{E}\, dv \qquad (4.2)$$
$$+ i\omega\mu_0 \iint_{\Gamma} \left(\hat{n} \times \vec{E}\right) \cdot \vec{H}\; ds + \iiint_{\Omega} \vec{E} \cdot \vec{J}\, dv.$$

(By extremize, I mean forcing $\delta\mathbb{J} = 0$, where δ is the variational operator.) Here Ω and Γ are the problem domain and boundary, respectively. For azimuthally-symmetric structures, the material parameters (μ_r and ε_r) are functions of ρ and z only, and I may separate out the ϕ dependence in (4.2) by assuming

$$E_\phi \backsim \cos(m\phi), \qquad (4.3)$$

and

$$E_\rho,\, E_z \backsim \sin(m\phi), \qquad (4.4)$$

where m is the azimuthal mode number. For integer m, the integrals over $\phi = [0, 2\pi]$ yield a constant factor which may be ignored, effectively reducing the dimension of the problem from three to two. In addition, since different azimuthal modes are orthogonal, I may deal with each value of m independently.

For lasing mode analysis, I set the source current $\vec{J}$ to zero, making (4.1) a source-free eigenmode problem. By assuming perfect conducting boundary conditions $\left(\hat{n} \cdot \vec{E} = 0\right)$ on Γ, which I justify in Section 4.3, the surface integral in (4.2) drops out and I am left with

$$\mathbb{J}(\vec{E}) = \iiint_{\Omega} \frac{1}{\mu_r}\left(\nabla \times \vec{E}\right) \cdot \left(\nabla \times \vec{E}\right) dv - k_0^2 \iiint_{\Omega} \varepsilon_r \vec{E} \cdot \vec{E}\, dv. \qquad (4.5)$$

Here Ω represents the two-dimensional domain (of the VCSEL) over the $\rho - z$ plane. My task is then to find the $\vec{E}$ field which extremizes (4.5). That is, I must find the $\vec{E}$ that satisfies

$$\iiint_{\Omega} \frac{1}{\mu_r}\left(\nabla \times \vec{E}\right) \cdot \left(\nabla \times \delta\vec{E}\right) dv - k_0^2 \iiint_{\Omega} \varepsilon_r \vec{E} \cdot \delta\vec{E}\, dv = 0, \qquad (4.6)$$

for all field variations $\delta\vec{E}$. Equation (4.6) is a generalized eigenvalue problem,

$$\mathcal{S}(\vec{E})-\xi\mathcal{T}(\vec{E}) = 0. \tag{4.7}$$

The $\mathcal{S}$ and $\mathcal{T}$ operators are defined by

$$\mathcal{S}(\vec{\Psi}) \equiv \iint_{\Omega} \frac{1}{\mu_r}\left(\nabla\times\vec{\Psi}\right)\cdot\left(\nabla\times\delta\vec{\Psi}\right)\, dv, \tag{4.8}$$

and

$$\mathcal{T}(\vec{\Psi}) \equiv \iint_{\Omega} \varepsilon_r\, \vec{\Psi}\cdot\delta\vec{\Psi}\; dv. \tag{4.9}$$

The eigenvalue ξ is defined as

$$\xi \equiv k_0^2 = \frac{\omega^2}{c^2}. \tag{4.10}$$

All the desired mode information may be found by solving (4.6). For each mode, the eigenvalue is the square of the (generally complex) free-space propagation constant, which is related to the modal wavelength (λ_0) (4.22) and the total optical loss or threshold gain (g_{th}) (4.26). The eigenvectors are simply the time-harmonic (vector) electric fields $\left(\vec{E}\right)$. I approximate the solution to (4.6) using the finite element method.

4.2 Finite Elements and Matrices

The formalism developed in the last section is general and could apply to any of several variational approaches to solving Maxwell's equations. In this section, I narrow my attention to the finite element method (FEM). In the finite element method, the solution to (4.6) is approximated by limiting the space of admissible functions $\vec{E}$ to the linear superposition of a finite set of basis functions (generally characterized by the fact that they are non-zero only over a subdomain Ω_e, the domain of mesh element e). In my vector FEM, I expand the fields over a basis of *vector functions* [49],

$$\vec{E} = \sum_{i=1}^{N} x_i\vec{\psi}_i. \tag{4.11}$$

Here N is the total number of basis functions in the expansion, x_i are unknown coefficients, and $\vec{\psi}_i$ are the vector basis functions. These functions are second order node, edge, and face element functions, given in Appendix C. They are specifically designed to model $m = 1$ modes. Substituting (4.11) into (4.6) and exchanging the order of summation and integration yields

$$\sum_{i=1}^{N} x_i \left\{ \iint_\Omega \frac{1}{\mu_r} \left(\nabla \times \vec{\psi}_i \right) \cdot \left(\nabla \times \vec{\psi}_j \right) dv - k_0^2 \iint_\Omega \varepsilon_r \vec{\psi}_i \cdot \vec{\psi}_j \, dv \right\} = 0. \tag{4.12}$$

Ensuring (4.12) holds for all $\vec{\psi}_j$ (same set of functions as $\vec{\psi}_i$), ensures it will hold for any linear superposition of $\vec{\psi}_j$, the finite basis analogy of $\delta\vec{E}$. The N equations represented by (4.12) are *exactly* (4.7)–(4.9) taken over a finite basis, written conveniently in linear algebra notation as

$$\mathbf{SX} - \xi \mathbf{TX} = \mathbf{0}, \tag{4.13}$$

where,

$$s_{i,j} \equiv \iint_\Omega \frac{1}{\mu_r} \left(\nabla \times \vec{\psi}_i \right) \cdot \left(\nabla \times \vec{\psi}_j \right) dv, \tag{4.14}$$

$$t_{i,j} \equiv \iint_\Omega \varepsilon_r \, \vec{\psi}_i \cdot \vec{\psi}_j \, dv, \tag{4.15}$$

and the eigenvalue (ξ) definition (4.10) remains unchanged.

I define my basis set over a triangular mesh in the $\rho - z$ plane, as illustrated in Figure 4.1. By using (randomly shaped) triangular elements, I can accommodate general VCSEL designs—including for example *tapered oxides*—and avoid creating an artificial, mesh-driven predisposition to any given vector field component. Due to the form of my basis expansion and the use of absorbing regions (discussed below), $\mathbf{S}$ and $\mathbf{T}$ will be very large ($N \sim 50,000$), sparse, non-Hermitian matrices. As a result, special matrix techniques are required to solve (4.13). In practice this is the most challenging part of the finite element solution, and certainly the most time consuming. I chose to solve the eigenvalue problem using an iterative Arnoldi algorithm [46, 62] with spectral transformation; this algorithm allows me to search for "mildly complex" (e.g., $\mathrm{Re}(\xi) \gg \mathrm{Im}(\xi)$) eigenvalues over a given range of the real axis.

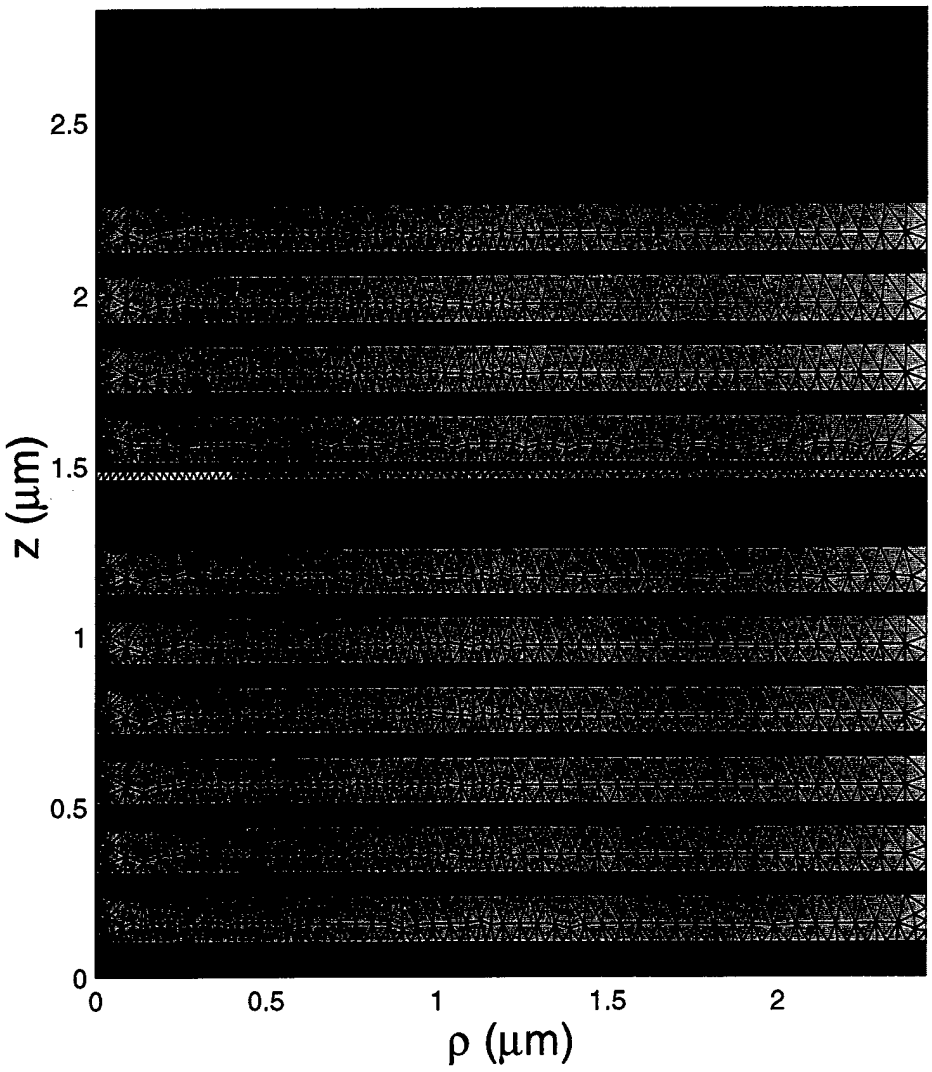

Figure 4.1 Sample finite element mesh for an oxide-apertured, oxide DBR VCSEL.

4.3 Mesh Termination

By far the greatest potential error source in the finite element VCSEL analysis is mesh termination. Due to the incomplete optical confinement of both the oxide apertures and the VCSEL mirrors, the true domain of a VCSEL field solution extends to infinity in all directions. Hence, an artificial mesh termination is required for FEM application. A properly designed mesh termination for this problem must mimic the unbounded nature of the domain, eliminating nonphysical reflections at the mesh edge. In addition, since the FEM computational demand—both CPU time and memory—scales super-linearly with N, I prefer to place my termination as close as possible to the primary domain of interest, thereby minimizing the amount of "wasted" mesh space.

To terminate my mesh, I insert an artificial *absorbing layer* (AL) between the principle problem (VCSEL) domain (Ω_V) and the problem boundary (Γ) [37]. This layer allows me to use perfect conductor boundary conditions on Γ, as I assumed in Section 4.1, eliminating the surface integral term in the variational form and dramatically simplifying the FEM analysis. I define Ω_V by a rectangular region in the $\rho - z$ plane, bounded by the bottom mirror-to-substrate plane (Γ_B) and the top mirror-to-air plane (Γ_T) in the $\hat{z}$ direction, and the transverse lasing mode size (Γ_S) in the $\hat{\rho}$ direction. I determine Γ_S *a-posteriori*, as discussed in Appendix D.3. I surround Ω_V by the AL as illustrated in Figure 4.2, where the AL domain is the union of the top, side, and bottom AL regions ($\Omega_{AL} = \Omega_T \cap \Omega_S \cap \Omega_B$). Due to the high reflectance of the distributed Bragg reflectors (DBRs), my main concern is absorbing any radiation incident on the radial boundary Γ_S. Therefore, I focus my analysis on the radial AL (Ω_S); the optimal axial AL design (Ω_T and Ω_B) falls out of the radial analysis as I show in Appendix D.

A basic requirement for minimizing reflection is that the impedance $\left(\sqrt{\mu/\varepsilon}\right)$ of the absorbing layer in each region must match the radially adjacent VCSEL region. I enforce

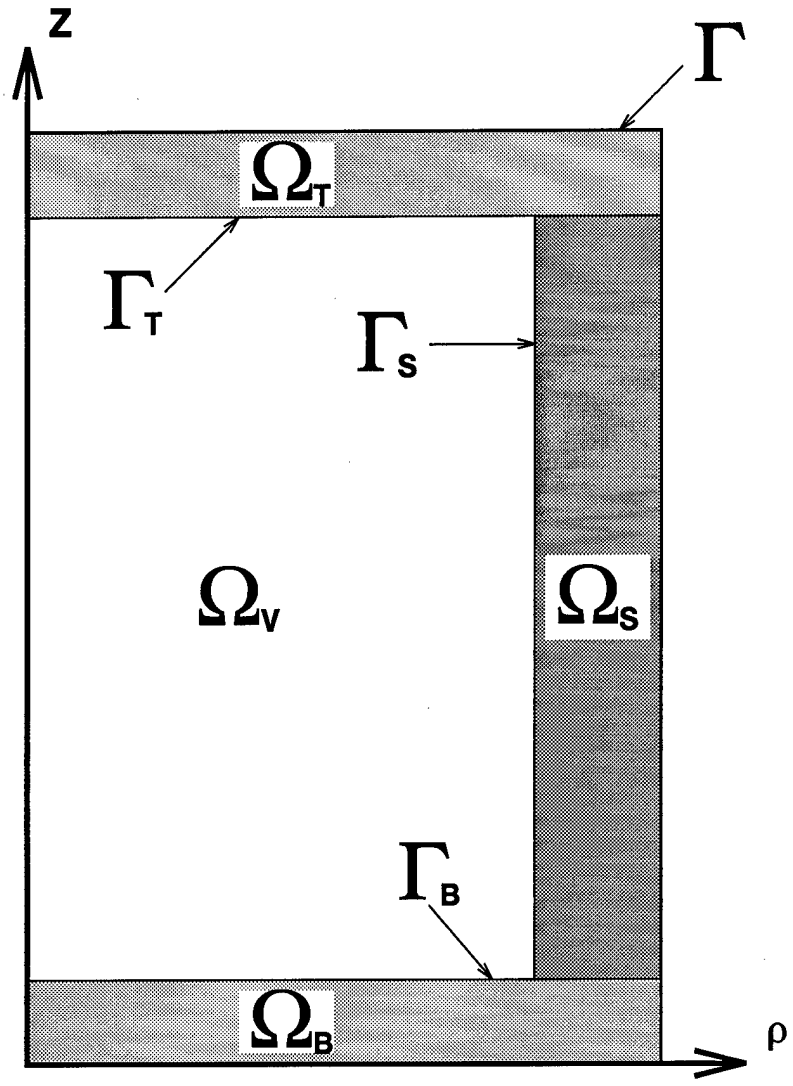

Figure 4.2 Illustration of the FEM VCSEL problem domain: Ω_V is the VCSEL domain, and Ω_S, Ω_T, and Ω_B are the side, top, and bottom absorbing layer (AL) domains, respectively. The VCSEL and AL domains are separated by the boundaries Γ_S, Γ_T, and Γ_B, and the entire problem domain is bounded by the closed cylinder Γ.

this condition by defining the absorbing layer material parameters as[1]

$$\varepsilon_{r,j}^{AL}(\rho) \equiv a(\rho)\varepsilon_{r,j}, \qquad \text{and} \qquad \mu_{r,j}^{AL}(\rho) \equiv a(\rho)\mu_{r,j}. \tag{4.16}$$

Here $\varepsilon_{r,j}$ and $\mu_{r,j}$ are the VCSEL material parameters in axial region j (defined by $z_{j-1} < z < z_j$) radially adjacent to the AL (e.g., just to the left of Γ_S), and

$$a(\rho) \equiv 1 - ib(\rho). \tag{4.17}$$

The absorbing layer performance depends entirely on the function $b(\rho)$. I arrive at a suitable function $b(\rho)$ through a detailed design optimization. First, I obtain a rough estimate using an asymptotic description of the fields and reflections, as described in Appendix D.1. Then I fine-tune the layer by minimizing the exact reflection values as obtained by a rigorous transfer matrix calculation, described in Appendix D.2.

4.4 Results and Analysis

To illustrate the application of the FEM for VCSELs, I analyze several versions of a basic 870 nm oxide-apertured, oxide DBR VCSEL [67]. The VCSEL has five and a half periods of $Al_{0.3}Ga_{0.7}As/Al_xO_y$ in the bottom DBR and four in the top DBR. The cavity is 1λ thick and contains a single 600 Å GaAs *bulk* gain region centered between two $Al_{0.3}Ga_{0.7}As$ barrier layers. A 300 Å AlAs layer is included in the top barrier to form an oxide aperture. Although an actual oxide aperture formed in AlAs would have a square cross-section, I treat it as circular to maintain the azimuthal symmetry. The entire structure including the GaAs substrate is illustrated in Figure 4.1. The versions of this structure I examined are:

- 1λ–1THIN the structure as described above,
- 1λ–1THICK same structure with a 600 Å thick oxide aperture,

[1]Before choosing (4.16), I considered a diagonal anisotropic $\overline{\overline{a}}(\rho)$ for a *perfectly* matched layer (PML) design [45,63]. However, I found that the extra degrees of freedom provided no advantage for absorbing *general* outward propagating cylindrical waves of the form $\left(H_m^{(2)}(k\rho)\, e^{i\beta z} e^{im\phi}\right)$.

- 1λ–2THICK same structure with a 600 Å thick oxide aperture in both the top and bottom barrier regions, and
- $\lambda/2$–1THICK same DBRs but with a $\lambda/2$ cavity and a 600 Å thick oxide aperture in the top barrier region.

All materials indices are assumed to be real so that the only source of field loss is through absorption in the ALs. For this particular structure, the absorbing layer function $b(\rho)$ is derived in Appendix D.3.

4.4.1 Lasing Mode Fields. In Figures 4.3 and 4.4 I plot $|E_\phi|$ and the time averaged electromagnetic energy density,

$$w \equiv \frac{1}{4}\left[\varepsilon_0 \varepsilon_{r,j} \left|\vec{E}\right|^2 + \mu_0 \left|\vec{H}\right|^2\right], \tag{4.18}$$

for the sample 1λ–1THIN, $\rho_{ox} = 0.4\,\mu$m VCSEL; these plots are representative of the general lasing mode profiles for all the VCSELs I tested. The fields are found by substituting the lasing mode eigenvector ($\mathbf{X}$) into the field expansion given in (4.11). The E_ϕ profile (Figure 4.3) is similar to the familiar standing wave profile obtained via simple scalar field techniques, however, I anticipate my result is more accurate due to the full vector solution. The energy density (4.4) is found by estimating $\vec{H}$ from the $\vec{E}$ field expansion (4.11) and Faraday's law. Although this is less familiar than the E_ϕ profile, it is a more accurate representation of the spatial mode energy distribution throughout the VCSEL.

4.4.2 Confinement Factor. Using the spatial mode profile, I estimate the total and transverse confinement factors as

$$\Gamma^{\text{tot}} \equiv \frac{\int_{\Omega_{\text{pump}}} w\, dv}{\int_{\Omega_V} w\, dv}, \tag{4.19}$$

and

$$\Gamma^{\text{tr}} \equiv \frac{\int_{\Omega_{\text{pump}}} w\, dv}{\int_{\Omega_{\text{gain}}} w\, dv}, \tag{4.20}$$

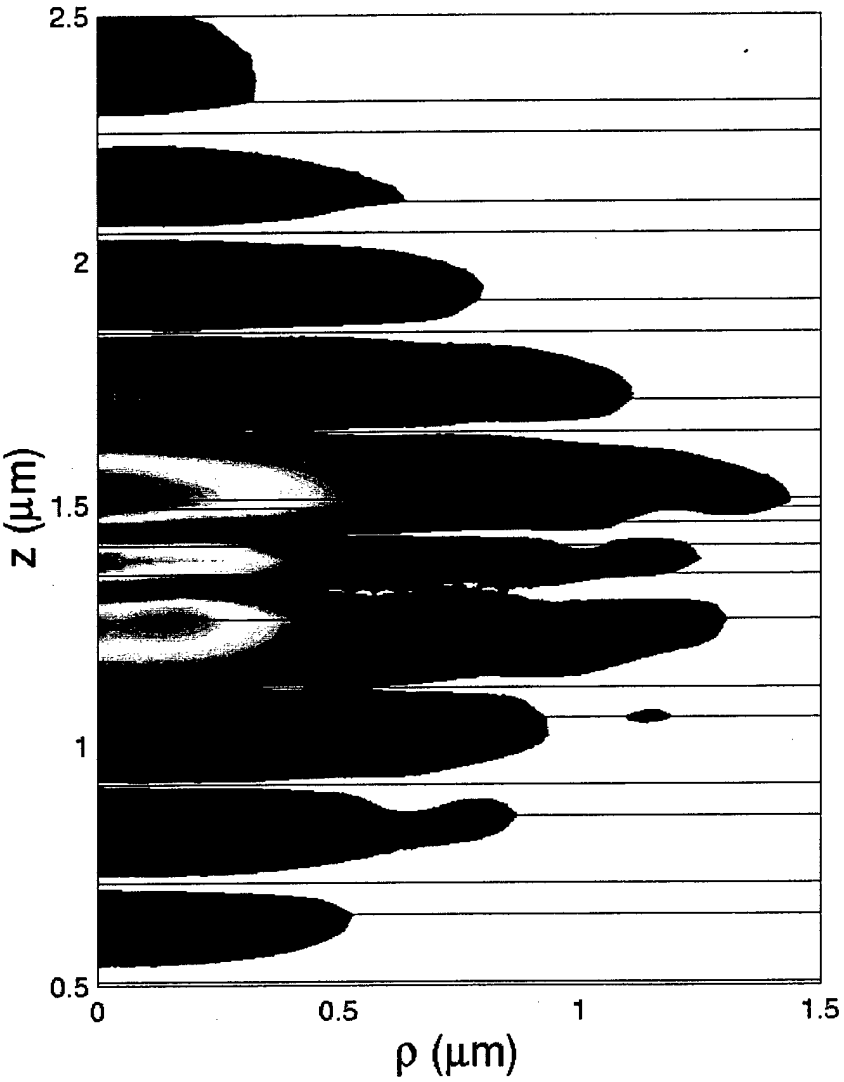

Figure 4.3 Example plot of $|E_\phi|$ for the 1λ–1THIN structure with oxide aperture radius $\rho_{ox} = 0.4$ μm. To increase clarity, the figure domain is smaller than the calculation domain, and the background intensity is set to white.

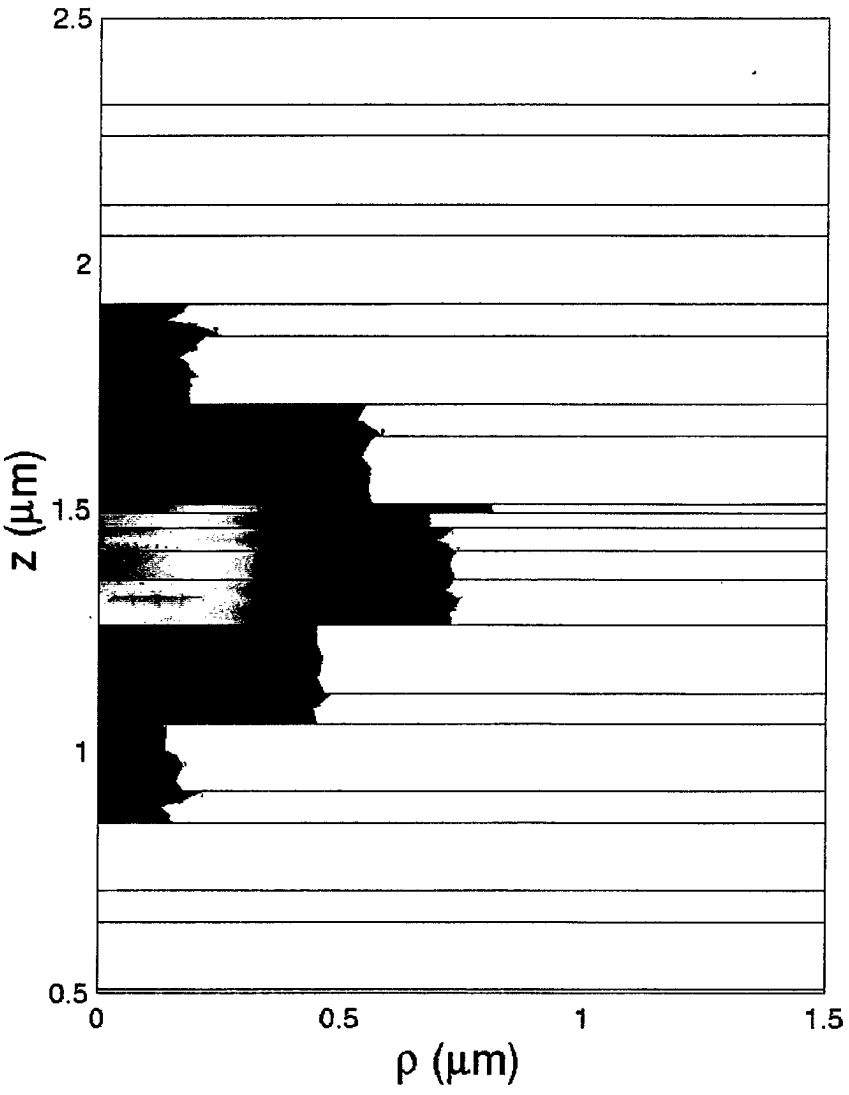

Figure 4.4 Example plot of the stored energy density w for the 1λ–1THIN structure with oxide aperture radius $\rho_{ox} = 0.4$ μm. To increase clarity, the figure domain is smaller than the calculation domain, and the background intensity is set to white.

respectively; Ω_V is the VCSEL volume, and Ω_{pump} and Ω_{gain} are the pumped and total volume of the gain region, respectively. For purpose of calculation, I estimate Ω_{pump} as the volume of the active layer inside the oxide aperture (e.g., with $\rho \leq \rho_{ox}$). The total confinement factor represents the percentage of the mode *energy* overlapping the active gain region[2]. I use this later in the Fabry-Perot laser equation to estimate material threshold gain from the total modal loss (4.26). The transverse confinement factor has less quantitative application but is a nice indicator of how well the lasing mode is confined in the transverse dimension.

I plot Γ^{tr} for each of the VCSEL structures in Figure 4.5. The results for the 1λ cavity are somewhat intuitive: for any given radius more and thicker oxides yield greater confinement. For the $\lambda/2$ case, the oxide aperture does not overlap well (in the z direction) with the standing wave. Therefore, the transverse confinement is relatively small, however, the total confinement factor—due to the short cavity—is very large, as shown in Figure 4.6. The high contrast DBRs allow less field penetration and therefore a very high total confinement factor for all four test cases, compared to analogous semiconductor DBR VCSELs.

4.4.3 Resonant Wavelength, Total Optical Mode Loss, and Threshold Gain. Due to the absorbing layers, the eigenvalues of (4.10) are complex, and take the general form

$$\xi_i = k_i^2 = \frac{\omega_i^2}{c^2} \equiv (r_i + i\, q_i)^2 \,. \tag{4.21}$$

Here r_i and q_i are the real and complex parts of the (total) propagation constant k_i of mode i. From (4.21) I immediately recognize the mode resonance as

$$\lambda_i = \frac{2\pi}{r_i}. \tag{4.22}$$

By definition, the fields vary harmonically as

$$\exp(i\omega_i t) = \exp(ik_i ct) = \exp(ir_i ct)\exp(-q_i ct), \tag{4.23}$$

[2]This is a somewhat different definition than the more standard definition using the standing wave *intensity* $\left(\sim \left|\vec{E}\right|^2\right)$. However, the two definitions should yield similar results in most cases .

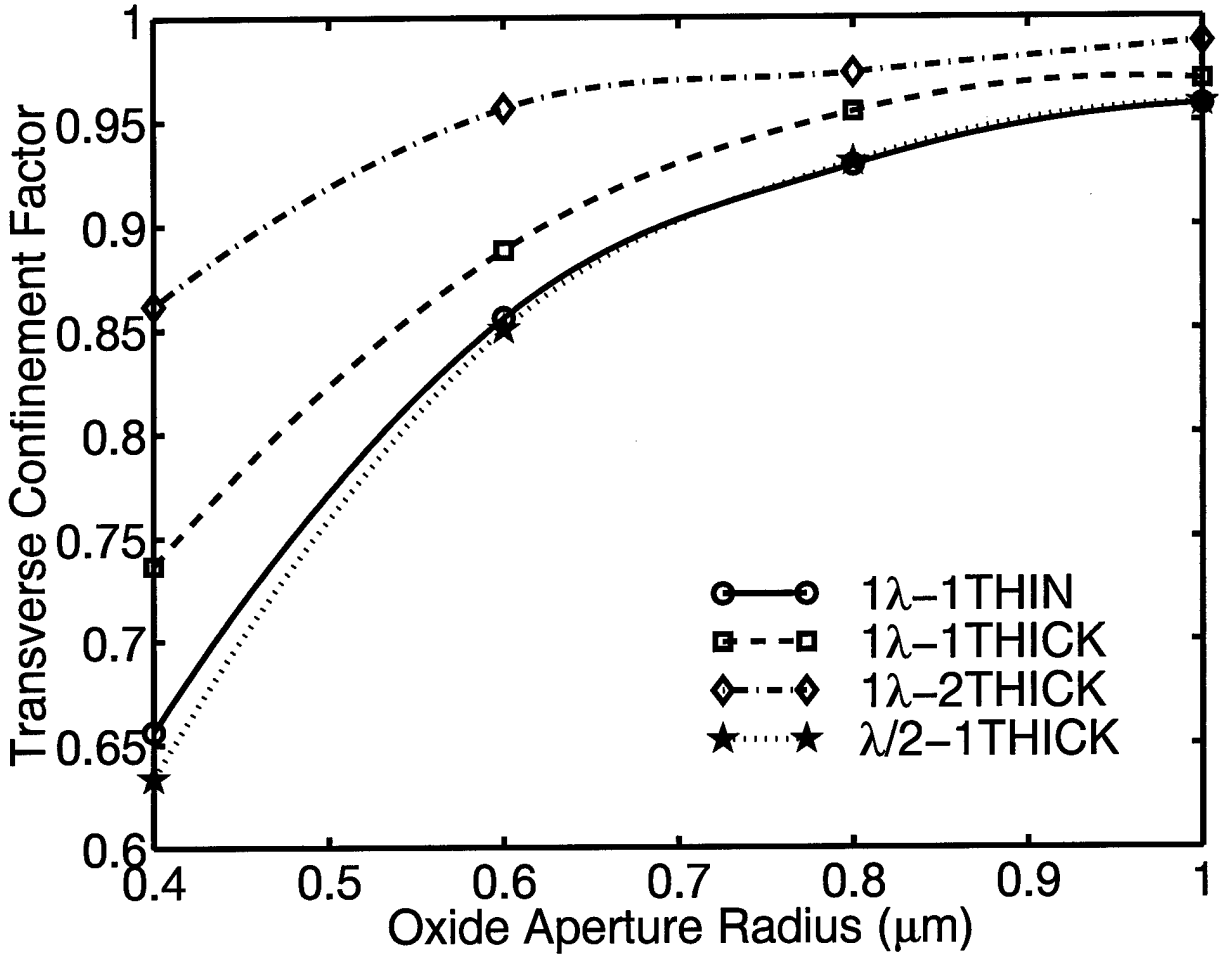

Figure 4.5 Transverse confinement factor verses oxide aperture radius for the fundamental lasing mode. The lines are cubic spline fits of the discrete calculation data.

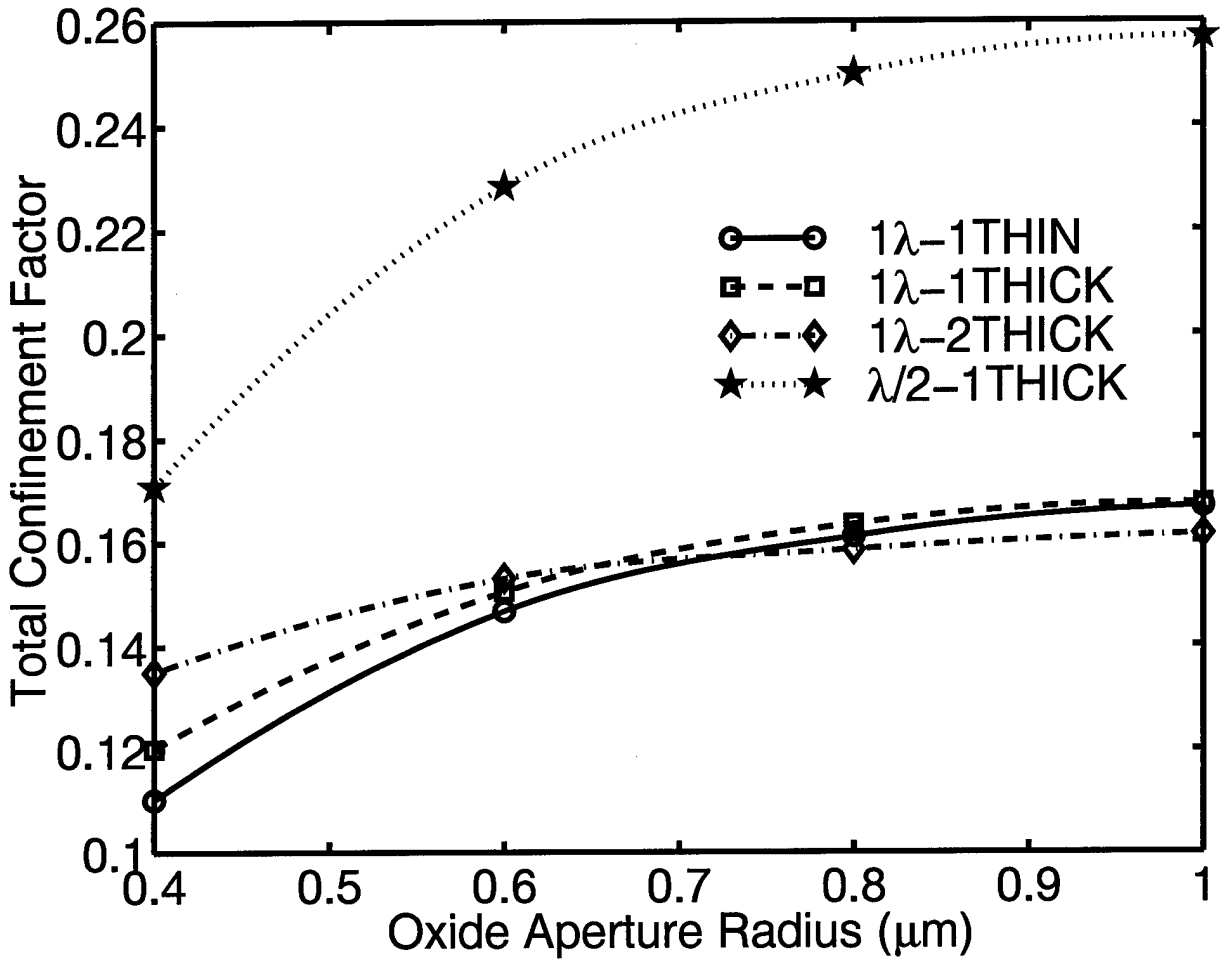

Figure 4.6 Total confinement factor verses oxide aperture radius for the fundamental lasing mode. The lines are cubic spline fits of the discrete calculation data.

where the mode frequency is $\mathrm{Re}(\omega_i) = r_i c$ and the *total* cavity loss rate (1/seconds) is $l_i \equiv q_i c$. These results describe a three-dimensional leaky cavity, losing energy at a rate of l_i. I would prefer to express my results in terms of the more familiar Fabry-Perot (F-P) laser model. To do this, I convert ω_i to a complex propagation constant

$$\beta_i \equiv \frac{\omega_i^*}{c} n_{\mathrm{gain}}, \tag{4.24}$$

where * is the complex conjugate, required such that a lossy ω_i maps to a lossy β_i. The imaginary part of β_i gives the *field* loss rate (for $\mathrm{Im}(\beta_i) > 0$) in cm^{-1}. Since energy is proportional to the *square* of the field, the *intensity* lost per unit length (α_i) is given by

$$\alpha_i \equiv 2\,\mathrm{Im}(\beta_i). \tag{4.25}$$

In deriving α_i *all* I have done is convert energy lost per time to energy lost per propagation length. To apply this loss rate to a "textbook" Fabry-Perot laser, the cavity length would have to be adjusted in accordance with the blueshift [26]. Finally, I calculate the threshold gain (g_{th}) from the F-P lasing condition,

$$\Gamma_i^{\mathrm{tot}} g_{th,i} = \alpha_i. \tag{4.26}$$

In Figures 4.7 – 4.9 I plot the modal resonance, total optical loss, and threshold gain as a function of oxide aperture radius for all four test VCSELs. The resonance results show the now familiar blueshift, with more and thicker oxide apertures yielding a larger shift. Interpretation of the loss and threshold gain curves is more complicated. I discuss these results, in detail, in Section 4.5.

4.4.4 Cavity Q and Spectral Mode Width. From ω_i and α_i, I estimate the cavity Q and spectral half width at half maximum for each of the eigenmodes as [65]

$$Q_i \approx \left| \frac{\mathrm{Re}(\omega_i)}{v_p \alpha_i} \right| = \left| \frac{r_i}{2 q_i} \right|, \tag{4.27}$$

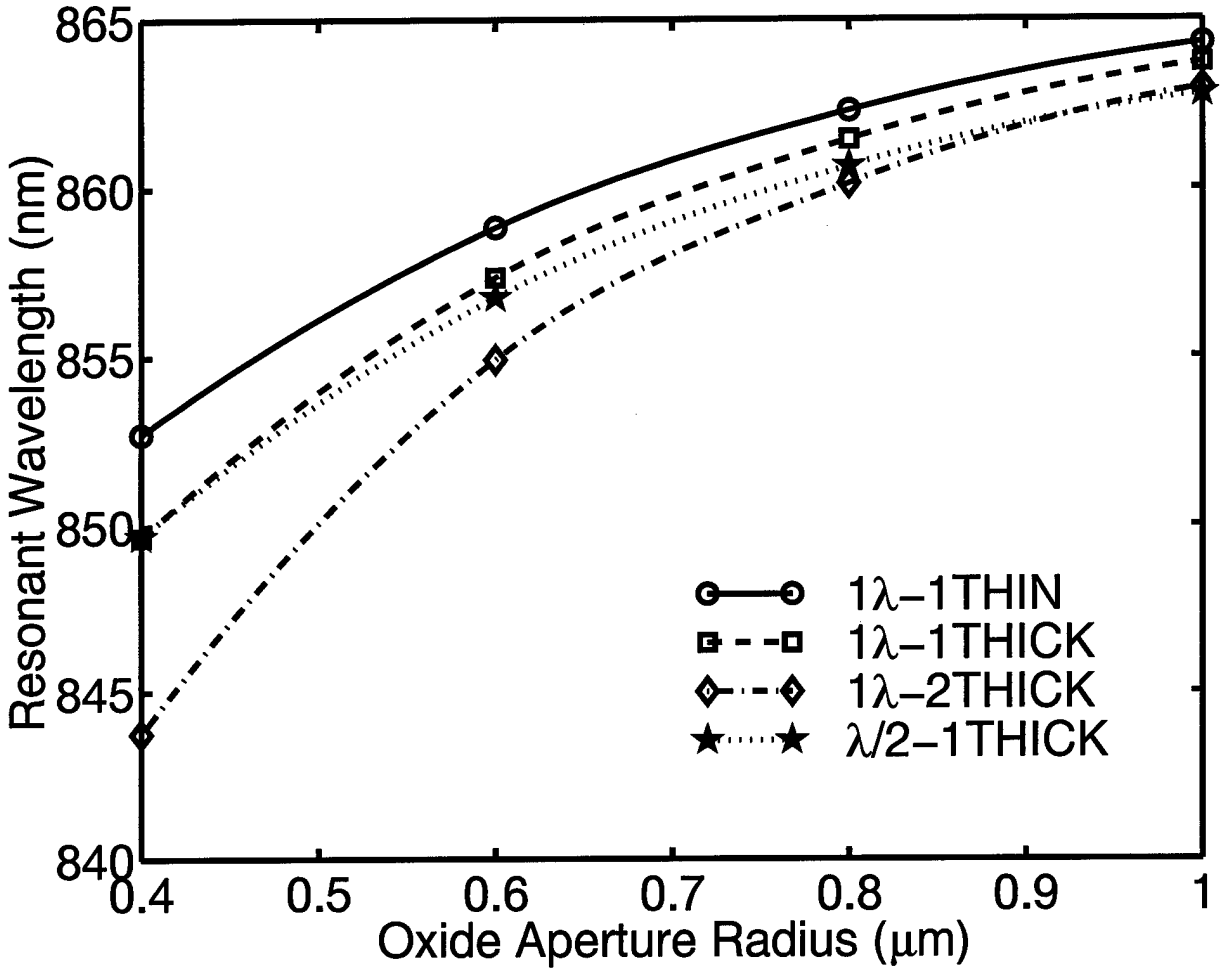

Figure 4.7 Lasing mode resonance verses oxide aperture radius. The lines are cubic spline fits of the discrete calculation data.

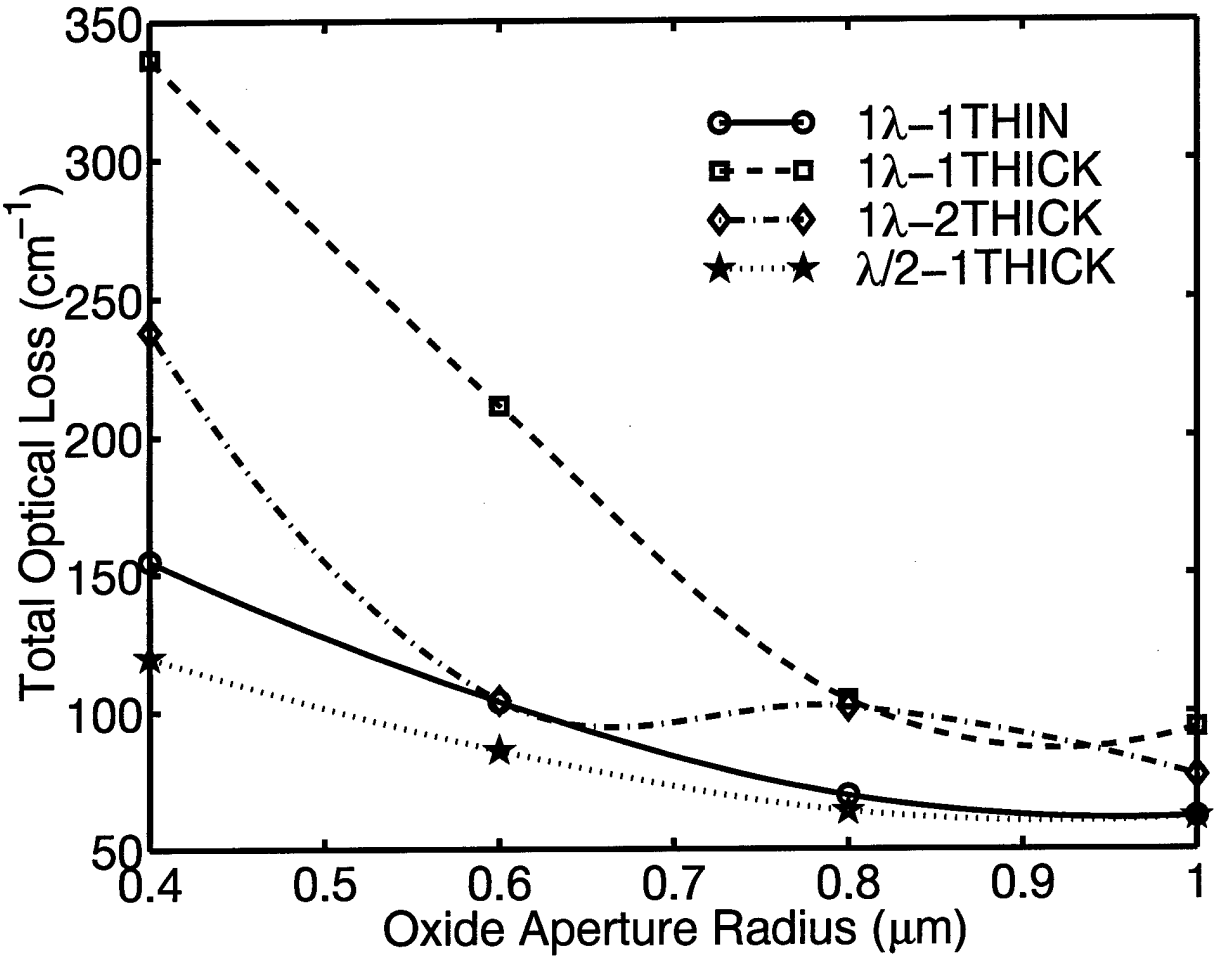

Figure 4.8 Lasing mode total optical loss verses oxide aperture radius. The lines are cubic spline fits of the discrete calculation data.

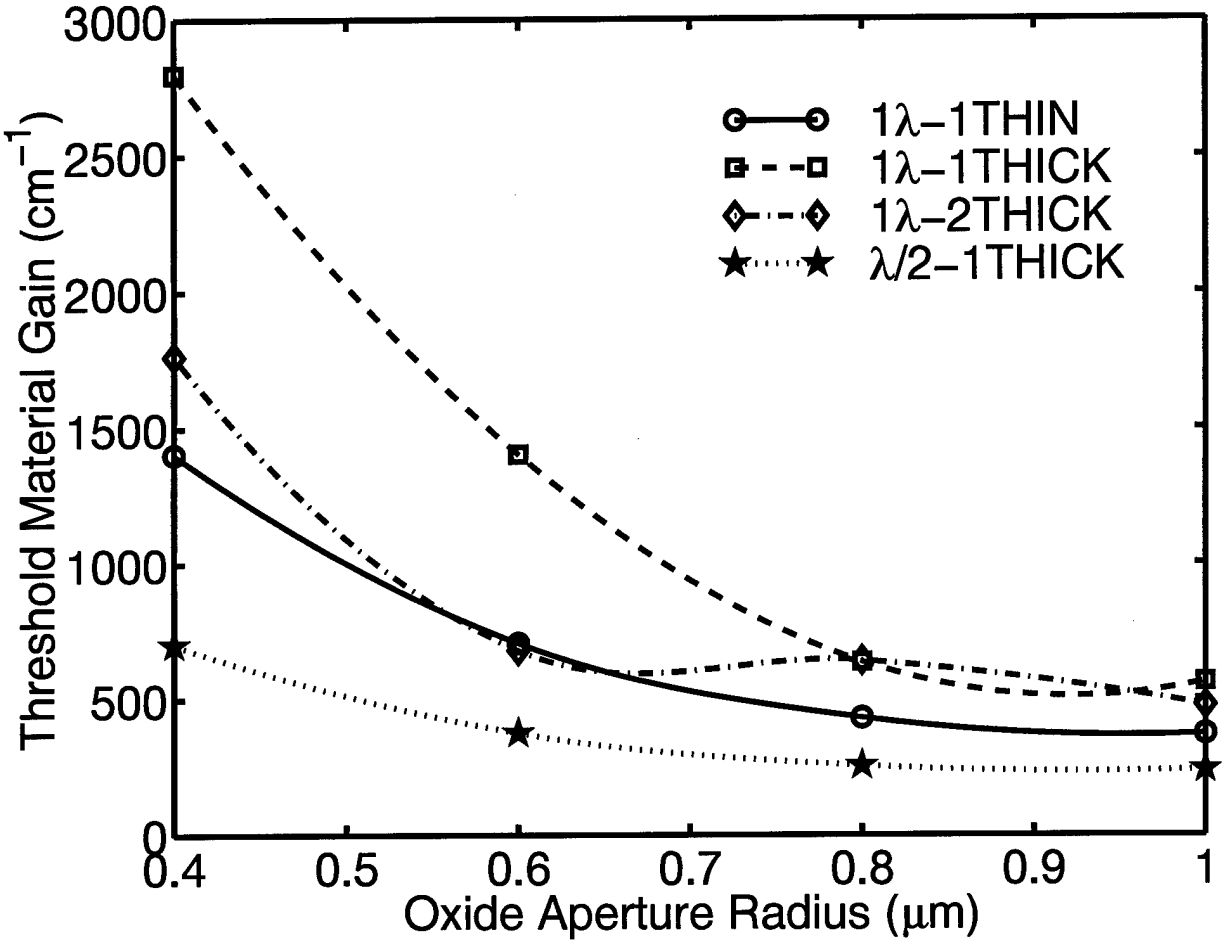

Figure 4.9 Threshold (material) gain verses oxide aperture radius. The lines are cubic spline fits of the discrete calculation data.

and

$$\delta\omega_i \approx |v_p \alpha_i| = \mathrm{Im}(\omega_i), \tag{4.28}$$

respectively. This $\delta\omega_i$ estimate, along with the ω_i and α_i results, may be used to estimate the discrete optical mode spectrum within a spontaneous emission rate calculation. This should yield results more accurate than the typical plane wave mode expansion, particularly for the case of highly confined VCSELs where the resonant modes deviate substantially from plane waves. To illustrate this application, I plot the eigenmodes for the 1λ–1THIN VCSEL in Figure 4.10. Each of the modes has an associated field distribution which may be used in the emission rate equations[3].

4.4.5 Radial and Axial Mode Loss. To better understand the optical loss sources, I would like to divide the total optical mode loss (α_i) into a mirror loss $\left(\alpha_i^{(\text{mirror})}\right)$, due to emission out the ends of the VCSEL, and a diffraction loss $\left(\alpha_i^{(\text{diffraction})}\right)$, due to loss out the VCSEL side. To do this, I use conservation of energy and the relationship between α and the radiated power and stored energy [7],

$$\alpha = \frac{P_V}{v_p W_V}. \tag{4.29}$$

Here v_p is the field phase velocity,

$$P_V \equiv \frac{1}{2}\mathrm{Re}\left\{\iint_{\Gamma_V} \left(\vec{E} \times \vec{H}^*\right) \cdot d\vec{s}\right\} \tag{4.30}$$

is the total time averaged (real) power exiting the VCSEL (Ω_V) through Γ_V, and

$$W_V \equiv W_V^e + W_V^m \tag{4.31}$$

[3]Note that in some cases (not shown) the lasing mode (the mode with the smallest α_i) does not have the longest wavelength. This is not a problem, since the longer wavelength, higher loss eigenmodes have very little spatial overlap with the gain region, and therefore will not contribute significantly to the emission rate.

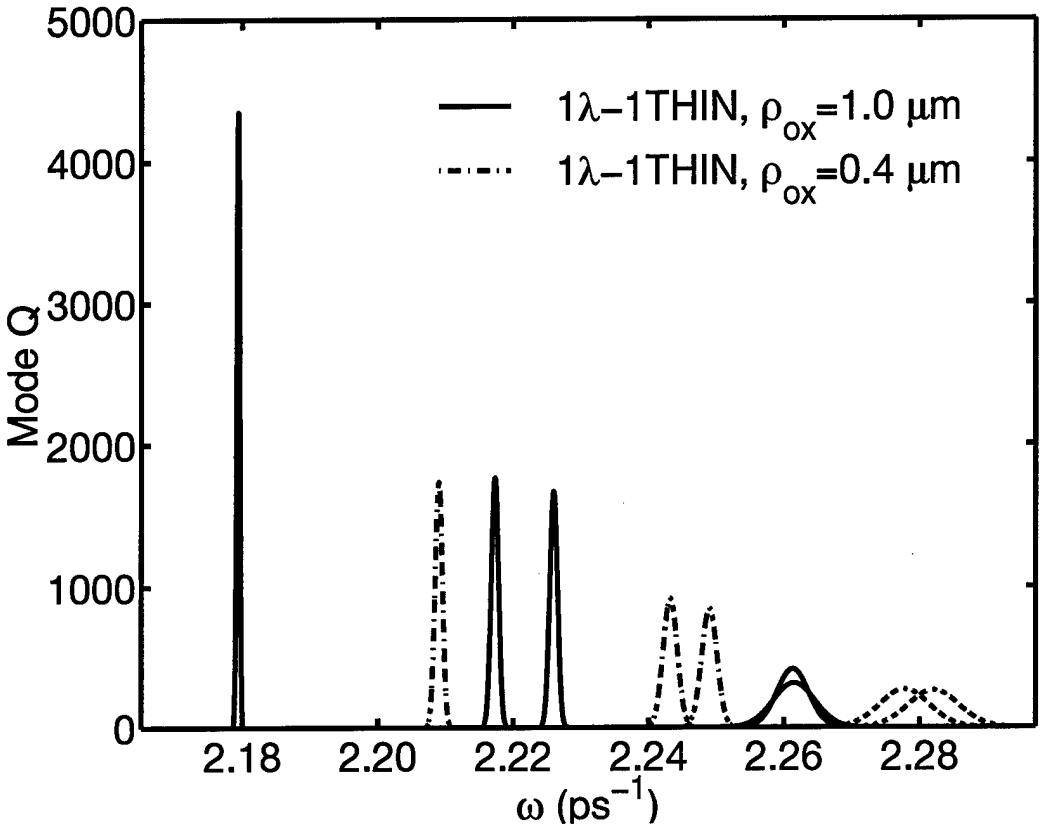

Figure 4.10 Illustration of the discrete $m = 1$ mode spectrum for the 1λ–1THIN structure. The modes are depicted as Gaussian with height equal to the mode Q and full width half maximum equal to the line width defined in Section 4.4.4. The mode search range was limited to ω values corresponding to λ_0 ranging from 870 nm to 820 nm.

is the total time averaged stored energy. This consists of the electric and magnetic field energies,

$$W_V^e \equiv \frac{1}{4}\iiint_{\Omega_V} \varepsilon_0 \varepsilon_{r,j} a \left|\vec{E}\right|^2 dv, \tag{4.32}$$

and

$$W_V^m \equiv \frac{1}{4}\iiint_{\Omega_V} \mu_0 a \left|\vec{H}\right|^2 dv, \tag{4.33}$$

respectively. Equation (4.29) is derived from the relationship between cavity Q and loss rate, adapted to the F-P laser model. I find in practice that numerical application of (4.29) gives results *exactly* matching those obtained with (4.25), verifying the general approach. It is then a simple matter to break α into radial and axial components,

$$\alpha^{(\text{diffraction})} = \frac{P_S}{v_p W_V}, \tag{4.34}$$

and

$$\alpha^{(\text{mirror})} = \frac{P_T + P_B}{v_p W_V}. \tag{4.35}$$

Here

$$P_V = P_S + P_T + P_B, \tag{4.36}$$

breaks the total power exiting the VCSEL into that leaving through the side (P_S), and that leaving through the top and bottom surfaces (P_T) and (P_B), respectively. These powers are calculated by restricting the integral in (4.30) to the corresponding surfaces. Note that for these calculations, I assume the VCSEL materials are lossless and calculate "cold cavity" radiative loss parameters. Although absorptive loss may be significant in operating VCSELs, this calculation should give a good estimate of the diffraction loss. The calculation can be easily modified to fold in absorptive losses if required.

In Figures 4.11 – 4.13, I plot the radial mode loss, the axial mode loss, and the radial percentage of the total mode loss, respectively. Comparing the scales in Figures 4.11 – 4.13, I see that $\alpha^{(\text{mirror})}$ is relatively constant, and that most of the change in α with aperture radius is due to $\alpha^{(\text{diffraction})}$. This is not surprising, since I expect the change in mirror reflectivity to be relatively small and the diffraction to increase as the aperture size decreases.

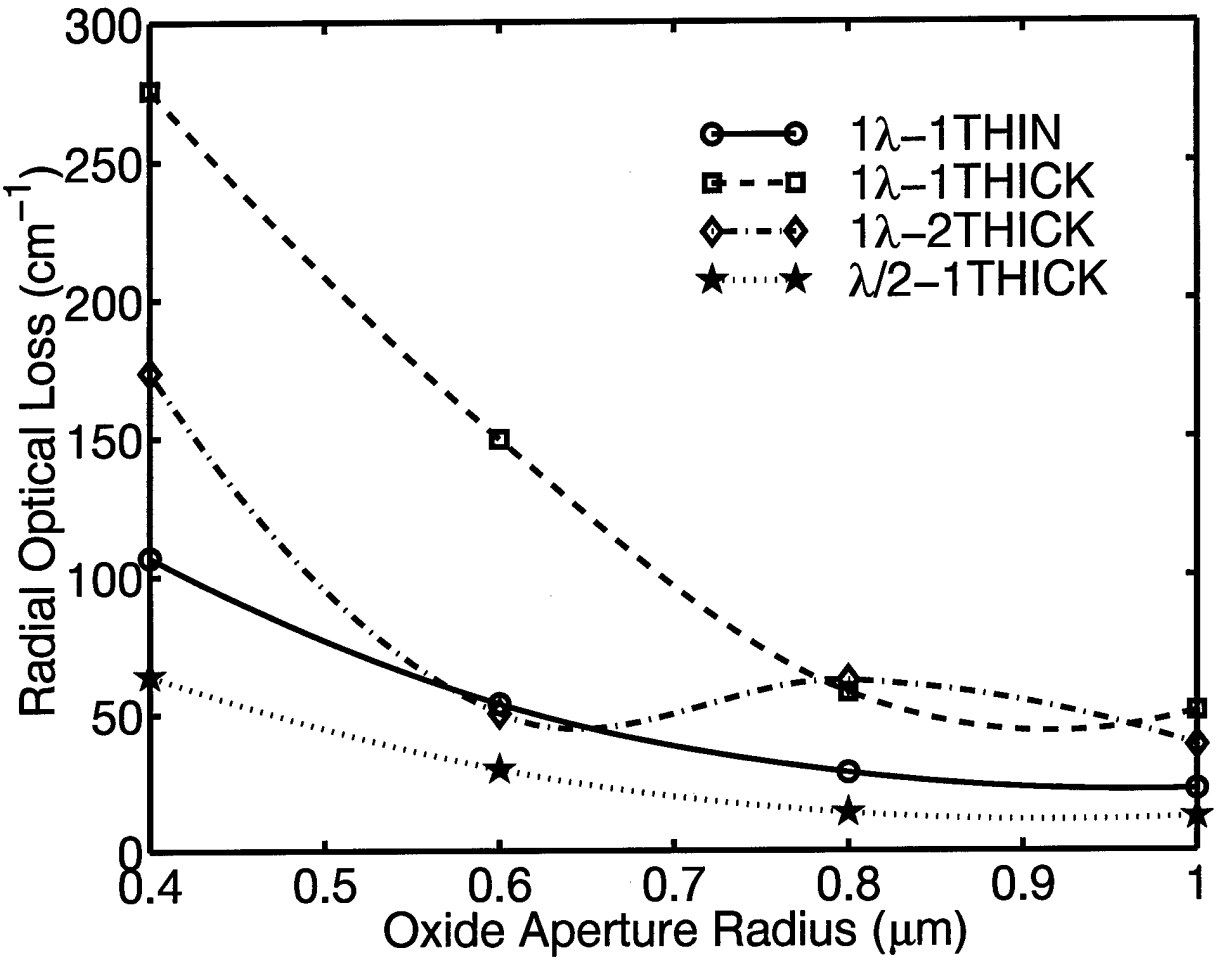

Figure 4.11 Radial mode loss verses oxide aperture radius for the fundamental lasing mode. The lines are cubic spline fits of the discrete calculation data.

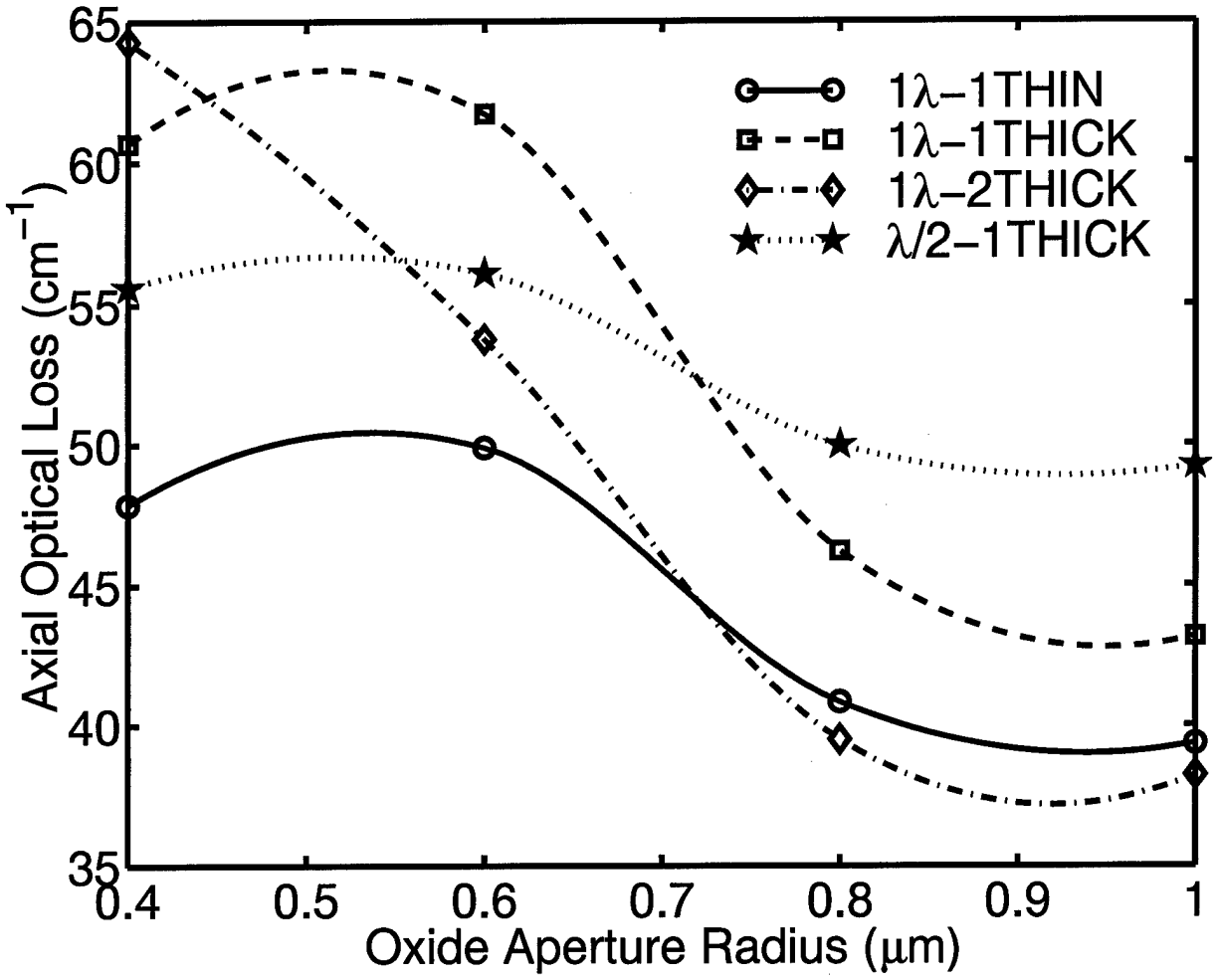

Figure 4.12 Axial mode loss verses oxide aperture radius for the fundamental lasing mode. The lines are cubic spline fits of the discrete calculation data.

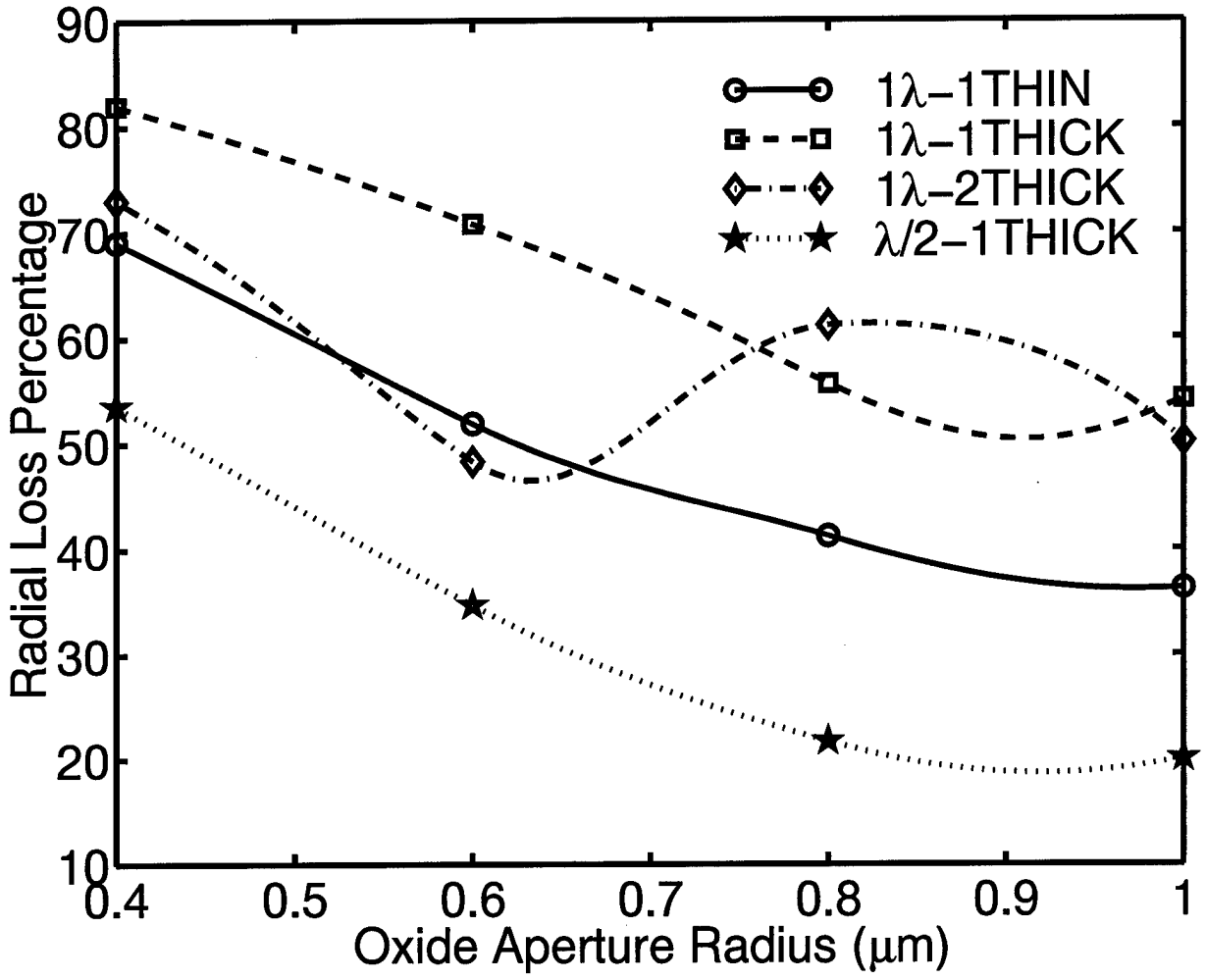

Figure 4.13 Percentage of the total mode loss due to radial losses for the fundamental lasing mode. The lines are cubic spline fits of the discrete calculation data.

4.5 Diffraction Mechanisms

By examining the loss characteristics for each VCSEL design, I may deduce the physical mechanisms governing diffraction. My results support the idea that diffraction may be viewed as a coupling between the bound eigenmode and the continuum of parasitic modes [19]. These are *radially* propagating slab modes in the unapertured (cladding) region. Deppe explains in [21] that for a cavity bound by perfectly conducting mirrors, the parasitic mode density will resemble a slanted staircase following the three dimensional density of modes. The jumps in the staircase occur at each vertical resonance in the cladding region. Deppe's results suggest that shorter cavities are superior since the eigenmode overlaps with a smaller density of parasitic modes. This idea is illustrated in Figure 4.14.

For my high contrast DBRs, I expect very similar behavior to this ideal mirror case. Comparing the threshold gains of each structure (Figure 4.9), the $\lambda/2$ cavity threshold is consistently lower than all the 1λ cases. Moreover, comparing the percentage of the total mode energy lost to diffraction (Figure 4.13), the $\lambda/2$ VCSEL is again superior. These results can't be attributed to transverse confinement, since the $\lambda/2$ VCSEL has the smallest Γ^{tr} of all four cases. However, these results *could* be attributed to the larger *total* confinement factor (Figure 4.6), *or* to a smaller density of parasitic modes interacting with the $\lambda/2$ cavity eigenmode. It turns out that these two factors are closely related: the *longitudinal* confinement factor—or effective cavity length in the *cladding* region—determines the location of the steps in the parasitic mode density (Figure 4.14).

Adopting Deppe's parasitic mode density interpretation, I can explain the difference in threshold between the $\lambda/2$ and 1λ cavity VCSELs, but I *cannot* easily explain the disparity among the three 1λ cases, which should have very similar parasitic mode densities. Furthermore, the parasitic mode density is *solely* a function of (effective) cavity length, and therefore cannot address radius-dependent changes in diffraction. To capture these radius-dependent effects, and to distinguish the various 1λ cavity structures, I propose that the diffractive loss is a function of *both* the density of parasitic modes *and* the coupling strength between the eigenmode and the parasitic modes. Moreover, this coupling strength is a function of two

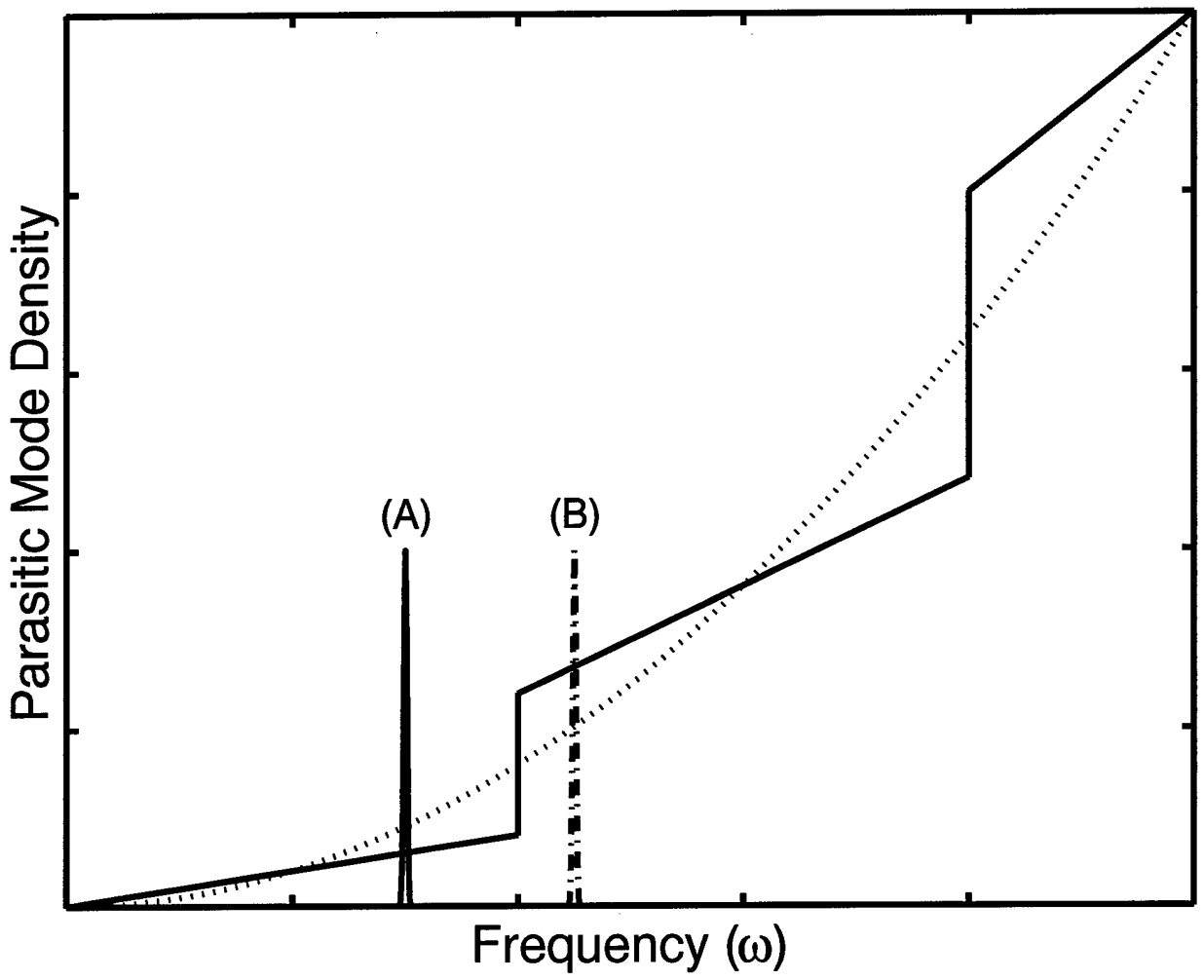

Figure 4.14 Illustration of the "slanted staircase" parasitic mode density. The density follows the three-dimensional, free-space density of optical modes (dotted line). The jumps in the staircase occur at each vertical resonance in the cladding region. The two discrete modes are representative of a low threshold (A), and a higher threshold (B) lasing mode.

factors: (1) the relative alignment of the eigenmode and parasitic mode propagation vectors, and (2) the eigenmode penetration into the cladding region.

The 1λ–1THIN VCSEL exhibits the lowest threshold and the lowest diffraction loss (Figure 4.11) of all three 1λ VCSELs. Because of the weak transverse confinement (Figure 4.5) and the resulting mode spread, the field in this structure is more planar and the propagation vector is paraxial with respect to normal to the planar interfaces. As a result, the eigenmode wavevector is nearly *orthogonal* to the parasitic mode wavevectors, which lie principally in the plane of the layer structure. The parasitic mode wavevectors can have components out of the plane, but the larger these components are the less energy they will carry away in the radial direction. I attribute the low threshold for this design to this misalignment between the eigenmode and parasitic mode wavevectors. This hypothesis is further supported by the peculiar results for the double-apertured 1λ–2THICK VCSEL.

The double-apertured VCSEL has the largest transverse confinement factor of all three 1λ cavity VCSELs. Using the weighted index method [50], I showed that this transverse confinement has two primary effects:

1. It *confines* the mode energy within the aperture region.
2. It causes the eigenmode propagation vector to *tilt* away from normal to the DBRs.

The first effect acts to *decrease* the parasitic mode (or diffractive) loss by containing the mode energy, while the second acts to *increase* it through stronger coupling (better propagation vector alignment) to the parasitic modes. These processes compete, and, depending on VCSEL design and aperture radius, either effect may dominate. For the 1λ–2THICK VCSEL, the transverse confinement is ≥ 0.95 for aperture radii from 1.0 to 0.6 μm; for these radii, the first effect dominates. However, somewhere between 0.6 and 0.4 μm enough mode energy exists outside the oxide aperture such that the strong parasitic mode coupling causes the optical loss to rapidly increase. In essence, the cavity in the unapertured region ($\rho \geq \rho_{ox}$) forms a waveguide whose source is the lasing eigenmode. When the eigenmode penetration into the waveguide region becomes large enough, the waveguide appears to "siphon" energy

away from the eigenmode. This effect is clearly illustrated in the plots of $|E_\phi|$ for the 0.6 and 0.4 μm cases in Figures 4.15 and 4.16, respectively.

In this chapter, I have ascertained the physical mechanisms governing diffraction in oxide apertured VCSELs. The diffraction is well described by the parasitic mode picture. In the next chapter, I augment my weighted index method to *perturbatively* include coupling to the parasitic modes. The result is a *fast*, semi-analytic method for estimating *all* the relevant optical laser parameters for microcavity VCSELs.

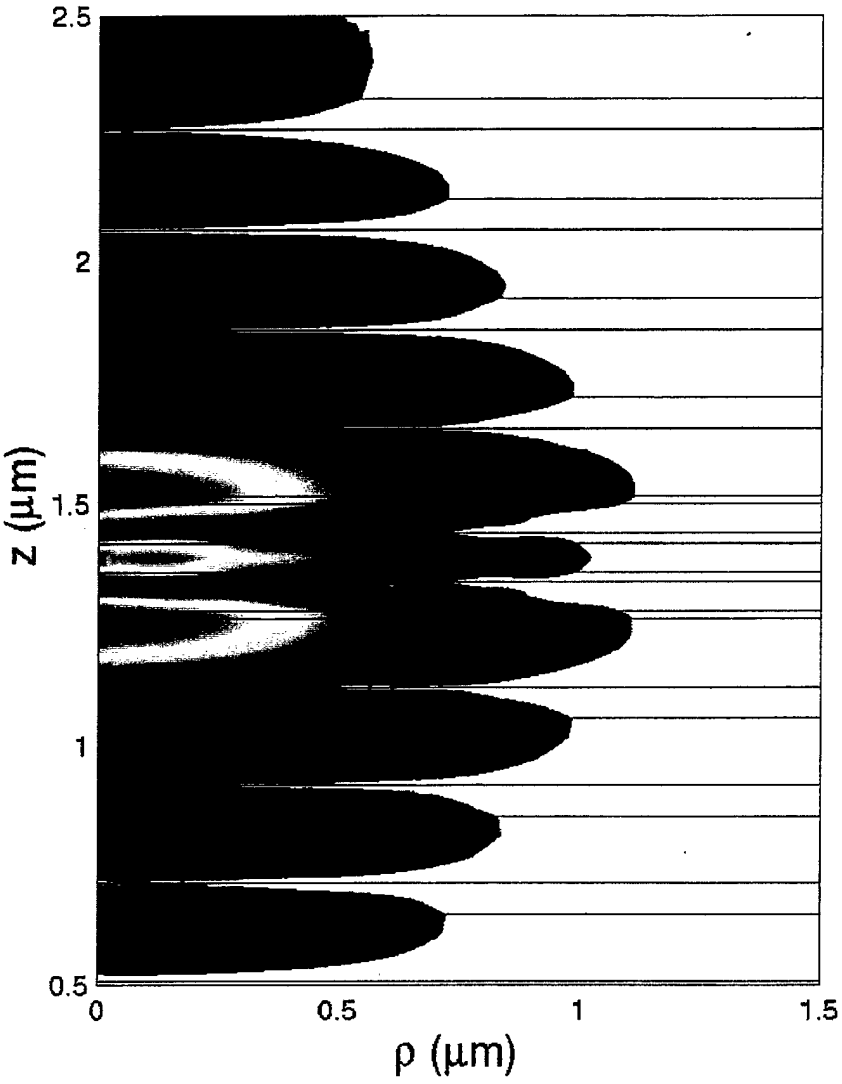

Figure 4.15 $|E_\phi|$ for the 1λ–2THICK structure with oxide aperture radius $\rho_{ox} = 0.6$ μm. The background intensity has been set to white to increase contrast.

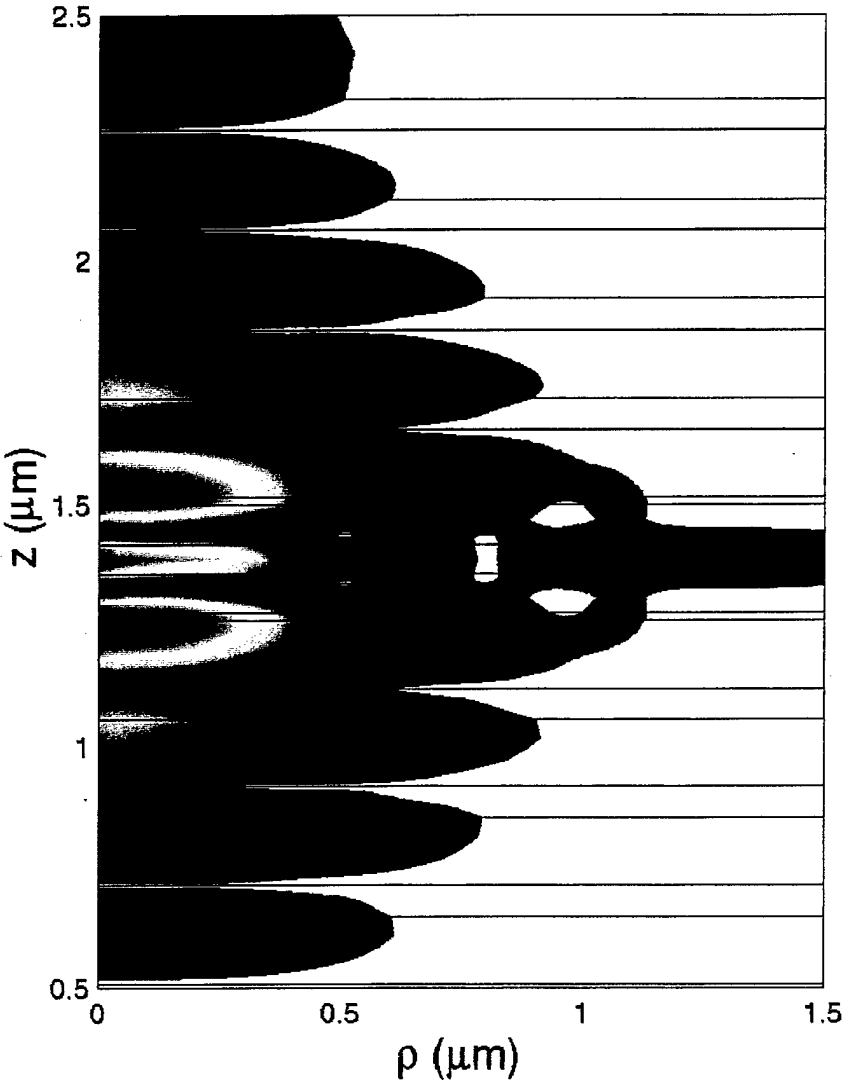

Figure 4.16 $|E_\phi|$ for the 1λ–2THICK structure with oxide aperture radius $\rho_{ox} = 0.4$ μm. Note the field leakage into the waveguide formed by the oxide apertures and the cavity. The background intensity has been set to white to increase contrast.

V. Diffractive or Parasitic Mode Loss

"Things should be made as simple as possible, but not any simpler."

... Albert Einstein

The weighted index method applied to the vector Helmholtz equation is a powerful tool for analyzing the optical properties of azimuthally symmetric, but otherwise arbitrarily complex VCSELs. From this simple variational model I was able to predict the lasing mode blueshift, confinement factors, spatial field profile, and mirror and absorption losses. This led to the discovery of a new phenomenon, a polarization dependence of the mirror loss due to the change in the DBR reflectance with aperture radius [52]. This effect is well documented in edge emitters but had not previously been predicted or observed in VCSELs. The reason it hasn't been observed results from the fact that—for the current VCSEL state-of-the-art—diffraction is the dominant loss mechanism. It is orders of magnitude larger than the change in mirror loss in the regime where the DBR polarization dependence is significant.

In the last chapter, I was able to ascertain the fundamental physical parameters determining diffraction loss in apertured VCSELs. The results suggested that the parasitic mode concept proposed by Deppe [21] accurately depicts the diffractive loss. In this chapter I present a *new* perturbative technique for incorporating the parasitic modes and calculating diffractive loss within the WIM formalism.

Since the change in reflection with radius is the only polarization dependent effect observed for the vector WIM, and since the resulting change in mirror loss is much smaller than the diffraction loss, I simplify my WIM implementation to a scalar solution using the well established linear polarization (LP) approximation. LP modes are much simpler in form and yield a much more robust and rapid calculation: roughly a factor of two faster than the full vector WIM for HEM modes. This increased efficiency comes with virtually no degradation in accuracy. Furthermore, the simpler form of the LP modes facilitates my diffraction calculation, which requires rigorous coupling of the lasing modes to a set of *resonant* parasitic modes.

5.1 *Linear Polarization Approximation for the Lasing Eigenmodes*

To solve for a hybrid ($m \neq 0$) mode in the full vector WIM, I must iteratively solve a 2×2 TM, a 2×2 TE, and a 4×4 radial transfer matrix equation. Since mode convergence requires convergence of the resonant wavelength and threshold gain for *all three equations*, the HEM mode calculation is significantly slower (by roughly an order of magnitude) than pure TE and TM mode calculations. Furthermore, despite the fact A_z and F_z are separable, the HEM field components are not, requiring a non-trivial sum of A_z and F_z contributions. Based on the importance of the HEM modes—the HEM_{11} mode is the fundamental lasing mode—it would be convenient if a simpler technique could be derived for calculation of these modes. I do this using the linearly polarized (LP) mode approximation, originally applied to the weakly guiding fiber.

The LP modes are an approximation to the full waveguide modes in the limit of vanishing difference between core and cladding index of refraction. Equivalently, the LP modes are the scalar modes of the cylindrical waveguide. Most often, the LP modes are derived by assuming $\varepsilon_r^{\mathrm{core}} \approx \varepsilon_r^{\mathrm{clad}}$ within the fiber-optic eigenmode equation [58]

$$\left[\frac{J_n'(u)}{uJ_n(u)} + \frac{K_n'(w)}{wK_n(w)}\right]\left[\frac{\varepsilon_r^{\mathrm{core}}}{\varepsilon_r^{\mathrm{clad}}}\frac{J_n'(u)}{uJ_n(u)} + \frac{K_n'(w)}{wK_n(w)}\right] = n^2\left(\frac{1}{u^2}+\frac{1}{w^2}\right)\left(\frac{\varepsilon_r^{\mathrm{core}}}{\varepsilon_r^{\mathrm{clad}}}\frac{1}{u^2}+\frac{1}{w^2}\right), \tag{5.1}$$

where $u \equiv k_{\mathrm{core}}a$, $w \equiv k_{\mathrm{clad}}a$, and a is the fiber radius. This assumption simplifies (5.1) to the LP eigenmode equation

$$\frac{uJ_m'(u)}{J_m(u)} = \frac{wK_m'(w)}{K_m(w)}, \tag{5.2}$$

which is equivalent to enforcing continuity of the scalar field and its first derivative at $\rho = a$. The azimuthal index $m \neq n$ because the LP modes describe the Cartesian/scalar field components, while the exact fiber-optic modes are given in cylindrical components. Furthermore, within the basic[1] LP mode approximation $E_z = H_z = 0$.

[1] As is the case with most perturbational techniques, several variations of the LP mode approximation exist. Some authors include $\hat{z}$ field components, by either estimating them from the in-plane Cartesian components [24] or by deriving the LP modes using a power series in $\Delta \approx (n_{core} - n_{clad})/n_{core}$ and keeping higher order terms [70]. In any case, the basic approximation is the most popular and is quite adequate in most situations.

LP-mode	Constituent Fiber Modes	Degeneracy
LP_{01}	HEM_{11}	2
LP_{11}	TE_{01}, TM_{01}, HEM_{21}	4
LP_{21}	HEM_{11}, HEM_{31}	4
LP_{02}	HEM_{12}	2
LP_{31}	HEM_{21}, HEM_{41}	4
LP_{12}	TE_{02}, TM_{02}, HEM_{22}	4

Table 5.1 First six lowest order LP modes, their constituent cylindrical modes, and their total (polarization and azimuthal) degeneracy

The LP modes are waveguide modes with no polarization effects included. Therefore, when the LP mode approximation is valid the constituent fiber modes are nearly degenerate, sharing the same propagation constant and cross-sectional intensity distribution. For example, the LP_{11} mode consists of the doubly degenerate HEM_{21} mode, and the TE_{01} and TM_{01} modes, all characterized by an intensity pattern with a single null at the center. Table 5.1 lists the six lowest order LP modes, their corresponding cylindrical (fiber) modes, and their total degeneracy due to polarization and azimuthal field dependency: either $\sin(m\phi)$ or $\cos(m\phi)$ [58]. For VCSELs, I expect the same criteria will apply, and the LP approximation should be valid for nearly degenerate modes. The vector WIM LP_{11} resonance results (Figure 3.13) show very little splitting throughout the convergent range of the calculation, suggesting the validity of the LP approximation for this case. This conclusion is further supported by the DBR reflectance calculation which displayed a relatively small difference between modes over the entire span of radii investigated. Lastly, I note that the LP approximation is equivalent to a paraxial approximation, suggesting it should be most valid for the lowest order WIM modes. Overall, I suspect the error due to the LP approximation will be no worse than the error introduced by the fundamental separability assumption upon which the WIM is based.

Proceeding with the "standard" LP modes, I write the lasing mode *fields* as

$$\vec{E} \approx E_x\hat{x} = F(\rho)\,G(z)\cos(m\phi)\,\hat{x}, \tag{5.3}$$

$$\vec{H} \approx H_y\hat{y} = \frac{i}{\omega\mu_0}F(\rho)\,G'(z)\cos(m\phi)\,\hat{y}. \tag{5.4}$$

Here

$$F(\rho) \equiv \begin{cases} c_1 J_m(k_1\rho) & \rho < \rho_{ox} \\ c_2 K_m(k_2\rho) & \rho > \rho_{ox} \end{cases}, \tag{5.5}$$

$$G(z) \equiv a_j e^{i\beta_j z} + b_j e^{-i\beta_j z}, \tag{5.6}$$

and I have limited the geometry to two radial regions: core ($\rho < \rho_{ox}$) and cladding ($\rho > \rho_{ox}$). To solve for modes, I enforce continuity of the field and its first derivative at each axial and radial interface. The remaining analysis parallels the vector TE mode solution presented in Chapter II, with the exception that I now solve directly for the fields rather than the vector potentials.

For the axial problem, I find roots of the TE threshold condition (2.43). For each resonant mode, the β_j are found from the axial dispersion relation

$$\beta_j^2 = \frac{\omega^2}{c^2}\langle \varepsilon_{r:F,j} \rangle - \langle k \rangle^2. \tag{5.7}$$

Here $\langle \varepsilon_{r:F,j} \rangle$ and $\langle k \rangle$ are the weighted relative permittivity and radial propagation constants, respectively defined by

$$\langle \varepsilon_{r:F,j} \rangle \equiv \frac{\langle F \,|\, \varepsilon_{r:i,j} \,|\, F \rangle}{\langle F \,|\, F \rangle} \quad \text{and} \quad \langle k \rangle \equiv \sqrt{\frac{\langle F \,|\, k_i^2 \,|\, F \rangle}{\langle F \,|\, F \rangle}}. \tag{5.8}$$

Since there can be no confusion with the polarization of the weighting functions for LP modes, no α superscript is required. It is then a simple matter to back solve the individual transfer matrices (2.37) to find the a_j and b_j. For the radial problem I find the roots of the LP eigenmode equation (5.2). This is precisely the same as solving the radial TE threshold condition (2.60) for two regions. The core and cladding propagation constants are given by the radial dispersion relation

$$k_i^2 = \frac{\omega^2}{c^2}\langle \varepsilon_{r:i,G} \rangle - \langle \beta \rangle^2. \tag{5.9}$$

Here $\langle \varepsilon_{r:i,G} \rangle$ and $\langle \beta \rangle$ are defined as

$$\langle \varepsilon_{r:i,G} \rangle \equiv \frac{\langle G \,|\, \varepsilon_{i,j} \,|\, G \rangle}{\langle G \,|\, G \rangle} \quad \text{and} \quad \langle \beta \rangle \equiv \sqrt{\frac{\langle G \,|\, \beta_j^2 \,|\, G \rangle}{\langle G \,|\, G \rangle}}, \tag{5.10}$$

respectively. For each mode, the coefficients c_1 and c_2 may be found by the field continuity condition. The axial and radial problems are alternately solved, iterating until both the resonant wavelength and material gain converge. The result of this analysis is a set of LP lasing modes, all bound in the radial direction and radiative in the axial direction. In order to capture diffractive effects I must augment these modes. I accomplish this by coupling *each* lasing mode to a set of *resonant* parasitic modes.

5.2 Parasitic Modes

To calculate lasing modes with the weighted index method, I enforce radiation conditions in the axial direction and evanescent decay in the radial direction to form constraint equations on the mode frequency and material gain. To calculate parasitic modes with the weighted index method, I relax the evanescent condition and allow for (outward) radial propagation. Alternatively, I may derive the parasitic modes as *exact* field solutions in the cladding region ($\rho > \rho_{ox}$). As I will show below, these two versions of the parasitic modes are *equivalent.*

Since parasitic modes may propagate at any angle with respect to the planar interface normal ($\hat{z}$), *I do not make the LP approximation* and instead solve explicitly for TE and TM cylindrical modes. By dividing the modes into TE and TM, they may be conveniently described by a single longitudinal field component: H_z for TE modes and E_z for TM modes. For HEM lasing modes, the relative strength of the TE and TM components was important in order to match the tangential field components across radial boundaries. But, for the parasitic modes there is no such requirement: I am only concerned with their behavior in the cladding region. Furthermore, the TE and TM parasitic modes each obey the axial boundary conditions on their own, implying they may be dealt with independently regardless of the azimuthal mode order.

Based on the azimuthal form of the LP modes, I choose[2]

$$H_z^{\mathrm{PM}} \equiv P(\rho)Q(z)\sin(n\phi), \tag{5.11}$$

$$E_z^{\mathrm{PM}} \equiv P(\rho)Q(z)\cos(n\phi), \tag{5.12}$$

where

$$P(\rho) \equiv \begin{cases} c_1 J_n(k_1\rho) & \rho < \rho_{ox} \\ c_2 H_n^{(2)}(k_2\rho) & \rho > \rho_{ox} \end{cases}, \tag{5.13}$$

$$Q(z) \equiv a_j e^{i\beta_j z} + b_j e^{-i\beta_j z}. \tag{5.14}$$

Since the TE and TM modes are dealt with independently, no polarization superscript is required, and I am free to use the same functions (P, Q) for E_z^{PM} and H_z^{PM}. The choice of $E_z^{\mathrm{PM}} \sim \cos(n\phi)$ and $H_z^{\mathrm{PM}} \sim \sin(n\phi)$ is necessary, due to azimuthal orthogonality, for the lasing mode to couple with the parasitic modes. For each lasing mode, I calculate a set of *resonant* parasitic modes following a procedure analogous to the first axial iteration of the TE/TM vector mode solution given in Section 2.4.

To solve the axial problem, I must first calculate a set of weighted material parameters $\langle \varepsilon_{r:P,j} \rangle$, found via

$$\langle \varepsilon_{r:P,j} \rangle \equiv \frac{\langle P \,|\, \varepsilon_{r:i,j} \,|\, P \rangle}{\langle P \,|\, P \rangle}. \tag{5.15}$$

Since the parasitic modes are radiative in the radial direction, the inner product over ρ (2.19),

$$\langle P \,|\, P \rangle = \int_0^\infty |P(\rho)|^2 \, \rho \, d\rho, \tag{5.16}$$

will not converge. However, employing an appropriate limiting procedure, (5.15) *will converge*, and gives the material values in the cladding region,

$$\langle \varepsilon_{r:P,j} \rangle = \varepsilon_{r:2,j}. \tag{5.17}$$

[2]Note, to avoid excessive sub/superscripting, I have recycled the P and Q functions, redefining them from their original designation in Chapter II.

Similarly, the weighted radial propagation constant will equal the cladding value,

$$\langle k \rangle \equiv \sqrt{\frac{\langle P \mid k_i^2 \mid P \rangle}{\langle P \mid P \rangle}} = k_2. \tag{5.18}$$

This implies that the parasitic mode solution obtained via the WIM procedure is *precisely* the same as the exact cylindrical mode solution in the cladding region. The dispersion relation for the axial problem is

$$\frac{\omega^2}{c^2}\varepsilon_{r:2,j} = k_2^2 + \beta_j^2. \tag{5.19}$$

Since I am looking for parasitic modes resonant with a particular lasing mode, I set $\omega = \omega_{\text{lase}}$ and solve for the complex k_2 roots of the axial threshold condition

$$t_{22}(k_2) = 0. \tag{5.20}$$

Equation (5.20) is the same as the TE/TM threshold condition given in Chapter II (2.43), the only difference is the argument for which the roots are found. I allow k_2 to be complex, rather than solve for a real k_2 and κ_{active}, since material gain does not apply to the parasitic modes. The source of the parasitic modes is the *lasing mode.* Furthermore, the complex k_2 term compensates for the axial radiation of the parasitic modes. As I will show in Section 5.4, the $\text{Im}(k_2)$ has no impact on the energy carried away from the lasing mode. Since this energy "siphoning" is the only effect I am after, I allow k_2 to be complex as a matter of practical convenience in my root search algorithm, ignoring the $\text{Im}(k_2)$ for all subsequent calculations.

Once (5.20) is solved, I could continue with the WIM procedure and solve the radial problem, determining weighted $\langle \beta \rangle$ and $\langle \varepsilon_{r:i,Q} \rangle$, and finding the k_1 and c_1 that satisfy the radial TE/TM (or HEM) boundary conditions. However, these results will have no bearing on $Q(z)$, implying the axial solution is *uncoupled* from the radial solution. Moreover, these results will have no effect on $P(\rho)$ for $\rho > \rho_{ox}$, since k_2 is completely determined by the axial solution (5.20) and the radial boundary conditions only give c_1 in terms of c_2 (i.e., one degree of freedom exists in the radial solution, typically this is used to normalize $P(\rho)$). As

I will demonstrate in Section 5.3, only the cladding region behavior is required to calculate the diffractive loss. Therefore, for each parasitic mode I only solve (5.20) and ignore $P(\rho)$ for $\rho < \rho_{ox}$, substantiating my earlier claim that TE and TM modes may be solved for independently. Based on this discussion, and to facilitate the following analysis, I simplify the parasitic mode definition to

$$H_z^{\mathrm{PM}} = H_n^{(2)}(k\rho)\, Q(z) \sin(n\phi), \tag{5.21}$$

$$E_z^{\mathrm{PM}} = H_n^{(2)}(k\rho)\, Q(z) \cos(n\phi). \tag{5.22}$$

Here $k = k_2$ from (5.13), and the fact that these only apply for the cladding region is implicitly understood. An illustration of the standing wave intensity profile for a TM parasitic mode is given in Figure 5.1.

5.3 Lasing Mode-to-Parasitic Mode Coupling

The WIM lasing modes are *not* eigenmodes of the non-separable VCSEL cavity, but are instead a product of (one-dimensional) eigensolutions of the weighted axial and radial problems. One could envision a separable cavity with $\varepsilon_r(\rho, z) = \varepsilon_r(\rho) + \varepsilon_r(z)$ for which the WIM lasing mode *was* a true eigenmode. In this case, each WIM lasing mode would be independent and exact, and there would be no mechanism for coupling to the parasitic modes. This may in fact be a viable *new* design approach. Theoretically, if such a device could be fabricated, the (WIM) lasing modes would suffer *no diffraction loss.* An illustration of this type of device is shown in Figure 5.2. The diffraction or parasitic mode loss results from the non-separability of the VCSEL structure[3], which effectively couples the lasing mode to the parasitic modes. To calculate this coupling, I employ two basic electromagnetic theorems: surface induction and reciprocity.

[3]In analogy to quantum optics theory, the WIM lasing mode and the resonant parasitic modes are "bare" field modes. The *true* three-dimensional, lossy cavity modes are "dressed" field modes. The coupling between the WIM lasing mode and the parasitic modes determines the weighting coefficients of the various bare modes in the representation of a single dressed mode.

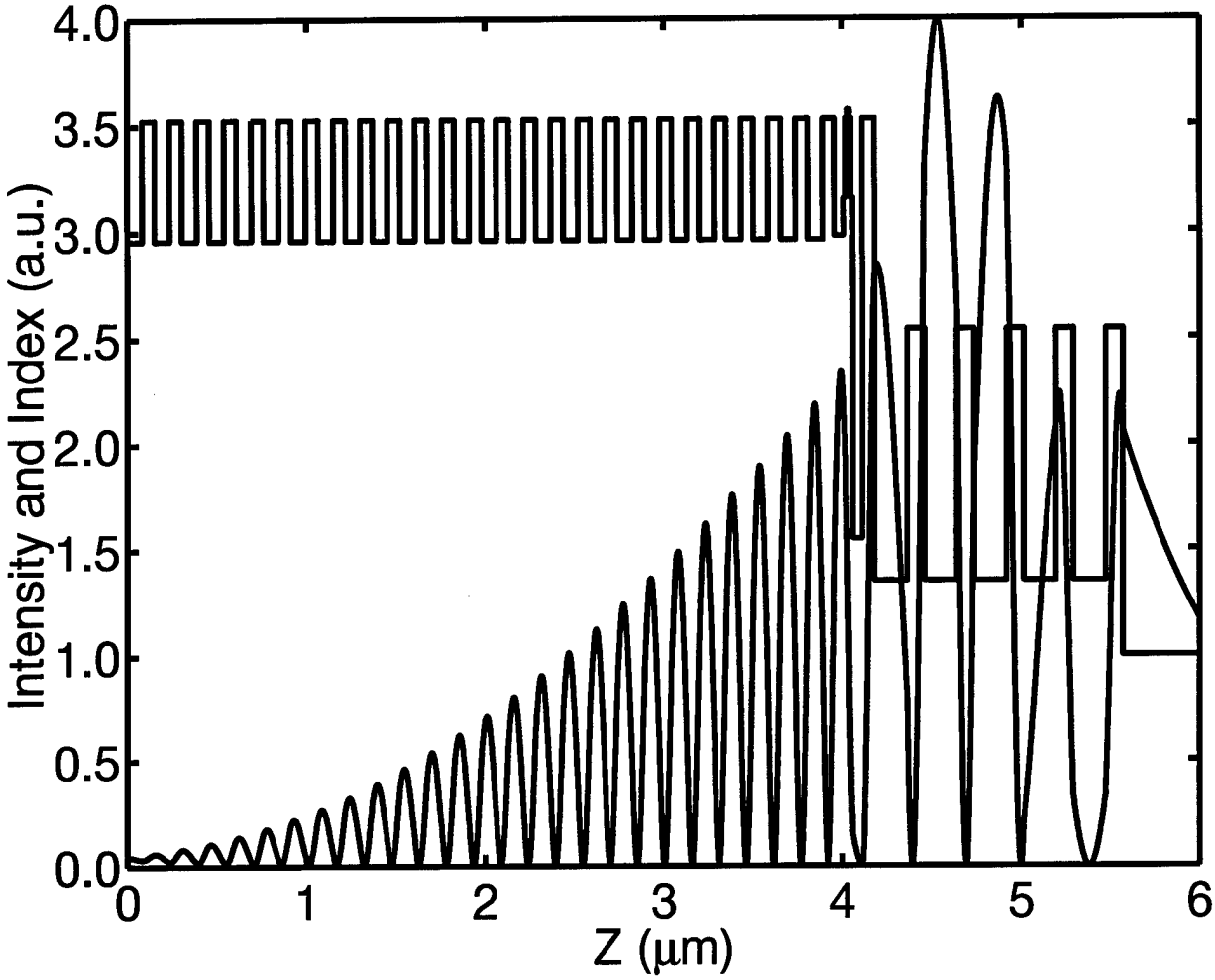

Figure 5.1 Illustration of the standing wave intensity profile for a TM parasitic mode.

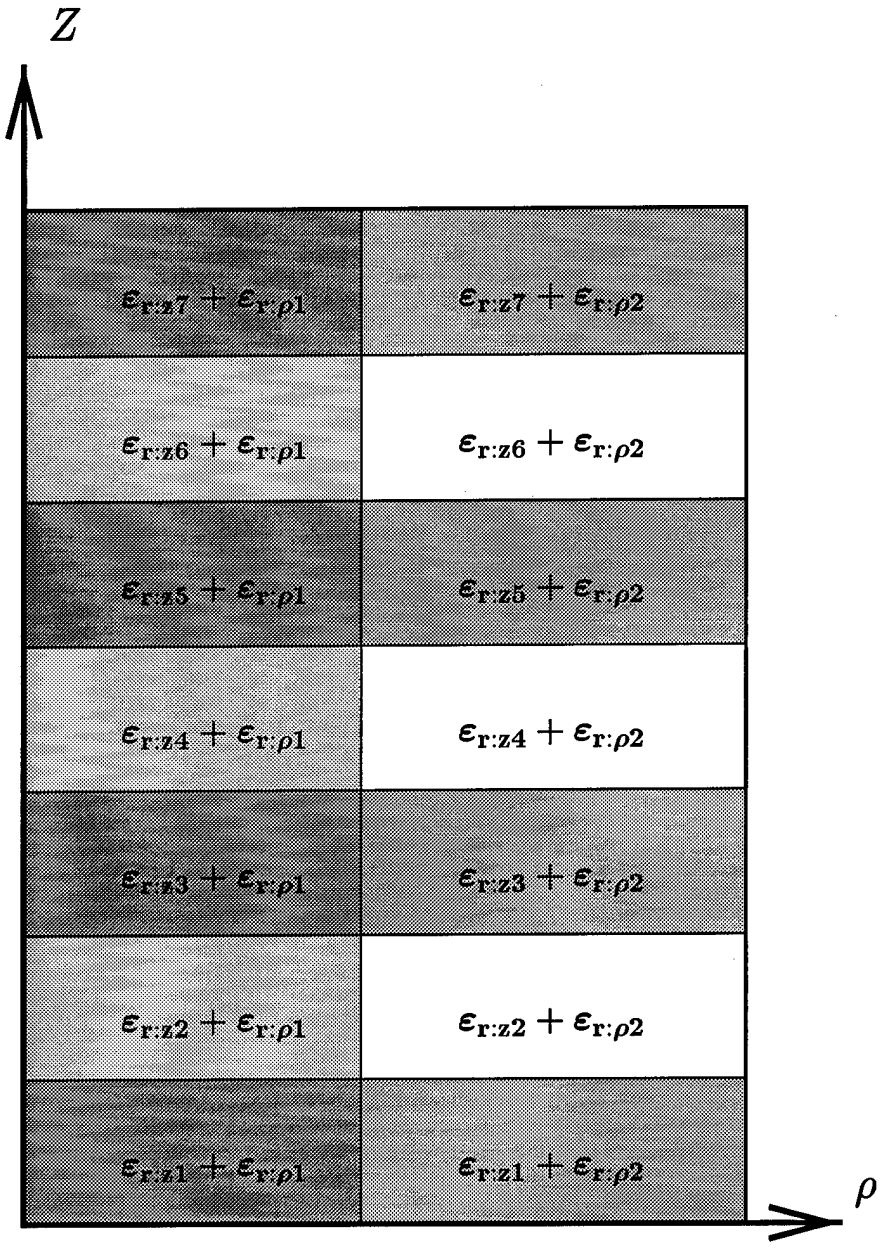

Figure 5.2 Illustration of an azimuthally symmetric, *separable* VCSEL geometry. The change in relative permittivity as a function of z produces the Fabry-Perot cavity structure. The change in relative permittivity as a function of ρ defines the lasing modes analogous to fiber-optic waveguide modes. If such a VCSEL could be fabricated, theoretically the lasing modes would suffer *no diffraction loss.*

5.3.1 Surface Induction. For the first step in my coupling calculation, I derive fictitious electric $\left(\vec{J}^{eq}\right)$ and magnetic $\left(\vec{M}^{eq}\right)$ surface currents in the cladding region ($\rho > \rho_{ox}$). These currents *replace* the eigenmode in the cladding region and act as a source for the parasitic modes. The *sole* purpose for performing this substitution is to mathematically isolate the parasitic mode fields from the eigenmode fields, making it much easier to solve for the coupling strength to each parasitic mode. It is crucial to realize that *all* I am doing is restating the field problem in a different, but equivalent, form. The combination of the currents and the parasitic modes in the cladding region is *exactly* equivalent to the *real* electromagnetic problem involving the eigenmode *and* parasitic modes. The surface induction theorem[4] [7] describes *how* to represent the fields with equivalent currents.

To derive equivalent currents, I assume the total field in the core region ($\rho < \rho_{ox}$) is accurately represented by the WIM lasing mode,

$$\vec{E}^{\text{core}}(\rho,\phi,z) \approx \vec{E}^{\text{WIM}}(\rho < \rho_{ox},\phi,z), \tag{5.23}$$

$$\vec{H}^{\text{core}}(\rho,\phi,z) \approx \vec{H}^{\text{WIM}}(\rho < \rho_{ox},\phi,z). \tag{5.24}$$

In the cladding region, I assume the total field may be written as the sum of the lasing mode and the resonant parasitic modes,

$$\vec{E}^{\text{clad}}(\rho,\phi,z) \approx \vec{E}^{\text{WIM}}(\rho > \rho_{ox},\phi,z) + \sum_{l=1}^{N_{\text{PM}}} A_l \vec{E}_l^{\text{PM}}(\rho > \rho_{ox},\phi,z), \tag{5.25}$$

$$\vec{H}^{\text{clad}}(\rho,\phi,z) \approx \vec{H}^{\text{WIM}}(\rho > \rho_{ox},\phi,z) + \sum_{l=1}^{N_{\text{PM}}} A_l \vec{H}_l^{\text{PM}}(\rho > \rho_{ox},\phi,z). \tag{5.26}$$

Here N_{PM} is the total number of parasitic modes which couple to the lasing mode (includes both TE and TM parasitic modes) and A_l is the amplitude of the l'th parasitic mode. These assumptions are required for a "clean" electromagnetic problem but are otherwise not directly related to surface induction. These fields constitute the "actual problem,"

[4]The inductance theorem is closely tied to the uniqueness theorem which states that the fields in a closed region are uniquely specified by the sources with the region plus the tangential field components on the boundary.

illustrated in Figure 5.3. In the actual problem, no sources exist and the total tangential fields are continuous across the $\rho = \rho_{ox}$ interface.

To apply surface induction, I consider the "closed" surface Γ_{clad} which encompasses the cladding region volume[5],

$$\Omega_{\text{clad}} \equiv [\rho_{ox}, \infty] \times [0, 2\pi] \times [-\infty, \infty]. \tag{5.27}$$

Within Ω_{clad}, I *replace* the WIM eigenmode fields with the equivalent electric and magnetic currents. Therefore, in the "surface inductance equivalent problem," illustrated in Figure 5.3, the *total* fields in the cladding region are given by

$$\vec{E}_{\text{SI}}^{\text{clad}}(\rho, \phi, z) = \sum_{l=1}^{N_{\text{PM}}} A_l \vec{E}_l^{\text{PM}}(\rho > \rho_{ox}, \phi, z), \tag{5.28}$$

$$\vec{H}_{\text{SI}}^{\text{clad}}(\rho, \phi, z) = \sum_{l=1}^{N_{\text{PM}}} A_l \vec{H}_l^{\text{PM}}(\rho > \rho_{ox}, \phi, z). \tag{5.29}$$

Here SI denotes surface inductance equivalent fields.

In the actual problem, no currents exist and the fields obey the tangential field continuity relations. In the surface induction equivalent problem, the equivalent currents are *required* to enforce continuity of the tangential fields. The electric and magnetic currents are defined by

$$\vec{J}^{eq} \equiv \hat{n} \times \left(\vec{H}^{\text{core}} - \vec{H}_{\text{SI}}^{\text{clad}} \right), \tag{5.30}$$

$$\vec{M}^{eq} \equiv \left(\vec{E}^{\text{core}} - \vec{E}_{\text{SI}}^{\text{clad}} \right) \times \hat{n}, \tag{5.31}$$

where $\hat{n}$ is the outward normal to Γ_{clad}. The difference in form between (5.30) and (5.31) is strictly due to convention. Since the lasing mode is evanescent in the cladding region, the equivalent currents are only non-zero along the boundary[6] $\rho = \rho_{ox}$. Hence, the outward

[5]Here I have assumed that Γ_{clad} may be closed at infinity, a common practice within theoretical electromagnetics.

[6]Consistent with the general WIM procedure, I assume the currents go to zero for $z > z_{\text{top}}$ and $z < z_{\text{bottom}}$, the upper and lower VCSEL boundary planes

normal $\hat{n} = -\hat{\rho}$ and the equivalent *surface* currents are

$$\begin{aligned}
\vec{J}^{eq} &= (-\hat{\rho}) \times \left\{ \vec{H}^{\mathrm{WIM}}(\rho_{ox}^{-}, \phi, z) - \sum_{l=1}^{N_{\mathrm{PM}}} A_l \vec{H}_l^{\mathrm{PM}}(\rho > \rho_{ox}, \phi, z) \right\} \\
&= \vec{H}^{\mathrm{WIM}}(\rho_{ox}^{+}, \phi, z) \times \hat{\rho}, \qquad (5.32) \\
\vec{M}^{eq} &= \left\{ \vec{E}^{\mathrm{WIM}}(\rho_{ox}^{-}, \phi, z) - \sum_{l=1}^{N_{\mathrm{PM}}} A_l \vec{E}_l^{\mathrm{PM}}(\rho > \rho_{ox}, \phi, z) \right\} \times (-\hat{\rho}) \\
&= \hat{\rho} \times \vec{E}^{\mathrm{WIM}}(\rho_{ox}^{+}, \phi, z). \qquad (5.33)
\end{aligned}$$

Here ρ_{ox}^{-} and ρ_{ox}^{+} lie just outside and inside of Γ_{clad}, respectively.

Note that I could have represented the WIM eigenmode in the cladding region using equivalent *volume* currents. In this approach, the equivalent currents arise from the difference in the weighted material parameters—for which the WIM solution is exact—and the actual material parameters. Unlike the surface induction solution, there is no magnetic volume current, since $\mu = \mu_0$ everywhere. However, the electric current has both a $\hat{\rho}$ and a $\hat{\phi}$ component, and therefore couples to *both* the TE and TM parasitic modes. This approach is attractive, since it allows for an easier *interpretation* of the source of the parasitic mode loss: the difference between the weighted and real geometries. I chose to use equivalent surface currents, since they allow for an easier *implementation* and yield the same diffraction loss results.

The surface induction picture is now complete: inside Ω_{clad} the total fields are given by the weighted sum of the parasitic modes ((5.28) and (5.29)), whose source is the magnetic and electric equivalent currents ((5.32) and (5.33)). The surface inductance problem, which is equivalent to the actual problem in the *cladding* region, is illustrated in Figure 5.3. All that remains is to couple the currents to the parasitic modes to find the amplitude (A_l)—or coupling strength—of each parasitic mode. For this, I use reciprocity.

5.3.2 Reciprocity. The reciprocity theorem is a simple rearrangement of the Maxwell curl equations using appropriate vector identities. It is commonly used in waveguides problems to calculate the coupling between two guides or the radiation from a source into a guide. I employ reciprocity in a similar capacity, to compute the A_l coefficients.

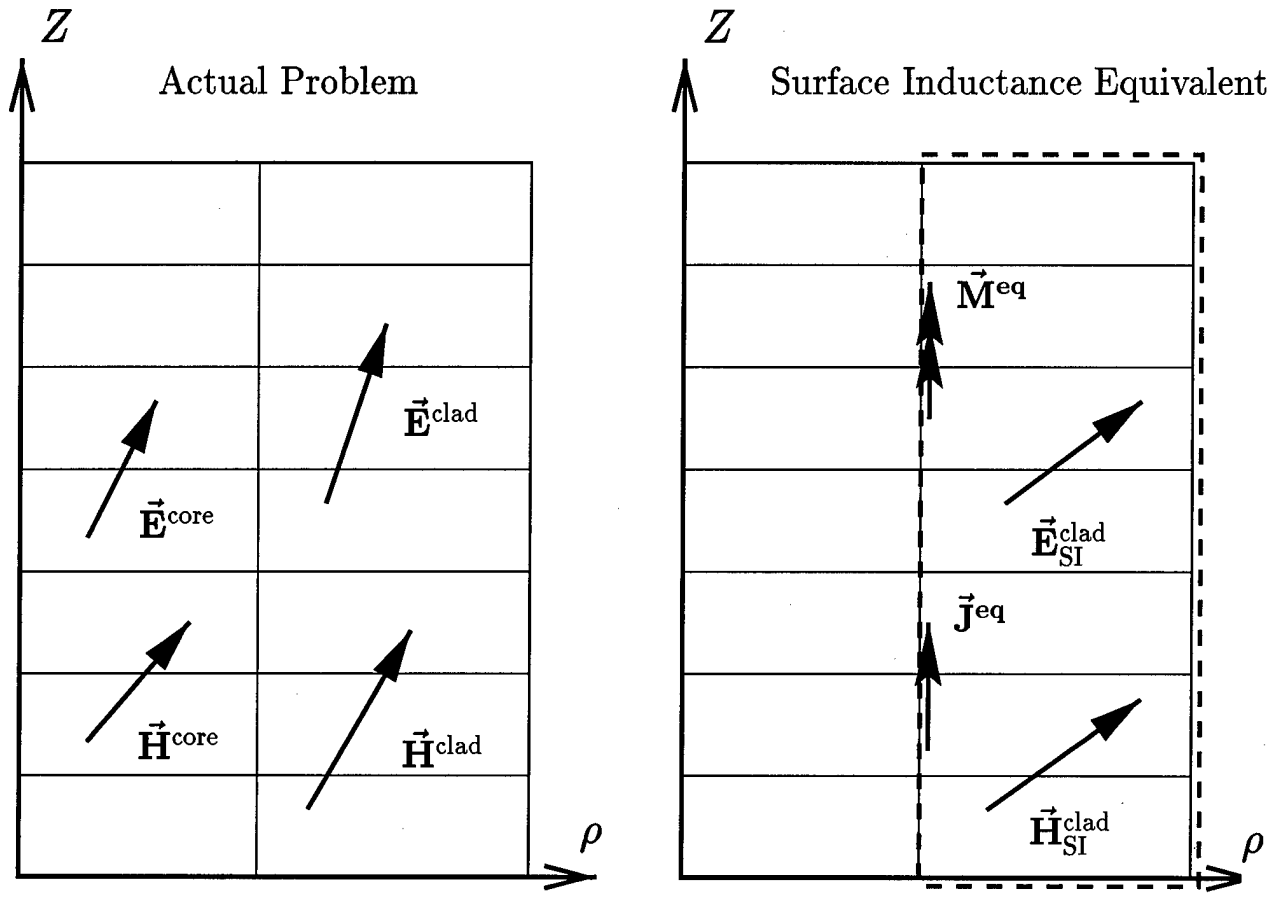

Figure 5.3 Illustration of the actual VCSEL electromagnetic problem (left) and the surface inductance equivalent problem (right). In the surface inductance problem the WIM fields in the cladding region, denoted by the dashed box, are replaced by equivalent surface currents $\vec{J}^{eq}$ (5.32) and $\vec{M}^{eq}$ (5.33). The *total* fields in the cladding region in the equivalent problem, $\vec{E}^{clad}_{SI}$ and $\vec{H}^{clad}_{SI}$, are given by the weighted sum of parasitic modes (5.28) and (5.29).

Reciprocity dictates that any two fields in the volume Ω_{clad} must satisfy

$$\iint_{\Gamma_{\text{clad}}} \left\{ \vec{E}^a \times \vec{H}^b - \vec{E}^b \times \vec{H}^a \right\} \cdot d\vec{s} = \iiint_{\Omega_{\text{clad}}} \left\{ \vec{E}^b \cdot \vec{J}^a - \vec{E}^a \cdot \vec{J}^b + \vec{H}^a \cdot \vec{M}^b - \vec{H}^b \cdot \vec{M}^a \right\} dV. \tag{5.34}$$

For my application, I assign the a fields and sources to the surface induction cladding fields ((5.28) and (5.29)) and equivalent currents ((5.32) and (5.33)). For the b fields, I use a fictitious "test" mode[7]: a single parasitic mode propagating radially *inward*. The test mode is a non-physical—since it propagates inward—parasitic mode, which otherwise obeys all of Maxwell's equations *and* the parasitic mode orthogonality relation (5.49). Since the strength of the parasitic modes is *completely* determined by the equivalent currents (and therefore, the eigenmode), I solve for TE and TM parasitic mode A_l separately, even for $m \neq 0$ modes.

First, I consider the TE parasitic modes. I define the test mode or b fields (5.34) by

$$H_z^- \equiv H_n^{(1)}(k_l \rho)\, Q_l(z) \sin(n\phi). \tag{5.35}$$

H_z^- is an exact duplicate of one of the real parasitic modes, with the exception that it travels in the opposite direction. To apply reciprocity, I assign [60]

$$\vec{E}^a \equiv \vec{E}_{\text{SI}}^{\text{clad}} = \sum_{l=1}^{N_{\text{PM}}} A_l \vec{E}_l^{\text{PM}}, \tag{5.36}$$

$$\vec{H}^a \equiv \vec{H}_{\text{SI}}^{\text{clad}} = \sum_{l=1}^{N_{\text{PM}}} A_l \vec{H}_l^{\text{PM}}, \tag{5.37}$$

$$\vec{J}^a \equiv \vec{J}^{eq}, \tag{5.38}$$

$$\vec{M}^a \equiv \vec{M}^{eq}, \tag{5.39}$$

$$\vec{E}^b \equiv \vec{E}^-, \tag{5.40}$$

$$\vec{H}^b \equiv \vec{H}^-, \tag{5.41}$$

$$\vec{J}^b \equiv 0, \tag{5.42}$$

$$\vec{M}^b \equiv 0. \tag{5.43}$$

[7]The use of a "test" mode is standard practice in waveguide solutions; see, for example, [60].

Beginning with the surface integral in (5.34), I note that

$$d\vec{s} = (-\hat{\rho})\,\rho_{ox}\,d\phi\,dz \tag{5.44}$$

on $\rho = \rho_{ox}$. Substituting in $d\vec{s}$ and performing the cross and dot products, the surface integral reduces to

$$\int_{z_{\text{bottom}}}^{z_{\text{top}}} \int_0^{2\pi} \left\{ E_\phi^b H_z^a - E_\phi^a H_z^b \right\} \rho_{ox}\,d\phi\,dz, \tag{5.45}$$

assuming the surface region $[0, 2\pi] \times [z_{\text{bottom}}, z_{\text{top}}]$ is the only region contributing to the integral[8]. Calculating E_ϕ^a and E_ϕ^b via Ampere's law, (shown here tailored for TE modes)

$$E_\phi(\rho, \phi, z) = \frac{i\omega\mu_o}{k^2} \left\{ \frac{\partial}{\partial\rho} H_z(\rho, \phi, z) \right\}, \tag{5.46}$$

yields

$$E_\phi^b = \frac{i\omega\mu_0}{k_l} H_n^{(1)\prime}(k_l\rho)\,Q_l(z)\sin(n\phi), \tag{5.47}$$

$$E_\phi^a = \sum_{l=1}^{N_{\text{PM}}} A_l \frac{i\omega\mu_0}{k_l} H_n^{(2)\prime}(k_l\rho)\,Q_l(z)\sin(n\phi), \tag{5.48}$$

where $'$ denotes differentiation with respect to the argument. Before proceeding, I make the crucial *assumption* that the parasitic modes are orthogonal, obeying the relation

$$\iint_{\Gamma_{\text{clad}}} \left\{ \vec{E}^a \times \vec{H}^b \right\} \cdot d\vec{s} = 0 \quad \text{for} \quad a \neq b. \tag{5.49}$$

Equation (5.49) sifts the $l = \acute{l}$ mode out of the summation (5.48), reducing the surface integral (5.45) to

$$-A_{\acute{l}} \frac{i\omega\mu_0\rho_{ox}\pi}{k_{\acute{l}}} W(k_{\acute{l}}\rho_{ox}) \int_{z_{\text{bottom}}}^{z_{\text{top}}} [Q_{\acute{l}}(z)]^2\,dz. \tag{5.50}$$

[8]This assumption may be justified by including a very small amount of absorption in the cladding region, such that the parasitic modes go to zero at infinity.

Here $W(z)$ is the Hankel function Wronskian defined by [1]

$$W(z) \equiv H_{n+1}^{(1)}(z) H_n^{(2)}(z) - H_n^{(1)}(z) H_n^{(2)}(z) = \frac{-4i}{\pi z}, \tag{5.51}$$

and the azimuthal integral equals π. Finally, substituting in (5.51) and rewriting the integral over z in Dirac notation gives

$$\iint\limits_{\Gamma_{\text{clad}}} \left\{ \vec{E}^a \times \vec{H}^b - \vec{E}^b \times \vec{H}^a \right\} \cdot d\vec{s} = -A_l \frac{4\omega\mu_0}{k_l^2} \left\langle \widetilde{Q_l \,|\, Q_l} \right\rangle, \tag{5.52}$$

where the $\widetilde{}$ indicates the inner product is unconjugated.

Turning now to the right hand side of (5.34), I begin by noting that the LP modes have no $\hat{z}$ field component. Therefore, the effective currents calculated in (5.32) and (5.33) will be strictly $\hat{z}$ directed. Furthermore, $\vec{J}^{eq}$ and $\vec{M}^{eq}$ are surface currents, non-zero only on the boundary $\rho = \rho_{ox}$, reducing the volume integral in (5.34) to a surface integral. Making these simplifications, the right hand side of the reciprocity relation (5.34) becomes

$$-\int_{z_{\text{bottom}}}^{z_{\text{top}}} \int_0^{2\pi} H_z^b M_z^a \, \rho_{ox} \, d\phi \, dz, \tag{5.53}$$

where the only coupling occurs through $\vec{M}^{eq}$ (conversely, the TM parasitic modes will only couple through $\vec{J}^{eq}$). Explicitly calculating the magnetic current due to the LP lasing mode gives

$$\begin{aligned} M_z^{eq} &= \hat{z} \cdot (\hat{\rho} \times \hat{x}) \, F(\rho) G(z) \cos(m\phi) \\ &= \frac{1}{2} F(\rho) G(z) \left[\sin((m-1)\phi) - \sin((m+1)\phi) \right]. \end{aligned} \tag{5.54}$$

Substituting M_z^{eq} and H_z^- into (5.53) yields

$$\iiint\limits_{\Omega_{\text{clad}}} \left\{ \vec{E}^b \cdot \vec{J}^a - \vec{H}^b \cdot \vec{M}^a \right\} dV = -\frac{\rho_{ox}}{2} F(\rho_{ox}) H_n^{(1)}(k_l \rho_{ox}) \left\langle \widetilde{G \,|\, Q_l} \right\rangle \Phi^{\text{TE}}(\phi). \tag{5.55}$$

Here

$$\Phi^{\mathrm{TE}}(\phi) \equiv \int_0^{2\pi} [\sin((m-1)\phi) - \sin((m+1)\phi)] \sin(n\phi)\, d\phi$$
$$= \begin{cases} -2\pi & m = 0,\ n = m+1 \\ -\pi & m \geq 1,\ n = m+1 \\ \pi & m > 1,\ n = m-1 \end{cases}, \tag{5.56}$$

determines to which parasitic modes the lasing mode will couple. Setting the left hand side (5.52) equal to the right hand side (5.55), and solving for the coupling constant gives

$$A_l^{\mathrm{TE}} = \frac{\pi k_l^2 \rho_{ox}}{8\omega\mu_0} \frac{\widetilde{\langle G \,|\, Q_l \rangle}}{\widetilde{\langle Q_l \,|\, Q_l \rangle}} F(\rho_{ox}) H_n^{(1)}(k_l \rho_{ox}) \left[\delta_{n(m-1)} - \delta_{n(m+1)}(1 + \delta_{m0})\right]. \tag{5.57}$$

Here I have replaced $\Phi^{\mathrm{TE}}(\phi)$ with the corresponding sum of Kronecker delta functions (δ_{ab}), and added the TE superscript on A_l for clarity.

To calculate the TM parasitic mode coupling coefficient, I use the same a fields but consider a radially inward propagating TM mode for the b fields in (5.34),

$$E_z^- \equiv H_n^{(1)}(k_l \rho)\, Q_l(z) \cos(n\phi). \tag{5.58}$$

Following an analogous procedure, I apply reciprocity using the same field assignments given in (5.36) – (5.43). For this case, the surface integral is given by

$$\int_{z_{\mathrm{bottom}}}^{z_{\mathrm{top}}} \int_0^{2\pi} \left\{E_z^a H_\phi^b - E_z^b H_\phi^a\right\} \rho_{ox}\, d\phi\, dz. \tag{5.59}$$

Calculating H_ϕ^a and H_ϕ^b via Faraday's law, (shown here tailored for TM modes)

$$H_\phi(\rho, \phi, z) = \frac{-i\omega\varepsilon_0\varepsilon_r}{k^2} \left\{\frac{\partial}{\partial\rho} E_z(\rho, \phi, z)\right\}, \tag{5.60}$$

yields

$$H_\phi^a = -\sum_{l=1}^{N_{\rm PM}} A_l \frac{i\omega\varepsilon_0\varepsilon_r}{k_l} H_n^{(2)\prime}(k_l\rho)\, Q_l(z)\cos(n\phi), \tag{5.61}$$

$$H_\phi^b = \frac{-i\omega\varepsilon_0\varepsilon_r}{k_{\hat{l}}} H_n^{(1)\prime}(k_{\hat{l}}\rho)\, Q_{\hat{l}}(z)\cos(n\phi). \tag{5.62}$$

Substituting the fields into (5.59), and minding the orthogonality relation, gives

$$\begin{aligned}\iint_{\Gamma_{\rm clad}} \left\{\vec{E}^a \times \vec{H}^b - \vec{E}^b \times \vec{H}^a\right\}\cdot d\vec{s} &= A_{\hat{l}} \frac{i\pi\omega\varepsilon_0\rho_{ox}(1+\delta_{n0})}{k_{\hat{l}}} W(k_{\hat{l}}\rho_{ox}) \int_{z_{\rm bottom}}^{z_{\rm top}} \varepsilon_r \left[Q_{\hat{l}}(z)\right]^2 dz \\ &= A_{\hat{l}} \frac{4\omega\varepsilon_0}{k_{\hat{l}}^2} \left\langle Q_{\hat{l}} \,|\, \widetilde{\varepsilon_r} \,|\, Q_{\hat{l}} \right\rangle (1+\delta_{n0}). \end{aligned} \tag{5.63}$$

The TM volume integral couples the parasitic modes to the electric current,

$$\int_{z_{\rm bottom}}^{z_{\rm top}} \int_0^{2\pi} E_z^b J_z^a\, \rho_{ox}\, d\phi\, dz. \tag{5.64}$$

Explicitly calculating the current due to the LP lasing mode gives

$$\begin{aligned} J_z^{eq} &= \hat{z}\cdot(\hat{y}\times\hat{\rho})\frac{i}{\omega\mu_0} F(\rho)G'(z)\cos(m\phi) \\ &= -\frac{i}{2\omega\mu_0} F(\rho)G'(z)\left[\cos((m-1)\phi) + \cos((m+1)\phi)\right]. \end{aligned} \tag{5.65}$$

Substituting J_z^{eq} and E_z^- into (5.64) yields

$$\iiint_{\Omega_{\rm clad}} \left\{\vec{E}^b\cdot\vec{J}^a - \vec{H}^b\cdot\vec{M}^a\right\} dV = -\frac{i\rho_{ox}}{2\omega\mu_0} F(\rho_{ox}) H_n^{(1)}(k_{\hat{l}}\rho_{ox}) \left\langle \widetilde{G' \,|\, Q_{\hat{l}}} \right\rangle \Phi^{\rm TM}(\phi), \tag{5.66}$$

where

$$\Phi^{\rm TM}(\phi) \equiv \int_0^{2\pi} \left[\cos((m-1)\phi) + \cos((m+1)\phi)\right]\cos(n\phi)\, d\phi$$

$$= \begin{cases} 2\pi & m = 0,\ n = m+1 \\ \pi & m \geq 1,\ n = m+1 \\ 2\pi & m = 1,\ n = m-1 \\ \pi & m > 1,\ n = m-1 \end{cases} . \tag{5.67}$$

Setting the left hand side (5.63) equal to the right hand side (5.66), replacing $\Phi^{\mathrm{TM}}(\phi)$ with the corresponding sum of Kronecker delta functions, and solving for the coupling constant gives (5.68),

$$A_l^{\mathrm{TM}} = \frac{-i\pi k_l^2 \rho_{ox}}{8\omega^2 \mu_0 \varepsilon_0} \frac{\widetilde{\left\langle G' \mid Q_l \right\rangle}}{\widetilde{\left\langle Q_l \mid \varepsilon_r \mid Q_l \right\rangle}} F(\rho_{ox}) H_n^{(1)}(k_l \rho_{ox}) \left[\frac{\delta_{n(m+1)}(1+\delta_{m0}) + \delta_{n(m-1)}(1+\delta_{m1})}{1+\delta_{n0}} \right]. \tag{5.68}$$

The appearance of $H_n^{(1)}(k_l \rho_{ox})$ in (5.57) and (5.68) is at first disconcerting. One would assume the form of the test field would have no influence on the coupling. However, the analysis is not yet complete. To have any physical meaning A_l^{TE} and A_l^{TM} must be applied to the parasitic modes and the resulting *radiative loss* computed, as I show below.

5.4 Parasitic Mode Loss

The ultimate goal of the parasitic mode analysis is to determine the change in threshold gain from the WIM value due to diffraction. To do this, I define diffraction loss as *the eigenmode power coupled to the parasitic modes and radiated in the transverse direction.*

In the WIM solution, the calculated threshold gain $\left(g_{th}^{\mathrm{WIM}}\right)$ compensates for the absorption $\left(\alpha^{(\mathrm{absorption})}\right)$ and mirror $\left(\alpha^{(\mathrm{mirror})}\right)$ losses,

$$g_{th}^{\mathrm{WIM}} = \frac{1}{\Gamma^{\mathrm{tot}}} \left\{ \alpha^{(\mathrm{absorption})} + \alpha^{(\mathrm{mirror})} \right\}, \tag{5.69}$$

where Γ^{tot} is the total confinement factor. The *total* threshold gain, on the other hand, incorporates the absorption, mirror, *and* diffraction $\left(\alpha^{(\mathrm{diffraction})}\right)$ losses,

$$g_{th} = \frac{1}{\Gamma^{\mathrm{tot}}} \left\{ \alpha^{(\mathrm{absorption})} + \alpha^{(\mathrm{mirror})} + \alpha^{(\mathrm{diffraction})} \right\}. \tag{5.70}$$

As shown in Section 4.4.5 (4.29), the losses may be written in terms of the power dissipated $\left(P^{(\text{absorption})}, P^{(\text{mirror})}, P^{(\text{diffraction})}\right)$, the total stored field energy $(W_e + W_m)$, and the phase velocity (v_p) [7] as

$$\alpha^{(\text{source})} = \frac{P^{(\text{source})}}{v_p \left(W_e + W_m\right)}, \tag{5.71}$$

where source = absorption, mirror, or diffraction. By substituting the expressions for g_{th}^{WIM}, $\alpha^{(\text{absorption})}$, $\alpha^{(\text{mirror})}$, and $\alpha^{(\text{diffraction})}$ into g_{th} and rearranging, I may write the total threshold as

$$g_{th} = g_{th}^{\text{WIM}} \left(1 + \frac{P^{(\text{diffraction})}}{P^{(\text{absorption})} + P^{(\text{mirror})}}\right). \tag{5.72}$$

Equation (5.72) gives the perturbative adjustment to the WIM threshold gain required to capture diffractive loss[9]. The only remaining task is to calculate the three dissipated power terms.

To find the power terms, I follow a procedure similar to the one presented in Section 4.4.5. In this approach, I assume the total threshold gain compensates for the total power exiting the cylindrical volume of the VCSEL core,

$$\Omega_{\text{core}} \equiv [0, \rho_{ox}] \times [0, 2\pi] \times [z_{\text{bottom}}, z_{\text{top}}], \tag{5.73}$$

either through absorption or radiation out the ends or the side. The power absorbed due to material loss (for example, free carrier losses) results directly from the imaginary part of the field energy distribution. For a lossy region, ε_r is complex and the total (time averaged) power absorbed from the electric field is given by

$$P^{(\text{absorption})} = -\frac{1}{2} \iiint_{\Omega_{\text{core}}} \varepsilon_0 \,\text{Im}\left(\varepsilon_r\right) \left|\vec{E}^{\text{WIM}}\right|^2 dV, \tag{5.74}$$

where the $\text{Im}\left(\varepsilon_r\right) < 0$ for absorption. There is no corresponding magnetic field term since $\mu = \mu_0$ throughout the structure. Substituting in the explicit form for the LP mode (5.3),

[9] In the derivation of (5.72), I have implicitly assumed that the parasitic modes only contribute to $P^{(\text{diffraction})}$, and that the absorption and mirror loss are well described by the WIM results.

$P^{(\text{absorption})}$ is given in Dirac notation as

$$P^{(\text{absorption})} = -\frac{\pi\varepsilon_0}{2} \langle F \,|\, F \rangle_{\text{core}} \langle G \,|\, \text{Im}(\varepsilon_r) \,|\, G \rangle \, (1 + \delta_{m0}) \,. \tag{5.75}$$

Here

$$\langle F \,|\, F \rangle_{\text{core}} \equiv \int_0^{\rho_{ox}} |F|^2 \, \rho \, d\rho, \tag{5.76}$$

is the standard inner product over ρ in the *core* region, and $\langle G \,|\, \text{Im}(\varepsilon_r) \,|\, G \rangle$ is found via the standard inner product over z (2.26). The two radiated power terms are calculated from the (time averaged) integrated Poynting vector,

$$P^{(\text{radiation})} \equiv \frac{1}{2} \text{Re} \left[\iint_\Gamma \left(\vec{E} \times \vec{H}^* \right) \cdot d\vec{s} \right], \tag{5.77}$$

where the $*$ indicates the complex conjugate. For the mirror loss, the fields are the WIM lasing mode fields and $d\vec{s} = \pm\hat{z}\,\rho\,d\phi\,d\rho$: $+$ for the top surface, and $-$ for the bottom. Substituting in the LP modes gives

$$P_{\text{top}}^{(\text{mirror})} = -\frac{\pi}{2\omega\mu_0} \langle F \,|\, F \rangle_{\text{core}} \text{Re} \left[iG(z_{\text{top}}) \{G'(z_{\text{top}})\}^* \right] (1 + \delta_{m0}) \,, \tag{5.78}$$

$$P_{\text{bottom}}^{(\text{mirror})} = \frac{\pi}{2\omega\mu_0} \langle F \,|\, F \rangle_{\text{core}} \text{Re} \left[iG(z_{\text{bottom}}) \{G'(z_{\text{bottom}})\}^* \right] (1 + \delta_{m0}) \,, \tag{5.79}$$

and $P^{(\text{mirror})} = P_{\text{top}}^{(\text{mirror})} + P_{\text{bottom}}^{(\text{mirror})}$.

For the diffraction loss, the fields in (5.77) are the parasitic mode fields and $d\vec{s} = \hat{\rho}\,\rho\,d\phi\,dz$. The unconjugated parasitic mode orthogonality relation (5.49) is general[10], and is equally valid in the conjugated form. As a result, I neglect the cross terms and pull the summation of modes outside the integral in (5.77) to give

$$P^{(\text{diffraction})} = \sum_{l=1}^{N_{\text{PM}}} \frac{1}{2} |A_l|^2 \, \text{Re} \left[\int_0^{2\pi} \int_{z_{\text{bottom}}}^{z_{\text{top}}} \left(\vec{E}_l^{\text{PM}} \times \left(\vec{H}_l^{\text{PM}} \right)^* \right) \cdot \hat{\rho}\,\rho\,dz\,d\phi \right]$$

[10]The conjugated form of the orthogonality relation holds for nonabsorbing materials. The unconjugated form holds for nonabsorbing *and* absorbing materials. This implies the unconjugated form is a more general form, encompassing the conjugated form. See Chapter 31 of [70] for a detailed discussion of the relationship between the two forms.

$$= \sum_{l=1}^{N_{\rm PM}^{\rm TE}} P_l^{\rm TE} + \sum_{l=1}^{N_{\rm PM}^{\rm TM}} P_l^{\rm TM}, \tag{5.80}$$

where $N_{\rm PM} = N_{\rm PM}^{\rm TE} + N_{\rm PM}^{\rm TM}$. For the TE parasitic modes the integral kernel is $E_{\phi,l}^{\rm PM} \left(H_{z,l}^{\rm PM}\right)^*$. Substituting in the TE parasitic mode fields given in (5.21) and (5.46) yields

$$P_l^{\rm TE} = \left|A_l^{\rm TE}\right|^2 \frac{\pi\omega\mu_0\rho_{ox}}{2} \,{\rm Re}\left[\frac{i}{k_l} H_n^{(2)\prime}\left(k_l\rho_{ox}\right)\left\{H_n^{(2)}\left(k_l\rho_{ox}\right)\right\}^*\right] \left\langle Q_l \,|\, Q_l \right\rangle \left(1-\delta_{n0}\right). \tag{5.81}$$

Substituting in (5.57) for $A_l^{\rm TE}$ gives

$$\begin{aligned} P_l^{\rm TE} &= \frac{\pi^3 \left|k_l\right|^4 \rho_{ox}^3}{128\,\omega\mu_0} \,{\rm Im}\left[\frac{-1}{k_l} H_n^{(2)\prime}\left(k_l\rho_{ox}\right)\left\{H_n^{(2)}\left(k_l\rho_{ox}\right)\right\}^*\right] \left\langle Q_l \,|\, Q_l \right\rangle \left(1-\delta_{n0}\right) \\ &\quad \times \left|\frac{\left\langle \widetilde{G \,|\, Q_l} \right\rangle}{\left\langle \widetilde{Q_l \,|\, Q_l} \right\rangle} F(\rho_{ox}) H_n^{(1)}\left(k_l\rho_{ox}\right)\right|^2 \left[\delta_{n(m-1)} - \delta_{n(m+1)}\left(1+\delta_{m0}\right)\right]^2. \end{aligned} \tag{5.82}$$

Here I have used the identity ${\rm Re}\,(z) = {\rm Im}\,(iz)$. Similarly, for TM parasitic modes the integral kernel is -$E_{z,l}^{\rm PM} \left(H_{\phi,l}^{\rm PM}\right)^*$, where $E_z^{\rm PM}$ is given in (5.22) and $H_\phi^{\rm PM}$ is found via Faraday's law,

$$H_\phi(\rho,\phi,z) = \frac{-i\omega\varepsilon_0\varepsilon_r}{k^2}\left\{\frac{\partial}{\partial\rho} E_z(\rho,\phi,z)\right\}. \tag{5.83}$$

Substituting the TM parasitic mode fields into (5.80) yields

$$P_l^{\rm TM} = \left|A_l^{\rm TM}\right|^2 \frac{\pi\omega\varepsilon_0\rho_{ox}}{2} \,{\rm Re}\left[\frac{-i}{k_l^*} H_n^{(2)}\left(k_l\rho_{ox}\right)\left\{H_n^{(2)\prime}\left(k_l\rho_{ox}\right)\right\}^* \left\langle Q_l \,|\, \varepsilon_r^* \,|\, Q_l \right\rangle\right] \left(1+\delta_{n0}\right). \tag{5.84}$$

Substituting (5.68) for $A_l^{\rm TM}$ gives

$$\begin{aligned} P_l^{\rm TM} &= \frac{\pi^3 \left|k_l\right|^4 \rho_{ox}^3}{128\,\left(\omega\mu_0\right)^2 \omega\varepsilon_0} \,{\rm Im}\left[\frac{1}{k_l^*} H_n^{(2)}\left(k_l\rho_{ox}\right)\left\{H_n^{(2)\prime}\left(k_l\rho_{ox}\right)\right\}^* \left\langle Q_l \,|\, \varepsilon_r^* \,|\, Q_l \right\rangle\right] \\ &\quad \times \left|\frac{\left\langle \widetilde{G' \,|\, Q_l} \right\rangle}{\left\langle \widetilde{Q_l \,|\, \varepsilon_r \,|\, Q_l} \right\rangle} F(\rho_{ox}) H_n^{(1)}\left(k_l\rho_{ox}\right)\right|^2 \left[\delta_{n(m+1)}\left(1+\delta_{m0}\right) + \delta_{n(m-1)}\left(1+\delta_{m1}\right)\right]^2. \end{aligned} \tag{5.85}$$

I now have all the elements required to calculate the diffraction loss contribution to the total threshold gain. To gain a better physical insight into the diffraction effects, it is useful to first interpret the TE and TM diffraction power terms.

P_l^{TE} and P_l^{TM} may be simplified by approximating the Hankel functions with their asymptotic forms,

$$H_n^{(1)}(z) \sim \frac{e^{iz}}{\sqrt{z}} \quad \text{and} \quad H_n^{(2)}(z) \sim \frac{e^{-iz}}{\sqrt{z}}. \tag{5.86}$$

Substituting into the two TE terms gives,

$$\begin{aligned} \mathrm{Im}\left[\frac{-1}{k_l} H_n^{(2)\prime}(k_l\rho_{ox}) \left\{H_n^{(2)}(k_l\rho_{ox})\right\}^*\right] &\approx \mathrm{Im}\left[\frac{1}{k_l}\left(i + \frac{1}{2k_l\rho_{ox}}\right) \frac{e^{-ik_l\rho_{ox}}}{\sqrt{k_l\rho_{ox}}} \left\{\frac{e^{-ik_l\rho_{ox}}}{\sqrt{k_l\rho_{ox}}}\right\}^*\right] \\ &= \frac{e^{2\,\mathrm{Im}(k_l)\rho_{ox}}}{|k_l^3\rho_{ox}|}\left\{\mathrm{Re}(k_l) - \frac{\mathrm{Re}(k_l)\,\mathrm{Im}(k_l)}{|k_l|^2\,\rho_{ox}}\right\} \\ &\approx \frac{\mathrm{Re}(k_l)\; e^{2\,\mathrm{Im}(k_l)\rho_{ox}}}{|k_l^3\rho_{ox}|}, \end{aligned} \tag{5.87}$$

and

$$\left|H_n^{(1)}(k_l\rho_{ox})\right|^2 \approx \frac{e^{-2\,\mathrm{Im}(k_l)\rho_{ox}}}{|k_l\rho_{ox}|}. \tag{5.88}$$

The exact same result is obtained for the two TM terms. Plugging these results into P_l^{TE} and P_l^{TM} yields

$$\begin{aligned} P_l^{\mathrm{TE}} &\approx \frac{\pi^3\,\mathrm{Re}(k_l)\,\rho_{ox}}{128\,\omega\mu_0} \langle\, Q_l \,|\, Q_l \,\rangle \left| \frac{\left\langle \widetilde{G \,|\, Q_l} \right\rangle}{\left\langle \widetilde{Q_l \,|\, Q_l} \right\rangle} F(\rho_{ox}) \right|^2 \\ &\quad \times (1-\delta_{n0}) \left[\delta_{n(m-1)} - \delta_{n(m+1)}\,(1+\delta_{m0})\right]^2, \end{aligned} \tag{5.89}$$

$$\begin{aligned} P_l^{\mathrm{TM}} &\approx \frac{\pi^3\,\mathrm{Re}(k_l)\,\rho_{ox}}{128\,(\omega\mu_0)^2\,\omega\varepsilon_0} \langle\, Q_l \,|\, \mathrm{Re}(\varepsilon_r) \,|\, Q_l \,\rangle \left| \frac{\left\langle \widetilde{G' \,|\, Q_l} \right\rangle}{\left\langle \widetilde{Q_l \,|\, \varepsilon_r \,|\, Q_l} \right\rangle} F(\rho_{ox}) \right|^2 \\ &\quad \times \left[\delta_{n(m+1)}\,(1+\delta_{m0}) + \delta_{n(m-1)}\,(1+\delta_{m1})\right]^2. \end{aligned} \tag{5.90}$$

From (5.89) and (5.90), the role of the ρ and z functions becomes more clear. The Hankel functions effectively cancel, assuaging my earlier concern that the results may be incorrectly

influenced by my choice of "test" function $\left(H_n^{(1)}\right)$. The only remnant of the radial parasitic mode functions is the Re (k_l) term, which is a normal weighting term in the Poynting vector[11]. Moreover, this supports my earlier thesis that the Im (k_l) does not affect the radiated power calculation.

The $F(\rho_{ox})$ term weights the power by the lasing mode penetration into the cladding region, thereby explicitly incorporating the confinement factor. The axial inner products give an intuitive weighting factor due to the parasitic mode overlap with the lasing mode. Note that there is no need to normalize the parasitic modes, since any constant factor will cancel in the radiated power expressions. Similarly, the same comment holds for the lasing mode, as evidenced by (5.72). This is only logical: any normalization just scales the mode amplitude. Finally, the constants and delta functions are simply dimensional scaling factors necessary to couple the various LP_m lasing and $\mathrm{TE}_n/\mathrm{TM}_n$ parasitic modes. In the next chapter, I apply this approach to calculate threshold gains (Figure 6.3) and currents in actual VCSELs; I find the results agree qualitatively with experiments [33].

[11]This can be understood by considering a plane wave: $\vec{E} \sim e^{-ikz}$, $\vec{H} \sim \frac{k}{\omega\mu_0} e^{-ikz}$, which implies the Poynting vector $\vec{S} \sim \frac{k}{\omega\mu_0}$.

VI. Spontaneous Emission and Laser Analysis

Ultimately, an optical analysis is incomplete until it is coupled to a semiconductor gain model to calculate measurable lasing parameters. These are: light verses current, threshold current, and the percentage of the total spontaneous emission that couples into the lasing mode (β). In this chapter, I combine my weighted index LP mode calculation—including diffraction—with J.P. Loehr's gain model [42] to calculate the laser operating characteristics for a low threshold VCSEL [33] structure for various oxide aperture radii.

To estimate the spontaneous emission properties, I compute a set of three-dimensional cavity eigenmodes. For each mode, I find the energy ($\hbar\omega$), spatial field profile $\left(\vec{E}(\vec{r})\right)$, confinement factor ($\Gamma^{\text{tot}}$), and threshold gain ($g_{th}$). These modes are then applied to a *new* spontaneous emission model, tailored to incorporate the partial transverse confinement afforded by oxide apertures. In past approaches, the optical modes were either dealt with as a two dimensional continuum [10, 18, 44, 75], which is appropriate for VCSELs with *no* transverse confinement, or as a discrete set of modes of a fully enclosed three-dimensional cavity [4, 5, 73, 77], which is most relevant for etched posts. Since the oxide aperture only results in *partial* transverse field confinement, I model the mode structure as the median of the two extremes. I use a discrete mode sum, due to the WIM eigenmodes, superimposed on a background two- and three-dimensional density of (plane wave) modes to represent the complete set of photon states which interact with the gain media. This is analogous to modeling the continuum states of a quantum well as a three dimensional density of states *plus* a discrete set of resonances.

Steady-state light verses current curves are calculated by solving the photon and carrier multimode related rate equations using the LP eigenmodes, Loehr's gain model, and the spontaneous emission results. By extrapolating these curves, the threshold current is estimated and compared with measurement.

6.1 Test Structure

I perform the lasing mode analysis on the University of Texas's semiconductor-dielectric composite 980 nm VCSEL [31,33]. The $\lambda/2$ cavity is formed by $Al_{0.97}Ga_{0.03}As$ surrounding a single 80 Å $In_{0.20}Ga_{0.80}As$ quantum well sandwiched between pairs of 100 Å GaAs and 100 Å $Al_{0.67}Ga_{0.33}As$ barrier layers. The lower DBR is a 26 period n-type GaAs/AlAs DBR. The top DBR is a post-growth electron-beam deposited 5 period CaF-ZnSe dielectric DBR. A p^+-GaAs quarter wave cap layer is included between the cavity and the upper dielectric DBR for electrical contacting. The entire structure and the standing intensity pattern are illustrated in Figure 6.1. In my model, I used $n = 1.35$ and 2.54 for CaF and ZnSe, respectively. The index and free carrier loss data for the semiconductor materials are listed in Table 3.1, Chapter III.

Circular apertures are formed in this VCSEL by oxidizing the top $Al_{0.97}Ga_{0.03}As$ *cavity* layer. The fact the oxides lay within the cavity, a unique design approach, has been credited with the low thresholds obtained from this device. The nearness of the oxide to the quantum well suggests the aperture will have a strong impact on the emitted fields, making this structure an ideal test subject for my microcavity VCSEL analysis.

6.2 Optical Modes

Using the LP mode analysis of the previous chapter, I calculated the eigenmode data for the test VCSEL with oxide aperture radii ranging from 0.5 μm to 4.0 μm in 0.5 μm steps. For each radius I found the pertinent optical mode parameters for each discrete eigenmode. In Figures 6.2 – 6.4, I plot the mode energy, radial confinement factor, and threshold gain for the LP_{01} and LP_{11} eigenmodes as a function of aperture radius. The longitudinal confinement factor is roughly 0.02 for all cases.

As I have now come to expect, the mode energy blueshifts and the transverse confinement decreases with decreasing aperture radius. The higher order modes are less confined and blueshift more than the lower order modes. The order of magnitude and behavior of the calculated threshold gain with aperture radius is in good qualitative agreement with experiment. However, to determine the threshold current—the *true* threshold metric—I need to

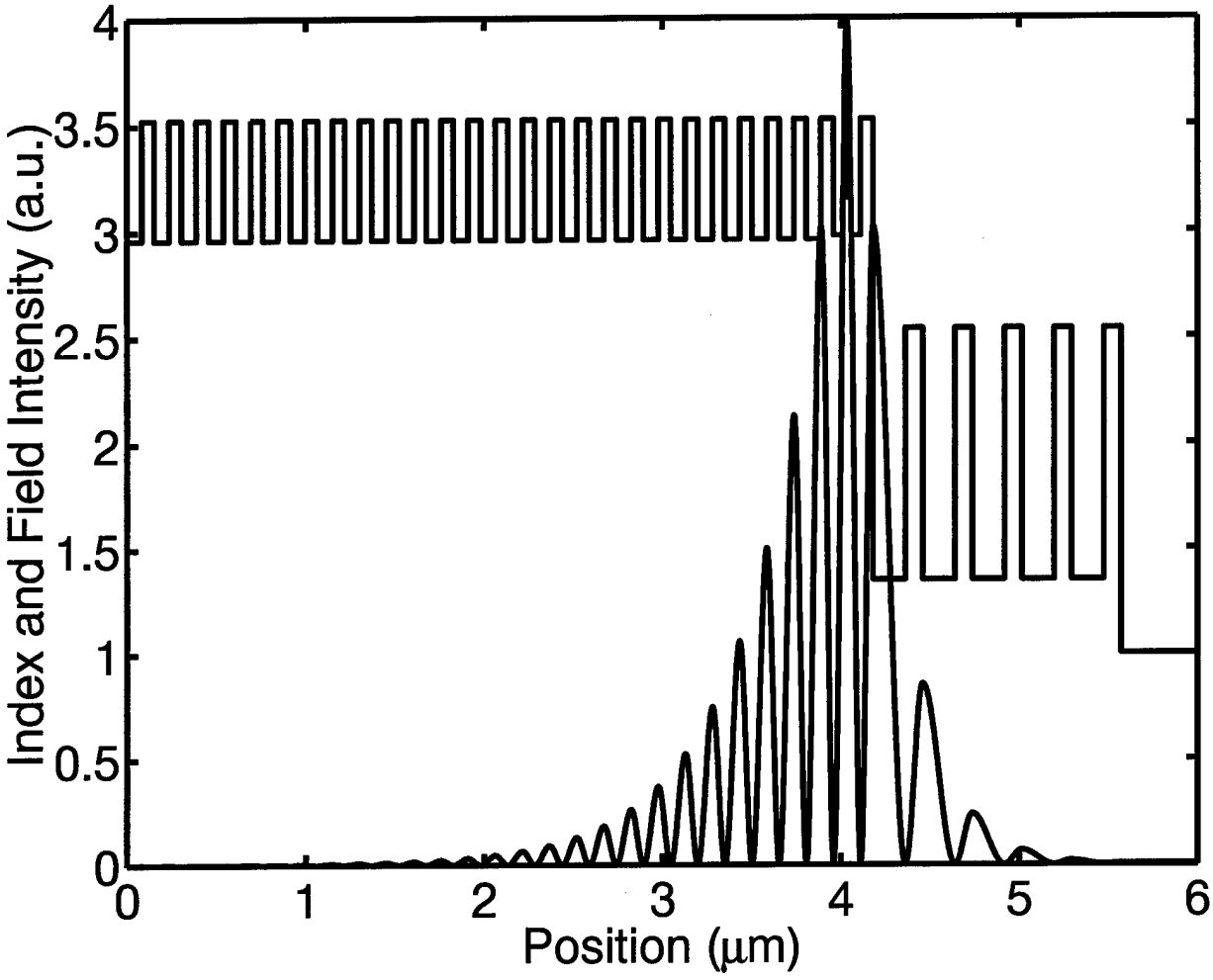

Figure 6.1 Index and standing intensity profile for the University of Texas's low threshold $\lambda/2$ cavity, dielectric DBR VCSEL.

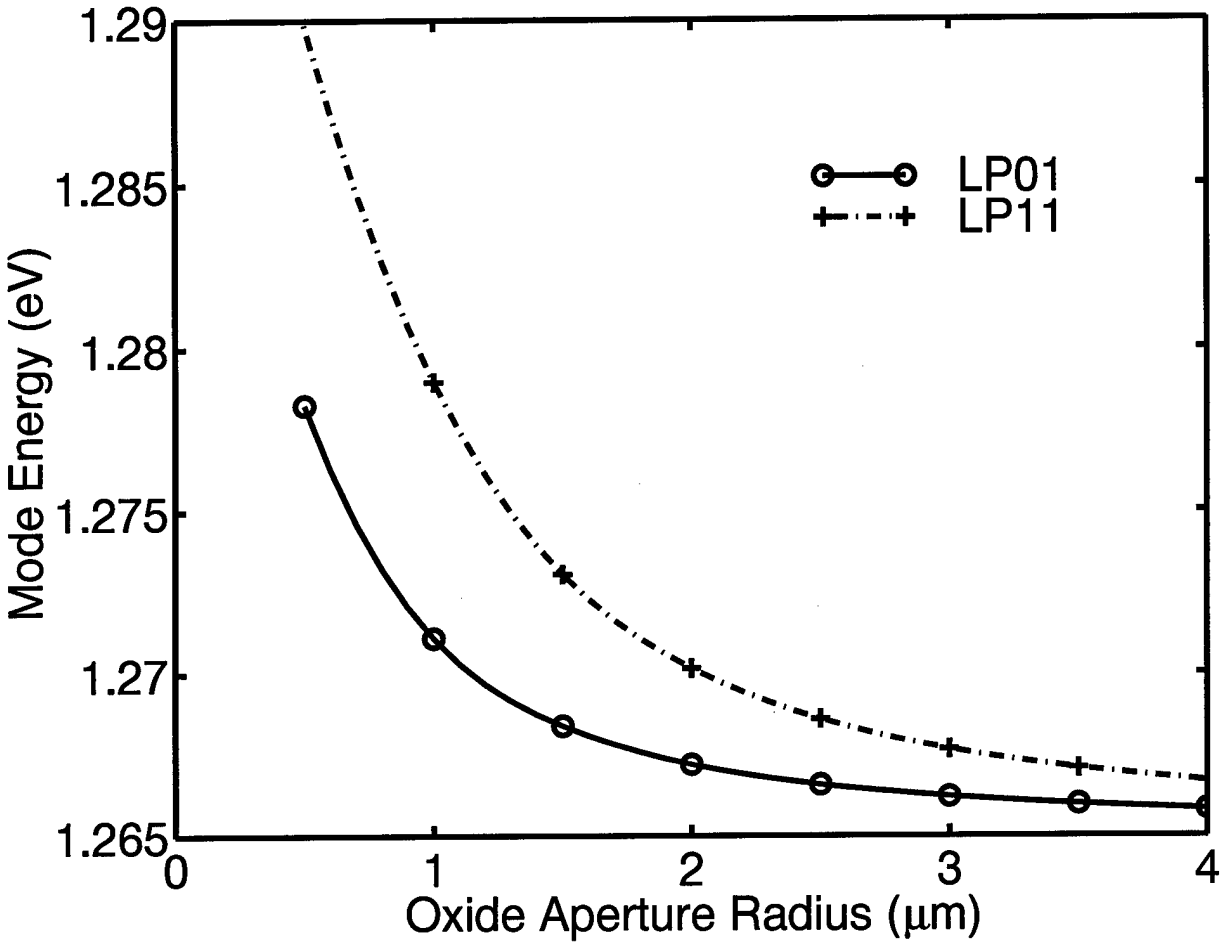

Figure 6.2 LP_{01} and LP_{11} mode energy vs radius. The solid and dashed curves are a cubic spline fit of the discrete data.

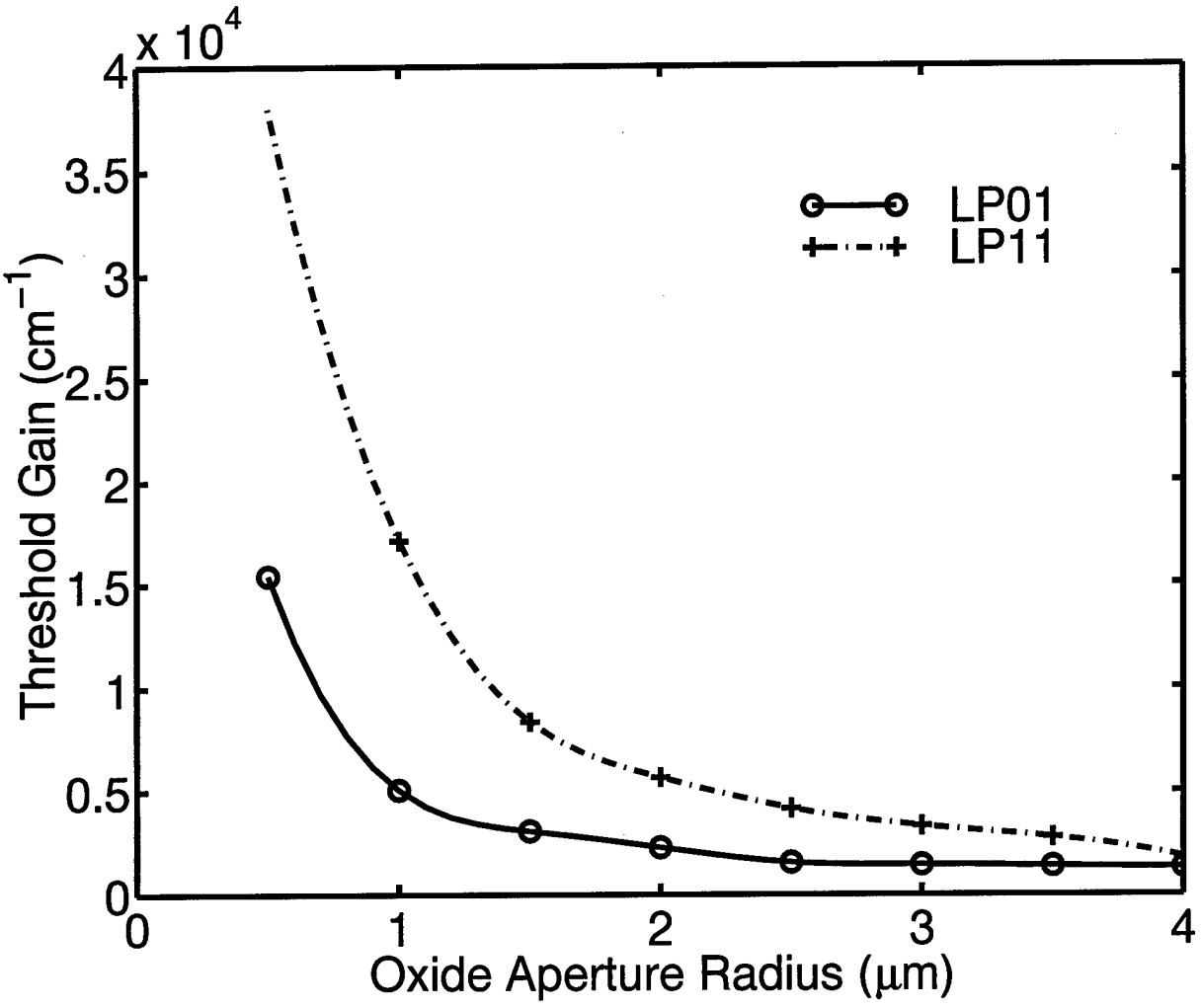

Figure 6.3 LP_{01} and LP_{11} mode threshold gain vs radius. The solid and dashed curves are a cubic spline fit of the discrete data.

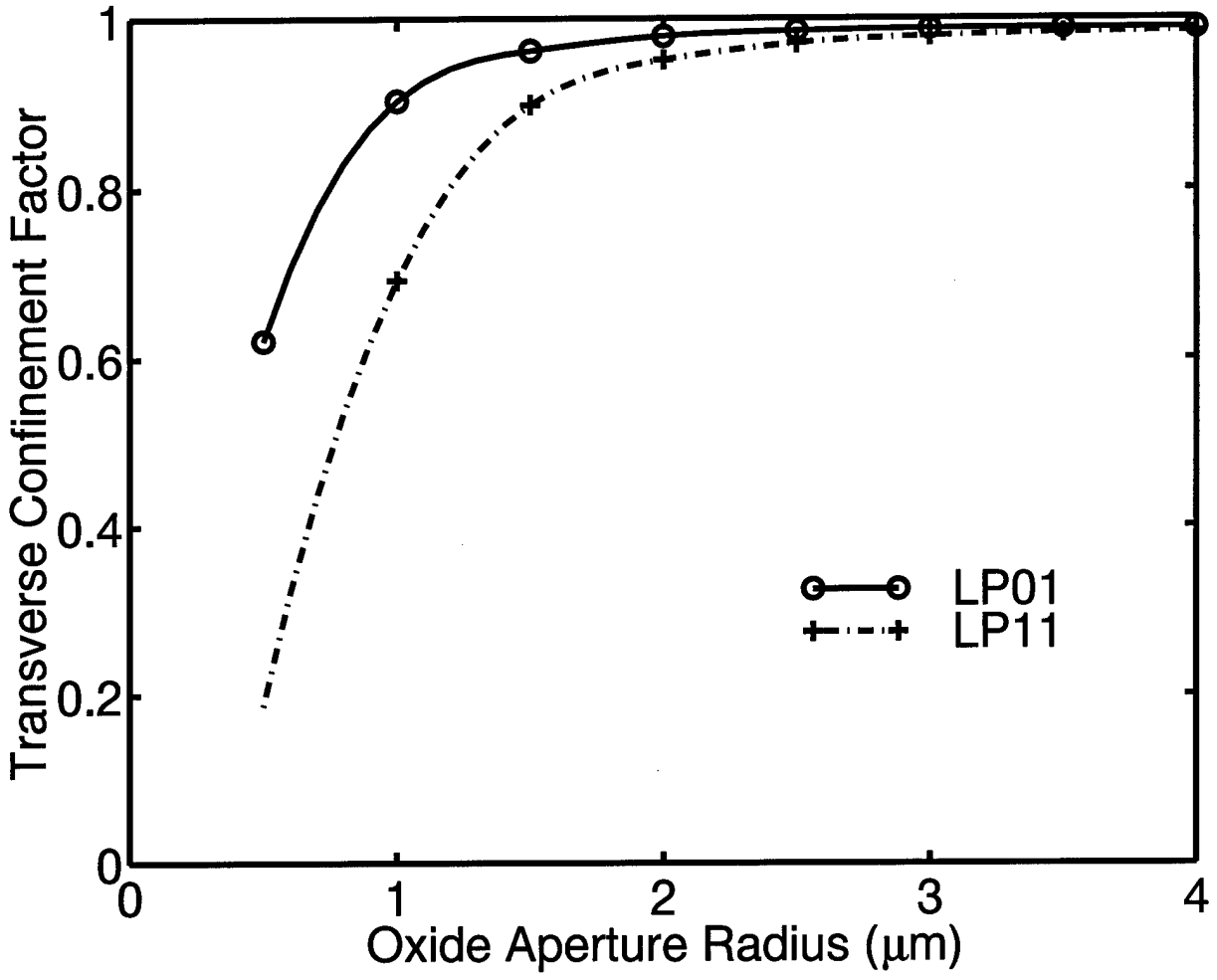

Figure 6.4 LP_{01} and LP_{11} mode transverse confinement factor vs radius. The solid and dashed curves are a cubic spline fit of the discrete data.

incorporate the eigenmodes with Loehr's quantum well gain results [42,43] into a full laser model. I do this in the next two sections.

6.3 Spontaneous Emission

Before I solve the related rate equations and compute the light verses current, I must calculate the spontaneous emission rate ($R_{\rm sp}$). To do this, I combine my WIM eigenmodes with Loehr's bandstructure and gain model. Spontaneous emission rates are then calculated using a new *hybrid* approach that combines emission into the photon continuum *and* emission into localized cavity eigenmodes. In both cases, the spontaneous emission rate is calculated using Fermi's golden rule [16,47].

To calculate optical emission and absorption rates, only transitions between the conduction subbands and the heavy- and light-hole states are considered; transitions to and from split-off bands are ignored. The quantum well material gain for a cavity eigenmode (m) (not to be confused with the field azimuthal mode number) with energy $\hbar\omega_m$ and (approximate) plane polarization $\hat{\boldsymbol{\epsilon}}_m$ is obtained using the standard single-particle gain expression [42]

$$\begin{aligned} g(\hat{\boldsymbol{\epsilon}}_m, \hbar\omega_m) \;=\; & \frac{4\pi^2 e^2 \hbar}{\eta c m_0^2 L \hbar\omega_m} \frac{1}{(2\pi)} \sum_{nn'} \frac{k_0}{\left| \frac{d}{dk} E_n^{(\mathrm{CB})}(k_0) - \frac{d}{dk} E_{n'}^{(\mathrm{HL})}(k_0) \right|} \\ & \times \left[f_e(E_n^{(\mathrm{CB})}(k_0), \mu_c) - f_e(E_{n'}^{(\mathrm{HL})}(k_0), \mu_v) \right] \\ & \times \sum_{\sigma\sigma'} \frac{1}{(2\pi)} \int_0^{2\pi} d\phi |\hat{\boldsymbol{\epsilon}}_m \cdot \mathbf{P}_{nn'}^{\sigma\sigma'}(k_0, \phi)|^2. \end{aligned} \tag{6.1}$$

Here η is the refractive index of the cavity, c is the speed of light, m_0 is the free electron mass, e is the electronic charge, L is the quantum well width, $f_e(E, \mu)$ is the Fermi-Dirac occupation function for electrons with energy E and chemical potential μ, and k_0 is defined by the energy-conservation condition

$$E_n^{(\mathrm{CB})}(k_0) - E_{n'}^{(\mathrm{HL})}(k_0) = \hbar\omega_m. \tag{6.2}$$

The *optical matrix elements* $\mathbf{P}^{\sigma\sigma'}_{nn'}(k_0,\phi)$ are given by

$$\mathbf{P}^{\sigma\sigma'}_{nn'}(\mathbf{k}_t) \equiv \sum_{j=\mathrm{HH}^\sigma,\mathrm{LH}^\sigma} \langle f^{(j)}_{n\mathbf{k}_t} | f^{(\mathrm{CB})}_{n'} \rangle \langle u_j | \mathbf{p} | u^{\sigma'}_{\mathrm{CB}} \rangle \tag{6.3}$$

where

$$\langle f^{(j)}_{n\mathbf{k}_t} | f^{(\mathrm{CB})}_{n'} \rangle \equiv \int dz f^{(j)*}_n(\mathbf{k}_t,z) f^{(\mathrm{CB})}_{n'}(z). \tag{6.4}$$

The functions $f^{(\mathrm{CB})}_n$ and $f^{(j)}_n$ refer to the envelope functions for electron and holes, respectively, in the quantum well; the corresponding energies are $E^{(\mathrm{CB})}_n$ and $E^{(\mathrm{HL})}_n$. The conduction (μ_c) and valence (μ_v) quasi-Fermi levels are set under high-level injection by forcing charge neutrality $n = p$ in the undoped quantum well: occupation of the continuum states above the barriers is also included.

The gain results are broadened by convolution with a 5 meV half-width Lorentzian lineshape function to obtain realistic gain spectra. Figure 6.5 shows the calculated material gain for plane-polarized (TE) modes. Since it is very difficult to calculate the exact peak gain wavelength, the peaks of the gain curves in Figure 6.5 are aligned with the energy of the lasing eigenmode by *a-posteriori* shifting of the gain spectrum.

The spontaneous emission rate for coupling to a three-dimensional photon continuum of plane waves is given by [42]

$$\begin{aligned} R^{(\mathrm{3D})}_{\mathrm{sp}}(\hbar\omega) \equiv\ & \frac{4\eta e^2\hbar\omega}{3m_0^2\hbar^2c^3}\frac{1}{(2\pi)}\sum_{nn'}\frac{k_0}{\left|\frac{d}{dk}E^{(\mathrm{CB})}_n(k_0)-\frac{d}{dk}E^{(\mathrm{HL})}_{n'}(k_0)\right|} \\ & \times f_e(E^{(\mathrm{CB})}_n(k_0),\mu_c)\left[1-f_e(E^{(\mathrm{HL})}_{n'}(k_0),\mu_v)\right] \\ & \times\sum_{\sigma\sigma'}\sum_{j=1,2,3}\frac{1}{(2\pi)}\int_0^{2\pi}d\phi|\hat{\mathbf{x}}_j\cdot\mathbf{P}^{\sigma\sigma'}_{nn'}(k_0,\phi)|^2. \end{aligned} \tag{6.5}$$

Similarly, the spontaneous emission rate for coupling to a *two*-dimensional photon continuum for emission in the $x-y$ plane, with the photon wavefunction localized to one wavelength

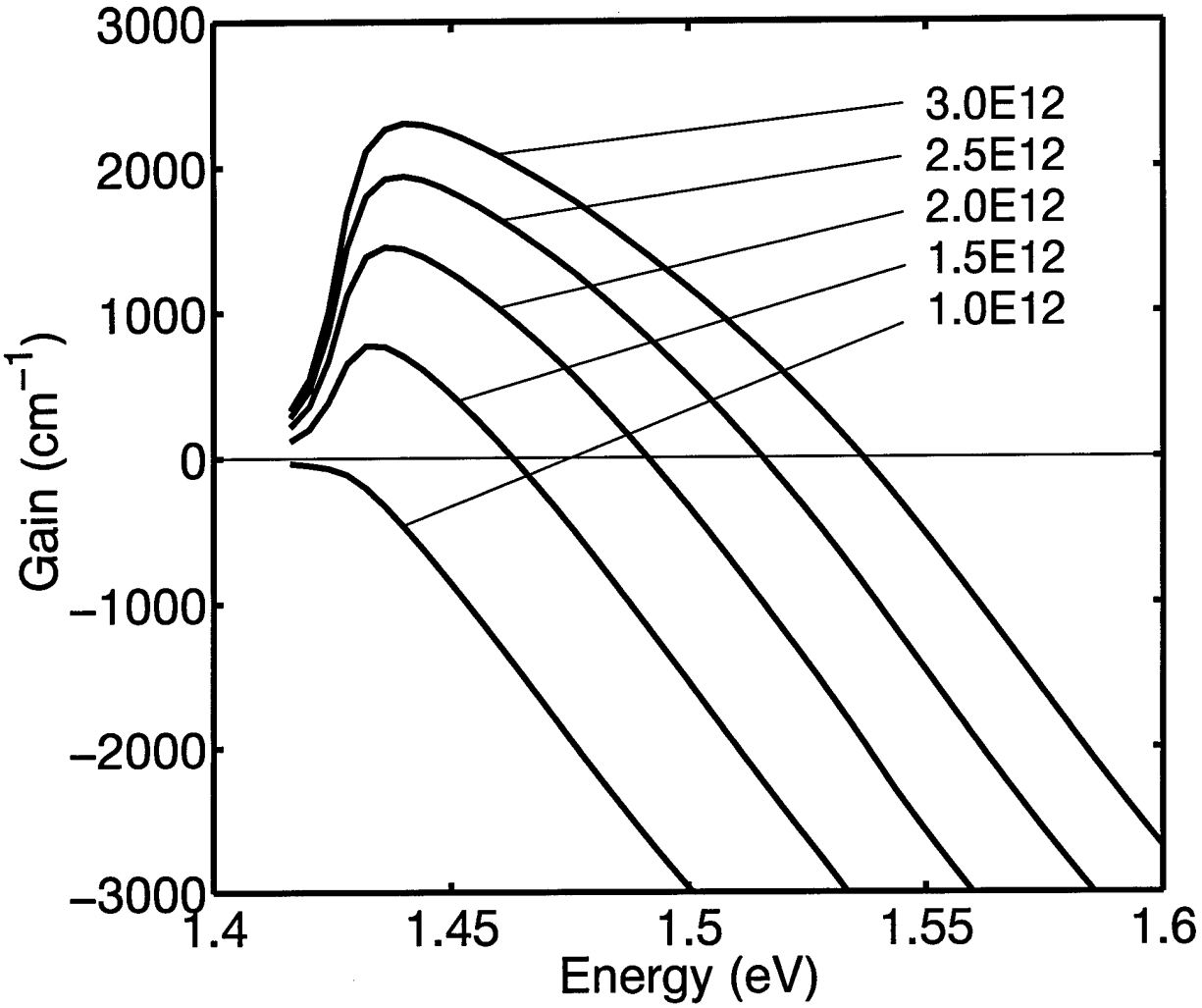

Figure 6.5 Material gain for an 80 Å $In_{0.2}Ga_{0.8}As/Al_{0.2}Ga_{0.8}As$ quantum well for various two-dimensional carrier densities (n).

along the z axis, may be calculated as

$$\begin{aligned} R_{\rm sp}^{(\rm 2D)}(\hbar\omega) \equiv & \frac{\eta e^2\hbar\omega}{2m_0^2\hbar^2c^3}\frac{1}{(2\pi)}\sum_{nn'}\frac{k_0}{\left|\frac{d}{dk}E_n^{(\rm CB)}(k_0)-\frac{d}{dk}E_{n'}^{(\rm HL)}(k_0)\right|} \\ & \times f_e(E_n^{(\rm CB)}(k_0),\mu_c)\left[1-f_e(E_{n'}^{(\rm HL)}(k_0),\mu_v)\right] \qquad (6.6) \\ & \times\sum_{\sigma\sigma'}\frac{1}{(2\pi)}\int_0^{2\pi}d\phi\left[|\hat{\mathbf{x}}\cdot\mathbf{P}_{nn'}^{\sigma\sigma'}(k_0,\phi)|^2+|\hat{\mathbf{y}}\cdot\mathbf{P}_{nn'}^{\sigma\sigma'}(k_0,\phi)|^2+2|\hat{\mathbf{z}}\cdot\mathbf{P}_{nn'}^{\sigma\sigma'}(k_0,\phi)|^2\right]. \end{aligned}$$

Essentially, this represents an estimate of the spontaneous emission into *all* parasitic modes, whether or not they are resonant with the eigenmode. Since the transitions in strained quantum wells occur predominantly between heavy hole bands, and since $\hat{\mathbf{z}}$-polarized light does not couple to pure heavy-hole states, the two rates may be related by the approximate ratio

$$R_{\rm sp}^{(\rm 2D)}(\hbar\omega)\approx\frac{3}{8}R_{\rm sp}^{(\rm 3D)}(\hbar\omega). \qquad (6.7)$$

Finally, I consider emission into the *localized* cavity eigenmodes (m) calculated in Section 6.2. Since I have already expended great effort to compute the electric field profiles of these modes, it is most useful to express the rate in terms of the average electric field $\langle E_m(0)\rangle$ at the center of the active region. In the dipole approximation, this rate can be calculated as

$$\begin{aligned} R_{\rm sp}^{(m)} \equiv & \frac{\hbar}{m_0^2(\hbar\omega)^2}|e\langle E_m(0)\rangle|^2\sum_{nn'}\frac{k_0}{\left|\frac{d}{dk}E_n^{(\rm CB)}(k_0)-\frac{d}{dk}E_{n'}^{(\rm HL)}(k_0)\right|} \qquad (6.8) \\ & \times f_e(E_n^{(\rm CB)}(k_0),\mu_c)\left[1-f_e(E_{n'}^{(\rm HL)}(k_0),\mu_v)\right] \qquad (6.9) \\ & \times\sum_{\sigma\sigma'}\frac{1}{(2\pi)}\int_0^{2\pi}d\phi|\hat{\boldsymbol{\epsilon}}_m\cdot\mathbf{P}_{nn'}^{\sigma\sigma'}(k_0,\phi)|^2. \end{aligned}$$

Note that this transition strength depends strongly on the "volume" $|\langle E_m(0)\rangle|^{-2}$ of the cavity eigenmode (m): smaller cavities will more tightly confine the mode and result in stronger transitions.

The total spontaneous emission rate will be a combination of 3D, 2D and localized mode emission. I assume that 2D photons are always present, since the vertical layer structure supports many (parasitic) guided modes that emit radially. Also, I assume that the 3D photon continuum begins once the photon energy exceeds that of the highest-energy cavity mode, which I denote by E_{3D}. Thus, I approximate the total spontaneous emission rate as

$$R_{sp}^{(TOT)}(n) = \sum_m R_{sp}^{(m)} + \int_0^{E_{3D}} d(\hbar\omega) R_{sp}^{(2D)}(\hbar\omega) + \int_{E_{3D}}^{\infty} d(\hbar\omega) R_{sp}^{(3D)}(\hbar\omega). \tag{6.10}$$

Here I have explicitly indicated that $R_{sp}^{(TOT)}$ depends on the quantum well carrier concentration n through the electron occupation function f_e.

6.4 Related Rate Equations

The optical gain, spontaneous emission, stimulated emission, injected *radiative* current (J_{rad}), and carrier concentration are linked by the *multimode related rate equations* [11,42],

$$\frac{dS_m}{dt} = \frac{c}{\eta}\left[\Gamma_m g(\hat{\epsilon}_m, \hbar\omega_m) - \alpha_m\right] S_m - R_{sp}^{(m)}, \tag{6.11}$$

$$\frac{dn}{dt} = \frac{J_{rad}}{e} - R_{sp}^{(TOT)}(n) - \frac{c}{\eta}\sum_m \Gamma_m g(\hat{\epsilon}_m, \hbar\omega_m) S_m. \tag{6.12}$$

Here S_m is the photon density *inside* the cavity for a localized mode m. Since the two-or three-dimensional continuum photons immediately leave the cavity after they are emitted, I assume that none of these can build up significant density. Because I consider very small cavity volumes, at most a few dozen localized cavity modes (m) are considered in (6.11) and (6.12).

I solve these rate equations only in steady-state. In this case, the left-hand-sides of (6.11) and (6.12) are both zero, and I immediately solve (6.11) for S_m, obtaining

$$S_m = \frac{R_{sp}^{(m)}(n)}{\frac{c}{\eta}\left[\alpha_m - \Gamma g(\hat{\epsilon}_m, \hbar\omega_m)\right]}. \tag{6.13}$$

By substituting this expression—for each mode m—into the steady-state equation (6.12), I obtain

$$J_{\text{rad}}(n) = e\left\{R_{\text{sp}}^{(\text{TOT})}(n) + \sum_m \frac{R_{\text{sp}}^{(m)}(n)\Gamma_m g(\hat{\epsilon}_m, \hbar\omega_m)}{[\alpha_m - \Gamma_m g(\hat{\epsilon}_m, \hbar\omega_m)]}\right\}. \tag{6.14}$$

By inverting (6.14) I compute $n(J_{\text{rad}})$ and, in turn, $S_m(J_{\text{rad}})$ via (6.13). Finally, I convert the modal photon densities *inside* the cavity to the total optical power P_{out} emitted *from* the cavity by computing

$$P_{\text{out}} = \pi r^2 \sum_m S_m(J_{\text{rad}})\hbar\omega_m \frac{c}{\eta}\alpha_m^{(\text{mirror})}, \tag{6.15}$$

where r is the cavity radius. (I include emission out of both the top and bottom mirrors.) To relate the laser current I to the current density J_{rad}, I consider the best-case scenario, ignoring carrier leakage, nonradiative recombination, and current spreading, and write

$$I = \pi r^2 J_{\text{rad}}. \tag{6.16}$$

By combining (6.15) and (6.16), I plot the light (P_{out}) verses current (I) for a variety of cavity radii in Figure 6.6.

My calculated light verses current curves give good agreement with measured thresholds. The measured threshold current in a 2 μm square aperture VCSEL fabricated from this layer structure is 91 μA [33]. My results underestimate this number by roughly a factor of three. My "best case" analysis is most likely to blame for this disparity; I may also have underestimated the free-carrier absorption losses. Note that the curvature near threshold becomes more pronounced as the radius decreases, indicating that a greater fraction of spontaneous emission is coupled into the lasing mode. Likewise, the external quantum efficiency decreases sharply for the smallest devices, indicating that much of the optical power is lost to diffraction.

By evaluating the fraction of the total emission that enters the lasing mode at "threshold"—which can be ambiguous [9]—I compute the spontaneous emission factor β as

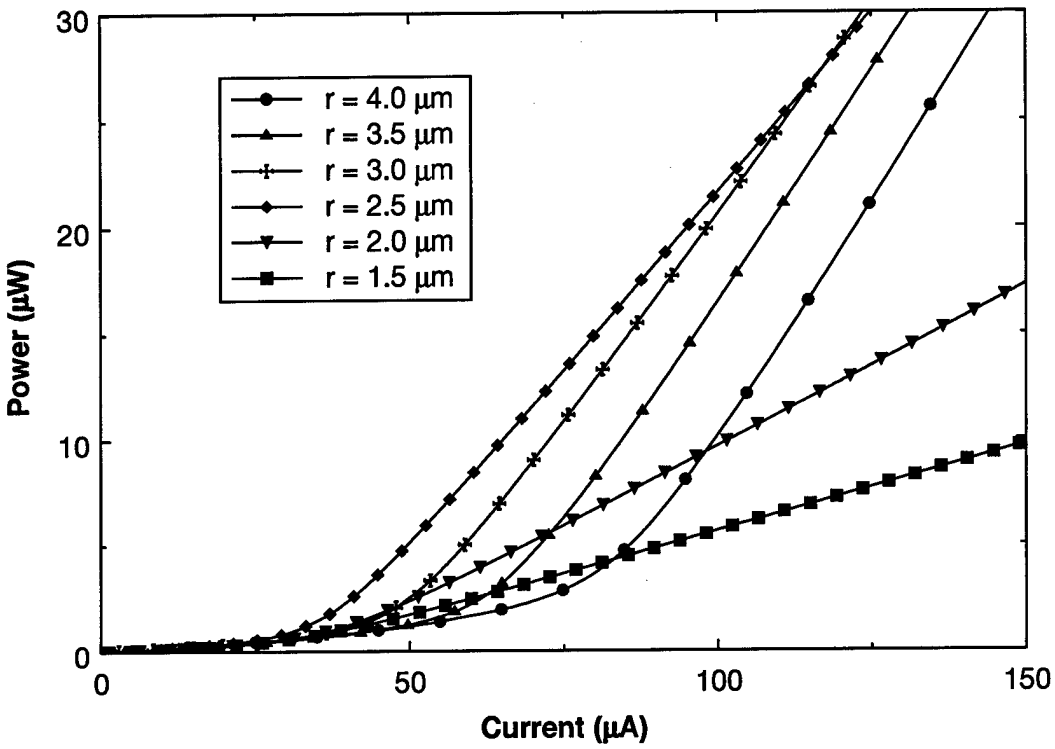

Figure 6.6 Output power (from both mirrors) verses current for various device radii.

$$\beta \equiv \frac{R_{\rm sp}^{(\rm lasing)}(n_{th})}{R_{\rm sp}^{(\rm TOT)}(n_{th})}. \tag{6.17}$$

In Figure 6.7 I plot β as a function of cavity radius. Note that even though β increases significantly as the cavity radius shrinks from 4 μm to 1.5 μm, it still does not approach unity even for $r = 1.5$ μm. The reason for this is that there is always significant coupling to the two-dimensional "parasitic" continuum of photons radiating out through the DBR layers. The only way to eliminate this coupling would be to fabricate a completely separable structure with very high transverse confinement, such as the design discussed in Section 5.3. Then the coupling to the two-dimensional modes would be eliminated, and $\beta \approx \frac{1}{2}$ operation could become possible. (If the fundamental mode is degenerate, as is usually the case, then $\frac{1}{2}$ is an upper bound for β.)

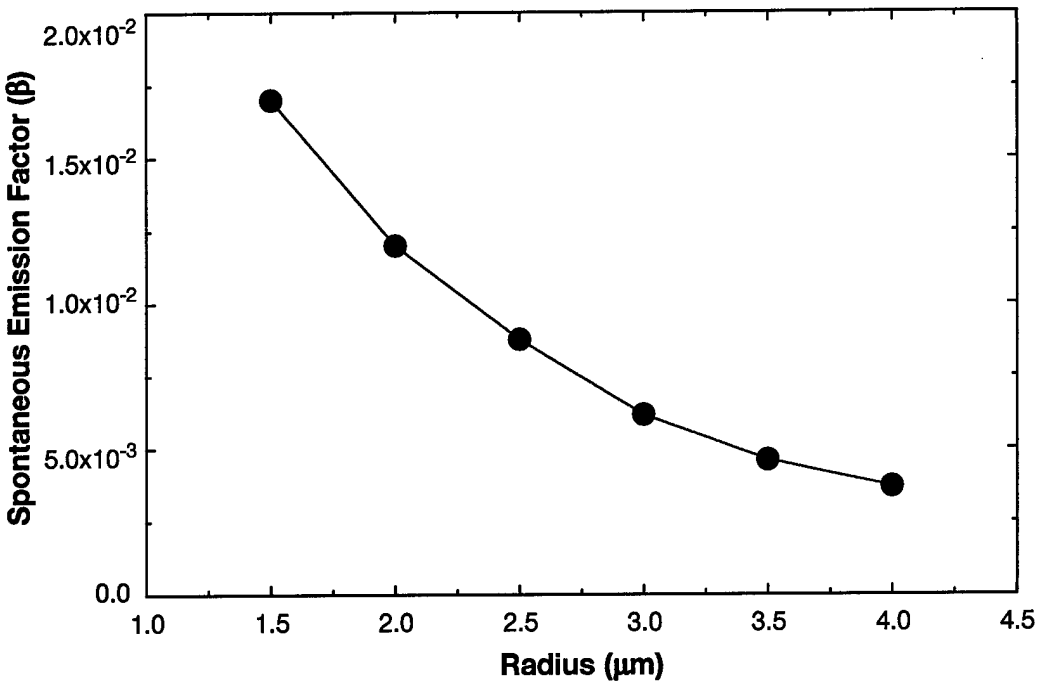

Figure 6.7 Spontaneous emission factor (β) verses device radius.

VII. Conclusions and Recommendations

7.1 Review of Present Work

The first vertical cavity surface emitting laser was reported in 1979 [71]. Since then, work has increased exponentially [17], with whole conference sessions and journal special editions dedicated to these devices. Much of the appeal of these devices over their in-plane counterparts results from their radically different, and in several respects improved, operating characteristics, better suiting them to many applications. This fact has only recently been recognized by the commercial community, which is just now adopting VCSELs for products such as print-heads and local communication fiber sources.

Despite their potential, these devices have not yet been optimized, and the ideal device has not yet been designed, let alone built. In fact, the VCSEL fabrication technology is just now maturing to the point where a discussion on ideal device design is reasonable. The latest (and perhaps last?) major advancement occurred when the University of Texas [33] researchers integrated an oxide aperture layer into the structure. Electrically, the oxide is insulating, and can provide excellent current confinement. Optically, the oxide index is lower than its host crystal. This index difference may provide index guiding, or perhaps optical scattering loss to the lasing mode. This dual nature of the oxide—providing waveguiding and/or scattering—has created substantial confusion with respect to VCSEL design. The primary goal of this thesis is to resolve this issue by understanding the physics of the oxide aperture within the VCSEL cavity. By constructing several optical models, I have explained the seemingly opposite reports on oxide effects and optimal oxide design, and have derived simple rules for low threshold VCSEL design.

Mathematically, the optical problem is a complex, second order, linear, boundary value problem. The principal difficulty arises from the fact that the governing differential equations are not separable in any coordinate system, greatly frustrating analytic solutions. Simple Fabry-Perot models, the staple of most semiconductor laser analysis, break down in the interesting realm of small, highly confining oxide apertures. For my first approach at solving this problem accurately, but economically, I employed a variational technique: the

weighted index method. In this technique the best separable solution is found in a variational sense. This iterative method converges on an "eigenmode" by alternately solving two coupled one-dimensional integro-differential equations. The seed for the search is the standard Fabry-Perot solution. Limiting my analysis to azimuthally symmetric structures, I used this technique to solve the full vector Helmholtz equation to calculate the basic optical lasing parameters: wavelength, confinement factor, and spatial field distribution for the fundamental and higher order lasing modes.

From the full vector weighted index analysis I was able to uncover two new effects: a polarization dependent change in mirror reflectance—previously only noted in edge-emitting lasers—and a change in spectral separation of the lasing modes with oxide aperture size and radius. The spectral mode separation results from the dispersion in blueshift rate with aperture size between the various cavity modes. I confirmed the blueshift by comparison with experiment for two different devices. My results matched the measurements better than any previous calculations. The spectral separation led me to a new concept for achieving low threshold, single mode lasing. In my approach, a spectrally sharp gain region is coupled to the modes of a highly confined VCSEL. For a sufficiently small and highly confined VCSEL, all but the lowest order lasing mode will be blueshifted away from the gain region, and only a single mode will lase. Ideally, the device would be made as small as possible for maximum mode separation. However, such small devices suffer enormous diffraction losses, *unless* a truly separable device geometry could be fabricated. In a separable structure, the cavity eigenmodes would theoretically suffer *no* diffraction and, ignoring absorption losses, the ultimate quantum optical threshold limit could be achieved. In this case, the polarization dependent change in mirror reflectivity predicted by the weighted index method may actually be observed.

Since the weighted index method is incapable of addressing diffraction on its own, I also employed a *quasi-exact* computational electromagnetic technique—the finite element method. My implementation of the finite element method employed new body-of-revolution, second-order vector edge and node elements. With the finite element method I was able to capture *all* of the VCSEL optical parameters, including the elusive diffractive loss. By

applying my model to a novel high index confinement VCSEL, I was able to discover the fundamental mechanisms governing diffraction in apertured VCSELs. These are:

1. The density of parasitic modes in the spectral vicinity of the eigenmode.
2. The relative alignment between the eigenmode and parasitic mode propagation vectors.
3. The transverse confinement of the optical mode to the core region.

These three factors may be used to qualitatively explain both the University of California at Santa Barbara and University of Texas group's oxide design results. The Santa Barbara group has suggested that thinner oxides placed at standing wave nodes are superior [29,30]. They consider semiconductor DBR VCSELs with longer effective cavity lengths and relatively large parasitic mode densities, approaching the three-dimensional density of modes. As a result, even weak coupling to the parasitic mode continuum will yield a large diffractive loss, implying that thinner oxides are better. The Texas group works with a VCSEL with one semiconductor and one dielectric DBR [20]. In their case, the cavity and corresponding optical density of modes is much smaller, and the confinement aspect of their oxide aperture is the dominant effect. Hence, they prefer thick oxides at standing wave peaks near the gain region.

The success of the parasitic mode picture in describing diffraction loss prompted me to try and incorporate these modes within the weighted index formalism. I successfully accomplished this by coupling a set of resonant parasitic modes to the eigenmode using a rigorous electromagnetic treatment of the coupling. In this treatment the implicit source of the parasitic modes is the weighted index method mode error. In the process of incorporating the parasitic modes, I simplified my weighted index model to a scalar solution. This resulted in a huge savings in complexity and computational effort with little cost in accuracy. The only real cost was that the scalar model forfeits the change in mirror reflectivity. But since this has not yet been observed, this was not much of a sacrifice. The advantages of this new approach are immense. The weighted index/parasitic mode calculation should provide the best semianalytic optical solution for apertured VCSELs, incorporating all the pertinent

physics within the field solution. Furthermore, it is fast and does not require a supercomputer to run, a distinct advantage over my finite element calculation.

Of course, you can model optical physics until you are blue in the face, but you won't raise an experimentalist's eyebrow until you can compute *measurable* device parameters. For this, I combined my optical data with Loehr's gain model and a new emission model containing both a sum of discrete modes and an integral over both a two- and three-dimensional continuum. This approach is designed to capture the incomplete confinement effects of oxide apertured devices. The full laser model was applied to the University of Texas's low threshold VCSEL [33] to compute all the standard laser parameters: light verses current, lasing threshold, and beta factors. My results are in good qualitative agreement with their measurements, differing by no more than a factor of three. They provide a good initial validation of the new emission model and my new weighted index/parasitic mode computation.

7.2 Suggestions for Future Study

As is often the case in research, for every door you shut two more open. Indeed, staying focused on a specific task may be the most challenging aspect of research. I certainly found this to be the case, with many research avenues presenting themselves to me through the course of my work. Having completed my dissertation, I feel that I now have the perspective to see where my work fits into the general body of knowledge, and to recommend future studies.

A model should pass through three distinct phases: derivation, validation, and application; I have completed the first phase and have just begun the second. Therefore, I suggest the following course of action. First, my two models should be comprehensively tested against one another. Before this can be accomplished, however, the finite element linear algebra solver must be revamped to address larger problems. Second, both models should be tested against experiment for threshold predictions. Along the same lines, the complete VCSEL model must be tested and refined to improve its overall accuracy. Third, the models should all be applied to optimize the VCSEL threshold. This is pretty much the

whole point of the work: the ultimate goal is to design a better device and take another step towards the "thresholdless grail."

Appendix A. Variational Justification of the WIM

The weighted index method (WIM) allows me to compute a separable, approximate solution to a two dimensional partial differential equation. In this appendix, I use the calculus of variations to demonstrate that the WIM solution represents the *best* separable approximation to the two-dimensional, azimuthally-symmetric Helmholtz equation.

I wish to solve

$$\left\{\nabla^2_{\rho,z} + \left(\frac{\omega^2}{c^2}\varepsilon_r(\rho,z) - \frac{m^2}{\rho^2}\right)\right\}\psi(\rho,z) = 0, \tag{A.1}$$

where $\nabla^2_{\rho,z}$ denotes the Laplacian with respect to the radial and axial coordinates and $\varepsilon_r(\rho,z)$ is the relative permittivity. Equation (A.1) is a Sturm-Liouville differential equation [3] of the form $\mathcal{L}\psi = 0$ with zero-Dirichlet boundary conditions at $\rho = \infty$, zero-Dirichlet ($m \neq 0$) or Neumann ($m = 0$) boundary conditions at $\rho = 0$, and zero-Robin (mixed Dirichlet/Neumann) boundary conditions at $z = \pm\infty$ (radiation conditions) [7].

I solve (A.1) variationally by forming a functional $\mathbb{J}[\psi]$ that, when extremized over the space of admissible functions $\psi(\rho,z)$, minimizes the Hilbert space distance

$$\int_{-\infty}^{\infty}\int_{0}^{\infty} |\psi(\rho,z) - \psi_{\text{exact}}(\rho,z)|^2 \rho\, d\rho dz. \tag{A.2}$$

Here ψ_{exact} denotes the exact solution to (A.1) [64]. I refer to the particular function minimizing (A.2) as the *best* variational solution. The variation $\delta\mathbb{J}[\psi]$ is given by

$$\delta\mathbb{J}[\psi] = \left\langle \delta\psi \,\middle|\, \left\{\nabla^2_{\rho,z} + \left(\frac{\omega^2}{c^2}\varepsilon_r(\rho,z) - \frac{m^2}{\rho^2}\right)\right\} \,\middle|\, \psi \right\rangle =$$
$$\left\langle \delta\psi \,\middle|\, \nabla^2_{\rho,z} \,\middle|\, \psi \right\rangle + \frac{\omega^2}{c^2}\left\langle \delta\psi \,\middle|\, \varepsilon_r(\rho,z) \,\middle|\, \psi \right\rangle - m^2\left\langle \delta\psi \,\middle|\, \rho^{-2} \,\middle|\, \psi \right\rangle = 0, \tag{A.3}$$

where the appropriately-weighted inner-product for this geometry is

$$\langle A \,|\, B \rangle = \int_{-\infty}^{\infty}\int_{0}^{\infty} (A^* B)\rho\, d\rho dz. \tag{A.4}$$

Integrating the first term on the second line of (A.3) by parts yields

$$\delta\mathbb{J}[\psi] = \frac{\omega^2}{c^2}\left\langle \delta\psi \,|\, \varepsilon_r(\rho,z) \,|\, \psi \right\rangle - m^2 \left\langle \delta\psi \,|\, \rho^{-2} \,|\, \psi \right\rangle - \left\langle \nabla_{\rho,z}\delta\psi \,|\, \nabla_{\rho,z}\psi \right\rangle = 0, \tag{A.5}$$

where the surface terms drop out for bound modes. Then $\mathbb{J}[\psi]$ is found by bringing the variational operator outside the inner-products to yield

$$\begin{aligned}\mathbb{J}[\psi] &= \frac{1}{2}\left[\frac{\omega^2}{c^2}\left\langle \psi \,|\, \varepsilon_r(\rho,z) \,|\, \psi \right\rangle - m^2 \left\langle \psi \,|\, \rho^{-2} \,|\, \psi \right\rangle - \left\langle \nabla_{\rho,z}\psi \,|\, \nabla_{\rho,z}\psi \right\rangle\right] \qquad \text{(A.6)} \\ &= \frac{1}{2}\left[\frac{\omega^2}{c^2}\int_{-\infty}^{\infty}\int_0^{\infty}\left\{\varepsilon_r(\rho,z)|\psi|^2\right\}\rho\, d\rho dz - \int_{-\infty}^{\infty}\int_0^{\infty}\left\{\left|\frac{\partial\psi}{\partial\rho}\right|^2 + \left|\frac{\partial\psi}{\partial z}\right|^2 + \frac{m^2}{\rho^2}|\psi|^2\right\}\rho\, d\rho dz\right].\end{aligned}$$

I now search for the optimal function ψ that extremizes $\mathbb{J}$, i.e. that gives $\delta\mathbb{J}[\psi] = 0$. This procedure yields differential equations of constraint—the Euler equations—on ψ. If I allowed ψ to range over the complete space of complex two dimensional functions, the constraint equation would be (A.1) and the whole exercise would be useless. However, by restricting the functional domain of ψ I can generate different constraint equations. In particular, I can find the best *separable* solution by taking the variation of (A.6) while restricting ψ to the space of all separable functions

$$\psi(\rho,z) = F(\rho)G(z). \tag{A.7}$$

To generate constraint equations for F and G, I take the total variation $\Delta\mathbb{J}[F,G]$. This is given by [23]

$$\Delta\mathbb{J}[F,G] = \mathbb{J}[F+\tilde{f}, G+\tilde{g}] - \mathbb{J}[F,G], \tag{A.8}$$

where $\tilde{f}$ and $\tilde{g}$ are incremental deviations from F and G. The first variation ($\delta\mathbb{J}$) is the principal part of the total variation given above. Substituting $F+\tilde{f}$ and $G+\tilde{g}$ appropriately into (A.6) and then taking the principal part (the part involving single terms of $\tilde{f}$ and $\tilde{g}$ to the first power) yields

$$\begin{aligned}\delta\mathbb{J}[F,G] \;=\; &\int_{-\infty}^{\infty}\int_0^{\infty}\left\{\left[\frac{\omega^2}{c^2}\varepsilon_r(\rho,z) - \frac{m^2}{\rho^2}\right]\left(F\tilde{f}G^2 + F^2G\tilde{g}\right) - \right. \qquad \text{(A.9)} \\ &\left.\left(F'\tilde{f}'G^2 + F^2G'\tilde{g}' + F\tilde{f}(G')^2 + (F')^2G\tilde{g}\right)\right\}\rho\, d\rho dz,\end{aligned}$$

where the prime denotes differentiation with respect to the argument. Integrating by parts and applying the appropriate Dirichlet and Neumann boundary conditions on $F(\rho)$ and $G(z)$, I remove the derivatives from $\tilde{f}$ and $\tilde{g}$ to yield

$$\begin{aligned}\delta\mathbb{J}[F,G] = & \\ \int_0^\infty \left[\int_{-\infty}^\infty \left\{\left[\frac{\omega^2}{c^2}\varepsilon_r(\rho,z) - \frac{m^2}{\rho^2}\right] FG^2 - F(G')^2 + \frac{1}{\rho}(\rho F')' G^2\right\} dz\right] \tilde{f}\,\rho\,d\rho & \\ + \int_{-\infty}^\infty \left[\int_0^\infty \left\{\left[\frac{\omega^2}{c^2}\varepsilon_r(\rho,z) - \frac{m^2}{\rho^2}\right] F^2G - (F')^2G + F^2G''\right\} \rho\,d\rho\right] \tilde{g}dz. &\end{aligned} \tag{A.10}$$

Since either $\tilde{f}(\rho)$ or $\tilde{g}(z)$ may equal zero, this implies that both the first and second terms must independently equal zero to extremize $\mathbb{J}[\hat{\psi}]$. Thus I generate from (A.11) the two independent variational equations:

$$F\int_{-\infty}^\infty \left\{\left[\frac{\omega^2}{c^2}\varepsilon_r(\rho,z) - \frac{m^2}{\rho^2}\right] G^2(z) - (G'(z))^2\right\} dz + \frac{1}{\rho}(\rho F')' \int_{-\infty}^\infty G^2(z)dz = 0, \tag{A.11}$$

and

$$G\int_0^\infty \left\{\left[\frac{\omega^2}{c^2}\varepsilon_r(\rho,z) - \frac{m^2}{\rho^2}\right] F^2 - (F')^2\right\} \rho\,d\rho + G''\int_0^\infty F^2\rho\,d\rho = 0. \tag{A.12}$$

Employing the axial and radial inner-products

$$\langle G \,|\, G\rangle = \int_{-\infty}^\infty |G|^2\,dz \tag{A.13}$$

and

$$\langle F \,|\, F\rangle = \int_0^\infty |F|^2\rho\,d\rho, \tag{A.14}$$

I can rewrite (A.11) and (A.12) as

$$\frac{1}{\rho}(\rho F')' + \left(\frac{(\omega^2/c^2)\langle G\,|\,\varepsilon_r\,|\,G\rangle - \langle G'\,|\,G'\rangle}{\langle G\,|\,G\rangle} - \frac{m^2}{\rho^2}\right) F = 0 \tag{A.15}$$

and

$$G'' + \left(\frac{(\omega^2/c^2)\langle F\,|\,\varepsilon_r\,|\,F\rangle - m^2\langle F\,|\,\rho^{-2}\,|\,F\rangle - \langle F'\,|\,F'\rangle}{\langle F\,|\,F\rangle}\right) G = 0. \tag{A.16}$$

Introducing further notation and applying the product rule to (A.15), I obtain the weighted index equations

$$F''(\rho) + \frac{1}{\rho}F'(\rho) + \left(k_{eff}^2[G,\rho] - \frac{m^2}{\rho^2}\right)F(\rho) = 0 \tag{A.17}$$

and

$$G''(z) + \beta_{eff}^2[F,z]G(z) = 0, \tag{A.18}$$

where,

$$k_{eff}^2[G,\rho] \equiv \frac{(\omega^2/c^2)\langle G \,|\, \varepsilon_r \,|\, G\rangle + \langle G \,|\, G''\rangle}{\langle G \,|\, G\rangle} \tag{A.19}$$

and

$$\beta_{eff}^2[F,z] \equiv \frac{(\omega^2/c^2)\langle F \,|\, \varepsilon_r \,|\, F\rangle + \langle F \,|\, F''\rangle + \langle F \,|\rho^{-1}\,|\, F'\rangle - m^2\langle F \,|\, \rho^{-2} \,|\, F\rangle}{\langle F \,|\, F\rangle}. \tag{A.20}$$

These variational constraint equations are exactly the same as (2.14) and (2.15) from Section 2.2. Therefore, the solution of these equations represents the best separable approximation to (A.1).

Appendix B. Transfer Matrix Generalization of Fabry-Perot Laser Theory

In this appendix, I show that the lasing conditions generated via transfer matrix techniques are in fact a generalization of the classic Fabry-Perot lasing conditions. Specifically, I show that for the simple plane-wave case the transfer matrix lasing conditions reduce to the Fabry-Perot conditions.

In classical Fabry-Perot laser theory the threshold gain and lasing mode wavelengths are given by a condition on the round-trip field amplitude and phase. In order for a lasing mode to be supported the round-trip change in amplitude must be ≥ 1. This is the gain/amplitude condition

$$R_1 R_2 e^{2L\Gamma^{\text{tot}} g_{th}} = 1, \tag{B.1}$$

or

$$\Gamma^{\text{tot}} g_{th} = \frac{1}{2L} \ln\left(\frac{1}{R_1 R_2}\right) = \alpha^{(\text{mirror})}. \tag{B.2}$$

Here Γ^{tot} is the total confinement factor, L is the cavity length, $\alpha^{(\text{mirror})}$ is the mirror loss, R_1 and R_2 are the mirror power reflectivities, and I have ignored any losses within the cavity. In order for a mode to be supported the round-trip change in phase must be an integer multiple of 2π or

$$2kL = m2\pi \Longrightarrow \lambda = \frac{2L}{m}, \tag{B.3}$$

where m is an integer. These conditions are illustrated in Figure B.1.

In transfer matrix theory the fields on either side of the VCSEL are related to one another by a 2×2 transfer matrix. In Figure B.2, the traveling wave amplitudes, E_{1+} and E_{1-}, in the substrate region at the substrate-to-VCSEL boundary are related to the traveling wave amplitudes, E_{3+} and E_{3-}, in free-space at the VCSEL-to-air boundary through a transfer matrix,

$$\begin{bmatrix} E_{3+} \\ E_{3-} \end{bmatrix} = \begin{bmatrix} m_{11} & m_{12} \\ m_{21} & m_{22} \end{bmatrix} \begin{bmatrix} E_{1+} \\ E_{1-} \end{bmatrix}. \tag{B.4}$$

A lasing condition is generated by requiring no incident radiation on either end of the

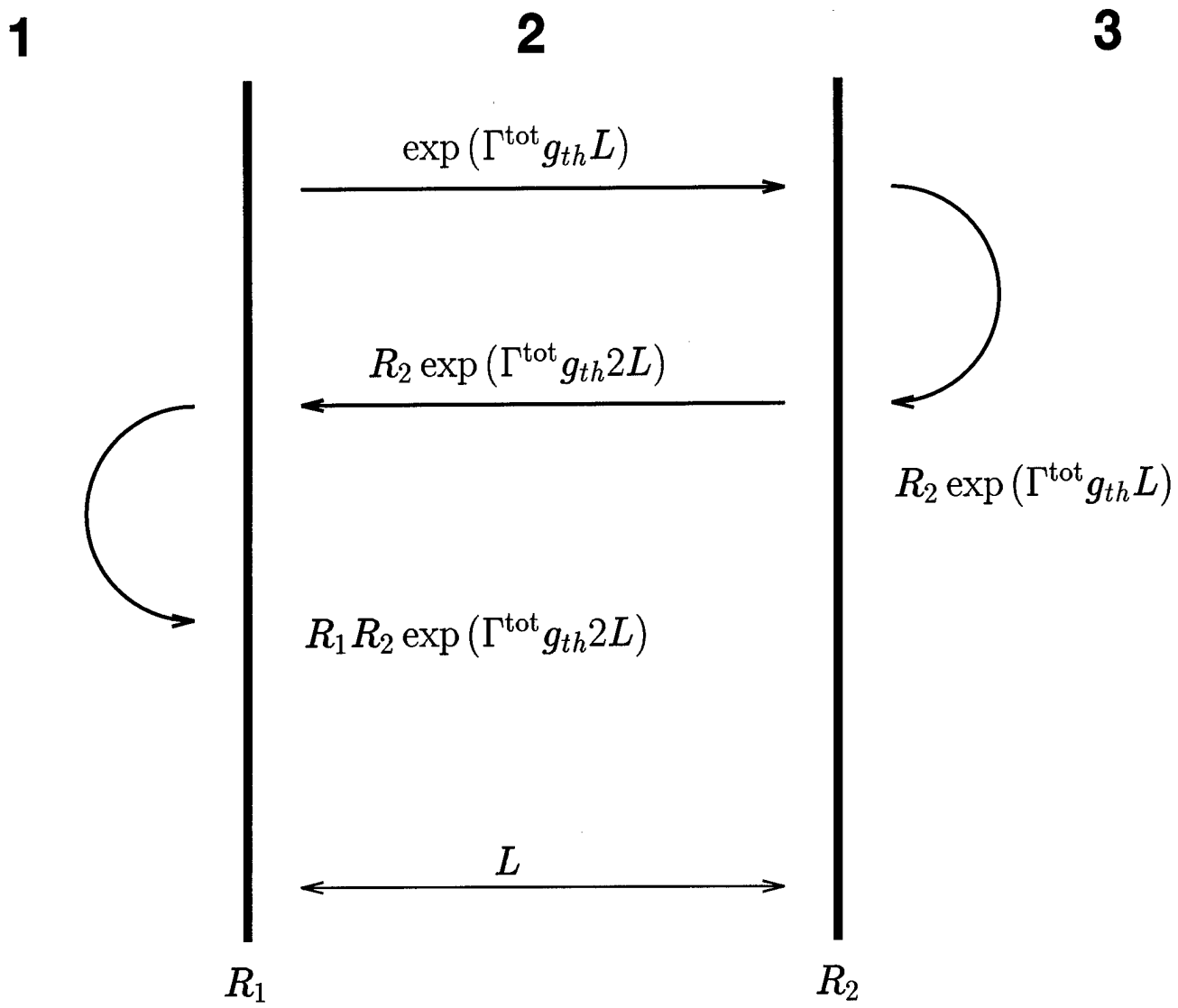

Figure B.1 Illustration of classical laser amplitude and phase conditions generated via Fabry-Perot theory.

VCSEL, i.e. $E_{3-} = E_{1+} = 0$. Hence, for a non-trivial solution to (B.4) I require $m_{22} = 0$, where m_{22} is complex, implying $\mathrm{Re}(m_{22}) = \mathrm{Im}(m_{22}) = 0$ (two conditions).

Based on the effective material parameters shown in Figure B.2,

$$m_{22} = \frac{e^{-i\phi_2}}{t_{32}t_{21}}\left(r_{32}r_{21} + e^{i2\phi_2}\right), \tag{B.5}$$

where t_{32}, t_{21} and r_{32}, r_{21} are the effective Fresnel transmission and reflection coefficients and $\phi_2 = \beta_{eff_2}L_2$ is the effective phase change for a single pass through the VCSEL of effective length L_2 with effective propagation constant β_{eff_2}. For realistic VCSELs, the first term in (B.5), $\frac{e^{-i\phi_2}}{t_{32}t_{21}}$, can not equal zero or infinity. Hence, the lasing condition reduces to

$$e^{i2\phi_2} = -r_{32}r_{21} = r_{23}r_{21}. \tag{B.6}$$

The Fabry-Perot amplitude condition can be recovered by taking the absolute value squared of (B.6),

$$e^{-4\frac{\omega}{c}\kappa_{th}L_2} = |r_{23}r_{21}|^2 = R_{23}R_{21}, \tag{B.7}$$

where κ_{th} is the effective threshold material gain, and R_{21} and R_{23} are the effective mirror power reflectance coefficients for a field impinging from inside the VCSEL. Recognizing that $\Gamma^{\mathrm{tot}}g_{th} = 2\frac{\omega}{c}\kappa_{th}$, (B.7) may be rewritten as

$$\Gamma^{\mathrm{tot}}g_{th} = \frac{1}{2L_2}\ln\left(\frac{1}{R_{21}R_{23}}\right), \tag{B.8}$$

which is equivalent to (B.2) with the substitution of the appropriate effective parameters.

The Fabry-Perot phase condition is found by equating the phase terms on either side of (B.6). Expanding each side of the equation yields

$$^{\circ}\angle\, e^{i2\frac{\omega}{c}n_2L_2} = {}^{\circ}\angle\left(\frac{n_2 + i\kappa_{th} - n_3}{n_2 + i\kappa_{th} + n_3}\right)\left(\frac{n_2 + i\kappa_{th} - n_1}{n_2 + i\kappa_{th} + n_1}\right), \tag{B.9}$$

where $^{\circ}\angle$ denotes the complex phase angle. For realistic VCSEL structures $\kappa_{th} \sim 0.01$ while $n_1 - n_2 > 0.5$ and $n_2 - n_3 > 1.0$, hence I may assume the phase of the right hand side of

(B.9) is approximately zero. Thus,

$$2\frac{\omega}{c}n_2 L_2 = 2m\pi \Longrightarrow \lambda = \frac{2L_2}{m}, \tag{B.10}$$

which is equivalent to (B.3) with the substitution of the effective cavity length L_2 for L.

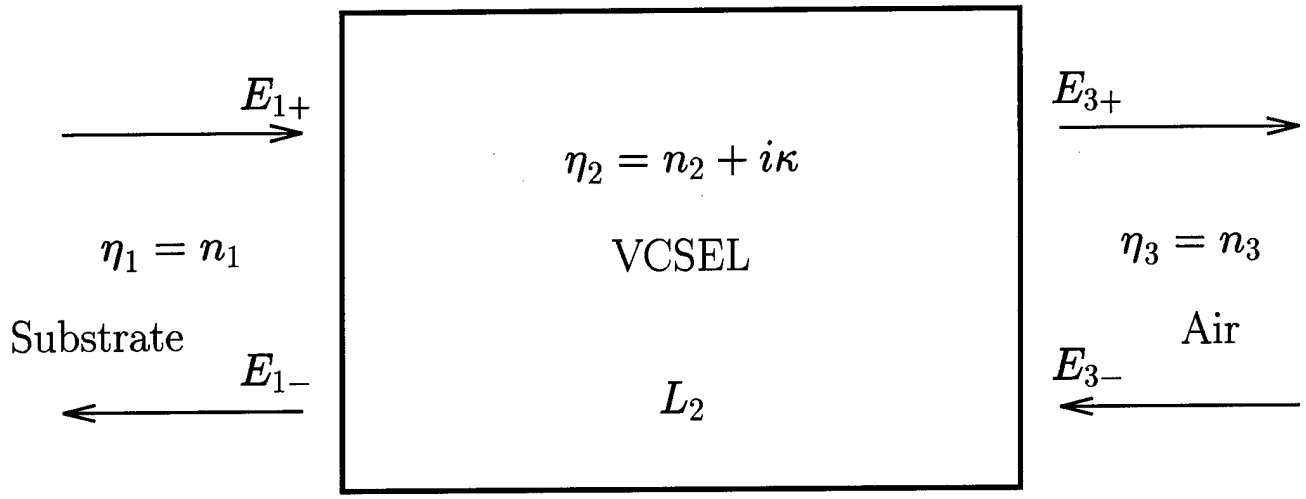

Figure B.2 Illustration of transfer matrix solution to the plane-wave VCSEL problem.

Appendix C. Vector Basis Functions for m=1 Modes

In this appendix, I review the vector basis functions employed in my finite element model. Based on the literature, I choose to span the mesh using second order node, edge, and face element functions [25, 59]. These functions have been shown to be a good compromise between mesh density and function order, roughly minimizing the total number of unknowns required to obtain a given solution accuracy. For each triangle in the mesh there are 14 basis functions: 6 node based $\left(\vec{N}_0 - \vec{N}_5\right)$, 6 edge based $\left(\vec{W}_0 - \vec{W}_5\right)$, and two face based $\left(\vec{W}_6, \vec{W}_7\right)$, as illustrated in Figure C.1 [35, 59]. To define the 14 element functions, I use simplex (or barycentric) coordinates, defined over the triangular element via the affine transformation [13, 68],

$$\begin{bmatrix} 1 \\ \rho \\ z \end{bmatrix} = \begin{bmatrix} 1 & 1 & 1 \\ \rho_0 & \rho_1 & \rho_2 \\ z_0 & z_1 & z_2 \end{bmatrix} \begin{bmatrix} \zeta_0 \\ \zeta_1 \\ \zeta_2 \end{bmatrix}. \tag{C.1}$$

Here (ρ_0, z_0), (ρ_1, z_1), and (ρ_2, z_2) are the three corners of the triangle, and ζ_0, ζ_1,and ζ_2 are the simplex coordinates. Based on the ζ_i, the element *vector* functions are

$$\vec{N}_0 \equiv (2\zeta_0 - 1)\,\zeta_0 \left(\hat{\phi} + \hat{\rho}\right), \tag{C.2}$$

$$\vec{N}_1 \equiv (2\zeta_1 - 1)\,\zeta_1 \left(\hat{\phi} + \hat{\rho}\right), \tag{C.3}$$

$$\vec{N}_2 \equiv (2\zeta_2 - 1)\,\zeta_2 \left(\hat{\phi} + \hat{\rho}\right), \tag{C.4}$$

$$\vec{N}_3 \equiv 4\zeta_0\zeta_1 \left(\hat{\phi} + \hat{\rho}\right), \tag{C.5}$$

$$\vec{N}_4 \equiv 4\zeta_1\zeta_2 \left(\hat{\phi} + \hat{\rho}\right), \tag{C.6}$$

$$\vec{N}_5 \equiv 4\zeta_0\zeta_2 \left(\hat{\phi} + \hat{\rho}\right), \tag{C.7}$$

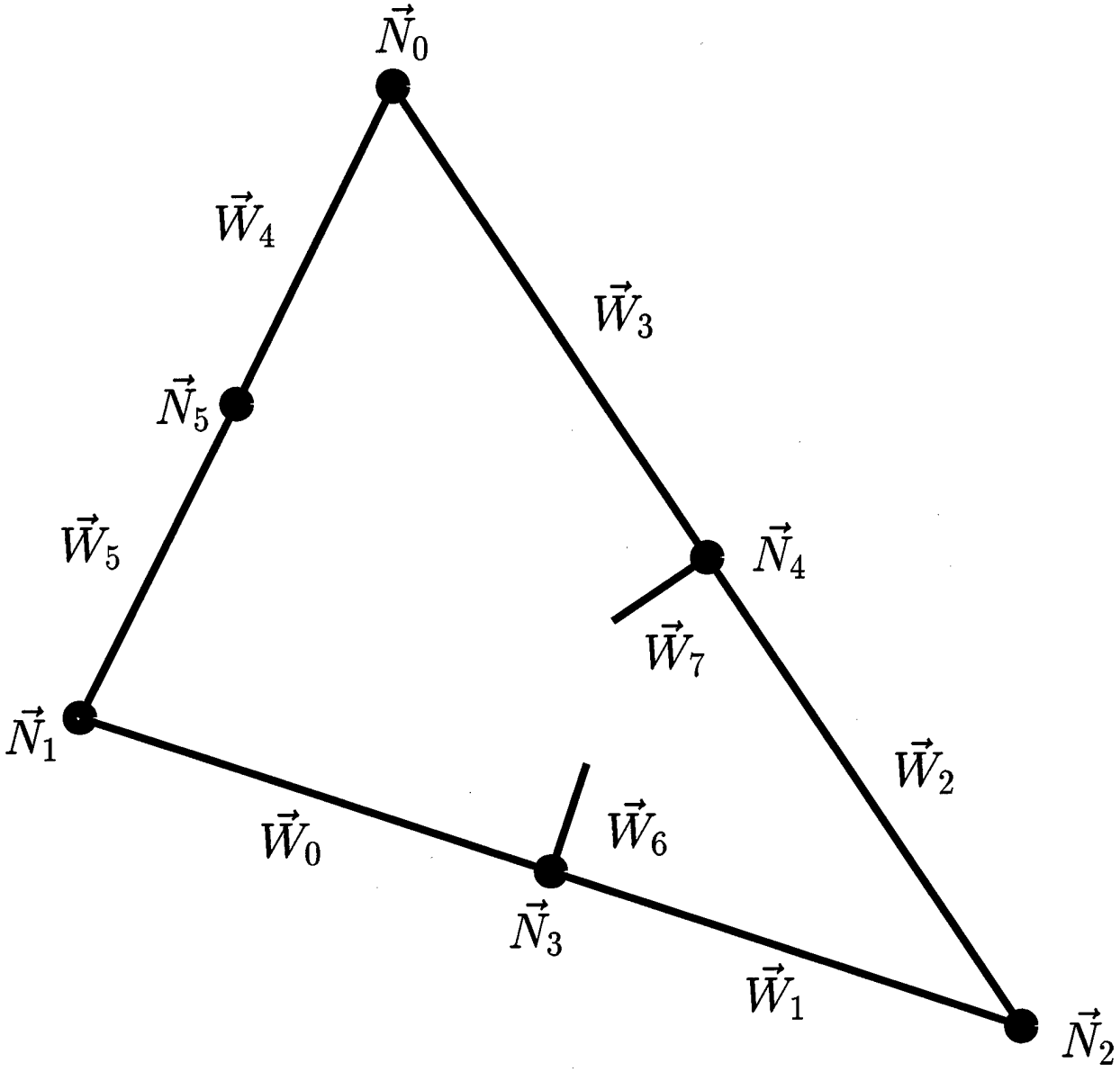

Figure C.1 Numbering convention of the six node, six edge, and two face based element functions.

$$\vec{W}_0 \equiv \rho\zeta_1\nabla_\tau\zeta_2 = \frac{\rho\zeta_1}{\Delta}\left\{b_2\hat{\rho} + c_2\hat{z}\right\}, \tag{C.8}$$

$$\vec{W}_1 \equiv \rho\zeta_2\nabla_\tau\zeta_1 = \frac{\rho\zeta_2}{\Delta}\left\{b_1\hat{\rho} + c_1\hat{z}\right\}, \tag{C.9}$$

$$\vec{W}_2 \equiv \rho\zeta_2\nabla_\tau\zeta_0 = \frac{\rho\zeta_2}{\Delta}\left\{b_0\hat{\rho} + c_0\hat{z}\right\}, \tag{C.10}$$

$$\vec{W}_3 \equiv \rho\zeta_0\nabla_\tau\zeta_2 = \frac{\rho\zeta_0}{\Delta}\left\{b_2\hat{\rho} + c_2\hat{z}\right\}, \tag{C.11}$$

$$\vec{W}_4 \equiv \rho\zeta_0\nabla_\tau\zeta_1 = \frac{\rho\zeta_0}{\Delta}\left\{b_1\hat{\rho} + c_1\hat{z}\right\}, \tag{C.12}$$

$$\vec{W}_5 \equiv \rho\zeta_1\nabla_\tau\zeta_0 = \frac{\rho\zeta_1}{\Delta}\left\{b_0\hat{\rho} + c_0\hat{z}\right\}, \tag{C.13}$$

$$\vec{W}_6 \equiv \rho 4\zeta_1\left(\zeta_2\nabla_\tau\zeta_0 - \zeta_0\nabla_\tau\zeta_2\right) \tag{C.14}$$

$$= \frac{\rho 4\zeta_1}{\Delta}\left\{\zeta_2\left(b_0\hat{\rho} + c_0\hat{z}\right) - \zeta_0\left(b_2\hat{\rho} + c_2\hat{z}\right)\right\},$$

$$\vec{W}_7 \equiv \rho\ 4\zeta_2\left(\zeta_0\nabla_\tau\zeta_1 - \zeta_1\nabla_\tau\zeta_0\right) \tag{C.15}$$

$$= \frac{\rho 4\zeta_2}{\Delta}\left\{\zeta_0\left(b_1\hat{\rho} + c_1\hat{z}\right) - \zeta_1\left(b_0\hat{\rho} + c_0\hat{z}\right)\right\}.$$

Here

$$\nabla_\tau \equiv \frac{\partial}{\partial\rho}\hat{\rho} + \frac{\partial}{\partial z}\hat{z}, \tag{C.16}$$

the b_i and c_i are given by the inverse affine transformation,

$$\begin{bmatrix}\zeta_0\\ \zeta_1\\ \zeta_2\end{bmatrix} = \frac{1}{\Delta}\begin{bmatrix}a_0 & b_0 & c_0\\ a_1 & b_1 & c_1\\ a_2 & b_2 & c_2\end{bmatrix}\begin{bmatrix}1\\ \rho\\ z\end{bmatrix}, \tag{C.17}$$

and Δ is twice the area of the triangle,

$$\Delta \equiv \sum_{i=0}^{2}\rho_i\left(z_{i1} - z_{i2}\right) = \sum_{i=0}^{2}\rho_i b_i = \sum_{i=0}^{2} z_i c_i \tag{C.18}$$

(i, $i1$, and $i2$ are modulo 3). These functions are illustrated in Figures C.2 and C.3. These

functions have three important properties that make them ideal for electromagnetic calculation in cylindrical coordinates.

First, when filling the **S** and **T** matrices, functions based on the same node or edge of neighboring elements (not necessarily with the same element function number $\vec{N}_0 - \vec{W}_7$) are assigned the same coefficient x_i. As a result, the node and edge functions *naturally enforce tangential field continuity* (as illustrated in Figure C.4) *without necessarily forcing normal field continuity*, due to the two face functions.

Second, my element functions are modified from the more standard form [35] to force field regularity at $\rho = 0$ (the axis condition). The lasing modes I seek are analogous to the $(m = 1)$ LP_{01} fiber modes [58], where the azimuthal field dependence is $\sin(\phi)/\cos(\phi)$. The proper axis condition for the $m = 1$ modes is [74]

$$\lim_{\rho \to 0} E_\rho = E_\phi, \tag{C.19}$$

and

$$\lim_{\rho \to 0} E_z = 0. \tag{C.20}$$

This condition is included in (C.2) – (C.15) by weighting the "standard" [35] edge and face functions by ρ, and including the node functions as part of the $\hat{\rho}$ field expansion. Note that I may find $m = 0$ and $m > 1$ modes using a basis similar to (C.2) – (C.15), altered to accommodate the proper axis condition for these modes.

Third and least obvious, these elements properly model the null space of the curl operator, which has been shown to eliminate the occurrence of spurious solutions (modes) [40, 72].

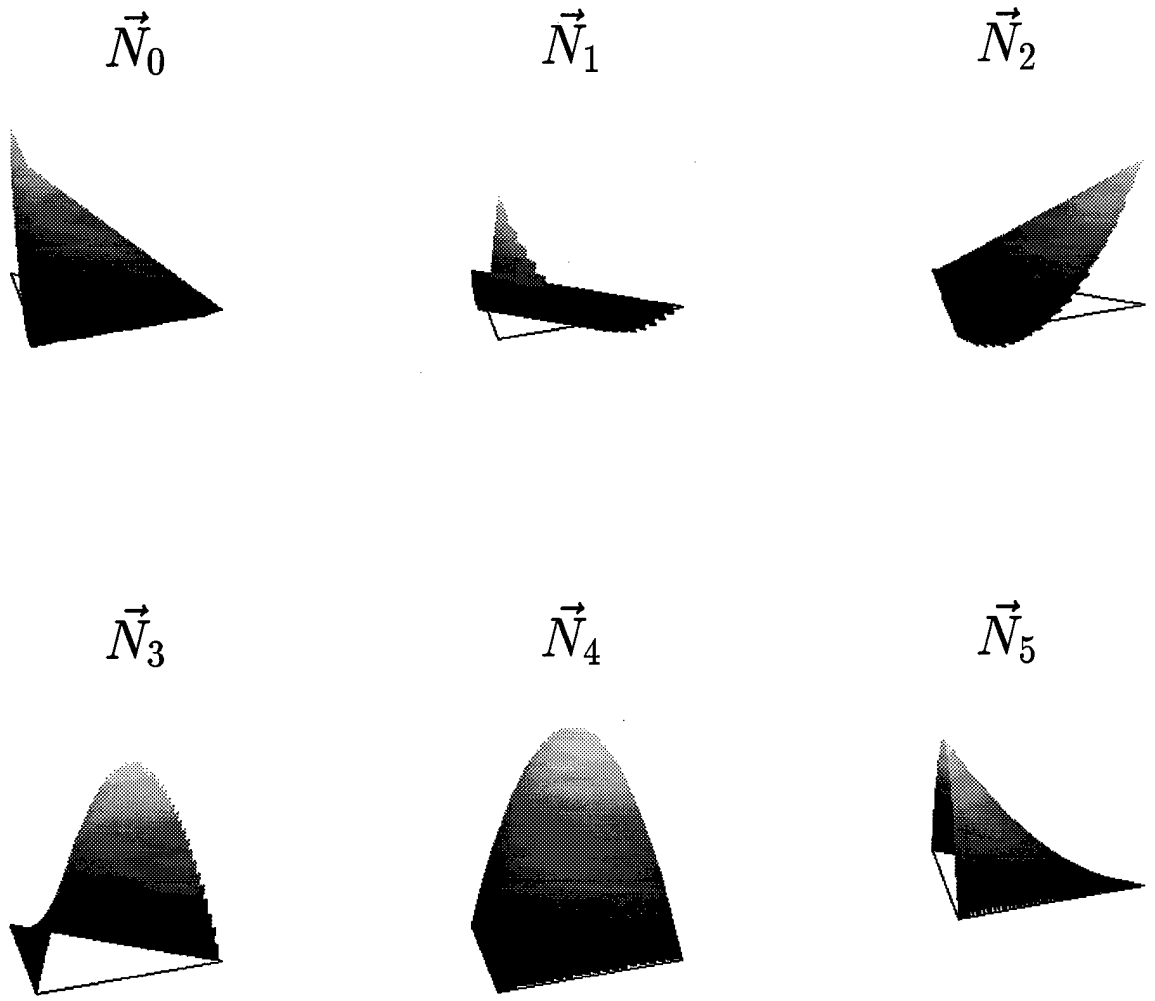

Figure C.2 Illustration of the six node based functions ($\vec{N}_0 - \vec{N}_5$) for a typical element; the functions are overlayed on a triangle outline of the element.

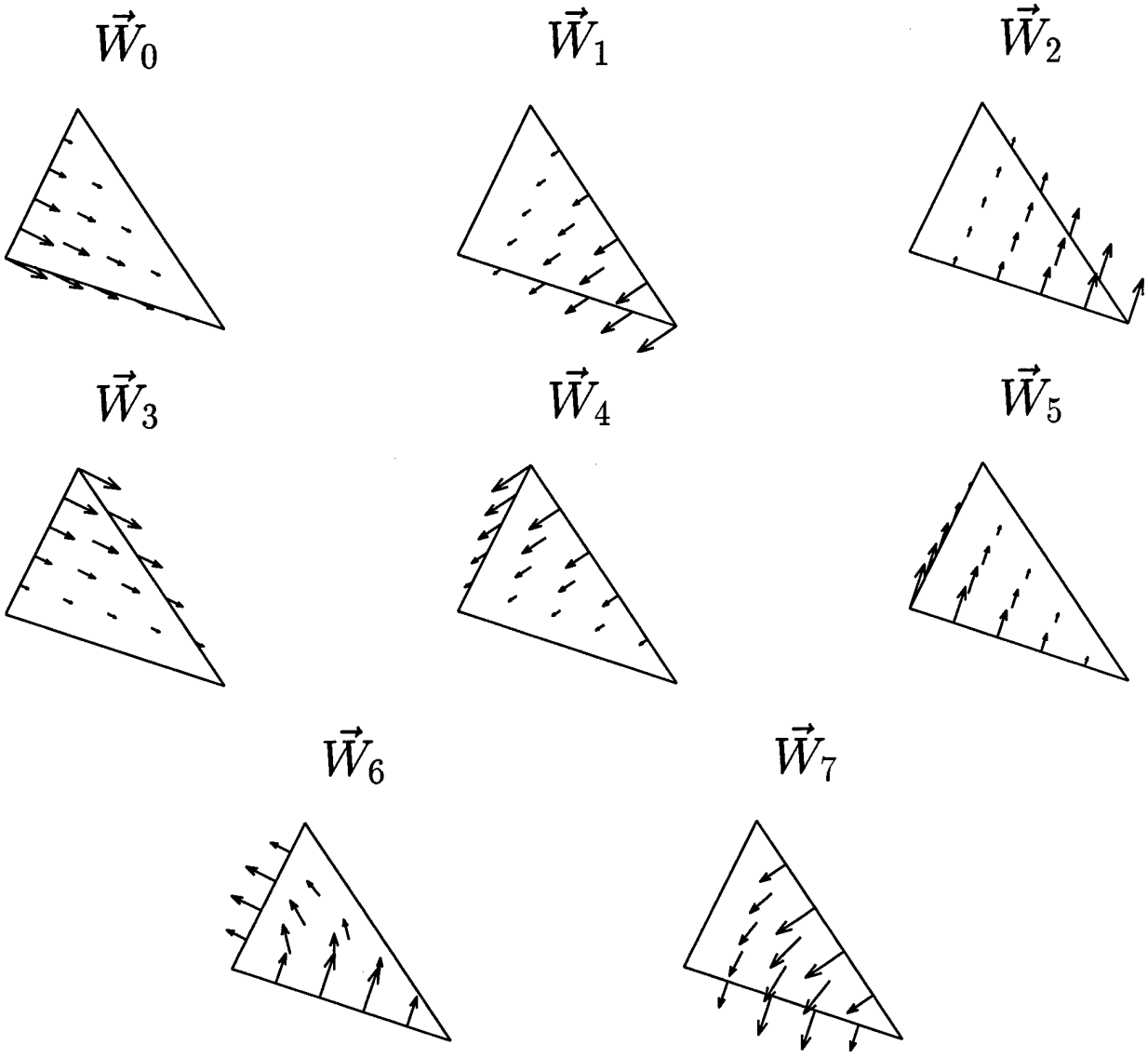

Figure C.3 Illustration of the six edge based ($\vec{W}_0 - \vec{W}_5$) and the two face based ($\vec{W}_6 - \vec{W}_7$) functions for a typical element; the functions are overlayed on a triangle outline of the element. These illustrations do not include the ρ weighting present in (C.8) - (C.15).

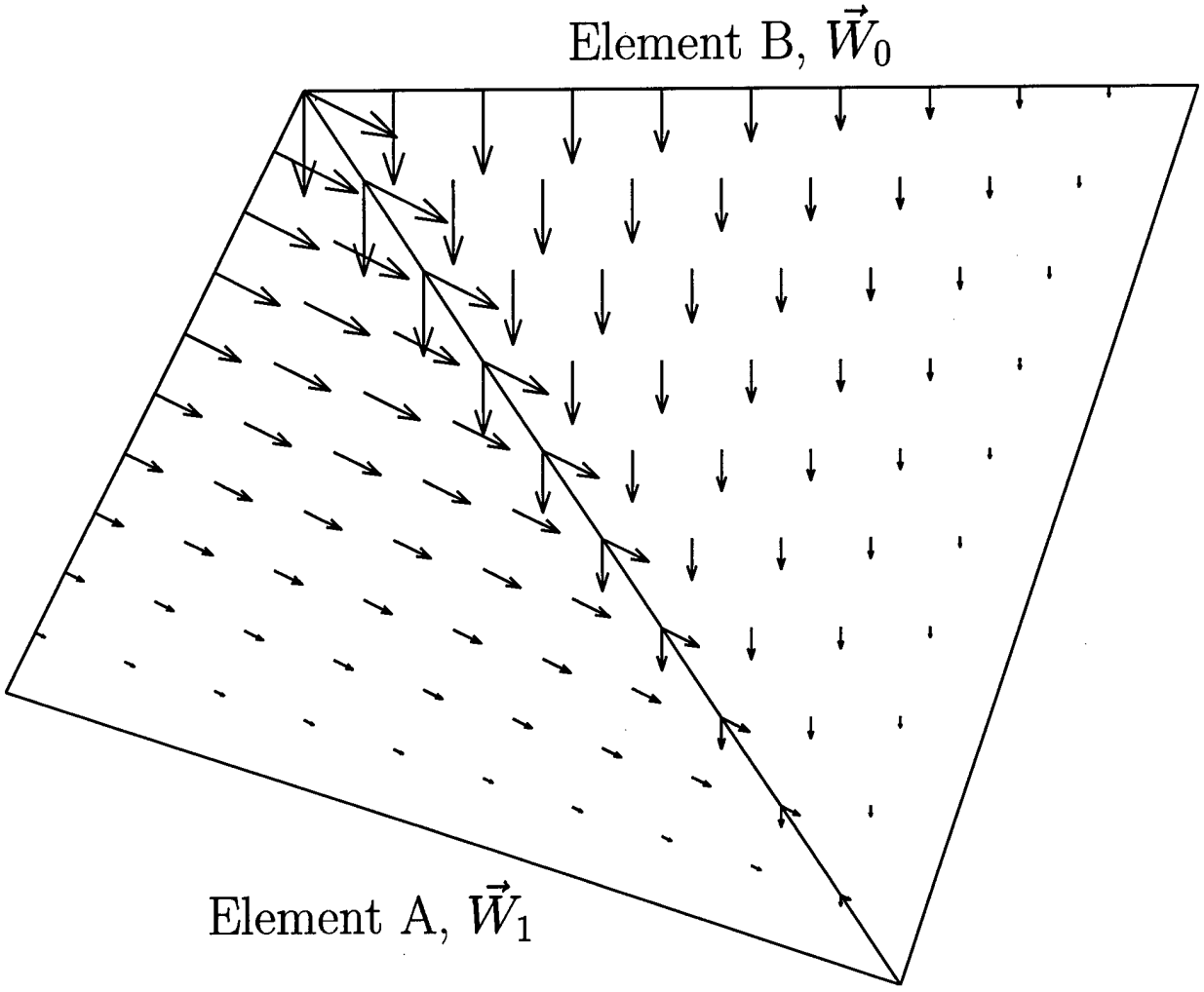

Figure C.4 Illustration of the natural tangential continuity between mesh elements. By assigning the same coefficient x_i to $\vec{W}_1$ of element A and $\vec{W}_0$ of element B, the vector sum of the two functions is tangential to their common edge.

Appendix D. Absorbing Layer Design

In this appendix, I give the details of a *new* absorbing layer design. I use a two step process to optimize $b(\rho)$, the absorbing layer loss function: First, I obtain a rough estimate using an asymptotic description of the fields and reflections. Second, I fine-tune the layer by minimizing the exact reflection values as obtained by a rigorous transfer matrix calculation. In both steps I model the *radial* AL (Ω_S) as a set of discrete cylinders, as shown in Figure D.1, approximating $a(\rho)$ as $a_n = a((\rho_n + \rho_{n-1})/2)$, where AL cylinder n is defined by $[\rho_{n-1}, \rho_n]$. To simplify further, I ignore the z dependence of the material parameters and perform my analysis using a single set of (ε_r, μ_r), the rough mean material values for the VCSEL. This should be sufficient, since I am not concerned about interfacial reflections between the various axial layers, and desire only to suppress nonphysical radial reflections. I choose $b(\rho)$ to minimize the reflection of cylindrical waves incident on the radial boundaries.

These waves are constructed from the $\hat{z}$ and $\hat{\phi}$ field components given in each region (cylinder) by

$$H_{z,n}(\rho,z) = \left(A_n^{\mathrm{TE}} H_0^{(2)}(k_n\rho) + B_n^{\mathrm{TE}} H_0^{(1)}(k_n\rho)\right) e^{i\beta_n z}, \tag{D.1}$$

$$E_{z,n}(\rho,z) = \left(A_n^{\mathrm{TM}} H_0^{(2)}(k_n\rho) + B_n^{\mathrm{TM}} H_0^{(1)}(k_n\rho)\right) e^{i\beta_n z}, \tag{D.2}$$

$$H_{\phi,n}(\rho,z) = \frac{-i\omega\varepsilon_0\varepsilon_r a_n}{k_n^2}\frac{\partial E_z}{\partial\rho} \tag{D.3}$$

$$= \frac{i\omega\varepsilon_0\varepsilon_r a_n}{k_n}\left(A_n^{\mathrm{TM}} H_1^{(2)}(k_n\rho) + B_n^{\mathrm{TM}} H_1^{(1)}(k_n\rho)\right) e^{i\beta_n z},$$

$$E_{\phi,n}(\rho,z) = \frac{i\omega\mu_0 a_n}{k_n^2}\frac{\partial H_z}{\partial\rho} \tag{D.4}$$

$$= \frac{-i\omega\mu_0 a_n}{k_n}\left(A_n^{\mathrm{TE}} H_1^{(2)}(k_n\rho) + B_n^{\mathrm{TE}} H_1^{(1)}(k_n\rho)\right) e^{i\beta_n z},$$

where $a_0 = 1$ ($b_0 = 0$) in Ω_V and I have assumed nonmagnetic materials ($\mu_r = 1$). The coefficients A_n^{pol} and B_n^{pol} are the magnitude for the outward and inward propagating waves, and pol = TE or TM labels the (uncoupled) polarizations of the $m = 0$ modes. It has been shown [45] that absorbing layers that perform well for these $m = 0$ modes will also work well for the $m = 1$ modes that I am interested in.

I can describe cylindrical waves incident at an *angle* θ—measured from the normal to Γ_S in the $\rho - z$ plane ($\hat{n}_{\Gamma_S}$)—to the radial interface by writing the radial (k_n) and axial (β_n) propagation constants as

$$k_n = k_0 \eta a_n \cos(\theta), \tag{D.5}$$

$$\beta_n = k_0 \eta a_n \sin(\theta). \tag{D.6}$$

This choice ensures that k_n and β_n satisfy the dispersion relation

$$\omega^2 \mu_0 \varepsilon_0 \varepsilon_r a_n^2 = k_0^2 \varepsilon_r a_n^2 = k_n^2 + \beta_n^2, \tag{D.7}$$

in each region, where the (generally complex) index of refraction is

$$\eta \equiv \sqrt{\varepsilon_r}. \tag{D.8}$$

D.1 Initial Design: Theory of Small Reflections

For the initial AL design analysis I employ the theory of small reflections [60], approximating the total Fresnel reflection for a cylindrical wave incident on the AL at ρ_0 as

$$r \approx |r_0| + |r_1|\, t_1 + |r_2|\, t_{1,2} + \ldots + \left|r_{N_{cyl}}\right|\, t_{1,2,\ldots,N_{cyl}}. \tag{D.9}$$

Here N_{cyl} is the total number of cylinders in the AL, r_n is the Fresnel reflection coefficient at ρ_n, and $t_{1,2,\ldots,n}$ gives the attenuation due to the propagation from ρ_0 to ρ_n and back. I use $|r_n|$ rather than r_n in (D.9) to minimize the interference effects, since I am after a broadband AL design optimized for all angles of incidence. I estimate r_n using the asymptotic form for cylindrical waves in each region n. Due to the form of (4.16) and (D.1) – (D.4), the magnitude of the TE and TM Fresnel reflection coefficients are the same, hence I need only

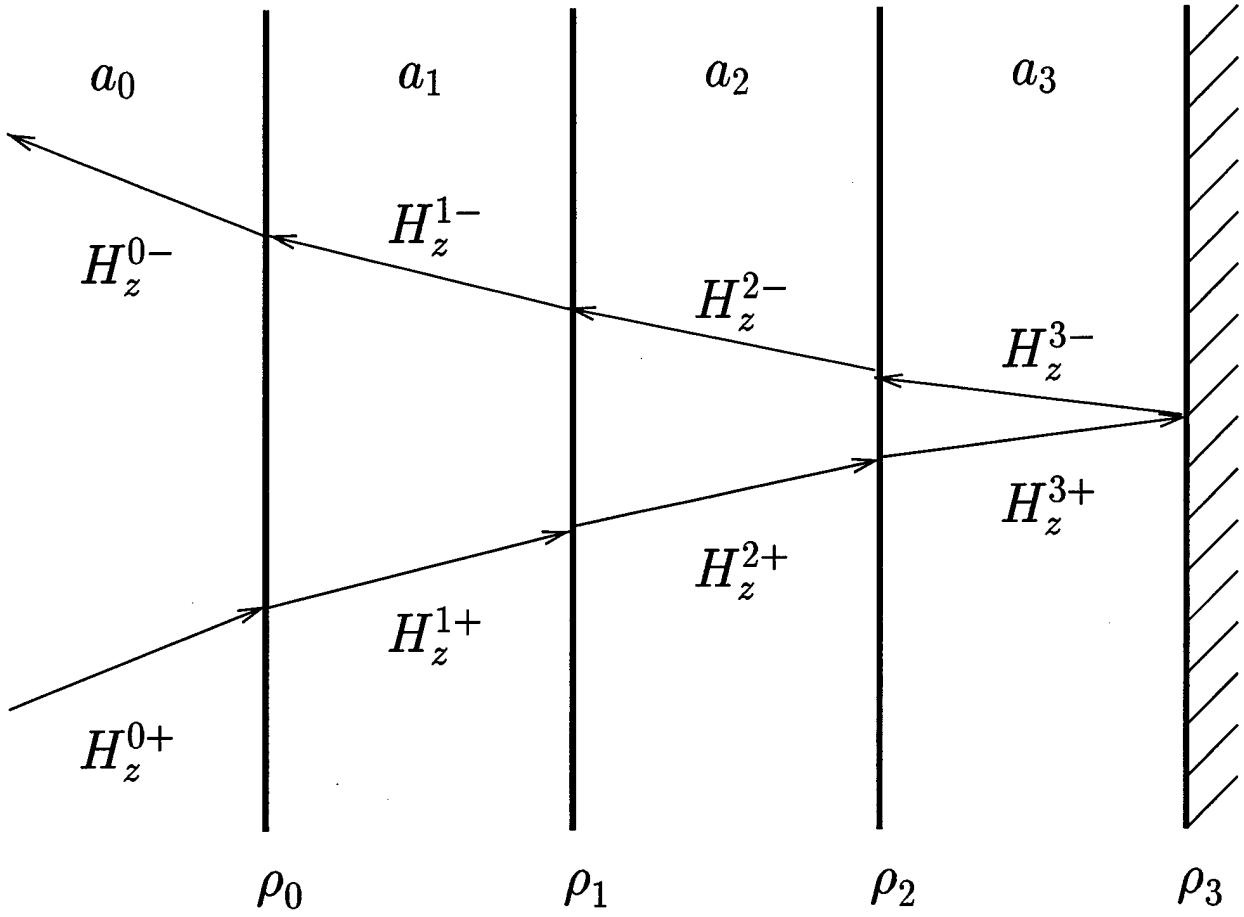

Figure D.1 Illustration of the geometry used to design the radial AL. Ω_S is broken into discrete cylinders, each with a constant AL parameter $a_n = a((\rho_n + \rho_{n-1})/2)$.

perform the analysis once. Taking the asymptotic form for the Hankel functions,

$$\lim_{\rho\to\infty} H_0^{(1)/(2)}(k_n\rho) \backsim \frac{e^{\pm ik_n\rho}}{\sqrt{k_n\rho}}, \tag{D.10}$$

(+ applies to (1) and − applies to (2)) and enforcing tangential field continuity, I find

$$\begin{aligned} |r_n| &= \left|\frac{a_n k_{n+1} - a_{n+1}k_n}{a_n k_{n+1} + a_{n+1}k_n}\right| \\ &= \left|\frac{\cos(\theta_{n+1}) - \cos(\theta_n)}{\cos(\theta_{n+1}) + \cos(\theta_n)}\right|, \end{aligned} \tag{D.11}$$

for $n = 0$ to $N_{cyl} - 1$. θ_n and θ_{n+1} are the (complex) propagation angles with respect to $\hat{n}_{\Gamma_S}$ in regions n and $n+1$, respectively. I set $|r_{N_{cyl}}| = 1$ to enforce the perfect conductor boundary condition at the mesh edge (Γ). Keeping only the first (lowest order) term in the derivatives of (D.10), I approximate

$$t_{1,2,\ldots,n} = t_1 t_2 \ldots t_n, \tag{D.12}$$

where

$$t_n \equiv e^{-i2k_n l_n}, \tag{D.13}$$

and k_n and $l_n \equiv \rho_n - \rho_{n-1}$ are the radial propagation constant and cylinder thickness in region n. Substituting (D.11) – (D.13) into (D.9) and taking the magnitude yields,

$$|r| \approx \left|\sum_{n=0}^{N_{cyl}} |r_n| \prod_{\acute{n}=0}^{n} e^{-i2k_{\acute{n}}l_{\acute{n}}}\right|, \tag{D.14}$$

which I may solve for a given $a(\rho)$ to find $|r(\theta_i)|$, the magnitude of the total Fresnel reflection for a general (e.g., includes axial propagation $\exp(i\beta z)$) cylindrical wave incident on the AL at angle θ_i. Note that (D.14) is equivalent to the result obtained via a plane wave, planar interface analysis, and may therefore be directly applied to the *axial* AL design (Ω_T and Ω_B), in addition to the radial design (Ω_S).

D.2 Final Design: Transfer Matrix Solution

To finalize my radial AL design I use a 2×2 transfer matrix solution for the TE or TM fields. Enforcing continuity of (D.1) and (D.4), *or* (D.2) and (D.3) at each radial interface ρ_n, I have

$$L_n \begin{bmatrix} A_n \\ B_n \end{bmatrix} = R_{n+1} \begin{bmatrix} A_{n+1} \\ B_{n+1} \end{bmatrix}, \tag{D.15}$$

where

$$L_n \equiv \begin{bmatrix} H_0^{(2)}(k_n\rho_n) & H_0^{(1)}(k_n\rho_n) \\ \frac{a_n}{k_n} H_1^{(2)}(k_n\rho_n) & \frac{a_n}{k_n} H_1^{(1)}(k_n\rho_n) \end{bmatrix}, \tag{D.16}$$

and

$$R_{n+1} \equiv \begin{bmatrix} H_0^{(2)}(k_{n+1}\rho_n) & H_0^{(1)}(k_{n+1}\rho_n) \\ \frac{a_{n+1}}{k_{n+1}} H_1^{(2)}(k_{n+1}\rho_n) & \frac{a_{n+1}}{k_{n+1}} H_1^{(1)}(k_{n+1}\rho_n) \end{bmatrix}. \tag{D.17}$$

I have dropped the pol=TE/TM superscript since (D.15) holds for both polarizations. At the mesh boundary (Γ), I enforce $E_\phi = 0$ which relates the coefficients in the outermost AL cylinder by

$$A_{N_{cyl}} = -B_{N_{cyl}} \frac{H_1^{(1)}(k_{N_{cyl}}\rho_{N_{cyl}})}{H_1^{(2)}(k_{N_{cyl}}\rho_{N_{cyl}})}. \tag{D.18}$$

For convenience, I choose $A_{N_{cyl}} = -H_1^{(1)}(k_{N_{cyl}}\rho_{N_{cyl}})$ and $B_{N_{cyl}} = H_1^{(2)}(k_{N_{cyl}}\rho_{N_{cyl}})$. Beginning in the outer AL cylinder and working inward via repeatedly applying (D.15), I calculate A_0 and B_0. The total Fresnel reflection coefficient for an outward propagating wave incident on the AL is given by

$$|r| = \left| \frac{B_0}{A_0} \right|. \tag{D.19}$$

D.3 Results for Structures Analyzed

To design my AL, I ran the analysis outlined in Sections D.1 and D.2 with VCSEL material parameters $\varepsilon_r = 9$ and $\mu_r = 1$. I assumed a polynomial form for the AL loss function,

$$b(\chi) \equiv \sum_{i=1}^{\text{order}} \tilde{b}_i \chi^i. \tag{D.20}$$

Here order refers to the polynomial order, $\tilde{b}_i$ are the polynomial coefficients, and

$$\chi \equiv \frac{\rho - \rho_{\Gamma_S}}{\rho_\Gamma - \rho_{\Gamma_S}} \tag{D.21}$$

is the normalized radial coordinate ranging from 0 at Γ_S, the VCSEL–AL interface, to 1 at Γ, the problem/mesh boundary. Through a numerical optimization, I found that a second order polynomial with coefficients,

$$\tilde{b}_1 = 0.1178, \tag{D.22}$$

$$\tilde{b}_2 = 0.7433, \tag{D.23}$$

worked best for $b(\chi)$. In addition, I found an AL thickness of 1.5λ (at $\lambda = 870$ nm) was superior, with little change in the AL properties for greater thicknesses. The reflection coefficient (calculated with the transfer matrix approach) verses angle is given in Figure D.2. The key point to recognize from Figure D.2 is the intensity reflection, $R_{dB} \equiv 20\log_{10}(|r|) \leq -50\,dB$ for $\theta_i \leq 40°$, indicating a good "wide-angle" absorber design.

To provide a more practical test of my AL design, I analyzed the 1λ–1THIN VCSEL (introduced in Section 4.4), tracking the lasing mode (defined as the lowest loss mode, e.g., the mode with the smallest Im(ξ)) eigenvalue as a function of $\rho_{\Gamma_S} - \rho_{ox}$, which is the separation between the VCSEL-AL boundary and the oxide aperture. I tested two different oxide aperture radii, 0.5 μm and 1.0 μm, using my 1.5λ (= 0.435 μm), second order polynomial AL design. The resulting real and imaginary parts of the eigenvalue are shown in Figures D.3 and D.4, respectively. Clearly, the eigenvalues converge for $\rho_{\Gamma_S} - \rho_{ox} \geq 0.9\,\mu$m (corresponding to $\approx 3\lambda$), denoting the minimum allowable separation between the oxide aperture and Γ_S. It is interesting to note that for the 1.0 μm oxide aperture, the variation in the eigenvalue from $\rho_{ox} = 1.2\,\mu$m to 2.0 μm corresponds to a variation in the resonant wavelength of less than two angstroms, implying that the AL works well even when placed very close to the aperture. No analogous test was performed on the axial AL design; I assume that, based on the good results of the radial AL design and the high reflectance of the oxide DBRs, the optimized radial AL design should work for the axial AL as well. To perform

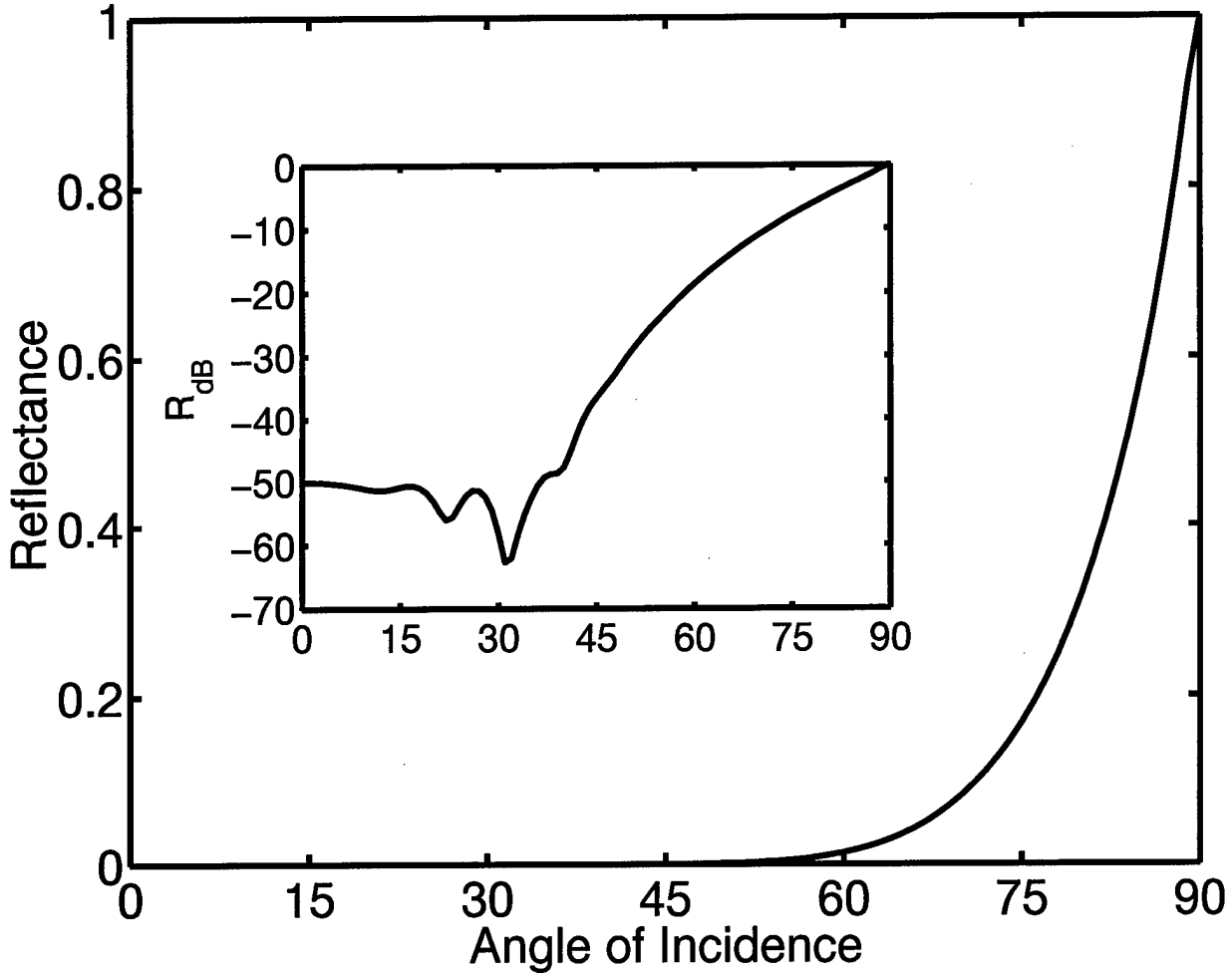

Figure D.2 Calculated intensity reflection $R \equiv |r|^2$ of the radial absorbing layer (AL) using the rigorous transfer matrix approach. The calculation is based on a 1.5λ thick AL at 870 nm, positioned with $\rho_{\Gamma_S} = 2.0$ μm. Thirty layers were used to discretize the AL loss function. Inset is the intensity reflection in decibels $R_{dB} \equiv 20\log_{10}(|r|)$.

the lasing mode analysis of Chapter IV, I used $\rho_{\Gamma_S} = 2.0\,\mu$m and varied the oxide aperture radius (ρ_{ox}) from $0.4\,\mu$m to $1.0\,\mu$m.

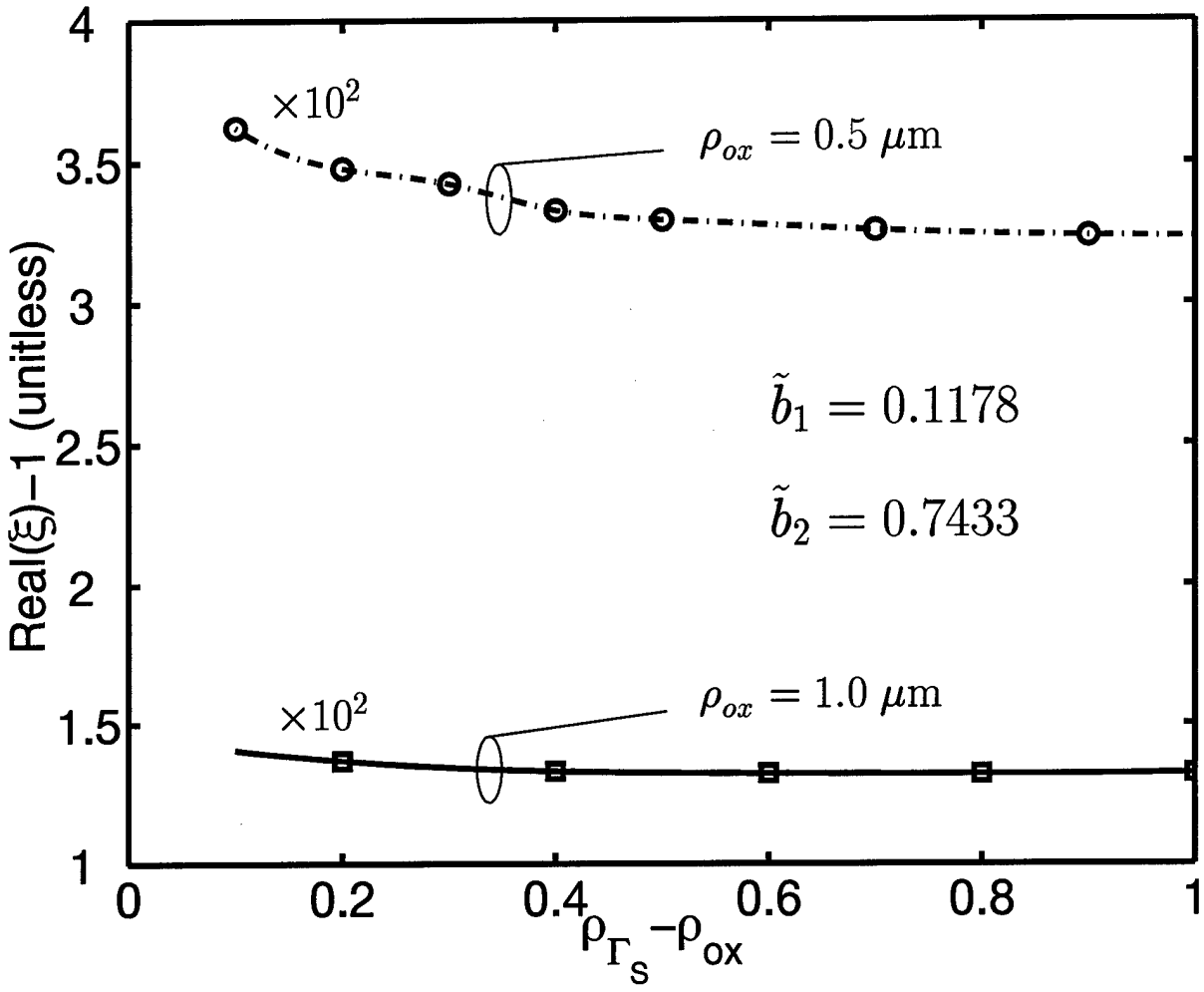

Figure D.3 Real part of the eigenvalue ξ vs separation between oxide radius (ρ_{ox}) and radial AL radius (ρ_{Γ_S}) for the 1λ–1THIN structure for two different oxide radii, 0.5 μm and 1.0 μm.

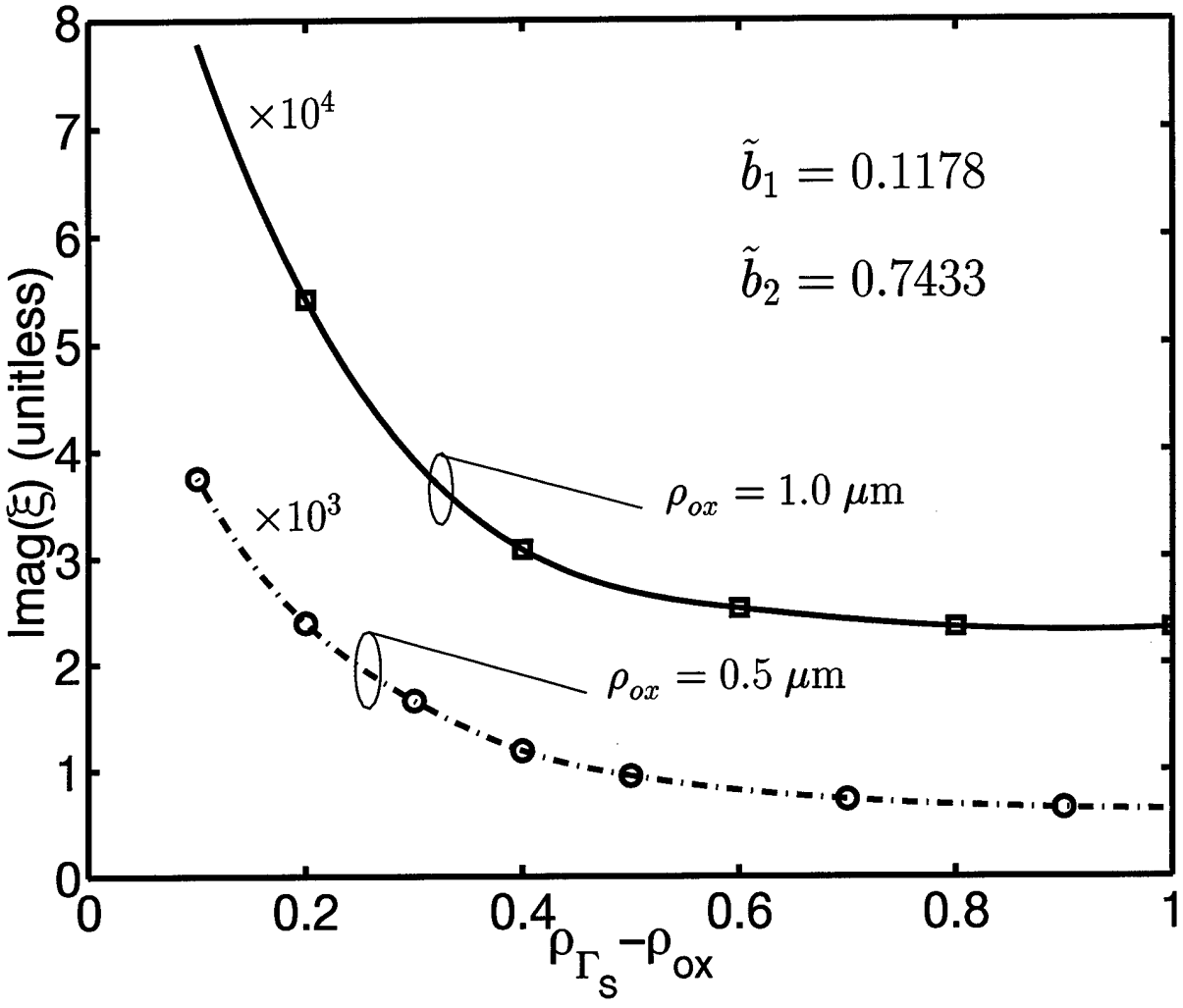

Figure D.4 Imaginary part of the eigenvalue ξ vs separation between oxide radius (ρ_{ox}) and radial AL radius (ρ_{Γ_s}) for the 1λ–1THIN structure for two different oxide radii, 0.5 μm and 1.0 μm.

Bibliography

1. Abramowitz, M. and I.A. Stegun, editors. *Handbook of Mathematical Functions with Formulas, Graphs, and Mathematical Tables*. National Bureau of Standards Applied Mathematics Series 55, Department of Commerce, 1964.
2. Agrawal, G.P. and N.K. Dutta. *Long-Wavelength Semiconductor Lasers*. Van Nostrand Reinhold, 1986.
3. Arfken, G. *Mathematical Methods for Physicists* (3rd Edition). Academic Press, 1958.
4. Baba, T., et al. "Spontaneous Emission Factor of a Microcavity DBR Surface-Emitting Laser," *IEEE Journal of Quantum Electronics*, *27*:1347–1358 (1991).
5. Baba, T., et al. "Spontaneous Emission Factor of a Microcavity DBR Surface Emitting Laser (II) - Effects of Electron Quantum Confinements," *IEEE Journal of Quantum Electronics*, *28*(5):1310–1319 (1992).
6. Babić, D.I., et al. "Room-Temperature Continuous-Wave Operation of 1.54-μm Vertical-Cavity Lasers," *IEEE Photonics Technology Letters*, 7(11):1225–1227 (November 1995).
7. Balanis, C.A. *Advanced Engineering Electromagnetics*. John Wiley and Sons, 1989.
8. Björk, G., et al. "Spontaneous-Emission Coupling Factor of Planar Dielectric Microcavity Lasers," *Physical Review A*, *47*(5):4451–4463 (1993).
9. Björk, G., et al. "Definition of a Laser Threshold," *Physical Review A*, *50*(2):1675–1679 (1994).
10. Björk, G., et al. "Modification of Spontaneous Emission Rate in Planar Dielectric Microcavity Structures," *Physical Review A*, *44*(1):669–681 (1991).
11. Björk, G. and Y. Yamamoto. "Analysis of Semiconductor Microcavity Lasers using Rate Equations," *IEEE Journal of Quantum Electronics*, *27*(11):2386–2396 (November 1991).
12. Burak, D. and R. Binder. "Cold-Cavity Vectorial Eigenmodes of VCSELs," *IEEE Journal of Quantum Electronics*, *33*(7):1205–1215 (July 1997).
13. Cendes, Z.J. "Vector Finite Elements for Electromagnetic Field Computation," *IEEE Transactions on Magnetics*, *27*(5):3953–3966 (September 1991).
14. Choquette, K.D., et al. "Scalability of Small-Aperture Selectively Oxidized Vertical Cavity Lasers," *Applied Physics Letters*, *70*(7):823–825 (February 1997).
15. Choquette, K.D., et al. "Fabrication and Performance of Selectively Oxidized Vertical-Cavity Lasers," *IEEE Photonics Technology Letters*, 7(11):1237–1239 (1995).
16. Cohen-Tannoudji, C., et al. *Quantum Mechanics, II*. John Wiley and Sons, 1977.
17. Coldren, L.A., et al. "Recent Advances and Important Issues in Vertical-Cavity Lasers." *Vertical-Cavity Surface-Emitting Lasers*. Number 3003 in Proceedings of the SPIE. 2–13. 1997.

18. DeMartini, F., et al. "Thresholdless Microlaser," *Physical Review A*, *46*(7):4220–4233 (October 1992).

19. Deppe, D.G., et al. "Oxide-Confined VCSELs with Quantum Well and Quantum Dot Active Regions." *LEOS '97 Conference Proceedings*. 287–288. November 1997.

20. Deppe, D.G., et al. "Low-Threshold Vertical-Cavity Surface-Emitting Lasers Based on Oxide-Confinement and High Contrast Distributed Bragg Reflectors," *IEEE Journal of Selected Topics in Quantum Electronics*, *3*(3):893–904 (June 1997).

21. Deppe, D.G., et al. "Eigenmode Confinement in the Dielectrically Apertured Fabry-Perot Microcavity," *IEEE Photonics Technology Letters*, *9*(6):713–715 (June 1997).

22. Feld, S., et al., "Microcavity Surface Emitting Lasers." Patent Disclosure, 1997. AF Inv D00227.

23. Gelfand, I.M. and S.V. Fomin. *Calculus of Variations*. Prentice-Hall, Inc., 1963.

24. Gloge, D. "Weakly Guiding Fibers," *Applied Optics*, *10*:2252–2258 (1971).

25. Graglia, R.D., et al. "Higher Order Interpolatory Vecgtor Bases for Computational Electromagnetics," *IEEE Transactions on Antennas and Propagation*, *45*(3):329–342 (March 1997).

26. Hadley, G.R. "Effective Index Model for Vertical-Cavity Surface-Emitting Lasers," *Optics Letters*, *20*(13):1483–1485 (July 1995).

27. Hadley, G.R., et al. "Understanding Waveguiding in Vertical-Cavity Surface-Emitting Lasers." *Technical Digest, Conference on Lasers and Electro-optics*. 1996 Technical Digest Series. 425. May 1996.

28. Harrington, R.F. *Time-Harmonic Electromagnetic Fields*. New York: McGraw-Hill Book Company, 1961.

29. Hegblom, E.R., et al. "Scattering Losses from Dielectric Apertures in Vertical-Cavity Lasers," *IEEE Journal of Selected Topics in Quantum Electronics*, *3*(2):379–389 (April 1997).

30. Hegblom, E.R., et al. "Towards Microcavity Vertical Cavity Lasers: Aperture and Cavity Design for High Efficiency and Low Threshold." *IEEE Summer Topical Meetings: Vertical-Cavity Lasers*. August 1997.

31. Huffaker, D.L., et al. "Native-Oxide Defined Ring Contact for Low Threshold Vertical-Cavity Lasers," *Applied Physics Letters*, *65*(1):97–99 (July 1994).

32. Huffaker, D.L., et al. "Threshold Characteristics of Planar and Index-Guided Microcavity Lasers," *Applied Physics Letters*, *67*(1):4–6 (July 1995).

33. Huffaker, D.L., et al. "Low Threshold Half-Wave Vertical-Cavity Lasers," *Electronics Letters*, *30*(23):1946–1947 (November 1994).

34. Ikegami, T. "Reflectivity of Mode at Facet and Oscillation Mode in Double-Heterostructure Injection Lasers," *IEEE Journal of Quantum Electronics*, *QE-8*(6):470–476 (June 1972).

35. Itoh, T., et al., editors. *Finite Element Software for Microwave Engineering.* John Wiley and Sons, Inc., 1996.

36. Jackson, J.D. *Classical Electrodynamics* (2nd Edition). John Wiley and Sons, 1975.

37. Jin, J. *The Finite Element Method in Electromagnetics.* John Wiley and Sons, Inc., 1993.

38. Kardontchik, J.E. "Mode Reflectivity of Narrow Stripe-Geometry Double Heterostructure Lasers," *IEEE Journal of Quantum Electronics, QE-18*(8):1279–1286 (August 1982).

39. Kendall, P.C., et al. "Theory for Calculating Approximate Values for the Propagation Constants of an Optical Rib Waveguide by Weighting the Refractive Indices," *IEE Proceedings, 134 pt A*(8):699–702 (September 1987).

40. Lee, J.-F., et al. "Tangential Vector Finite Elements for Electronagnetic Field Computation," *IEEE Transactions on Magnetics, 27*(5):4032–4035 (September 1991).

41. Lewin, L. "A Method for the Calculation of the Radiation-Pattern and Mode-Conversion Properties of a Solid-State Heterojunction Laser," *IEEE Transactions on Microwave Theory and Techniques, MTT-23*(7):576–585 (July 1975).

42. Loehr, J.P. *Physics of Strained Quantum Well Lasers.* Kluwer Academic Publishers, 1997.

43. Loehr, J.P., et al. "Effects of Native Oxides and Optical Confinement on Microcavity VCSEL Spontaneous Emission." *Physics and Simulation of Optoelectronic Devices VI 3283.* Proceedings of the SPIE. January 1998.

44. Lott, J.A. and M.J. Noble. "Model of Intra and Extracavity Photodetection for Planar Resonant Cavity Light Emitting Diodes." *24th International Symposium on Compound Semiconductors.* 1997.

45. Maloney, J., et al. "Generalization of PML to Cylindrical Geometries." *13th Annual Review of Progress in Applied Computational Electromagnetics.* 900–908. 1997.

46. The MathWorks, Inc. *Partial Differential Equation Toolbox 2.0: User's Guide*, 1997. Documentation for Beta test.

47. Meystre, P. and M. Sargent III. *Elements of Quantum Optics.* Springer-Verlag, 1991.

48. Michalzik, R. and K.J. Ebeling. "Generalized BV Diagrams for Higher Order Transverse Modes in Planar Vertical-Cavity Laser Diodes," *IEEE Journal of Quantum Electronics, 31*:1371–1379 (1995).

49. Nedelec, J. C. "Mixed Finite Elements in $\mathbf{R}^3$," *Numerische Mathematik, 35*:315–341 (1980).

50. Noble, M.J., et al. "Analysis of Microcavity VCSEL Lasing Modes using a Full Vector Weighted Index Method," *IEEE Journal of Quantum Electronics* (1997). In Review.

51. Noble, M.J., et al. "Calculation of Microcavity VCSEL Field Modes using a Doubly Iterative Weighted Index Method." *Physics and Simulation of Optoelectronic Devices V*. Number 2994 in Proceedings of the SPIE. 259–266. February 1997.

52. Noble, M.J., et al. "Calculation of VCSEL lasing mode threshold gain with the weighted index method." *LEOS '97 Conference Proceedings2*. 354–355. November 1997.

53. Noble, M.J., et al. "Optimization of Microcavity VCSELs." *Vertical Cavity Surface Emitting Lasers II*. Number 3286 in Proceedings of the SPIE. January 1998.

54. Noble, M.J., et al. "Analysis of Three Dimensionally Confined Microcavity Surface Emitting Lasers using Vector Finite Elements." *IEEE Summer Topical Meetings: Vertical-Cavity Lasers*. August 1997.

55. Noble, M.J., et al. "Design of Low-Threshold, Single-Transverse Mode VCSELs using the Transverse Confinement Optical Mode Separation." *Advances in Vertical Cavity Surface Emitting Lasers 15*. OSA Trends in Optics and Photonics, edited by C. Chang-Hasnain, Optical Society of America, 1997.

56. Noble, M.J., et al. "Rigorous Optical Analysis of Oxide-Apertured Microcavity VCSELs using Vector Finite Elements," *IEEE Journal of Quantum Electronics* (1998). In Review.

57. Noble, M.J., et al. "Calculation and Measurement of Resonant-Mode Blueshifts in Oxide-Apertured VCSELs," *IEEE Photonics Technology Letters*, *10*(4) (April 1998).

58. Okoshi, T. *Optical Fibers*. New York: Academic Press, 1982.

59. Polstyanko, S.V. and J.-F. Lee. "$H_1(curl)$ Tangential Vector Finite Element Method for Modeling Anisotropic Optical Fibers," *Journal of Lightwave Technology*, *13*(11):2290–2295 (November 1995).

60. Pozar, D.M. *Microwave Engineering*. Addison-Wesley, 1990.

61. Robertson, M.J., et al. "The Weighed Index Method: A New Technique For Analyzing Planar Optical Waveguides," *IEEE Journal of Lightwave Technology*, 7(12):2105–2108 (December 1989).

62. Saad, Y. *Numerical Methods for Large Eigenvalue Problems*. Manchester University Press, 1992.

63. Sacks, Z.S., et al. "A Perfectly Matched Anisotropic Absorber for Use as an Absorbing Boundary Condition," *IEEE Transactions on Antennas and Propogation*, *43*:1460–1463 (1995).

64. Sadiku, M.N.O. *Numerical Techniques in Electromagnetics*. CRC Press, 1992.

65. Saleh, B.E.A. and M.C. Teich. *Fundamentals of Photonics*. John Wiley and Sons, Inc., 1991.

66. Shin, H.-E., et al. "780 nm Oxidised Vertical-Cavity Surface-Emitting Lasers with $Al_{0.11}Ga_{0.89}As$ Quantum Wells," *Electronics Letters*, *32*(14):1287–1288 (July 1996).

67. Shin, J.-H., et al. "Very Small Oxide-Confined Vertical Microcavity Lasers with High-Contrast AlGaAs/Al_xO_y Mirrors," *IEEE Photonics Technology Letters* (June 1998).

68. Silvester, P.P. and R.L. Ferrari. *Finite Elements for Electrical Engineers* (3rd Edition). Cambridge University Press, 1996.

69. Snitzer, E. "Cylindrical Dielectric Waveguide Modes," *Journal of the Optical Society of America*, *51*(5):491–498 (May 1961).

70. Snyder, A.W. and J.D. Love. *Optical Waveguide Theory*. Chapman and Hall, 1983.

71. Soda, H., et al. "GaInAsP/InP Surface Emitting Injection Lasers," *Japanese Journal of Applied Physics*, *18*(12):2329–2330 (December 1979).

72. Sun, D., et al. "Spurious Modes in Finite-Element Methods," *IEEE Antennas and Propagation Magazine*, *37*(5):12–24 (October 1995).

73. Vurgaftman, I. and J. Singh. "Spatial and Spectral Characteristics of Spontaneous Emission from Semiconductor Quantum Wells in Microscopic Cylindrical Cavities," *Applied Physics Letters*, *67*(26):3865–3867 (December 1995).

74. Wong, M.F., et al. "Axisymmetric Edge-Based Finite Element Formulation For Bodies Of Revolution: Application To Dielectric Resonators." *IEEE Microwave Theory and Techniques (MTT-S) Digest*. 285–288. 1995.

75. Yamamoto, Y., et al. "Microcavity Semiconductor Laser with Enhanced Spontaneous Emission," *Physical Review A*, *44*(1):657–667 (July 1991).

76. Yang, G.M., et al. "Ultralow Threshold Current Vertical-Cavity Surface-Emitting Lasers Obtained with Selective Oxidation," *Electronics Letters*, *31*(11):886–888 (1995).

77. Yokoyama, H. and K. Ujihara, editors. *Spontaneous Emission and Laser Oscillation in Microcavities*. CRC Press, 1995.

Vita

Captain Noble was born on 18 Aug 1967 in Ft. Meade, MD. He attended Rensselaer Polytechnic Institute where he graduated in 1989 with a Bachelor of Science Degree in Electrical Engineering. Upon graduation, he accepted a commission in the United States Air Force. In July 1989, Captain Noble reported to his first duty station at Norton AFB, CA. During his four year tour at Norton AFB Captain Noble performed acquisition management and engineering duties at the Ballistic Missile Organization. In May 1993, Captain Noble was assigned to the Air Force Institute of Technology, where he has earned a Masters of Science degree in Electrical Engineering in 1994, and continued on to pursue the Doctor of Philosophy degree.

Permanent address: 5117 Pumphery Drive
Fairfax, Virginia 22032

REPORT DOCUMENTATION PAGE	Form Approved OMB No. 0704-0188

1. AGENCY USE ONLY *(Leave blank)*	2. REPORT DATE	3. REPORT TYPE AND DATES COVERED
	18 Mar 98	Dissertation

4. TITLE AND SUBTITLE
Optical Physics of Microcavity Surface Emitting Lasers

5. FUNDING NUMBERS

6. AUTHOR(S)
M.J. Noble

7. PERFORMING ORGANIZATION NAME(S) AND ADDRESS(ES)
AFIT/ENG, 2950 P Street, Bldg 640, WPAFB, OH 45433

8. PERFORMING ORGANIZATION REPORT NUMBER
AFIT/DS/ENG/98-03

9. SPONSORING/MONITORING AGENCY NAME(S) AND ADDRESS(ES)
Dr. John P. Loehr
AFRL/AADP, Bldg 620, WPAFB, OH 45433
(937) 255-2227 x3388

10. SPONSORING/MONITORING AGENCY REPORT NUMBER

11. SUPPLEMENTARY NOTES

12a. DISTRIBUTION AVAILABILITY STATEMENT
UNLIMITED

12b. DISTRIBUTION CODE

13. ABSTRACT *(Maximum 200 words)*

This dissertation consists of an in-depth theoretical analysis of the optical impact of transverse index confinement on the lasing modes of microcavity surface emitting lasers. Two different variational techniques were employed to calculate the relevant optical laser parameters: modal resonance, field profile, confinement factor, and threshold gain.

Through a semianalytic field analysis, two new confinement related effects were discovered: a polarization dependent change in mirror reflectance with aperture radius, and a mode dependent blueshift. Through a numerical field analysis, the physical mechanisms governing diffraction were ascertained. These are: the transverse confinement of the optical mode, the degree of tilt of the mode propagation vector away from normal to the mirror surfaces, and the density of parasitic modes in the spectral vicinity of the lasing mode. Based on these results, a new semianalytic technique was derived for estimating diffraction loss via rigorous coupling to the parasitic modes. Finally, this model was combined with a gain model and a new mode density model to compute spontaneous emission rate, light verses current, threshold current, and spontaneous emission factors for a low threshold oxide-apertured device.

14. SUBJECT TERMS	15. NUMBER OF PAGES
Microelectronics, Semiconductor Lasers	188
	16. PRICE CODE

17. SECURITY CLASSIFICATION OF REPORT	18. SECURITY CLASSIFICATION OF THIS PAGE	19. SECURITY CLASSIFICATION OF ABSTRACT	20. LIMITATION OF ABSTRACT
UNCLASSIFIED	UNCLASSIFIED	UNCLASSIFIED	UL